UNIVERSITAT DE LES ILLES BALEARS
DEPARTAMENT DE FISICA

Nonlinear Dynamics and Synchronization of Bidirectionally Coupled Semiconductor Lasers

Tesi presentada per Raúl Vicente, en el Departament de Física de la Universitat de les Illes Balears, per optar al grau de Doctor en Física.

Palma, June 2006

El director de tesi Claudio R. Mirasso Santos Titular Universitari
de la Universitat de les Illes Balears certifica que aquesta tesi doc-
toral ha estat realitzada pel Sr. Raúl Vicente Zafra, i perquè quedi
constància escrita firma

a Palma 5 de Juny de 2006.

Claudio R. Mirasso Santos

A mis padres, por recordarme tantas veces que sabe más el zorro por viejo que por zorro.

Agradecimientos

En primer lugar, y no podía ser de otra manera, quisiera agradecer a Claudio Mirasso la confianza, el respeto y la amistad que me ha brindado durante todos estos años. Este trabajo se ha beneficiado directamente de su diligente coordinación y del clima que ha sabido generar para que el intercambio de ideas y discusiones fueran bienvenidos en cualquier momento. También me quiero acordar aquí del afecto expresado hacia mi por Alejandra y Nico (mi mamita y hermanito en Los Angeles) cuando estaba lejos de casa.

Este trabajo no hubiera sido el mismo sin la gran ayuda y constante revisión de Josep Mulet, a quien le agradezco profundamente todas las horas de provechosas discusiones que hemos pasado y de quien espero se me haya pegado algo de su saber hacer.

A Toni Pérez le debo probablemente el estar escribiendo estas lineas ahora mismo. Él fue quien me habló por primera vez de un proyecto relacionado con láseres caóticos y demás. Son incontables las horas de trabajo científico y de diversión que hemos compartido dentro de la EFE y fuera de ella. Por toda la ayuda prestada en tantas ocasiones, miles de GRACIAS!

A Pere Colet, con quien he tenido la oportunidad de colaborar en alguna ocasión, me gustaría también mostrarle mi gratitud por estar siempre abierto a escuchar y debatir cualquier tipo de problema científico con el que uno le vaya a molestar a su despacho.

En definitiva, gracias a todo el personal del IMEDEA y del Departamento de Física de la UIB con quienes siempre me he encontrado todas las puertas abiertas. También quiero agradecer explícitamente a Maxi (aunque todavía no tenga la camiseta ni la gorra del IMEDEA...) el hecho de que nos obligue a ir a los seminarios. En cinco años de charlas uno llega a desarrollar un interés por lo interdisciplinar difícilmente fomentable de alguna otra manera.

Quisiera también mencionar a Javier Buldú por su ayuda y colaboración tanto

en trabajos científicos como por lo bien que lo hemos pasado en distintas conferencias por el mundo (Atenas, Pavia, Metz, etc...) y a Jordi García-Ojalvo, María Carme Torrent y Cristina por hacer de la UPC en Terrasa un sitio tan acogedor y agradable para hacer ciencia.

Ingo Fischer ha sido sin duda uno de los artífices de que este trabajo llegue a buen puerto. Le agradezco enormemente no sólo la amabilidad y paciencia que ha tenido conmigo sino también la calidad y cantidad de las ideas que me ha comunicado desde que le conocí y algunas de las cuales se encuentran en las siguientes páginas. Marc Sciamanna es otro gran investigador de quien uno puede aprender mucho y a quien mucho la colaboración que tuvimos sobre la dinámica de VCSELs. A Michael Peil tambien le agradezco las discusiones que hemos tenido juntos y la fiabilidad de sus resultados experimentales que han permitido validar y fomentar muchos de los resultados aquí expuestos.

El Profesor Jia-ming Liu fue quien me dio la oportunidad de visitar UCLA (la segunda mejor universidad del mundo despues de la UIB) y vivir por una temporada (casi nueve meses) en Estados Unidos. Es a él y a mis companeros de laboratorio Howard, Steven, Shuo, Frank, Nelson, Margaret, Juan, Rose Mary, Manuel y Rider a quienes les debo gran parte de que mi estancia en Los Angeles sencillamente maravillosa. No tengo palabras para agradecer el trato y cariño allí recibido por la genial cantante de Jazz y mejor compañera de piso, Shirlee. Todavía echo de menos a Matilda, las visitas al Cafe Roma y tus cinnamon rolls!

De los compañeros en la EFE que voy a decir después de que me hayan tenido que aguantar durante casi 5 años!!! Mis compañeros de cubículo, desde los solares como Iñigo, Jaume, Toni o Pep, hasta los más interdisciplinares como Pau, Iacyel y Dani se merecen lo mejor. Todos los miembros de la EFE, los nuevos y los veteranos, han sido excelentes a la hora de crear un agradable lugar de trabajo. Siempre me acordaré de las tertulias con Lolo, del incombustible Pierre, o de Juanjo guardando la bandera de la EFE... Gracias también al duo Tessone-Adrian (o Linux vs Windows) por aclararme cualquier duda informática casi en tiempo real. A Yanne también le quiero expresar mi simpatía ya que he disfrutado mucho hablando con él sobre muchos temas que iban desde los retos del África de hoy hasta divagaciones de cosmología o mecánica cuántica.

Ya en el plano completamente personal, como me iba a olvidar del G5: Miguel, Nieto, José, Alfredo y Juanmi con quienes desde que nos conocimos en San José he crecido y compartido tanto, incluso ese inolvidable viaje en coche por toda California y alrededores. Lo que pasa en Las Vegas se queda en Las Vegas! David Esteban es otro de esos viejos amigos que siempre están ahí cuando se los necesita.

Muy especialmente quiero agradecer a Dana Alic su amistad y comprensión mientras escribía esta tesis. Gracias de verdad.

Lo mejor del curso del CAP (después de la V de Godwing por supuesto) es el haber conocido a Penelope Glamour (na Joana), na Marineta, na Lida y en Xavi. Lo que nos hemos reído juntos y lo que nos queda. Gracias por todo chicos!

En definitiva, gracias a todos aquellos de los que he aprendido algo y a quienes me tienen que soportar voluntaria o involuntariamente cada día. Por cierto, Zidane probablemente nunca llegue a leer esto pero gracias por esos magníficos domingos por la tarde que los miembros de la EFE imitamos tan mal en los partidillos de los jueves.

A mi familia, padres, hermanos y sobrinos, decirles que sin ellos no sería nada y que esto por pequeño que sea, va por ellos!

Junio 2006, Palma, Raúl Vicente Zafra

Acknowledgments

First, I would like to thank Claudio Mirasso for the trust, respect, and friendship that he has offered to me during all these years. This work has been directly benefitted from his diligent coordination and from the environment that he has generated to foment the exchanges of ideas and discussions at any moment. I would also like to mention the goodwill and affection I received from Alejandra and Nico when I was far away from home.

This work would have never been the same without the help and constant supervision of Josep Mulet, to whom I profoundly thank all the time we have spent on fruitful discussions and improving this work.

Toni Perez is probably the responsible of the fact that I am writing this words right now. He was the first in telling me about a project related to chaotic lasers and more... The hours we have spent working hard on a scientific problem or having fun inside or out of the EFE Agency are just countless. For all the help, THANK YOU!

To Pere Colet, with whom I have had the opportunity to collaborate with, I would like to express my acknowledgments for his open mind and willing to listen and discuss about almost any problem with which one can visit him in his office.

In summary, thanks to everybody at IMEDEA and the Departament de Física where I have always found all the doors opened. I would also like to particularly thank Maxi (even though I am still waiting for the IMEDEA T-shirt and cap) to force us to attend to all the seminars. In five years of talks one develops an interest for interdisciplinary research very difficult to promote in any other way.

I would also like to mention Javier Buldú for his help and collaboration in both scientific works and social life around the world (Athens, Pavia, Metz, etc...) and to Jordi García-Ojalvo, María Carme Torrent and Cristina to make the UPC at Terrassa a homy and comfortable place to do Science.

Ingo Fischer have been without any doubt one of the persons who contribute most to this work. I really thank his kindness and the huge quality and quantity of the ideas he has transmitted to me since we met and which some of them are collected in the following pages. Marc Sciamanna is another great researcher from whom one can really learn and I thank him a lot the collaboration on the VCSELs dynamics. I thank Michael Peil the profitable discussions we have maintained and the quality of his experimental research that has lead to the validation and deeper motivation of the results exposed here.

Professor Jia-ming Liu was the person who gave me the unforgettable opportunity to visit UCLA (the second best university after UIB) and to live for a while (almost nine months) in the amazing city of Los Angeles. He and my lab mates Howard, Steven, Shuo, Frank, Nelson, Margaret, Juan, Rose Mary, Manuel and Rider (thanks for the tequila amigo) are big responsibles for the great time I had in LA. I have no words to express my gratitude towards the kindly treat and support I received from the genial Jazz singer and best roommate, Shirlee. I still miss Matilda, the visits to Cafe Roma, and your cinnamon rolls!

What can I say about my EFE mates after they stood me for so long. My office mates, from the Solar guys Iñigo, Jaume, Toni and Pep, to the more interdisciplinary souls Pau, Iacyel and Dani deserve a place in heaven. All the people from the Agency, the newcomers and the veterans, have been excellent companions and have created a great working place. I will always remember the countless laughs I shared with Lolo, the energy of Pierre or Juanjo the tireless... Thanks also to the pair Tessone-Adrian (or Linux vs Windows) for kindly clarifying in real time all the computer science doubts I had. I would also like to express my sympathy to Yanne for the enjoyable discussions about the most diverse topics.

In the personal dimension how could I forget about the G5 team: Miguel, Nieto, José, Alfredo and Juanmi with whom I have grown up since we met in San José, including a great trip we made through California and surroundings. What happen in Vegas, stay in Vegas! David Esteban is a good and old friend who has helped me in many cases. Thanks guys!

Very specially I would like to thank Dana Alic her friendship and support while writing this these. My most sincere and profound gratitude for everything Danuca!

The best from the CAP classes (of course, after the Godwing V lesson) it has been to meet Penelope Glamour (na Joana), na Marineta Cafeina, na Lida GPS, and en Xavi (alias en Farril Carril). We have shared great moments and I hope that there is still a lot more to come.

In conclusion, thanks to everybody from who I have learned something in this life and to those who stand me everyday voluntarily or not. Zidane, you will never read this words but thanks for these wonderful Sunday afternoons.

To my family, parents, brother, syster, and nephews, I would like to tell you that I would not be anything without you, and this work even small is dedicated to you!

Contents

Chapter 1

Preface

$\mathcal{S}$YNCHRONIZATION is the dynamical process by which two or more oscillators adjust their rhythms due to a weak interaction [1]. Part of the universality of this phenomenom comes from the vast variety of systems able to experience this effect. By just thinking about the many different objects present in Nature that periodically repeat its state, i.e., oscillate, and that these systems are generally not isolated but interacting with each other, it is easy to recognize that synchronization must be acting on a huge number of structures at different scales [2]. From an audience in which people tend to accommodate their claps to sound in unison [3], to thousands of pacemaker cells in our heart tissue spiking their action potentials together to induce a beat in our heart every few seconds, the objects able to experience sync cover a wide spectrum [4]. Today, synchronization is studied in hundreds of examples of engineering and physical sciences, as well as in the less understood and challenging biological and social entities [1, 4, 5].

To explain the basics of synchronization let us take a brief glance to a modern adaptation of one of the earliest examples in which sync was ever noticed more than three centuries ago. The historical setup consisted of a set of two pendulum clocks hanging from a common support [1]. In a more recent and musical version of such an experiment we consider two almost identical pendulum metronomes resting on a light wooden board which lies on two soda cans [6]. The setup can be seen in Figure 1.1. Usually, one can set any of the metronomes to beat from few decades to hundreds of times per minute. By prescribing slightly different frequencies of oscillation to both metronomes, one expects that their pendula would remain swinging at different rhythms. However, when both timekeepers sit on the same movable platform, it is usually observed that their formerly uncorrelated audible ticks start to approach in time, and eventually they end up being heard in unison. Then, we say that the metronomes have synchronized. The almost unnoticeable motion of the base is responsible for the momentum transfer, or "communication", between both metronomes in such a way that it usually favors the

simultaneous swing of both pendulum bobs. How long it takes the system to reach this state and whether this sympathy of swings occurs with the pendula bobs moving toward the same or opposite directions, are questions whose solution depends on the details of the system, such as the mass of the pendula and the friction of the base. But the important point here is that this effect is by no means a matter of chance. It develops for a determined range of disaccord in the frequencies of both metronomes before coupling them, and when it appears is stable to small perturbations of the system. It is this robust capability of a precise matching of oscillations between different systems what the concept of synchronization is about.
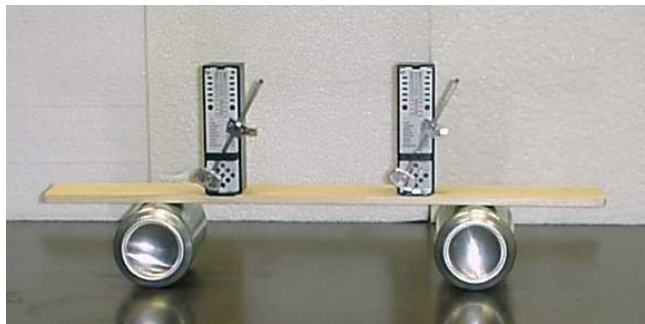
Figure 1.1. A pair of similar metronomes laying on a light wooden base is a very simple and illustrative system demonstrating synchronization. The horizontal movement of the platform is the responsible for coupling the motion of both oscillators. After Ref. [5].

Since it was first formally described by Christiaan Huygens in 1665 [1] synchronization, understood as an agreement or entrainment of rhythms, has been extensively reported in very diverse fields. It is exploited for hightech applications in devices such as electric power generators or Josephson junctions SQUIDs[1] [1]. By the same phenomenon, chemical oscillations are able to be entrained to a given period, as in the famous Belousov-Zhabotinsky reaction subject to optical forcing [1]. In other order of complexity, physiological levels of different hormones and proteins are governed by biological clocks, which are able to adjust and lock their rhythms to the frequency of an appropriate external modulation. In a clear example, circadian rhythms in our bodies are consequences of the adaptation of our biological clocks to the 24-hours day-night oscillation of variables such as temperature or illuminance [1, 4, 5]. Spectacular cases of synchronization are also found in large populations of living organisms. The simultaneous chirp of some singer crickets in a house yard or the coincident flashing of thousands of fireflies (Figure 1.2) in the riverbanks of southeast Asia have amazed the scientists and the general public for centuries [5]. Sometimes, however, the appearance of synchronization has unexpected side effects that are not funny at all. In its opening day, a lateral excitation of the London's Millennium Bridge was induced by the hundreds of people's synchronized walking pace. The amplitude of the oscillation of the

---

[1]SQUID stands for Superconducting QUantum Interfering Device and it is the most sensitive magnetic field detector known to man.

bridge exceeded seven centimeters and it was enough to spread an unpleasant and even scaring feeling among the pedestrians [5].

The examples commented before concern very diverse systems and nevertheless, all of them share the characteristic of falling into the category of either periodic oscillators or rotators. If this was the full story, even occupying an important place in science and technology, synchronization would have not become one of the hottest research topics in nonlinear science as it is considered today. A great boost that was to shake the investigation in synchronization came in the early nineties, from probably one of the more unexpected ways.

Figure 1.2. Thousands of fireflies from the *Lampyridae* family flashing simultaneously in a cave in New Zealand.

In February of 1990, Lou Pecora and Tom Carroll, from the US Naval Research Laboratory at Washington D.C., published in Physical Review Letters a paper entitled "Synchronization in Chaotic Systems" [7]. By that time, just to have in mind the idea of synchronizing two of such systems could be easily qualified by any expert in the field as a hopeless task. Chaos is a dynamical regime in which a system becomes extremely sensitive to initial conditions and reveals an unpredictable and random-like behavior, even though the underlying model of a system exhibiting chaos can be deterministic and very simple[2]. If there was a system challenging the capability of synchronizing that was a chaotic one. And yet, Pecora and Carroll were right. They demonstrated that chaotic synchronization could be achieved by driving or replacing one of the variables of a chaotic system with a variable of another similar chaotic device. A pair of Lorenz systems, being considered as one of the most paradigmatic models in chaos theory, was selected in their paper to numerically prove chaotic synchronization for the first time.

The illustration of the convergence of two chaotic trajectories to the same values opened a new perspective to fundamental questions in the previously independent chaos and synchronization themes. Applications, on the other hand, found in the newborn chaotic synchronization a promising tool to be exploited in spread spectrum communications and cryptography. In this last field, the main idea consists of hiding or encrypting a message into the noise-like trace of a chaotic output and use the chaotic synchronization property by an authorized part to recover the message. The masking of the message to be encoded is usually performed at the

---

[2]Only three nonlinear ordinary differential equations or even one non-invertible map are enough to produce a chaotic flow of data in a computer.

physical layer by the "mix" of the signal with a chaotic carrier generated by a nonlinear element. After the transmission over an appropriate communication channel, the recovery of the message is based on the synchronization phenomenon, by which a receiver, quite similar to the transmitter, is able to reproduce the chaotic part of the transmitted signal. Then, by a proper comparison of the input and output at the receiver, an efficient decoding of the message can be performed. In 1993, two researchers from the MIT experimentally demonstrated the working principle of this private communication scheme [8]. They used analog electronic circuits emulating the behavior of two chaotic Lorenz systems. However, electronic circuits suffer from severe drawbacks that make them unsuitable for practical communication schemes. Electronic circuits have in general a restricted bandwidth limited to a few tens of kHz, and moreover their output signal is not suited for modern communication transmission lines based on optical fibers. A natural question was then, is there any source with a large bandwidth, inherently nonlinear and ready to be used in real communications standards?

The answer had five letters, LASER. Since May 1960, when Theodore H. Maiman succeeded for the very first time in History to maintain a laser action in a ruby crystal[3], these devices have truly revolutionized industries such as communications or medicine. In 1994, Pere Colet and Rajarshi Roy working then at the Georgia Institute of Technology, proposed a solid-state laser system to demonstrate synchronization and message encryption in the optical domain [9]. However, very soon the attention moved toward another class of lasers much more promising for this and other applications in consumer electronics and information technology, the Semiconductor Lasers (SLs).

Figure 1.3. Typical semiconductor laser with its package capsule.

While in the beginning of the laser era the dream of any laser scientist was to achieve a stable, high-intensity and spectral pure laser beam, the modern perspective today is to promote the understanding and control of the laser instabilities, i.e., deviations from its continuous wave (CW) emission. In this respect, it took little time to realize that SLs are nonlinear dynamical systems able to generate a rich variety of behaviors and that we could actually take a great advantage from it. The generation of ultrashort pulses, all-optical processing of information, creation of carrier signals in the microwave range, or cryptography based on chaotic communications are just a few examples of applications that benefitted from our present control on the dynamics of lasers. The scenarios leading to dynamical instabilities in a SL are diverse. Either by modulating its injection current, injecting light into its active material,

---

[3]Interestingly several investigators though to have demonstrated by that time that laser emission could not be generated with ruby as an amplifier medium.

or feeding back part of the emitted light, a SL is capable of exhibiting dynamical instabilities. These cases are paradigmatic examples where a self-interaction or unidirectional influence on a SL leads to a complex dynamical behavior. Fortunately, they are not the only options to explore the exciting properties of the dynamics of lasers.

This work is devoted to the investigation of the instabilities due to mutual interaction between two SLs. The reasons for the convenience of such a study are multiple. First, under the nonlinear dynamics vision, this configuration serves as an excellent testbed model for one of the most ubiquitous processes in Nature, i.e., the mutual interaction of two oscillators. It is worth to note that the reciprocal or bidirectional action between two systems should not be considered just as a double unidirectional problem. The intuition gained in studies of unidirectional schemes can easily fail when applied to a bidirectional configuration. In a mutually coupled situation, for instance, the time the signal needs to come from one system to propagate up to the other might become a critical parameter. This is the case for SLs. Due to the huge speed of the light, two SLs a few centimeters apart involve interaction delay times of the same order than the time scale of the SL dynamics, typically in the subnanosecond range. The fact that these two time scales are comparable makes the interaction delay time an extremely important consideration in the qualitative and quantitative behavior of the system. Second, from the applications point of view the study of the instabilities arising from the coupling of several SLs can produce some practical benefits. The coherent summation of the oscillations of the electric fields of many SLs has been used since years as a simple way to obtain high-intensity laser beams, while locking is a key phenomenon in synchronization that is of interest in applications such as frequency stabilization and wavelength tunability. Optical bistability is another feature present in the mutually coupled scheme of two SLs and its use is of central importance for all-optical information processing techniques. Finally, a better understanding of chaotic synchronization in bidirectionally coupled arrays of SLs can lead to new ideas and improvements in applying optical chaos to encryption purposes.

What type of dynamical instabilities will arise when coupling two or more similar SLs? Under what conditions will these instabilities be able to come into sync? How does a delay in the interaction between two of such systems affect their synchronization? How do the number of units in an array of SLs and the topology of the network of connections influence their state of sync? Which features of synchronization are model-independent and which are specific to the details of the SL nature? Certainly, with such interesting questions some efforts have already been made in order to explore the instabilities in mutually coupled configurations of lasers [10–12]. However, a general overview of the mechanisms of synchronization in the presence of a time delayed interaction is still necessary. Essentially, the

aim of this thesis is to contribute to a satisfactory answer to the former questions and some related aspects. A principal objective is then, to track the routes of the emergence of complex instabilities arising from the mutual interaction of SLs and study their synchronization properties.

To successfully accomplish this goal, it is necessary to analyze appropriate models of semiconductor lasers under the nonlinear dynamics perspective. Consequently, in the next chapters of this thesis, the necessary concepts and tools to carry out this task are developed. Starting by defining what synchronization means and identifying the requirements that are needed to call the simultaneous variation of two variables synchronization, it is proceeded with the presentation of the different hallmarks and measurements of sync (Chapter 2). The next chapter is dedicated to the study of delay-differential equations (DDE) and their stability. This type of equations naturally appears in our modeling of schemes of coupled SLs and their understanding and manipulation is basic for any analysis of the models. The fourth chapter collects a short description of the most popular bifurcations occurring in dynamical systems. Finally, a summary of the basics of SLs modeling and dynamics is presented in Chapter 5.

The description of the subsequent chapters proceeds as follows:

- Chapter 6. This chapter investigates the dynamics of a system consisting of two SLs with an optoelectronic interaction. In this type of coupling the output light from each laser is converted into a photocurrent and the resulting electronic flow is used to drive the bias current of the other SL. In a similar way, a delayed self-interaction is introduced through a feedback loop. The feedback strength and delay time are quantities that control the dynamical state of the uncoupled SLs. By changing the value of these parameters one can tune the laser optical intensity to operate in a CW state, oscillate, emit short pulses, or even behave in a chaotic way.

  First, an appropriate modeling of the system to describe the SLs′ dynamics up to the required temporal resolution is needed. The work progresses with the application of bifurcation theory to the dynamical system resulting from the model. This analysis is sometimes far from trivial due to the appearance of delayed variables in the equations. When possible, analytical descriptions of the regions in the parameter space where a given instability develops are reported. If not, extensive numerical simulations are performed to characterize and illustrate specific phenomena, like the quenching of oscillations in the system due to their delayed interaction, also known as "death by delay" effect [13, 14], or some symmetry-breaking events. Bifurcation diagrams and the computation of the cross-correlation function and Hilbert phase are used to evaluate the synchronization dynamics of the system upon variation of the coupling rate and delay time. Still in the synchronization issue, the

Arnold tongues' dependence on the delay time is numerically demonstrated.

Laboratory experiments regarding the route to chaos and the "death by delay" effect were performed in collaboration with the Electrical Engineering Department of the University of California, Los Angeles (UCLA). These results are used to check the corresponding theoretical and numerical predictions and motivate further investigation of the system.

- Chapter 7. The optical field description of a typical Edge-Emitting Laser (EEL) is basically scalar. These devices generally emit in a single and well defined polarization state and the dynamics of the optical intensity follows the one of the carriers number. How two vectorial oscillators behave and synchronize under their bidirectional interaction is therefore a question that one cannot answer by studying typical EELs. Another laser structure with more degrees of freedom is required for such studies. Vertical-Cavity Surface-Emitting Lasers (VCSELs) are, on the other hand, extremely interesting and useful devices that can help us in this respect. Their main characteristic is that they lase in the orthogonal direction to the junction plane. A direct consequence of this feature is that their polarization direction is not fully fixed. They usually emit linearly polarized (LP) light along one of two orthogonal preferred directions ($\hat{x}$ and $\hat{y}$) due to the weak material and cavity anisotropies [15]. VCSELs are then, excellent candidates to study the synchronization properties of vectorial oscillators. From the nonlinear dynamics point of view, this type of lasers has also the advantage of suffering from instabilities not easily found in an isolated EEL, such as polarization switching (PS) and an inherent polarization bistability. In this chapter the nonlinear dynamics of two bidirectionally linked VCSELs is studied. This time, however, the interaction between the two lasers is chosen to be of coherent nature. Each laser is subjected to the direct light injection of its counterpart.

  After adapting a well known model of a solitary VCSEL to take into account the mutual influence between the lasers, the origin of the PS induced by the mutual coupling of two VCSELs is presented. The exact mechanism is explained in terms of the bifurcations that the fixed points of the system undergo. A characterization of the bistable PS is performed with views to fast switching applications. The study of the effects of a misalignment between the two eigenaxes of the coupled VCSELs results into another type of PS which can be induced by rotating one of the VCSELs with respect to the other. Moreover, by this rotation stable elliptic polarization modes are found to be stable in this condiguration. Finally, under the idealized hypothesis of the non-existence of anisotropies, the synchronization of the polarization dynamics of two bidirectionally coupled VCSELs is reported. In this case,

both polarization vectors diffuse around the equator of the Poincaré sphere because of noise sources. However, computation of the cross-correlation function between the Poincaré components of both VCSELs reveals a clear entrainment between them.

- Chapter 8: In an ensemble of interacting systems, as important as the dynamics of the individual agents is the network of connections that link the nodes. It is natural then to ask how the synchronization would look like in an array of three or more SLs with different type of connections. In 1990, Herbert G. Winful and Luftur Rahman [16] already demonstrated chaos synchronization in a linear array of three mutually coupled SLs. They observed the identical synchronization between the first and third lasers in the array, while the temporal traces of any of the extreme lasers and the central one remained uncorrelated. A few years later, Rajarshi Roy and collaborators [17, 18] conducted experiments in 1-d and 2-d arrays of laterally coupled Nd:YAG lasers, in search for synchronization patterns across the array. In all these setups, however, the semiconductor or solid-state lasers interact through the overlap of their evanescent electric fields. For these cases the coupling is instantaneous. Then, some immediate questions pop up: how does a delay in the interaction between the lasers modify this picture? What type of synchronization solutions will be obtained? Is the number of lasers in the array a critical parameter in the sync structure?

  Here, we analyze the behavior of arrays of three up to six SLs mutually interacting with a finite time delay to provide an answer to the former questions. Computation of the cross-correlations index as a function of coupling strength and other parameters is performed for two different networks of connections; the open-end and loop configurations. Symmetry reasons show up to be responsible for the spatial distribution of the synchronization solution.

- Chapter 9: The main contributions and conclusions to this work are summarized. Future perspectives of the study of synchronization and dynamics of lasers is also conjectured in this section of the thesis.

Part I

Introduction

Chapter 2

An overview to synchronization

THE fundamentals of the synchronization phenomena, which will be studied in forthcoming chapters for interacting semiconductor lasers, were first noticed by the great Dutch scientist Christiaan Huygens as early as 1665. While sick and staying at bed for a couple of days watching two clocks hanging on a common support, Huygens observed "a wonderful effect that nobody could have thought before" and which later on in his memoirs he described as

> ... *It is quite worth noting that when we suspended two clocks so constructed from two hooks embedded in the same wooden beam, the motions of each pendulum in opposite swings were so much in agreement that they never receded the least bit from each other and the sound of each was always heard simultaneously.*

This historical example of synchronization and many other phenomena (as the synchronized dynamics of mutually-coupled lasers) can be understood within the unifying framework of the nonlinear sciences. We will start by defining what we mean by synchronization in the language of the nonlinear dynamics.

2.1 Definition

The modern definition of synchronization is an **adjustment of rhythms of oscillating objects due to their weak interaction**. Before going further in the exposition of the main features of sync, first, it is important to make clear what we exactly mean by concepts such as oscillating object, rhythm, or weak interaction.

Self-sustained oscillators

Strictly speaking, synchronization is only properly defined for a specific class of dynamical systems, namely nonlinear dissipative self-sustained oscillators. One should note that this statement is not so restrictive as it might seem.

Dissipation of energy occurs in most of macroscopic processes and it is responsible for the appearance of attractors in the phase space of a dynamical system. A limit cycle, i.e., an isolated closed curve in the phase space, is for instance the attractor associated to the motion of a dissipative periodic oscillator. Quasiperiodic and chaotic behavior develop on more complex geometrical patterns living in the phase space, as the torus and the so-called strange attractors, respectively. The appearance of such attracting structures is fundamental for the system to "forget" about its initial condition and make its motion stable under small perturbations. A conservative system, however, cannot stand as an adequate description of stable oscillations. As soon as the periodic movement of a conservative configuration is perturbed there is a variation in the energy of the system. Due to the need of conserving the newly acquired energy level any spontaneous returning to the old oscillatory orbit is strictly forbidden. Moreover, the nonlinearity of the system is a necessary condition to sustain stable oscillations. Linear dissipative systems are unable to maintain oscillations with a constant amplitude.

On the other hand, a self-sustained oscillator mainly differs from a driven one by the fact that the former is an autonomous system, whereas the later shows an explicit temporal dependence. Indeed, the periodical forcing in a driven oscillator imposes a "clock" on the dynamics that makes its motion on the oscillatory cycle being anchoraged or pinned to the external force. As a consequence forced oscillators are not able to experience synchronization with another system. Self-sustained oscillators, however, can easily shift their location or "phase" within the oscillatory loop and adapt their rhythms of oscillations.

Therefore, synchronization is mainly studied in regular (periodic) and complex (chaotic or quasiperiodic) self-sustained oscillators in dissipative dynamical systems. The peculiarities of synchronization in noise-induced oscillators will be presented in the following sections.

The rhythm of oscillations

The main attribute of the rhythm of a given oscillatory object is the characteristic time it takes the system to repeat a characteristic event. For a periodic oscillator, this characteristic time is obviously given by the period of the oscillation T. The inverse of the period, the cyclic frequency $f = 1/T$, is the principal quantifier of the rhythm of a self-sustained oscillator used along this work. Since a chaotic oscillator never repeats its state the characterization of its rhythm must be refined in this case. Thinking about a chaotic waveform as a series of cycles with different

amplitude and period, it is possible to define the mean frequency of the chaotic process as the number of cycles within a large interval of time. For noise-induced oscillators one can define the rhythm of the oscillations as the frequency of the transitions between different states of the system. Thus, in the stochastic bistable oscillator the "frequency" is defined as the inverse of the characteristic switching time between the two stable states. When a local potential description of the bistable problem is available this frequency is sometimes computable from the potential characteristics and noise intensity. The inverse of this frequency is usually known as the Kramers' time.

The strength of the interaction

The interaction or coupling between two oscillators can occur through rather complex mechanisms. Nevertheless, there is usually a small set of parameters that controls the intensity of the interaction, namely the coupling strength. Thus, the coupling rate regulates how strong an oscillator affects the motion of another. Of course, the mutual interaction need not to be symmetric. The extreme case of asymmetric coupling corresponds to an unidirectional influence of one oscillator on another. In any case, when the coupling strength is so strong that it implies severe restrictions on the degrees of freedom of the composed system, and as a result the motion of the two subsystems becomes necessarily unified, the synchronous motion of both subsystems becomes trivial. Loosely speaking, we talk about a true synchronization effect only if the coupling strength is weak enough. The frontier between a weak and strong coupling is not always clear. As a rule of thumb we will say that the interaction is weak, and consequently, one can speak about the appearance of a synchronization process, if the introduction of a coupling meets two requisites. First, it must not qualitatively change the behavior of the subsystems compared when they were isolated. And second, even coupled the individuality of each subsystem should be maintained.

In conclusion, synchronization can occur if:

- the systems are able to oscillate by their own, i.e., when isolated both systems exhibit stable self-sustained oscillations;

- the adjustment of rhythms between oscillators is achieved via a weak interaction.

Upon the requirement of such conditions, some phenomena that produce a correlated variation of two variables must be disregarded as true synchronization processes. This is the case, for instance, of the resonance of forced linear oscillators. Another example is the synchronous variation of coupling-induced instabilities.

When isolated these systems remain stable, and it is only after the introduction of a coupling term that they develop some kind of dynamical behavior. This phenomenom is preferred to be called entrainment of oscillations rather than sync.

The physical reasons why some coupled dynamical systems tend to sync are as diverse as the systems themselves. In a more abstract level, however, one can track this predisposition independently of the origin of the entities involved in the process. The next section tackles the appearance of synchronization in a unifying framework by ignoring the details of the oscillatory process and focusing on the generic properties of any limit cycle.

2.2   Why does synchronization take place?

In a dynamical system the Lyapunov Exponents (LEs) give the rate of exponential divergence from perturbed initial conditions [19]. Since the rate of separation can be different for different orientations of the initial separation vector, the number of LEs is equal to the dimension of the phase space considered. The Lyapunov spectrum is formed by all the Lyapunov exponents and they are a very important measure that give us a lot of information about a dynamical system. For instance, their sum indicates the average divergence of trajectories in a dynamical system. A negative sum indicates that we are dealing with a dissipative flow, whereas a zero value is, by the Liouville′s theorem, the signature of conservatives ones. The appearance of a chaotic regime is also registered by at least one LE becoming positive.

From its very definition, a zero LE is related to a direction in the phase space along which the distance between two initial conditions does not converge nor diverge. It is easy to prove that in a continuous dynamical system there is at least one LE that is zero and this corresponds to the direction of the flow, i.e., the trajectory of the system in the phase space. As a consequence, a perturbation over the length of that orbit can easily produce a displacement in the point describing the state of the system in the phase space. But what does this have to do with synchronization?

Well, it is precisely the **neutral stability along the orbit** of a limit cycle, i.e., the attractor associated to a periodic self-sustained oscillator, **the essential property which the synchronization effect relies on**. Let us see how this "freedom" in the motion along the limit cycle is the main attribute confering the system the possibility to synchronize.

By the phase of the oscillation one usually describes the position of a system within a cycle of its periodic waveform. The phase of a self-sustained oscillator is then the variable associated to a zero LE that corresponds to an orbit around its limit cycle. As a result, there is no a prefererred value for the phase but this can be easily adjusted by a weak perturbation or interaction. When such a perturbation

comes from the coupling with another oscillator, the outcome is a phase pulling which usually tends to fix the phase difference between them. For synchronization to occur, the phase pulling effect must dominate over another mechanism that goes in the opposite direction, this is the detuning in frequencies. The balance between this two mechanisms, natural detuning and phase pulling due to the coupling, dictates if synchronization eventually occurs. Only when the phase pulling is able to overcome the natural dispersion due to an uni- or bidirectional interaction synchronization shows up.

In large populations of coupled systems, **synchronization** can also be understood **as a self-organization process**. Without any master or leader entity governing the dynamics, the individual systems might spontaneously tend to oscillate in synchrony. Under appropriate conditions, the phase pulling effects on each oscillator manage to consistently evolve towards a state where a large fraction of the population maintains synchronous oscillations at a common frequency. In these cases, the network of connections between the elevated number systems is essential to determine if synchronization takes place or not. The most popular architectures in physical, biological, and social problems include the global or all-to-all coupling, lattice, random, small-world and scale-free networks. In this thesis, however, we mainly focus our studies in the synchronization and nonlinear dynamics of SLs in an 1-dimensional lattice. In Chapter 8 we tackle the importance of the opened or closed nature of this lattice.

The main distinctions of sync have already been commented above, interacting systems are able to achieve a common frequency of oscillation and maintain a bounded phase difference. A proper analysis and measurement of these synchronization marks are studied in the next section.

2.3   The hallmarks of synchronization

In the Huygens classical notes about the sympathy of sea clocks, one can also find a description of how the concordance between the pendula movements was maintained, even if initially one of the clocks was slightly accelerated.

The observation that, due to a proper interaction, oscillatory systems with different natural periods are able to end up oscillating at the same frequency is at the heart of the synchronization concept. It is precisely this effect what the adjustment of rhythms in the synchronization definition refers to. Today, the coupling-induced coincidence of frequencies of several interacting systems is known as frequency entrainment or locking. Intimately related to this effect, one encounters the fact that the phases of the oscillators involved in the locking must keep a fixed linear relation. In this way, when the phase difference between two oscillators is bound,

they are said to be phase locked. Both effects, frequency and phase locking, find multiple applications such as the tuning of powerful generators by the injection of a very precise but weak signal or the bit synchronization in modern communications schemes or demodulation of frequency-modulated signals with phase-locked loops (PLLs).

In the systems under study in this work, coupled semiconductor lasers, the frequency and phase locking will be one of the main signatures of the occurrence of sync and the basic criteria to establish whether periodic synchronization has taken place. In the former section, we have shown what characteristics are necessary for a system to have the possibility to experience sync. Under what conditions does this process eventually develop and which are the mechanisms involved, are fundamental questions in the synchronization theory that we review below.

2.3.1 Frequency locking

Imagine two nonidentical oscillators, like the pair of metronomes in the introductory section. When isolated the two systems oscillate, in general, at different rhythms. This is, they exhibit a certain mistmach in their natural frequencies or detuning $\Delta f = f_2 - f_1$. Once coupled, the phase pulling effect on each oscillator modifies their frequencies of oscillation to new values F_1 and F_2. A basic question in synchronization is: how is the curve $\Delta F = F_2 - F_1$ as a function of the natural detuning Δf for a pair of coupled systems?

For a fixed and weak coupling strength κ one can guess some aspects of this curve without entering into the exact details and origin of the oscillators. Assuming that a weak interaction can only induce small changes in the frequencies of the oscillators, it is clear that there must be a critical detuning beyond which the frequency locking cannot be possible. For small detuning, on the other hand, one typically observes that a moderate coupling induces the frequencies of both oscillators to become identical. The crucial point here is that this occurs not only for one specific value of the natural detuning but for a finite range of Δf. This results in the appearance of a plateau in the ΔF versus Δf curve, i.e., the relation $F_1 = F_2$ holds for a finite interval of Δf. Figure 2.1 (a) plots the typical aspect of ΔF as a function of Δf.

Usually, the stronger the coupling the wider the plateau. By plotting the locking band width for different levels of coupling strengths one obtains the so-called major Arnold tongue. The name is after the Russian mathematician Vladimir Arnold who studied these synchronization regions for a dynamical system known as the sine circle map[1] and which typically resemble the tip of a tongue [20]. Figure 2.1 (b) shows the usual shape of the main synchronization region in the

---

[1]The sine circle map is given by iterating $\theta_{n+1} = \theta_n + \Omega - \kappa/2\pi \sin(2\pi\theta_n)$, where κ and Ω may be interpreted as the coupling strength and driving frequency, respectively.

coupling strength (κ) versus detuning (Δf) plane.
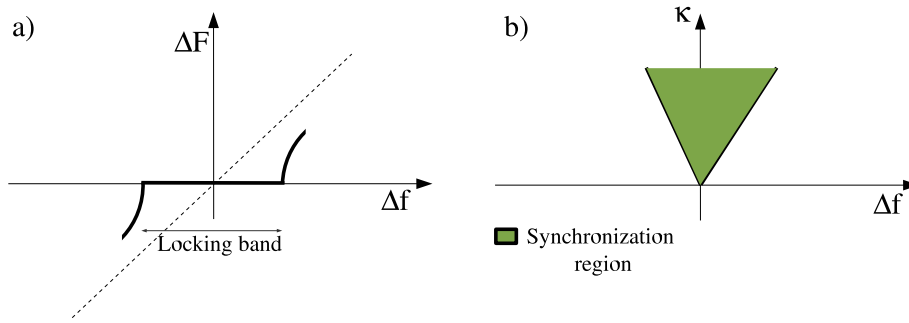
Figure 2.1. a) Typical curve of ΔF as a function of Δf. The plateau of the curve for small detuning is the frequency locked region. b) Scheme of the main Arnold tongue or synchronization region for two weakly interacting oscillators.

In terms of bifurcation theory, a brief description of which is summarized in Chapter 4, one can give a widely general interpretation of the synchronization process. In order to fix ideas, we consider the situation where the natural frequency mismatch between the oscillators is increased for a fixed coupling strength and thus, inducing a transition to a non-synchronized regime. This corresponds to an horizontal cut of the Arnold tongue in Fig. 2.1 (b). For zero detuning, the phase difference between the oscillators is fixed and it can be visualized as operating in a stable fixed point. A small detuning may change the location of the fixed point, but still this continues being stable and therefore, representing a locking solution. Further increment of the detuning, however, tends to eventually destabilize the fixed point. The route towards desynchronization usually occurs through different mechanisms depending on how this fixed point becomes unstable. Saddle-node (for small κ) and Hopf (for moderate κ) are the most common bifurcations that the fixed point undergoes as the frequency mismatch is varied. In both cases the system is lead to a quasiperiodic regime which eventually induces a loss of the frequency locking in the immediate neighborhood of the Arnold tongue. For very large coupling strength or highly nonlinear oscillators, there are more complex bifurcation scenarios that can lead to the destruction of synchronization and the appearance of chaos [1].

At this point, it is illustrative to compare the frequency locking properties between an unidirectional and a bidirectional coupling. In an unidirectional scheme, only one oscillator (master) influences or forces another (slave). In this case, the only possible frequency locked solution is that of the slave system shifting its frequency towards the master one ($F_{slave} = f_{master}$). Consequently, inside the

Arnold tongue region the locking frequency is constant and identical to the forcing frequency. On the contrary, when two oscillators affect each other in both directions of interaction, they usually "negotiate" the common frequency at which they lock. The locking frequency is normally found between the natural frequencies of both oscillators but not necessarily. This time, however, the common frequency of oscillation varies within the synchronization region and it is a function of both the coupling strength and detuning.

The main Arnold tongue, between one-way or mutually interacting oscillators, was defined as the region where both systems achieve a common frequency of oscillation. This is, inside the synchronization region the ratio between the coupling-induced frequencies in both systems is exactly one. For large detuning, however, it is relatively common to find one oscillator operating at a frequency which is a multiple of the other. For instance, if isolated the oscillators exhibit frequencies such that $f_1 \simeq 2f_2$, then once coupled it is highly probable that they will lock their rhythms to $F_1 = 2F_2$, instead of $F_1 = F_2$. In general, there are many regions where the frequencies of the oscillators keep a defined relation between each other without being identical. These are higher order synchronization regions. Within the lockbands of these zones the ratio between frequencies is a rational number, i.e., $F_1/F_2 = q/p \in \mathbb{Q}$. One speaks then of synchronization of order $p : q$.

2.3.2 Phase locking

Since the frequency gives the rate of growth of the phase of an oscillator, the phases of two systems with their frequencies locked share the same rhythm of increment. Therefore, an immediate consequence is that the phase difference $\psi = \phi_2 - \phi_1$ between two locked oscillators, even fluctuating, must remain bounded. We say then that the systems have also achieved a phase locking. Mathematically, this is expressed as $\mid \phi_2 - \phi_1 \mid < constant$. More generally, we can consider phase locking of order $p : q$ if $|p\phi_1 - q\phi_2| < constant$.

The actual value of the phase shift between the oscillators ψ is a very important quantity characterizing the synchronization solution obtained. The coupling between identical systems leads, in general, to a phase-attractive or phase-repulsive interaction between the phases which favours the in-phase or anti-phase dynamics, respectively. Anti-phase dynamics ($\psi \simeq \pi$) refers to the cases where the oscillators are mostly encountered in opposite states of their motion cycles, while in-phase ($\psi \simeq 0$) stands for the solutions where the systems are in the same position along the oscillatory orbit. The original observation by Huygens with both pendula swinging in opposition is a clear example of anti-phase synchronization. The selection of the shift between phases is eventually determined by the coupling network, interaction strength, and detuning.

One of the simplest mathematical models describing the dynamics of the phase difference between two weakly coupled oscillators is given by the Adler equation [21]

$$\frac{d\psi}{dt} = \Delta f + \kappa \sin \psi \, . \qquad (2.1)$$

Provided the condition $\mid \Delta f \mid < \mid \kappa \mid$ this equation has at least a pair of real solutions in the $(0, 2\pi)$ interval, one of which is stable and consequently predicts the phase locking of the oscillators.

One must realize then that an accurate determination of the phase and frequency of each individual oscillator involved in the interaction is of fundamental importance for identifying a synchronization process. Without a good estimation of these quantities the former locking fingerprints become useless from a practical point of view. However, only in a very limited number of cases a straightforward computation of the phase from the modeling equations, if any, is possible. In the next section, analytic representation, a technique borrowed from signal processing, and other methods are explained in order to obtain a measure of the phase and frequency of an arbitrary signal.

2.3.3 Instantaneous amplitude and phase of a signal

In the same sense that a pure harmonic oscillation $A\cos(\omega t)$ is often represented by the complex expression $A\cos(\omega t)+iA\sin(\omega t) = A\exp(i\omega t)$ to simplify some algebraic manipulations, the generalization of this conception to arbitrary signals is given by the analytical representation [22]. The idea is to equip the signal with an imaginary part so that concepts such as the phase and amplitude of the process are more accessible. The analytical signal of a real-valued variable $x(t)$ is defined by the complex function $\chi(t) = x(t) + iy(t)$, where $y(t)$ is the Hilbert transform of $x(t)$.

The Hilbert transform [23] of a real function is an integral transform obtained from the convolution of the signal $x(t)$ with $1/(\pi t)$, i.e.,

$$y(t) = \mathcal{H}\left[x\right](t) \equiv \frac{1}{\pi t} * x(t) = \frac{1}{\pi} \int_{-\infty}^{\infty} \frac{x(t')}{t - t'} dt' \, , \qquad (2.2)$$

where the integral must be taken in the Cauchy principal value sense in order to avoid the singularity at $t = t'$. When applying the Hilbert transform to the function $\cos(\omega t)$, one obtains the function $\cos(\omega t - \pi/2) = \sin(\omega t)$. In general,

the Hilbert transform of a signal produces a function with the phase of each one of its spectral components delayed by $\pi/2$. By analogy with the pure harmonic case, one can already guess that the analytical signal can motivate a definition for the amplitude and phase of any signal. In fact, when written in polar form $\chi(t) = x(t) + iy(t) = A(t)\exp(\phi(t))$ the analytical representation gives rise to the envelope amplitude

$$A(t) = \mid \chi(t) \mid = \sqrt{(x(t)^2 + y(t)^2)} \ , \qquad (2.3)$$

and instantaneous phase

$$\phi(t) = \arg(\chi(t)) = \arctan\left(\frac{y(t)}{x(t)}\right) \qquad (2.4)$$

of the signal $x(t)$. Then, the instantaneous frequency of the signal can be defined in a straightforward way as $\omega(t) = d\phi/dt$. However, it must be remarked that a physical interpretation of the former definition is only meaningful if $x(t)$ is a narrow-band signal. If so, the instantaneous frequency can be interpreted as the frequency of the stronger component of the power spectrum of $x(t)$ when computed in a running window. The main drawbacks of the analytical representation approach used here, is the sensitivity of the Hilbert transform to the mean value of the signal and to low-frequency trends in the data. Specially, the non-stationarity of the data might result in the lost of some loops when computing the value of the phase. Recently, a similar technique based on a wavelet transform that overcomes some of the problems that the analytical representation presents has been proposed by Lachaux et al. [24].

In summary, when carefully computed, the analytical signal approach can provide an useful generalization of the concept of phase for irregular oscillators, and in particular for chaotic systems.

Another measure of the phase of an irregular temporal trace can be designed by completely different means; a Poincaré map of the signal. The procedure is based on defining a Poincaré surface at which every cross of the trajectory of the signal is assumed to represent that the oscillator has completed a full cycle, i.e., its phase has increased in 2π. By linear interpolating the phase between the crossing events one ends up with a functional definition of the phase of an arbitrary signal.

This technique is specially suited when the studied temporal series contains a train of marker events, such as action potentials in electrocardiogram (ECG) or electroencefalogram (EEG) recordings. These episodes can then be used as reference points or crossing times along the Poincaré surface. Denoting by t_j the times at which the jth well-defined event occur, one can estimate the phase at those points as $2\pi j$. The phase is then calculated as

$$\phi(t) = 2\pi j + 2\pi \frac{t - t_j}{t_{j+1} - t_j} \; .$$
(2.5)

In this case the definition of the frequency of the process is taken as the number of characteristic events per unit time. Note that the derivative of the phase is a discontinuous function at the crossings of the Poincaré surface t_j.

In any case, both procedures (Hilbert or wavelet transforms and Poincaré maps) enable one to investigate the phase dynamics of an irregular oscillator and detect possible relation between several of them.

2.4 Different kinds of synchronization

Recently, the word synchronization has gained popularity in the nonlinear dynamics literature [25]. Not only used to describe the process of adjusting of rhythms that we have introduced in this section, it is also applied to give account for a number of related phenomena. Different types of synchronization capture different relationships between the signals $\mathbf{x}_1(t)$ and $\mathbf{x}_2(t)$ of two interacting systems. Below, the most important characteristics of the different kinds of synchronization are summarized.

In **chaotic systems** one can distinguish the following types of synchronous motion:

- *Identical or complete synchronization.* It refers to the coincidence of the outputs of two chaotic systems due to their coupling. The evolution of the coupled system occurs then within the hyperplane defined by $\mathbf{x}_1(t) = \mathbf{x}_2(t)$. In general, this exact solution only exists for identical chaotic oscillators and its stability, and therefore its observation, is related to the negativity of the maximum LE of the variational equation for $\mathbf{x}_\perp \equiv \mathbf{x}_2 - \mathbf{x}_1$. This is, only for those coupling schemes which damp out perturbations transverse to the synchronization manifold the identical synchronization is observable [7, 25, 26].

  The statistical nature of LEs allows for some structures within the synchronization hyperplane to be transversally unstable and still the ergodic average of the maximum LE be negative. Consequently, when the system wanders near these unstable sets some bursts of desynchronization are usually detected and alternate with a perfect identical synchronization solution. Curiously, not always a stronger interaction between the subsystems leads to a more stable synchronization manifold, but sync is only stable in a given range of coupling strengths. Regarding this issue an important advance was

developed by Pecora and Carroll in Refs. [27, 28]. There, a master stability function able to predict the desynchronization thresholds and size limits for the identical sync of an array of linearly coupled systems was devised.

- *Generalized synchronization.* This type of synchronization attempts to capture a more general relation between two coupled systems. Generalized synchronization is usually defined as the existence of a smooth and invertible mapping $\mathcal{F} : \mathbf{x}_2(t) = \mathcal{F}\left[\mathbf{x}_1(t)\right]$ between the trajectories of two coupled chaotic dynamical systems [29]. Some authors distinguish between strong and weak synchronization depending on this mapping $\mathcal{F}$ being smooth or not [30]. More recently, the definition of generalized synchronization has been extended to a general functional relation $\mathbf{F}(x_1, x_2) = 0$ between the states of two coupled oscillators [31].

  In unidirectionally coupled systems this type of synchronized solution has a clear interpretation; it means that the state of the slave system can be completely determined or predicted by observing the master. Commonly, the task of proving the existence of generalized synchronization in a system is much easier than finding the actual function that relates both outputs. In particular, the auxiliary approach suggested by Abarbanel et al. [32, 33] provides a simple test to check the existence of generalized synchronization. This test is explained in the next section.

- *Phase synchronization.* Since the phase of an oscillator is much more sensitive to perturbations than its amplitude, for low coupling strength two interacting oscillators can achieve an entrainment of their phases with the interaction hardly affecting their amplitudes. Phase synchronization expresses the regime where the phase difference between two irregular oscillators is bounded but their amplitudes remain uncorrelated [34]

- *Lag synchronization.* This type of synchronization takes into account relations between two systems when compared at different times [25]. The manifestation of a relations such as $x_1(t) = x_2(t - \tau)$ due to a coupling between the two systems is claimed as a lag synchronization. For positive (negative) τ the system 1 is said to lag (advance) the dynamics of system 2. This type of sync can appear in instantaneously coupled systems [35] but is prominent in cases where the interaction time between subsystems needs to be taken into account [36].

  Anticipated synchronization is a special type of lag synchronization. When system 1 affects unidirectionally to system 2, and still the latter is able to advance the dynamics of the first one [36], we call this counterintuitive process anticipated synchronization. The most common scheme to observe anticipatory sync appears when the transmitter is affected by a feedback long loop [37]. In this way, it is possible for the receiver to be influenced by the transmitter sooner than the transmitter is affected by its own feedback, and thus

the receiver can advance the dynamics of the transmitter without violating causality [38, 39].

Periodic systems typically exhibit:

- *Classical synchronization.* It refers to the classical adjustment of rhythms of interacting periodic oscillators as defined in Section 2.1.
- *Localized synchronization.* It is used to describe situations where two coupled oscillators display periodic oscillations at a common frequency but with very different amplitudes [40, 41]. Its phenomenology resembles to the one displayed by discrete breathers (i.e., periodic space-localized oscillations) in discrete and continuous media.

Noise effects in synchronization include:

- *Noise-induced synchronization.* When two non-interacting oscillators are subjected to the same fluctuating forces the trajectories of both systems can actually converge to the same values [42]. This synchronization induced by a common noise source is another example where random fluctuations can bring some order to a given dynamics, such as in the coherence or stochastic resonance phenomena [43]. In order to achieve synchronization, the addition of noise needs to make the individual oscillator exhibit a negative largest LE. One can argue then, that for noise-free chaotic systems this type synchronization only works when the addition of noise stabilize the intrinsic dynamics, i.e., the noise destroys the deterministic exponential sensitivity to initial conditions. However, even under such conditions the system is still noisy and therefore unpredictable [42].
- *Stochastic resonance.* This effect is often illustrated in threshold or bistable systems subject to a small external modulation. The stochastic resonance phenomenom is then described as the existence of an optimum noise level that produces a cooperative effect with the periodic forcing. This is, for an adequate degree of randomness the noise-induced transitions between states (the crossing of a threshold or the jumps between different equilibria) can enhance the periodic response of the system to the external force. In the synchronization framework, one can also consider this effect as a locking between the average noise-induced switching rate and the frequency of the external periodic forcing.

Even seemingly independent the former types of synchronization are often encountered in the same dynamical system. In general the changing of a control

parameter can induce passages between the different synchronization solutions for the same system. Rosemblum et al. [44] studied the transitions between synchronized states in two symmetrically coupled non-identical chaotic oscillators. They observed that when increasing the coupling strength, a system composed of two Rossler oscillators undergoes first a transition to phase synchronization. Further increase of the coupling rate induces the appearance of a lag synchronization solution before tending to a complete synchronization regime.

Certainly, most of the previous definitions can be adapted to more general cases as arrays of oscillators with a number of units larger than two or even oscillatory media. We will not further comment on these possible generalizations but proceed by analyzing the most used quantifiers and schemes for detecting the different types of synchronization.

2.5 Measures and detection of sync

As argued by Pikovsky et al. [1] in synchronization measurements one should distinguish the cases in which one is able to modify or change the internal parameters of the system under study or not. This difference leads to speak about active and passive experiments, and the techniques and tools to quantify and detect synchronization in both cases are in general quite different.

For periodic oscillators, the comparison of frequencies and phases before and after coupling them is the best test to check if classical or localized synchronization has taken place. A complete characterization of the synchronization process requires the computation of the different Arnold tongues or lockband regions. Therefore, for such a description, an active control of the detuning and coupling strength between oscillators becomes necessary.

When such a procedure is not an option, the assessment of the synchronization between two oscillators turns out to be less conclusive. In general, only an analysis of the interdependence of two signals (possibly noisy and non-stationary), which are assumed to be generated by two interacting oscillators is suitable. To this respect, cross-correlation analysis is very common since it allows to detect linear interdependences between two different processes. On the other hand, mutual information has been also used to quantify the overlap of information content of two systems, whereas the concept of transfer entropy has recently been proposed to measure the information exchange between two dynamical entities [45].

Along this thesis, cross-correlation will be the most important quantity in determining the degree or quality of the synchronization between two systems. The cross-correlation function gives a measure of the extent to which two signals correlate with each other as a function of the time displacement between

them. Its implementation from a series of bivariate data $\mathbf{x} = \{x_1, x_2, ...x_N\}$ and $\mathbf{y} = \{y_1, y_2, ...y_N\}$, which is sampled at regular intervals $t = i\Delta t$ is given by the discrete convolution of the two signals:

$$
\Gamma(k) = \begin{cases} \dfrac{\sum_{i=1}^{N-|k|} \left[(x_{i+|k|} - \overline{x})(y_i - \overline{y}) \right]}{\sqrt{\sum_{i=1}^{N}(x_i - \overline{x})^2}\sqrt{\sum_{i=1}^{N}(y_i - \overline{y})^2}}, & \text{for} \quad k < 0 \,; \\[4mm] \dfrac{\sum_{i=1}^{N-k} \left[(x_i - \overline{x})(y_{i+k} - \overline{y}) \right]}{\sqrt{\sum_{i=1}^{N}(x_i - \overline{x})^2}\sqrt{\sum_{i=1}^{N}(y_i - \overline{y})^2}}, & \text{for} \quad k \geq 0 \,, \end{cases}
\tag{2.6}
$$

where $\overline{x}$ and $\overline{y}$ represent the temporal average of the signals. This measures how similar two temporal series, once shifted by a lag $\tau = k\Delta t$, are and it is especially indicated to quantify the quality of complete and lag synchronization in chaotic systems. A cross-spectrum, on the other hand, is the Fourier transform of the cross-correlation function, and it is used to uncover correlations between two series at different frequencies.

When dealing with generalized synchonization most of the times one can only aspire to demonstrate the existence of a functional connection between the outputs of the two dynamical systems under consideration. The exact form of the mapping between systems is often reserved to academic examples. The standard test to check the existence of generalized synchronization between two unidirectionally coupled (master-slave) elements is provided by the auxiliary system approach developed by Abarbanel [32]. The steps in the test proceed like this:

- Consider an identical copy or replica of the slave system 2, which we call $2'$.

- Start evolving the systems 2 and $2'$ subject to the same unidirectional injection from the master but starting from different initial conditions.

- Then if both, the slave and replica systems, synchronize identically after a transient time ($\lim_{t \longmapsto \infty} x_2(t) = x_2'(t)$), one concludes that a functional relationship must relate the outputs of master and system 2, $x_2(t) = F(x_1(t))$.

An important generalization of this test has been elaborated by Zheng and collaborators [33]. They extended the procedure to detect generalized synchronization in bidirectional coupling schemes and more complicated networks.

From a time series analysis perspective the detection of phase synchronization in chaotic or noisy systems is performed by the computation of an appropriate phase difference between oscillators. In this case the most convenient technique to infer the individual phases of the oscillators (Hilbert, wavelet, Poincaré, etc.)

must be chosen depending on the type of data to be investigated, as mentioned in
Section 2.3.

When the number of interacting oscillators is large other methods to describe
synchronization are necessary. Sometimes it is useful to recall a concept from the
statistical physics of phase transtions; the order parameter. That was the approach
followed by Kuramoto to succesfully characterize the synchronization transition
in a set of globally coupled phase oscillators [46].

2.6   Oscillation quenching

The oscillation quenching or Bar-Eli effect [47] is the suppression of oscillations
of interacting systems due to its coupling. Strictly speaking, this is not a synchro-
nization process but we include it here as another coupling-induced phenomenon.
It usually appears for larger coupling strengths than the synchronization thresh-
old since affecting the amplitude of the oscillators requires a stronger interaction
than that necessary for only shifting their phases or frequencies. One of the first
descriptions of this effect was due to Lord Rayleigh [48], who observed that two
similar organ-pipes could drive each other to almost silence when standing side by
side.

The cease of the oscillatory behavior in weakly coupled limit cycle oscillators
can induce important consequences in both biological and physical systems. In
fact, the appearance of this phenomenon in some cell systems seems to be related
to severe pathologies [13]. Hopf or some spatio-temporal bifurcations have also
been associated to the dynamical behavior of diseases like respiratory or cardiac
arrest or epileptic seizures [49]. The modern perspective recognize then the impor-
tance of a dynamical understanding of these type of diseases in the identification
and treatment of various illnesses.

Regardless of its biological motivation, the bases of the quenching effect can
be illustrated through the study of two generic weakly coupled nonlinear oscil-
lators. To this end, a discrete version of the complex Ginzburg-Landau equation
provides a universal model of coupled oscillators near their oscillatory threshold
(Hopf bifurcation) [2]:

$$\dot{A}_1 = -i\Delta A_1 + \mu_1 A_1 - (\gamma_1 + \alpha_1)|A_1|^2 A_1 + (\kappa_c + i\delta_1)(A_2 - A_1) \qquad (2.7)$$

$$\dot{A}_2 = i\Delta A_2 + \mu_2 A_2 - (\gamma_2 + \alpha_2)|A_2|^2 A_2 + (\kappa_c + i\delta_2)(A_1 - A_2) \qquad (2.8)$$

In the model $A_{1,2}$ represent the complex amplitudes of each oscillator. The pa-
rameters μ and γ describe the linear and nonlinear gain/losses, while α takes

into account the dependence of the frequency of the oscillation on the amplitude. $\Delta = (\omega_2 - \omega_1)/2$ is the detuning or mismatch between the natural frequencies of the oscillators. Regarding the coupling coefficient, this is composed by a real (κ_c) and imaginary (δ) part representing dissipative and reactive terms.

For the illustration of the phenomenon a simplified version of the model can be used. Isochronous ($\alpha = 0$) and dissipatively coupled ($\delta = 0$) similar oscillators differing only in their natural frequencies of oscillation are considered here [50]. Exploring the coupling strength versus detuning parameter space several dynamical regimes can be obtained as shown in Figure 2.2. The quenching region is limited by the locking and phase drift areas, and it is noticed that a large detuning between the oscillators is needed in order to produce the death or quenching effect. Consequently, two identical (condition that requires $\Delta = 0$) instantaneously coupled oscillators are not allowed to experience a mutual quenching in their oscillations.
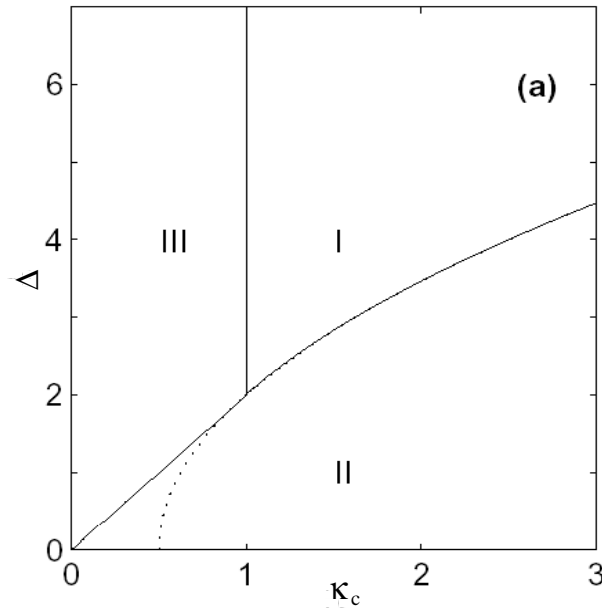
Figure 2.2. Dynamical regimes in the coupling versus detuning plane of two coupled oscillators. I) Quenching region, II) locking area, and III) phase drift zone. After Ref. [13].

Dynamically, the quenching area corresponds to the stabilization of the stationary or fixed point solution $A_1 = A_2 = 0$ due to the variation of either the detuning or coupling strength.

The effect of considering a time delay in the interaction between the oscillators

opens a new branch of possibilities for the synchronization and other coupling-induced effects. In particular, in the next chapter we review the important consequences of having a delayed interaction in the observation of the oscillation death.

Chapter 3

Delayed interactions

I<small>T</small> has been known for a long time that some problems need to be described by models that include past effects. Examples of such type of problems are found everywhere. In the two-body problem in electrodynamics, for instance, one must take into account that the interaction between two distant charged particles does not occur instantaneously, but the influence of particle 1 on particle 2 at time t must have been induced at some earlier instant $t - \tau$, and viceversa [51]. Control theory is another field where delayed interactions become extremely important. A typical strategy in control systems consists of an automatic controller that monitors the state of the system and makes adjustments to the system based on its observation. Since these adjusments can never be made instantaneously, a delay arises between the observation and the control action. Such a feedback scheme is a very common setup giving rise to dynamical systems in which its actual state depends on the past history of the own system [52].

As observed in the former examples and as it will be the case for spatially-separated interacting lasers, the finite propagation velocities of signals stands as one of the main causes for the occurrence of delayed interactions. However, it is not the only one. Latency periods are also typical sources of delays which model the time that a system needs to produce or process an output. For instance, in population dynamics the inclusion of latency times (describing the gestation or maturation periods of new individuals) induces also the appearance of delayed terms in the modeling of the process [53–55]. An important case is the famous Mackey-Glass equation

$$\dot{x}(t) = -bx(t) + \frac{ax(t - \tau)}{1 + x(t - \tau)^n} \, , \tag{3.1}$$

which models the dynamics of white blood cell production in the human body [56], and it is a paradigmatic example where the proliferation of a given population en-

tails a time delay.

Summarizing, there is a large and important class of dynamical systems in which the rate of change of the state is determined by the present and also by past states of the system. When the delay times are large enough, comparable to the internal time scales of the system, then Ordinary Differential Equations (ODEs) usually fail to accurately describe its dynamics. It is in this context where Delay Differential Equations (DDEs) naturally appear in the modeling of such systems.

In this thesis the physical distance between two coupled semiconductor lasers (propagation time) is the responsible for the dependence of the dynamics of laser 1 on the past state of laser 2, and viceversa. Therefore, the study of DDEs and the stability of their different solutions becomes crucial in any serious analysis of the dynamics of coupled SLs. To this end, in the following sections the definition, classification, and the linear stability issue for solutions of DDEs are introduced with views to be applied in our semiconductor laser modeling.

3.1 Delay Differential Equations

3.1.1 Definition

A delay differential equation is a functional differential equation where the highest order derivative only occurs with one value of the argument, and this argument is not less than the arguments of the unknown function and its remaining derivatives [52].

Such type of equations (as Eq. 3.1) are also called Retarded Functional Differential Equations (RFDEs) and belong to the more general type of differential equations with deviating argument. Next, we proceed to describe the types of DDEs and their most remarkable features when compared to ODEs.

3.1.2 Classification and main features

The different types of DDEs are usually classified according to several and possibly overlapping criteria.

Attending to the nature of the delays appearing in the delay differential equations one can distinguish between the following categories:

- **Constant**. In this case the possibly multiple delays involved in the equation are fixed $\tau_1 \equiv c_1, \tau_2 \equiv c_2, ... \tau_m \equiv c_m$. It is probably the most common and easy to analyze type of DDE, specially if the delays are commensurate.

- **Variable**. At least of one the delays is not constant but exhibits an explicit dependence on the time variable $\tau = \tau(t)$. Therefore, this class of systems is nonautonomous even if no other time dependence is contained in the terms of the equations.

- **State dependent**. When one or more of the delays is a function of the state of the system $\tau = \tau(x(t))$ the resulting DDE is rather complicate to analyze. Even its numerical simulation is far from trivial. One should notice that the grid points one must use for its evolution in a finite difference scheme are not known a priori and interpolation methods are needed.

Another classification refers to the number of delays involved in the right-hand side of the equations. When the number of delays appearing in the DDEs is finite they are called **discrete** DDEs, while if the delay is spread over a continuum of values then we are dealing with a **distributed** DDE [55].

The functional equations with deviating arguments that do not fit into the previous definition of RFDE are called **neutral**. One important example of neutral equations is given by equations in which the delayed term appears in the highest order derivative.

Regarding the dimensionality of the phase space described by a set of DDEs, it should be noticed that the initial condition needed to solve DDEs is given by the past history of the variables up to the maximum delay, i.e., $\mathbf{x}(t), \forall t \in (-\tau_{max}, 0)$. Since this is a continuum of points the phase space of DDEs is infinite-dimensional in the same way that Partial Differential Equations (PDEs) are also infinite-dimensional (see Figure 3.1). Another important property that DDEs share with PDEs is the fact that only one equation is needed in order to produce chaotic behavior, as opposite to what happens in ODEs where at least three coupled equations are required.
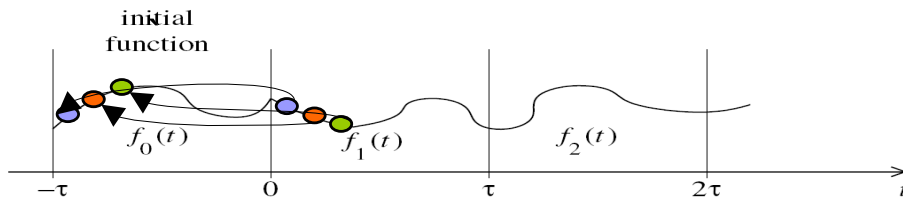
Figure 3.1. The initial condition of a DDE is given by the past history of the variable up to the maximum time delay. To evolve the solution of a DDE at time t the state of the system at time $t - \tau$ is needed. The continuum of states from $t = -\tau$ to $t = 0$ represents the appropriate initial condition.

The differences with respect to ODEs do not stop there. The experts in the

field of DDEs always try to put some words of caution on the tendency of treating DDEs on the same foot than ODEs [51,57]. They remark that the peculiarities and differences that delay differential equations exhibit with respect to ordinary differential equations are sometimes unexpected and the prolongation of results from one type of equations to the other is not only a matter of rigor. This practice occurs sometimes among some researchers yielding wrong results. The Taylor expansion of delayed terms (even with small delays) can fail to quantitatively describe the solutions of the system when compared to the original equation, as well as theorems for the existence and unicity of solutions in ODEs are not maintained for DDEs. Dynamically the differences are also noticeable even at linear regimes. For instance, a linear system of ODEs can only have decreasing or increasing exponential solutions but a linear set of DDEs can display non-trivial oscillatory behavior.

3.2   Stability theory

The question of the existence of a given solution is as important as its stability to attract nearby trajectories. The solutions of any dynamical system including delayed terms or not may be asymptotically stable (attractors), marginally stable (i.e., only Lyapunov stable) or unstable. In particular, the study of the stability of stationary and periodic solutions is accessible and can give us a great insight into the qualitative behavior of the system. To this end, one of the most useful techniques in determining the stability of solutions of dynamical systems, the linear stability approach, is explained here for RFDEs.

3.2.1   Linear stability of retarded functional differential equations

Linear stability analysis takes the first order approximation of the differential equations of motion and study the evolution of small perturbations around a given solution or trajectory $\mathbf{x}^*(t)$. Let us consider a system of RFDE, possibly including several constant discrete and distributed delays

$$\dot{\mathbf{x}}(t) = f\left(t, \mathbf{x}(t), \mathbf{x}(t-\tau_1), ..., \mathbf{x}(t-\tau_m), \bar{\mathbf{x}}(t); \mu\right), \qquad (3.2)$$

where $\mathbf{x} \in \mathbb{R}^n$ and f is a function of the time, the instantaneous and delayed variables and a set of parameters μ. $\bar{\mathbf{x}}(t)$ is the delayed variable weighted by a given distribution of delays

$$\bar{\mathbf{x}}(t) = \int_0^\sigma \mathbf{g}(t,\tau)\mathbf{x}(t-\tau)d\tau . \qquad (3.3)$$

The past dependence in the former equation is then composed by m fixed retards $\tau_1, \tau_2, ..., \tau_m$ and a delay distributed on a continuum interval of values $\tau \in (0, \sigma) \subset \mathbb{R}$.

The linearization of the system (3.2) around the solution $\mathbf{x}^*(t)$ leads the so-called variational equation for the variable $\mathbf{y}(t) = \mathbf{x}(t) - \mathbf{x}^*(t)$,

$$\dot{\mathbf{y}}(t) = A_0(t)\mathbf{y}(t) + \sum_{i=1}^{m} A_i(t)\mathbf{y}(t - \tau_i) + B(t) \int_0^{\sigma} g(t, \tau)\mathbf{y}(t - \tau)d\tau , \quad (3.4)$$

wherein the $n \times n$ matrices

$$A_i(t) = \frac{\partial f}{\partial \mathbf{x}(t - \tau_i)}\Big|_{(\mathbf{x}^*(t), \mathbf{x}^*(t-\tau_1), ..., \mathbf{x}^*(t-\tau_m), \bar{\mathbf{x}}^*(t); \mu)} , \quad (3.5)$$

and

$$B(t) = \frac{\partial f}{\partial \bar{\mathbf{x}}(t)}\Big|_{(\mathbf{x}^*(t), \mathbf{x}^*(t-\tau_1), ..., \mathbf{x}^*(t-\tau_m), \bar{\mathbf{x}}^*(t); \mu)} , \quad (3.6)$$

are the corresponding Jacobians of the discrete and distributed delayed variables, respectively.

For stationary solutions $\mathbf{x}^*(t) = \mathbf{x}^* \mid \dot{\mathbf{x}}^* \equiv 0$ an exponential ansatz for $\mathbf{y}(t)$ and linear algebraic theory tell us that the variational equation can only be satisfied with the non-trivial zero displacement solution if

$$\Delta(\lambda) \equiv det\left(\lambda I - A_0 - \sum_{i=1}^{m} A_i \exp(-\lambda\tau_i) - B \int_0^{\sigma} \exp(-\lambda\tau)g(\tau)d\tau \right) = 0 ,$$

$$(3.7)$$

where I is the $n \times n$ identity matrix.

The key point in these type of studies is that the distribution of the infinitely-many roots or eigenvalues λ of Eq. (3.7), which in general take complex values, rules the stability of the system through the following theorem [51, 52]:

> *a necessary and sufficient condition in order that all solutions of Eq. (3.4) approach zero as $t \rightarrow \infty$ is that all the roots of the characteristic equation 3.7 have negative real part.*

3.2.2   D-Subdivision method

Expanding out the determinant in Eq. (3.7) the characteristic equation takes the quasi-polynomial form

$$\Delta(\lambda) = \lambda^n + p_0(\lambda) + \sum_{i=1}^{m} p_i(\lambda) \exp(-\lambda\tau_i) + \int_0^{\sigma} \exp(-\lambda\tau)q(\lambda,\tau)d\tau \ , \quad (3.8)$$

where $p_0(\lambda)$, $p_i(\lambda)$, and $q(\lambda,\tau)$ are polynomials in λ of degree at most $n-1$. At this point, it is important to realize that since the zeros of this quasi-polynomial depend continuously on the various τ_i, σ, and the coefficients of the polynomials, the number of roots of $\Delta(\lambda;\mu) = 0$ can only change if a root crosses the imaginary axis.

Based on this key fact and the theorem stated in the former section a procedure known as D-Subdivision [55] works out the stability of the linear system (3.4). To determine the stability of a stationary solution in a given parameter space $(\mu_1,\mu_2,...,\mu_d)$ the method proceeds as

1. Locate the borders where the characteristic equation has a root with zero real part, i.e., $\lambda = i\omega$. These borders separate the parameter space into subregions with a different number of solutions with positive real part.

2. Check the direction of the crossing of the eigenvalues at these frontiers to know if the number of roots with positive real part increases or decreases at these boundaries. For example, if the parameter μ_k is varying, the derivative

$$\frac{d\Re(\lambda)}{d\mu_k} = \Re\left(\frac{d\lambda}{d\mu_k}\right) = -\Re\left(\frac{\partial\Delta}{\partial\mu_k}\Big/\frac{\partial\Delta}{\partial\lambda}\right) \ , \quad\quad (3.9)$$

   must be evaluated at the borders between subregions.

3. Determine how many zeros of the characteristic equation have positive real part in one of the subregions in which the step 1 divides the considered parameter space.

4. From the former steps one should be able to locate the subregions where all roots have negative real part, and therefore the system is stable.

The transcendent nature of Eq. (3.7) makes the analysis of the stability issue for DDEs much more delicate and cumbersome than for ODEs. In any case, from the infinitely-many complex roots $\lambda = \alpha + i\omega$ the borders of stability are determined by the pure imaginary eigenvalues $\lambda = i\omega$. A promising approach for

the computation of the former steps consists of the replacement of the exponential terms in the expression (3.8) by their Rekasius transform [58], i.e.,

$$\exp(-\lambda\tau_i) = \frac{1 - T_i\lambda}{1 + T_i\lambda} \;, \tag{3.10}$$

which is exact for pure imaginary values of $\lambda = i\omega$ with

$$\tau_i = \frac{2}{w}\arctan(\omega T_i) \;. \tag{3.11}$$

The main advantage of such a substitution is that the algebraic nature of the characteristic equation in terms of the new parameter T_i becomes polynomial. Of course, the price we have to pay is that the relation between T_i and τ_i is not polynomial. Nevertheless, with such a procedure a simple Routh-Hurwitz criteria can then be used for the counting of roots with positive real part [55]. Other root counting techniques have benefited from some theorems in complex variable theory such as the Argument Principle [52].

A remarkable feature of the characteristic equation is its invariance with respect to $\omega\tau_i \longmapsto \omega\tau_i + 2\pi l$, with $l \in \mathbb{N}$, which is known as the clustering property. It allows to describe a family of infinitely-many solutions (borders) with only one critical delay τ_c and this invariance property.

In some cases the stability of DDEs can be determined by other techniques different from linear stability analysis. For instance, the finding of a Lyapunov-Krasovkii functionals [36, 59] allows to interpret the dynamics of the system as a potential problem from which its stability is easily interpreted. Full computational approaches are also valid when physical insight to the stability problem is not required. The Matlab package DDE-biftool [60] allows to automatically continue and analyze the linear stability of stationary and periodic solutions of DDEs by numerically locating the eigenvalues of the characteristic equation. Its use in this thesis is restricted to the stability of the periodic orbits with a view to explain some bifurcation diagrams in Chapter 6.

3.3   Oscillation quenching revisited

In Chapter 2 we have seen how two coupled oscillators could stop oscillating provided their frequencies were different enough. The inclusion of delay times in the interaction between the oscillators is responsible for a series of modifications of this mutual quenching effect.

The influence of the delay in the amplitude of the oscillations can be modelled through the system [13]

$$
\begin{aligned}
\dot{A}_1 &= -i\Delta A_1 + \mu_1 A_1 - (\gamma_1 + \alpha_1)|A_1|^2 A_1 + (\kappa_c + i\delta_1)(A_2(t-\tau) - A_1) \\
\dot{A}_2 &= i\Delta A_2 + \mu_2 A_2 - (\gamma_2 + \alpha_2)|A_2|^2 A_2 + (\kappa_c + i\delta_2)(A_1(t-\tau) - A_2) \,,
\end{aligned}
$$

$$(3.12)$$

where $A_{1,2}$ represent the complex amplitudes of each oscillator and τ is the time delay in the interaction. Figure 3.2 shows the diagram of the different dynamical states of Eq. 3.12 in the coupling strength versus detuning plane (with $\alpha_i = \delta_i = 0$). It can be observed that, as opposite to the case of instantaneous coupled oscillators, detuning is not required in order to observe this quenching, and consequently a delay in the coupling line opens the possibility to observe oscillation death in coupled identical systems ($\Delta = 0$) [14].
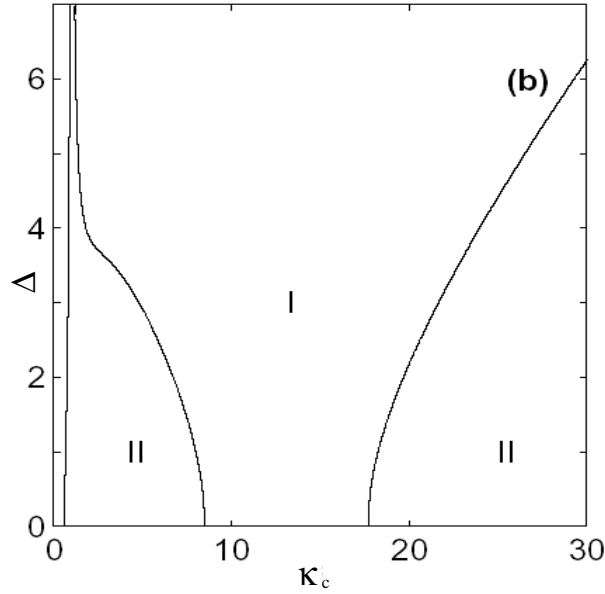
Figure 3.2. Dynamical regimes in the coupling versus detuning plane of two coupled oscillators. I) Quenching region, II) locking area. The delay is set to $\tau = 10$.

The first experimental confirmation of this "death by delay" effect was obtained in 2000 by Herrero and collaborators who studied the dynamics of two mutually coupled thermo-optical cells [61]. To our knowledge we present in this Chapter 6 the first experimental confirmation of this effect in a semiconductor laser setup.

Chapter 4

Basics of bifurcations

I~N~ this chapter we just attempt to sketch, without any kind of detail or mathematical rigor, some of the most common bifurcation scenarios that can occur in a nonlinear dynamical system. The identification of these qualitative changes in the behavior of a system allows to track the passage from simple to complex dynamics keeping a significant insight at every step of the transition. In the Results part of this thesis, we extensively apply bifurcation theory to trace the role of the delay and the network of connections in the emergence of chaotic and synchronization behavior between mutually-coupled semiconductor lasers.

4.1 Definition

It is important to recall that since most of real systems, including our models of laser systems, are dissipative entities their long-term dynamics eventually settle on attracting sets of zero phase volume. Each of the attractors present in a dynamical system is usually surrounded (although riddle basins are also possible) by its own basin of attraction, and motions started within a basin tend asymptotically to the attractor lying within that region of the phase space.

Then, by **bifurcation we mean a qualitative change in the topology of the attractor-basin phase portrait under the quasi-static variation of a control parameter**. At a bifurcation point $\mu = \mu_c$ the ensembles of trajectories that fill the phase space to generate the phase portrait suffer not only a quantitative but a qualitative modification.

As we will see later, bifurcations are usually related to the change of stability of existing attractors or the birth and death of these asymptotic solutions [62]. The nomenclature and classification of these bifurcating events are often not unified in the literature. In the following sections, we offer a simplified classification and summary of the most common type of bifurcations that will of great help in analyzing the different dynamics observed in Chapters 6-8 and we will set a proper

notation.

4.2   Classification

The different types of bifurcations can be organized according to several criteria.

When the characterization of a bifurcation can be reduced to the study of a small neighborhood of a single point in phase space, the bifurcation is said to be **local**. It is important to remind that by various techniques, such as Poincaré maps (see next section), the analysis of limit cycles and other attractors can be reduced to the study of a fixed point. **Global** bifurcations on the other hand, often involve connections between the invariant manifolds of distant saddle solutions, producing changes in the basin structure which cannot be described in a local region of the phase space [62, 63].

Bifurcations are also classified according to the number of parameters that one must change in order to achieve the structural stability of a given bifurcation (i.e., make it topologically robust against additional perturbations of the system). This number is said to be the **codimension** of the bifurcation [64]. Here, we restrict ourselves to introduce the most typical codimension-one and codimension-two bifurcations since they are the most often encountered in our laser setups.

Finally, another category of bifurcations can be distinguished depending on how an attractor loses its stability at a given bifurcating point, which to fix ideas we denote here by $\mu = \mu_c$. In **supercritical** bifurcations an attractor loses its stability as it intersects a stable attractor that only exists at supercritical values of the control parameter ($\mu > \mu_c$). In **subcritical** bifurcations, however, an attractor loses its stability by colliding with the unstable path of a structure that only exists at subcritical values of the control parameter ($\mu < \mu_c$) [62].

The consequences of the supercritical or subcritical nature of a type of bifurcation are quite important in the dynamics of a system and we will pay proper attention to it in the Results part of this thesis. The main difference lies in the fact that in a supercritical bifurcation the qualitative change in the dynamics of the system occurs through a smooth transition, i.e., the newborn attractor continuously grows from the bifurcating point, while in a subcritical bifurcation as soon as the original attractor loses its stability the system experiences a sudden jump to a distant and unrelated attractor. As a related property, we have that on reversal of the control parameter around the subcritical bifurcating point the system does not necessarily jump to operate again in the original attractor, and thus generates a hysteresis loop which might be interesting for some applications.

4.2.1   Basic local bifurcations for flows and maps

Local bifurcations in a dynamical system such as a vector field or flow

$$\dot{x} = f(x, \mu), \qquad \mathbf{x} \in \mathbb{R}^{\mathbf{n}}, \quad \mu \in \mathbb{R}^{\mathbf{P}}, \tag{4.1}$$

are characterized by the eigenvalues of its linearized dynamics $y = x - x^*$

$$\dot{y} = \frac{\partial f}{\partial x}\big|_{x^*} y, \tag{4.2}$$

on a given fixed point $x^* \mid f(x^*, \mu) = \mathbf{0}$, which is stable only if all the eigenvalues are on the left hand side of the complex plane.

Closely related, the theory for bifurcations of discrete time systems or maps

$$x \longmapsto f(x, \mu), \qquad \mathbf{x} \in \mathbb{R}^{\mathbf{n}}, \quad \mu \in \mathbb{R}^{\mathbf{P}}, \tag{4.3}$$

is very similar and relies on the study of the eigenvalues of the associated linearized map

$$y \longmapsto \frac{\partial f}{\partial x}\big|_{x^*} y. \tag{4.4}$$

In this case, however, the stability criteria now demands all the eigenvalues (or Floquet multipliers) of this map to lie within the circle of modulus 1 in the complex plane.

A key connection between both types of dynamical systems, flows and maps, is that a periodic solution in a continuous system can be associated to a fixed point of a map. This is the idea behind the Poincaré map technique of reducing the study of a limit cycle to the crossing points of the orbit with a given manifold or surface in the phase space (see Figure 4.1). This conception can be straightforwardly applied to more complicated orbits in phase space to reduce the dimensionality of the bifurcating structure.
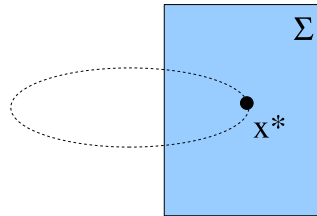
Figure 4.1: Poincaré return map of a periodic orbit.

In any case, the loss of stability of an attractor is usually associated with the crossing through the imaginary axis (unit circle for maps) of a small number of eigenvalues of the linearized dynamics of the system.

A very important result, stated as the Center-Manifold Theorem, tells us that a given local bifurcation can be studied and characterized by focusing only on the space spanned by the eigenvectors related to these critical eigenvalues [65]. This and other similar techniques basically allow us to reduce the dimension of the problem without loosing any essential information about the bifurcation. Normal forms are low dimensional and universal models representing different types of these simplified dynamics from which one can illustrate different local bifurcations as we do in this section.

Summarizing, in both classes of dynamical systems (flows and maps), different types of bifurcation are associated to the different paths the eigenvalues or multipliers can follow towards instability. Then, conditions such symmetries or other type of constrains help to distinguish between bifurcations with the same type of eigenvalue transition.

In the following, we highlight and briefly comment on the types of local bifurcations of codimension one associated to the most important normal forms for both flows and maps.

- **Saddle-node**. Also known as **fold bifurcation** or **limit point**, in this bifurcation two equilibria (one stable node and one unstable or saddle) simultaneously appear as a single control parameter μ passes a threshold μ_c. The bifurcation diagram in phase space and the eigenvalue conditions for flows and maps are collected in Figure 4.2.
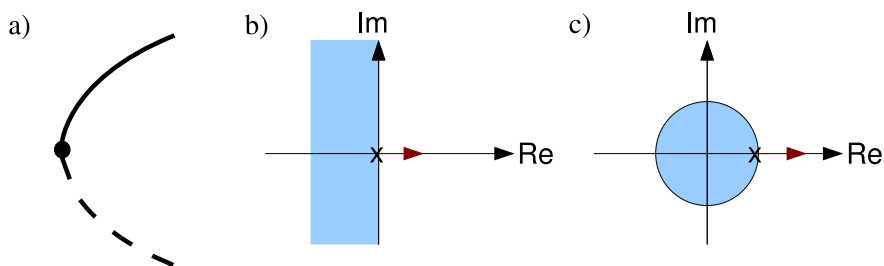
Figure 4.2. a) Saddle-node bifurcation diagram. b) Bifurcation condition for flows. c) Bifurcation condition for maps. In the bifurcation diagram, solid (dashed) lines indicate stable (unstable) structures.

- **Transcritical**. It occurs when one stable and one unstable steady-states collide at the bifurcation point μ_c and exchange their stability. Figure 4.3 shows

the underlying transition diagram and the bifurcating conditions.
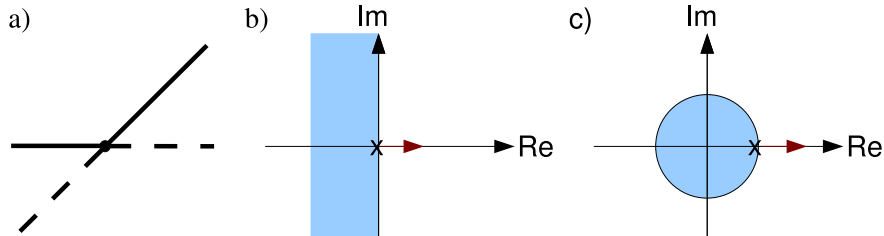
Figure 4.3. a) Transcritical bifurcation diagram. b) Bifurcation condition for flows. c) Bifurcation condition for maps. In the bifurcation diagram, solid (dashed) lines indicate stable (unstable) structures.

- **Pitchfork**. In the supercritical version of this bifurcation, a fixed point loses its stability as it produces two new stable fixed points when some control parameter is varied. In its subcritical form, the bifurcation occurs as a fixed point collides with the unstable branches of two previously existent fixed points. It is important to mention that this and other types of bifurcation only appear in dynamical systems with an appropriate symmetry (reflection invariance in this case). Bifurcation diagram and eigenvalues transition are shown in Figure 4.4.

- **Hopf (Naimark-Sacker for maps)**. In the supercritical Hopf bifurcation, a stable fixed point becomes unstable as a stable limit cycle is born from it. In its subcritical variation, a fixed point intersects an existing unstable branch of limit cycle orbits at the bifurcating threshold and as a consequence the steady-state loses its stability.

  In this type of bifurcation some properties about the limit cycle that is born or is intersected at the bifurcating point can be obtained. Its amplitude, for instance, typically grows as the square root of the distance of the control parameter to the bifurcation point, i.e., $A \propto |\mu - \mu_c|^{1/2}$. Regarding angular information, for continuous time systems the angular frequency of oscillation of these limit cycles near the bifurcating threshold is given by the imaginary part of the eigenvalues crossing the axis $\lambda = \pm i\omega$, while for maps the same quantity is given by the the argument of the complex pair of Floquet multipliers leaving the unit circle $\pm \exp i\phi$ as $\Omega = \phi/2\pi$ (see Figure 4.5). When the map is assumed to correspond to the crossing points of an orbit with a given Poincaré surface, the Naimark-Sacker bifurcation leads to a quasiperiodic motion with two independent frequencies such that if the ratio between frequencies Ω/ω_{return} is an irrational number then, the trajectory on the newborn attractor becomes dense on the surface of a torus. On the other hand, if $\Omega/\omega_{return} = p/q$ is a rational number the orbit after
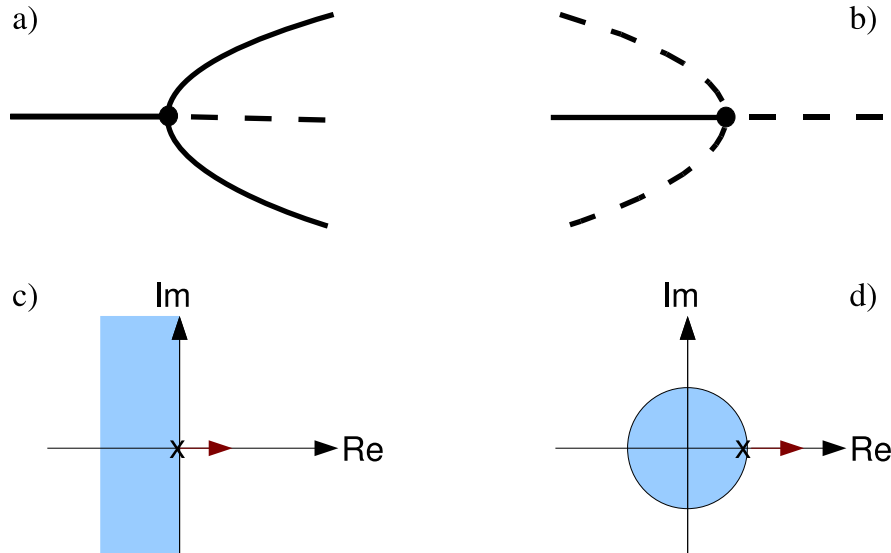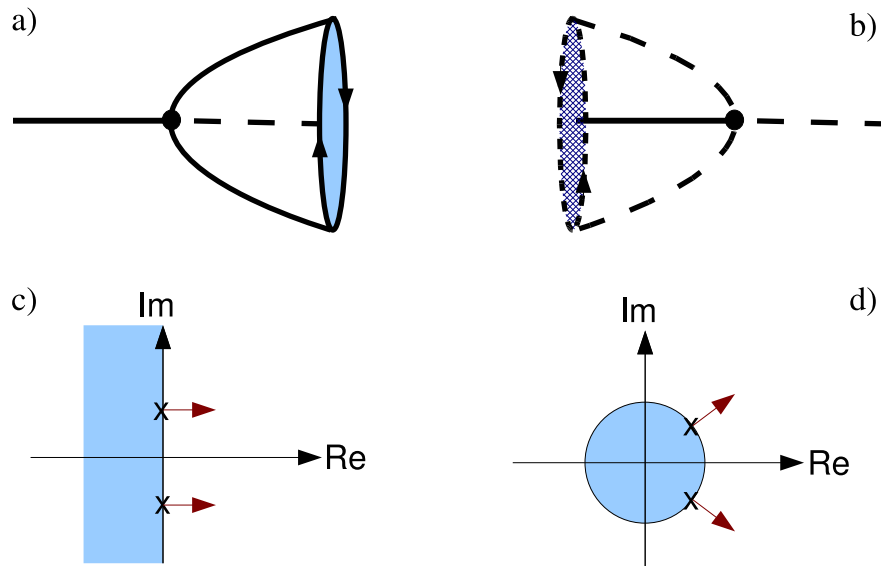
Figure 4.4. a) Pitchfork supercritical bifurcation diagram. b) Pitchfork subcritical bifurcation diagram. c) Bifurcation condition for flows. d) Bifurcation condition for maps. In the bifurcation diagram, solid (dashed) lines indicate stable (unstable) structures.

the bifurcation is still strictly periodic and one speaks about p/q resonances or locking since the ratio between both frequencies is usually maintained in a given region of the parameter space. In this context, strong or soft resonances refer to the cases where $q \leq 4$ and $q \geq 5$, respectively.

- **Flip**. This bifurcation formally occurs only for discrete time dynamical systems or maps. It is related to the instability of a fixed point (x^*) and the appearance of an orbit alternating or flipping between two points (x_- and x_+). From the perspective that the fixed point of the map undergoing the bifurcation describes the crossing of a periodic orbit (with period T) with a Poincaré section, the newborn solution represents a limit cycle with approximately twice the period of the original orbit, $\sim 2T$. For this reason this bifurcation is also known as period-doubling bifurcation. The eigenvalue characteristic of this type of bifurcation is the transition of one Floquet multiplier becoming more negative than -1 as indicated in Figure 4.6.

At this point, it is worth to remark that even if all the former bifurcations are of codimension one, not all of them are generic under the variation of a single control parameter μ. For instance, the transcritical and pitchfork bifurcations are structurally unstable under perturbation of their modeling equations or normal forms, and require further constrains or symmetries to physically appear upon changing

a)

b)

c)

d)

Figure 4.5. a) Hopf supercritical bifurcation diagram. b) Hopf subcritical bifurcation diagram. c) Bifurcation condition for flows. d) Bifurcation condition for maps. In the bifurcation diagram, solid (dashed) lines indicate stable (unstable) structures.

a)

b)
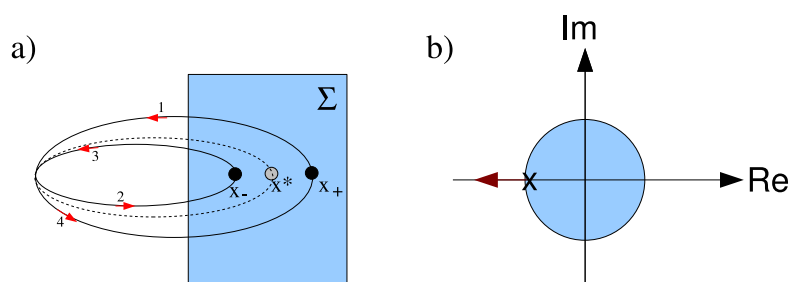
Figure 4.6. a) Flip bifurcation diagram. b) Bifurcation condition for maps. In the bifurcation diagram, solid (dashed) lines indicate stable (unstable) structures. The numbers in the figure help to follow the sequence of motion in the new orbit.

one parameter.

Some codimension-two local bifurcations, i.e., two control parameters need to be simultaneously varied in order to meet the bifurcation point, are reviewed below. These bifurcations are sometimes interpreted as the collision or intersection of two codimension-one bifurcations in a given parameter space. The importance of this points is that they typically act as organizing centers of the dynamics of a system. Thus, the unfolding of these bifurcations, i.e., the characterization of the dynamical regimes in the vicinity of the bifurcating point in a given parameter space, often leads to a rich variety of phenomena such as excitability, global bifurcations, etc... [66]. In the following we list some characteristic bifurcations for flows [65] that we will encounter in posterior chapters within our analysis of coupled lasers:

- **Gavrilov-Guckenheimer**. This type of bifurcation is often interpreted as the coincidence of a saddle-node and a Hopf bifurcation. At the bifurcating point a simple real eigenvalue and a a pure imaginary pair simultaneously cross to the real positive plane as shown in the left panel of Figure 4.7.

- **Takens-Bogdanov**. This bifurcation corresponds to an accumulation point of a Hopf bifurcation branch, i.e., a limit point in a family of Hopf bifurcation where the imaginary part of the eigenvalues tends to zero. Consequently, they are identified by a double zero of the characteristic equation as displayed by Figure 4.7.

- **Hopf-Hopf**. The intersection of two families of Hopf bifurcation leads to this type of codimension-two bifurcation, where two complex conjugate imaginary eigenvalues are simultaneously becoming unstable. The eigenvalues condition is represented at the third panel of Figure 4.7.
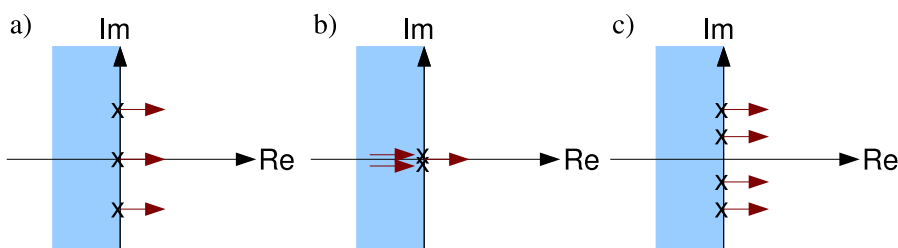
Figure 4.7. Eigenvalues conditions for a) Gavrilov-Guckenheimer, b) Takens-Bogdanov, and c) double Hopf bifurcations.

Successions of the former types of bifurcations (both codimension-one and two) often organize universal routes to chaos in a dynamical system as some parameter is changed. An infinite cascade of period-doubling bifurcations or a finite

sequence of Hopf bifurcations followed by the generic instability of a toroidal attractor are typical examples of such paths toward chaotic regimes.

The characterization of the route to chaos in mutually-coupled semiconductor lasers upon variation of the delay in their interaction is analyzed in Chapter 6. There, several of the former bifurcations are identified in the transition from simple to chaotic behavior in our laser setup. However, the full explanation of some elements of the bifurcation diagram towards chaos needs from the presence of bifurcations that cannot be described in a local region of the phase space. A simple passage over the most typical global bifurcations is presented below.

4.2.2   Global bifurcations

As mentioned before, global bifurcations are difficult to analyze since they typically involve changes in non-localized structures of the phase space. These events can also lead to chaos through different routes than local bifurcations do.

For instance, global bifurcations are often related to the creation of orbits $x(t)$ for which the limits

$$\lim_{t \longrightarrow -\infty} x(t) = x_1^* \qquad and \qquad \lim_{t \longrightarrow +\infty} x(t) = x_2^* \qquad (4.5)$$

exist. If $x_1^* = x_2^*$ represent the same steady-state, the newly created connecting orbit at the bifurcating point is said to be **homoclinic**, otherwise it is called **heteroclinic**. Both homoclinic and heteroclinic connections are important solutions that can organize the appearance of chaotic attractors. The key observation to understand why these connecting orbits lead to chaotic behavior is that their existence often implies an infinite number of intersections between the stable and unstable manifold of a saddle point. Thus, the tangle of intersection points induces then trajectories that are pushed away and pull back to the saddle point and thus seem to wander randomly around the phase space near to that point [64].

Crises are also a major source of bifurcating events in which a chaotic attractor collides with an unstable fixed point or limit cycle. The aftermath of such a crash is often the sudden disappearance or expansion of a chaotic attractor and its basin of attraction. Among the more important types of crises one can distinguish the **boundary** and the **interior** crises.

In the first class of crises an unstable fixed point or limit cycles collides with a chaotic attractor at the boundary of its basin of attraction as some parameter of the system is changed. As a consequence, trajectories that before were wandering around the chaotic attractor are now repelled by the unstable fixed point or limit

cycle toward another attracting structure in a different region of the phase space. Then the old attractor and its basin completely disappear after the bifurcation.

Interior crises, on the other hand, are also produced when a chaotic attractor touches an unstable fixed point or limit cycle which this time lives within its basin of attraction. When the impact between both structures occurs, the chaotic attractor experience a sudden increase in size because now trajectories that get close to the unstable fixed point or limit cycle, they are propelled to explore new areas of the phase space of its own basin of attraction.

Being a basic element in the investigation of nonlinear dynamics, the continuation and study of the bifurcations of fixed points and periodic solutions for continuous and discrete dynamical systems has been since long benefited from the existence of several computational packages. AUTO for ODEs, and DDE-Biftool and PDDE-Cont for DDEs are for instance, popular software for detecting different bifurcations by approximating the location of the eigenvalues of a characteristic equation [60]. However, a word of caution must be raised against the use of this type of programs as black boxes without an appropriate knowledge of the internal procedures and basics of bifurcating phenomena. In this thesis, when possible analytical approaches are always preferred. Only in Chapter 6 the package DDE-Biftool is used in order to compute the stability of periodic orbits.

4.3   Symmetry methods for bifurcations

Dynamical systems often exhibit a certain invariance which can be helpful in analyzing and understanding some general phenomena that, relying on symmetry properties, are typically model-independent. The different symmetries exhibited by both configurations, open-end and ring, allow us to expect different types of synchronization patterns.

Here it is important to realize that the invariance of the modeling equations of a system under a given set of transformations is, in general, a property not inherited by their solutions, i.e., a particular solution of symmetric ODEs or DDEs need not to be symmetric. However, the set of all solutions must be symmetric. For example, the normal form of the supercritical pitchfork bifurcation ($\dot{x} = \mu x - x^3$) is symmetric under the reflection of the sign of the state $x \longmapsto -x$, while each one of the newborn paths of stable fixed points is clearly not respecting (i.e., it is breaking) this symmetry (see Figure 4.4). Instead, what the symmetry of the system tells us is that the existence of one of these asymmetric branches implies the presence of the other so that the set of both solutions is invariant under reflection.

In order to make this type of statements more precise and provide a mathemat-

ical framework in which concrete predictions for the synchronization solutions of our laser systems could be made, it is necessary to introduce the concept of symmetry of a system of ODEs or DDEs. Thus, a symmetry of a system of equations

$$\dot{\mathbf{x}} = f(\mathbf{x}, \mathbf{x}(t - \tau), \mu) \,, \tag{4.6}$$

is described in terms of a set of transformations of the variables that preserves the structure of the system. This is usually expressed as the action of a group of transformations Γ on a vector space (in our case with laser models we deal typically with $\mathbb{R}^n$ or $\mathbb{R}^n \times \mathbb{S}^m$) such that for every solution of the system $x(t)$ and element of the group γ, $\gamma x(t)$ is also a solution [67]. It is in this precise sense that we mentioned that any of the two new paths of fixed points created in a pitchfork bifurcation breaks the reflection symmetry of the system, and still since the $\mathbb{Z}_2$-symmetry-group transforms one path of steady-states into the other, this is maintained for the set of solutions.

The most common symmetries that we will encounter in our networks of lasers are the dihedral group $\mathbb{D}_m$ (bidirectional ring of m lasers), the cyclic group $\mathbb{Z}_m$ (unidirectional ring of m lasers), and the permutation group $\mathbb{S}_m$. Open chains of lasers of length m will exhibit in general symmetries of the type $\mathbb{Z}_2 \times \mathbb{Z}_2...$ corresponding to the exchange of lasers equally distant from the center of the chain. For our interests, the theory of equivariant (symmetric) dynamical systems can be of great help in classifying these possible spontaneous symmetry-breaking events according to the specific symmetry groups of our configurations. In fact, different synchronization behaviors (our main subject of interest) can be understood as different ways of breaking a given symmetry. At this point, the main results from symmetry methods that we can use in order to obtain such a classification are rather technical. Loosely speaking they can be stated as the fact that when a symmetry of a group is broken there is a hierarchical arrangement of the subgroups under which the system can still be invariant. Such an arrangement is known as the isotropy lattice of the symmetry group [67] and it has been very helpful in classifying and selecting the possible behaviors in symmetric systems. In our specific case, special attention is paid to the role of the delay, and the importance of the length of the lasers chain m and the type of network, in the synchronization and symmetry-breaking properties.

Chapter 5

Basics of lasers

In the brief history of the laser the almost simultaneous announcement at the end of 1962 by groups from MIT, IBM, and General Research Laboratories of the creation of the first semiconductor lasers stands out. Its invention opened a door toward the miniaturization, cost-efficiency, and consequently massive use of this type of devices in multitude of applications we use in our everyday life. These kind of lasers, besides of having very interesting properties for practical applications, exhibit huge gain coefficients and an inherent non-linearity which make them excellent candidates to develop dynamical instabilities of high interest for academics and industry.

Here, we briefly review the basic ingredients of the lasing action in semiconductor lasers in order to establish a minimum background on which we could discuss the nonlinear dynamics and synchronization of such devices in the following chapters.

5.1   Once upon a laser

Stimulated emission is the process by which light passing through a fluorescent material can be amplified. The proposal of this mechanism in the light-matter interaction by Albert Einstein in 1916 is usually considered the beginning of the laser theoretical foundation. Einstein introduced the concept of induced or stimulated emission when studying the thermal equilibrium of a set of atoms with the electromagnetic radiation. He noticed that besides the absorption and spontaneous emission of a photon by an atomic system, a new process was necessary in order to recover from thermodynamical arguments the Planck formula for the black body radiation. Thus, the concept by which the encountering of an excited atom with a photon, which is resonant with an atomic transition, causes the emission of an identical photon, was first devised.

Although the first experimental evidence of stimulated emission was observed by Ladenburg and Kopferman in 1928, the interest on this effect decreased among the physicists. The main reason was the apparent impossibility of creating inverted populations with more atoms in the excited state than the ground state so that absorption would not dominate the process and stimulated emission could occur. In fact, it was clear that the Boltzmann distribution of occupation of energy levels assured that population inversion could not occur in a system in thermodynamical equilibrium. An external pumping of energy or the isolation of excited atoms could solve this problem but it was necessary to wait until 1954 when Charles H. Townes introduced the key element for the light amplification development. His idea of placing the amplifying medium inside a resonant cavity so that an oscillation could start, provided that the gain of the stimulated emission could overcome the cavity losses, led to the first practical microwave amplification by stimulated emission of radiation or MASER [1].

The transition from the maser to the laser, or equivalently, from the microwave to the optical domain was far from being trivial. In a seminal paper published in Physical Review in December of 1958, Townes and his postdoctoral assistant Arthur L. Schawlow described the first detailed proposal for building a laser with the fundamental idea of a pair of mirrors facing each other playing the role of the resonant cavity. The effect of the mirrors was to select from the non-directional light of the fluorescent material only those photons propagating along the cavity axis, and consequently made them to pass through the amplifying medium several times by bouncing back and forth between the mirrors before they escape through a partially transparent mirror, and hence generating a useful laser beam. The much smaller wavelength of the visible light compared to the microwave and the problem of finding the appropriate excitation media made the experimental development of the laser an exciting and difficult one. But in May of 1960, the American physicist Theodore H. Maiman eventually achieved the first laser action[2] in a pink ruby rod with its ends silver-coated and placed in a spring-shaped flashlamp.

Later on, many different laser systems have been successfully built but almost all of them (including the semiconductor laser that will be discussed below) still consist of the same three ingredients than the first original laser, namely, a) **an active medium hosting the stimulated emission**, b) **a pumping source responsible of creating the necessary population inversion and**, c) **a cavity providing a feedback and frequency selection mechanism**.

---

[1]Townes and the USSR physicists Basov and Prokhorov shared the Nobel Prize in Physics in 1964 for developing the maser.

[2]The emission of this first laser was pulsating because of the three level nature of the ruby system was unable to maintain a permanent population inversion.

5.2 Semiconductor lasers

5.2.1 Introduction

John Von Neumann, one of the fathers of the quantum theory, was also the first in proposing semiconductor materials as candidates to host light amplification as early as 1953. The idea of recombining electron-hole pairs in a p-n junction was culminated when the lasing action in semiconductors was first reported in 1962 by four independent groups from MIT, IBM and General Research Laboratories. The characteristics of this type of laser considerably differed from the first laser developed only two years before and required of an extraordinary effort. The pumping mechanism consisted of electronic injection rather than the intense discharge of photons from a flashlamp as used in the ruby laser. Moreover, the discrete levels of energy between which the laser transition took first place in the ruby had nothing to do with the energy bands of the semiconductor materials. The laser cavity is also very special and exclusive in a semiconductor laser and it was first formed by the polished facets perpendicular to the junction plane through the reflectivity that provides the index change in the interface of the semiconductor material and the air.

In 1963 Kroemer in USA and Alferov and Kazarinov in USSR independently suggested the crucial improvement of using heterostructures for semiconductor lasers. The heterostructure consists of placing the active material sandwiched between two semiconductor layers with a wider band gap (See Figure 5.1). The huge reduction in the injection current necessary to operate these new lasers and the improvement of characteristics such as the optical confinement due to the heterostructure addition permitted that with the advent of the first practical demonstration of this type of lasers in 1969, the semiconductor laser became for the very first time the small, cheap and fast source of light widely used today.
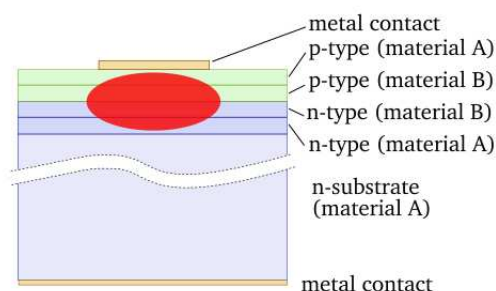
Figure 5.1. Diagram of the double heterostructure of a typical edge-emitting laser.

Of course, a lot of advances have taken place since those early days of the semiconductor laser history, but here we only want to mention the breakthrough

related to the introduction of the vertical-cavity surface-emitting lasers (VCSELs) in 1979. From the design point of view, the main novelty that this laser introduced was the fact that the output of light was normal to the junction plane, instead of parallel as in the conventional edge-emitter lasers (see Figure 5.2). Nowadays, this type of lasers are a hot topic of research and they offer better performance for several applications where a cheap, low power, and compact source of light is needed. However, these devices can suffer the problem of an uncontrolled dynamics of the polarization of the light they emit. A study of the mutual coupling of VCSELs is presented in Chapter 7.
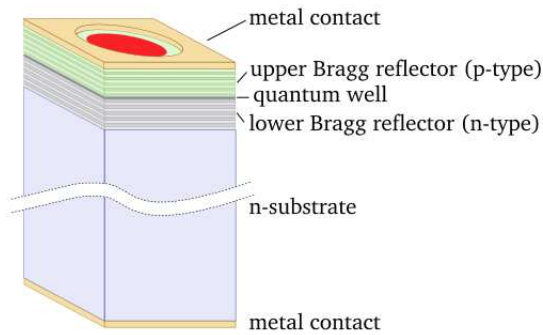
Figure 5.2. Diagram of a simple VCSEL structure highlighting the dielectric mirrors and the fact that their light output is perpendicular to the semiconductor material junctions.

5.2.2   Semiconductor laser rate equations

Most lasers are typically described through three macroscopic variables being the electric field, population inversion, and material polarization. Depending on the time scales in which the three variables decay, none of them, one, or even two of these variables can be adiabatically eliminated. A classification of lasers is made according to the number of variables eliminated. Hence, Class C lasers are those in which the three decay constants are of the same order of magnitude and no adiabatic elimination of any of the variables proceeds. In this case the three variables are needed to accurately describe the main physical processes in the laser. In Class B lasers only one of the variables is eliminated and two of them are still required to capture the dynamics of the laser. Finally, in Class A lasers, only one variable governs the evolution of the system.

Since in a semiconductor the relaxation time for the polarization is much shorter than for the rest of variables, it can often be adiabatically eliminated and then the semiconductor laser falls into the Class B group. Due to the complex nature of the electric field ($E = \sqrt{S}e^{i\varphi}$, where S is the optical intensity and φ is the optical phase) we end up with three equations, which can be deduced from Maxwell and Schrödinger equations after a series of important approximations, to

describe the dynamics of a typical edge-emitting semiconductor laser

$$\frac{dS}{dt} = (\Gamma g - \gamma_c)S \qquad (5.1)$$

$$\frac{dN}{dt} = \frac{J}{ed} - \gamma_s N - gS \quad (5.2)$$

$$\frac{d\varphi}{dt} = \frac{1}{2}\alpha(\Gamma g - \gamma_c), \qquad (5.3)$$

where N stands for the population inversion, γ_c is the photon decay rate, γ_s is the carrier decay rate, J is the current density injection, and $g = g(N, S)$ is the gain function.

As we can see, for a solitary laser the optical phase is just a "slave" of the population inversion and optical intensity variables, and as a consequence the dynamics of these variables are decoupled from the phase. This means that a single-mode class B semiconductor laser cannot exhibit chaotic dynamics because at least three ordinary differential equations are required in order to observe that complex behavior, and only two equations are coupled in the system of Eqs. (5.1)-(5.3).

However, the effect of external perturbations on the semiconductor laser introduces additional degrees of freedom able to excite very rich complex dynamical states as bistability, excitability, or even chaos. Among the variety of ways of perturbing a semiconductor laser, we point out the injection of light into the active region of the laser, the feedback of light from the same laser into its own active region, and the modulation of the current supply ($J = J(t)$). Any of these modifications of the solitary laser setup is subject to a great deal of analysis by the researchers because of intrinsic and applications interests. **In this work we study another kind of perturbation that consists of the mutual coupling of two or more semiconductor lasers and which allow us to study the phenomenon of synchronization**, which has been introduced in Chapter 2.

In the case of VCSEL devices the polarization properties of the electric field need to be considered. If in edge-emitting semiconductor lasers the geometry of the cavity is the predominant effect in selecting the polarization of the emitted light, in VCSELs (due to their cylindrical structure) the optical transitions occuring in the emission or absorption of photons become a key ingredient in determining the polarization state. A now standard approach to describe the polatization effects in VCSELs is the Spin Flip Model (SFM) [15]. This model considers only transitions between the conduction and the heavy-hole bands of the semiconductor material. Moreover, within the SFM framework such bands are approximated by discrete levels populated by two different spin carriers according to the third component of their angular momentum (see Figure 5.3).

$J_z=+1/2$ _____ γ_j _____ $J_z=-1/2$

          E_- E_+

$J_z=+3/2$ _____   _____ $J_z=-3/2$

Heavy hole levels
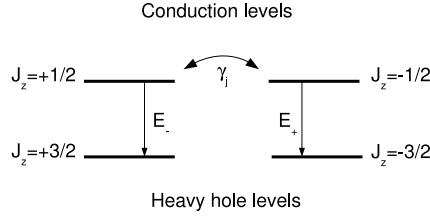
Figure 5.3. Level structure on which the SFM is based. E_+ and E_- represent lasing processes associated to right and left circularly polarized light, respectively. Both spin populations are coupled through the spin-flip mechanisms (γ_j).

For this four-level system the standard Maxwell-Bloch equations, after the macroscopic material polarization has been adiabatically eliminated, read

$$\dot{E}_\pm = \kappa(1 + i\alpha)[N \pm n - 1]E_\pm - (\gamma_a + i\gamma_p)E_\mp \qquad (5.4)$$

$$\dot{N} = -\gamma_e\left[N - \mu + (N + n)|E_+|^2 + (N - n)|E_-|^2\right], \quad (5.5)$$

$$\dot{n} = -\gamma_s n - \gamma_e\left[(N + n)|E_+|^2 - (N - n)|E_-|^2\right], \qquad (5.6)$$

where $E_\pm$ are the two circularly polarized components of the slowly varying amplitude of the electrid field, N is the total carrier density, and n is the population difference between the two spin reservoir sublevels. For the derivation of the model the decay rate $\gamma_s = \gamma_e + 2\gamma_j$, where γ_e is the decay rate of the electron-hole recombination processes, has been introduced in a phenomenological way. Such a spin relaxation mechanism is responsible for the coupling of the two two-levels systems associated to the emission of right and left circularly polarized photons.

5.2.3 Polarization of light

In Chapter 7, when studying the polarization dynamics of two mutually-coupled VCSELs we will follow the spin flip model to describe the solitary lasers plus an appropriate modification of the equations in order to account for the mutual optical injection.

An appropriate mathematical description of the polarization state of a VCSEL or any other source of light is given by the Stokes parameters. These are related to the circular and linear components of the electric field as follows:

$$S_0 = |E_+|^2 + |E_-|^2 = |E_x|^2 + |E_y|^2,$$

$$S_1 = 2\Re(E_+ E_-^*) = |E_x|^2 - |E_y|^2,$$

$$S_2 = -2\Im(E_+ E_-^*) = -2\Re(E_x^* E_y),$$

$$S_3 = |E_+|^2 - |E_-|^2 = -2\Im(E_x^* E_y).$$

Thus, the S_0 parameter describes the total light intensity and the ratios S_1/S_0, S_2/S_0, and S_3/S_0 define a vector pointing at the surface of a sphere which contains all the possible states of polarization of light. Such a sphere, known as the Poincaré sphere, is represented in Figure 5.4 where the polarization and ellipticity angles are also defined.
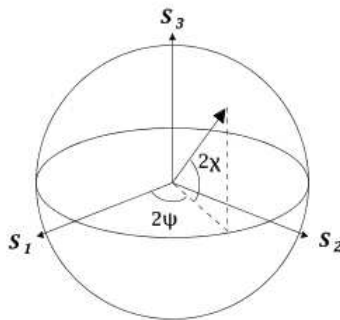
Figure 5.4. Poincaré sphere. The linear polarized states on light lie on the equator of the sphere, while the poles represent completely circular polarized states. The angles defined on the figure are known as the polarization angle ψ and ellipticity angle χ.

Part II

Results

Chapter 6

Mutually-coupled semiconductor lasers: stability, route to chaos, and synchronization

As[1] we have seen from the introductory chapters, a semiconductor laser array is just one of the many examples in which the interaction of several similar nonlinear systems can lead to rich variety of emergent behaviors [1]. Neurons, chemical oscillators, or Josephson junctions are other representative cases of coupled nonlinear oscillators that have attracted the attention of researchers from different fields. However, quite surprisingly, only recently have the effects of the finite propagation speed of the signals in the interaction or coupling between several of these systems been taken into account. In this chapter, we precisely focus on the effect of these delay times, which constitute a rich source of instabilities, on the dynamics and synchronization of semiconductor laser systems.

In Chapter 1, we emphasized the fact that semiconductor lasers are ideal candidates for exploring the behavior of nonlinear systems when they are coupled or subject to external perturbations. Besides their inherent nonlinearity these type of devices can be well characterized and controlled in experiments, as opposed to most of biologically oriented systems. Moreover, a long tradition accompanies the study of these type of devices. The nonlinear dynamics of semiconductor lasers have been an active field since the early 70's. Since then different configurations

---

[1]This chapter is based on the papers:

R. Vicente, S. Tang, J. Mulet, C.R. Mirasso, and J.M. Liu, Phys. Rev. E **70**, 046216 (2004);

S. Tang, R. Vicente, M. Chiang, C.R. Mirasso, and J.M. Liu, IEEE J. Selected Topics in Quantum Electron. **10**, 936 (2004) ;

R. Vicente, S. Tang, J. Mulet, C.R. Mirasso, and J.M. Liu, Phys. Rev. E **73**, 047201 (2006).

of SLs have been investigated theoretically and experimentally. In particular, the optoelectronic interaction of SLs has been mostly studied in a single device subject to feedback [68–73] or in unidirectionally coupled schemes [74–77], where applications to encoded communications have been extensively considered [78–80].

In this chapter, we investigate the dynamical properties of two semiconductor lasers subject to a bidirectional optoelectronic coupling. The organization of the chapter is splitted in two parts in order to separately approach the cases where each laser is subjected (additionally to the mutual coupling) to a feedback loop or not.

After a common theoretical model is presented in the next Section, in the first part of the chapter we consider lasers that when decoupled exhibit a continuous wave (CW) operation since no feedback loops are included. Thus, we focus on the instabilities arising from the lasers delayed interaction and the entrainment properties of these instabilities when the coupling strength is enhanced. Bifurcation theory is applied in Sections 6.2.1, 6.2.2, and 6.2.3 to analytically obtain different stability charts. There, the role of the delay in destabilizing the system is clarified as well as we identify a quasiperiodic route to chaos. The degree of similarity between the instabilities emerging in both lasers and their relative timing are obtained in Section 6.2.4 by cross-correlation analysis, while Section 6.2.5 collects a series of experimental results concerning the confirmation of a quasiperiodic scenario toward chaos and the achronal entrainment of instabilities between lasers. A brief summary of the results and the main conclusions of the investigation of this configuration is given in Section 6.2.6.

In the second part of the chapter, in addition to the mutual interaction, the effect of optoelectronic feedback loops acting on each of the lasers is considered. It is important to remark that this kind of configuration, in which both, the interaction between systems (mutual coupling) and the self-interaction (feedback loop) are subject to inherent time delays, is not specific to our laser setup. Just the opposite, it is very common to find that systems that establish an interaction with other elements also have a tendency to form self-feedback loops. Moreover, the inclusion of the feedback loops embodies the possibility to tune the dynamics of the uncoupled lasers between oscillatory, pulsating, or even chaotic behavior depending on the strength and delay time that characterize the feedback interaction. First, we start by discussing the new bifurcating scenario of this configuration in Section 6.3.1. The "death by delay" quenching of oscillations is an important effect in nonlinear dynamics and it is predicted for our laser system in Section 6.3.2. There, we also find new features of this phenomenom due to the inclusions of delayed feedback loops, which include the observation of this effect even for instantaneously coupled oscillators. The synchronization properties of the system are reviewed in Section 6.3.3 where the relative dynamics and the effect of the delay on the frequency locked regions (or Arnold tongues) is investigated. Laboratory confirmation of some of the predictions and main conclusions are given in

Sections 6.3.4 y and 6.3.5, respectively.

6.1 Model

Here, we illustrate the system under study and provide the modeling equations and values of the more relevant parameters. The fixed points or steady-states of the model are also included in this common section.

6.1.1 The system

In the general case, we consider the system, sketched in Figure 6.1, composed by two identical single-mode distributed-feedback (DFB) semiconductor lasers subject to optoelectronic coupling and feedback. Thus, in laboratory experiments the optical power emitted by each laser is first detected and converted into photocurrent by the PDs, to be later amplified and added to the bias current of its counterpart laser (optoelectronic coupling) and to its own injection current (optoelectronic feedback). These interactions are delayed due to the finite propagation times of both the optical and electrical signals. It is important to notice that with this setup negative couplings can be also achieved by subtracting the photocurrent from the bias current instead of adding it. In any case, through all this chapter we have maintained the strength of the optoelectronic interactions within reasonable limits, such that the total injection current applied to each laser is always positive.
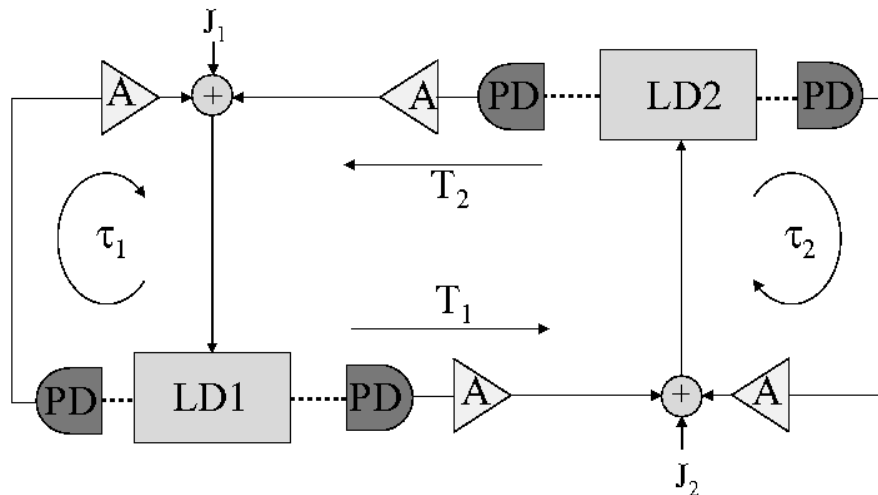
Figure 6.1. Scheme of two lasers subject to optoelectronic feedback and mutual coupling. LD: laser diode; PD: photodetector; A: electrical amplifier.

6.1.2 Modeling equations

Regarding the modeling of the system, we consider each solitary laser described by the usual single-mode semiconductor laser rate equations [81, 82]. Then, the dynamics of the photon S_j and carrier N_j densities are properly modified to include the coupling and feedback loops. The optical phase does not play any role in the modeling since the optoelectronic interaction is mediated through photodetectors which are insensitive to the phase of the electric field.

The bidirectional optoelectronic coupling is accounted for by adding in the carrier rate equation of each laser $\dot{N}_j$, a term with the delayed photocurrent generated by its counterpart laser, $\propto S_{3-j}(t - T_{3-j})$. Similarly, the effect of the feedback loops is taken into account by including to the bias of each laser the photocurrent generated by itself, $\propto S_j(t - \tau_j)$. Hence, the dynamics of the system is governed by the following rate equations for the evolution of the photon and carrier densities in both lasers

$$\frac{dS_1}{dt} = (\Gamma g_1 - \gamma_{c_1})S_1 \,, \tag{6.1}$$

$$\frac{dN_1}{dt} = \frac{J_1}{ed} + \xi_{c1} S_2(t - T_2) + \xi_{f1} S_1(t - \tau_1) - \gamma_{s_1} N_1 - g_1 S_1 \,, \tag{6.2}$$

$$\frac{dS_2}{dt} = (\Gamma g_2 - \gamma_{c_2})S_2 \,, \tag{6.3}$$

$$\frac{dN_2}{dt} = \frac{J_2}{ed} + \xi_{c2} S_1(t - T_1) + \xi_{f2} S_2(t - \tau_2) - \gamma_{s_2} N_2 - g_2 S_2 \,, \tag{6.4}$$

where $S_{1,2}$ is the intracavity photon density, $N_{1,2}$ is the carrier density, and $g_{1,2}$ is the material gain. The subindices 1 and 2 distinguish between both lasers. $\xi_{c1,2}$ and $\xi_{f1,2}$ stand for the coupling and feedback strengths, which can be easily controlled by adjusting the gain factor of the electrical amplifiers in Figure 6.1. $T_{1,2}$ are the delays in the coupling lines between lasers whereas $\tau_{1,2}$ are the delay times in the feedback loops. Other parameters appearing in the rate equations are the bias current density J, the cavity decay rate γ_c, the spontaneous carrier relaxation rate γ_s, the confinement factor of the laser waveguide Γ, the electron charge e, and the active layer thickness d. An infinite-bandwith photodetector-amplifier response is assumed for the moment. The effects of high or low cutoff frequencies of a filtered photodetection process are considered in Section 6.3.2.

To continue with the development of the model we need to know the dependence of g on the state variables. Numerical calculations and experimental measurements show that in a wide operation range the material gain has a linear dependence on both the carrier and photon densities. Therefore, $g(N, S)$ is expanded as

$$\mathrm{g} \approx \mathrm{g}_0 + \mathrm{g}_n(N - N_0) + \mathrm{g}_p(S - S_0) , \tag{6.5}$$

where $\mathrm{g}_0 = \gamma_c/\Gamma$ is the material gain at the solitary threshold, $\mathrm{g}_n = \partial\mathrm{g}/\partial N > 0$ is the differential gain parameter, $\mathrm{g}_p = \partial\mathrm{g}/\partial S < 0$ is the nonlinear gain parameter, N_0 is the carrier density at threshold, and S_0 is the free-running intracavity photon density when the lasers are decoupled from feedback or mutual interactions. The parameters g_n and g_p are taken to be approximately constants.

With a view to normalize the modeling equations, we define the following dimensionless variables for the photon density $\tilde{s} \equiv (S - S_0)/S_0$, carrier density $\tilde{n} \equiv (N - N_0)/N_0$, bias current $\tilde{J} = (J/ed - \gamma_s N_0)/\gamma_s N_0$, coupling $\kappa_c \equiv \xi_c\Gamma/\gamma_c$, and feedback strength $\kappa_f \equiv \xi_f\Gamma/\gamma_c$. Working with this normalization, $\tilde{s} = -1$ when no light is emitted by the laser while $\tilde{s} = 0$ when the optical intensity equals that of the solitary value, i.e., S_0. $\tilde{J}$ accounts for the excess of the bias current over the solitary threshold. After introducing Eq. (6.5) into Eqs. (6.1)-(6.4) the normalized rate equations read

$$\frac{d\tilde{s}_1}{dt} = \frac{\gamma_{c_1}\gamma_{n_1}}{\gamma_{s_1}\tilde{J}_1}\tilde{n}_1(\tilde{s}_1 + 1) - \gamma_{p_1}\tilde{s}_1(\tilde{s}_1 + 1), \tag{6.6}$$

$$\frac{d\tilde{n}_1}{dt} = \frac{\gamma_{s_1}\gamma_{p_1}}{\gamma_{c_1}}\tilde{J}_1\tilde{s}_1(1 + \tilde{s}_1) + \gamma_{s_1}\kappa_{f_1}\tilde{J}_1\left[1 + \tilde{s}_1(t - \tau_1)\right] \tag{6.7}$$

$$+ \gamma_{s_1}\kappa_{c_1}\tilde{J}_1\left[1 + \tilde{s}_2(t - T_2)\right] - \gamma_{s_1}\tilde{n}_1 - \gamma_{s_1}\tilde{J}_1\tilde{s}_1 - \gamma_{n_1}\tilde{n}_1(1 + \tilde{s}_1),$$

$$\frac{d\tilde{s}_2}{dt} = \frac{\gamma_{c_2}\gamma_{n_2}}{\gamma_{s_2}\tilde{J}_2}\tilde{n}_2(\tilde{s}_2 + 1) - \gamma_{p_2}\tilde{s}_2(\tilde{s}_2 + 1), \tag{6.8}$$

$$\frac{d\tilde{n}_2}{dt} = \frac{\gamma_{s_2}\gamma_{p_2}}{\gamma_{c_2}}\tilde{J}_2\tilde{s}_2(1 + \tilde{s}_2) + \gamma_{s_2}\kappa_{f_2}\tilde{J}_2\left[1 + \tilde{s}_2(t - \tau_2)\right] \tag{6.9}$$

$$+ \gamma_{s_2}\kappa_{c_2}\tilde{J}_2\left[1 + \tilde{s}_1(t - T_1)\right] - \gamma_{s_2}\tilde{n}_2 - \gamma_{s_2}\tilde{J}_2\tilde{s}_2 - \gamma_{n_2}\tilde{n}_2(1 + \tilde{s}_2),$$

where the differential and nonlinear carrier relaxation rates are defined as $\gamma_n \equiv \mathrm{g}_n S_0$ and $\gamma_p \equiv -\Gamma\mathrm{g}_p S_0$, respectively. At this point, it is important to note that since $S_0 = \tilde{J}\gamma_s N_0\Gamma/\gamma_c$, both γ_n and γ_p are not independent parameters but are related to the bias current. With these definitions the relaxation oscillation frequency (ROF) can be calculated as

$$f_r = \frac{1}{2\pi}(\gamma_c\gamma_n + \gamma_p\gamma_s)^{1/2} . \tag{6.10}$$

The values of the internal laser constants are taken from a laboratory characterization of devices that have been used for experimental studies in [72]. These

are $\gamma_c = 2.4 \times 10^{11}$ s^{-1}, $\gamma_s = 1.458 \times 10^9$ s^{-1}, $\gamma_n = 3\tilde{J} \times 10^9$ s^{-1}, and $\gamma_p = 3.6\tilde{J} \times 10^9$ s^{-1}.

The dimensionless coupling and feedback strengths can be related to the properties of the photodetection instruments as

$$\kappa_{c,f} = a_{c,f} \frac{\eta c \alpha_m \Gamma}{2 n_g \gamma_c} \eta_{ext} , \qquad (6.11)$$

$a_{c,f}$ being the coupling and feedback amplifier multiplication factors, respectively, η the quantum efficiency of the photodetectors, η_{ext} a parameter that takes into account additional external losses, c the speed of light in vacuum, α_m the laser facet losses and n_g the group refractive index. For a typical case ($\eta = 0.5$, $\eta_{ext} = 1$, $\alpha_m = 48$ cm^{-1}, $n_g = 3.5$, $\gamma_c = 0.24$ ps^{-1}, and $\Gamma = 0.3$) $\kappa_{c,f}$ is of the order of ~ 0.1, when $a_{c,f}$ is fixed to 1. Then, the magnitude of κ_c (or κ_f) can be easily modified just by changing the corresponding amplification factor or the external attenuation. In addition, the sign of κ_c (or κ_f) can be reversed by subtracting the generated photocurrent from the bias instead of adding it. In the analysis performed in the next sections we explore both positive and negative values for the coupling and feedback strengths.

6.1.3   Fixed points of the model

Apart from academic examples, full analytical solutions of nonlinear dynamical systems, like the model presented here, are very rare. In those cases, bifurcation studies of fixed points or other phase space structures can provide a systematic methodoloy to collect a great deal of information about the different dynamical regimes that can rise in the setup under investigation. Next, we proceed to locate the fixed points or equilibria of our laser model.

As a previous step we reduce the number of free parameters of the model by assuming that we are dealing with two device-identical lasers under symmetric operation. Hereafter, we adopt bias currents ($\tilde{J}_1 = \tilde{J}_2 \equiv \tilde{J}$), coupling strengths ($\kappa_{c_1} = \kappa_{c_2} \equiv \kappa_c$), feedback strengths ($\kappa_{f_1} = \kappa_{f_2} \equiv \kappa_f$), and feedback loop delays ($\tau_1 = \tau_2 \equiv \tau$) to be the same for both lasers. It is worth to stress that these approximations fit within the symmetric conditions in which the experiments were performed. Moreover, it is well known that this kind of degenerate conditions are responsible for the appearance of the organizing centers of the dynamics even under small asymmetries or perturbations. Nevertheless, it is worth to mention that albeit the assumption of symmetry there are still six free control parameters, namely $\tilde{J}$, κ_c, T_1, T_2, κ_f, and τ.

The conditions we impose to find fixed points solutions are $\tilde{s}_1(t) = \tilde{s}_{1st}$, $\tilde{s}_2(t) = \tilde{s}_{2st}$, $\tilde{n}_1(t) = \tilde{n}_{1st}$, and $\tilde{n}_2(t) = \tilde{n}_{2st}$. The search of equilibria in the system reveals the existence of four different fixed points. The first solution (FP1) is given by

$$
\begin{aligned}
\tilde{s}_{1st} &= -1 \,, \\
\tilde{n}_{1st} &= \tilde{J} \,, \\
\tilde{s}_{2st} &= -1 \,, \\
\tilde{n}_{2st} &= \tilde{J} \,. \qquad (6.12)
\end{aligned}
$$

This fixed point defines the "off" state of the lasers. There exist two additional fixed points (FP2 and FP3), which correspond to the case in which one laser is emitting while the other is switched-off. These solutions represent the only possible asymmetric steady-states of the system and read

$$
\begin{aligned}
\tilde{s}_{1st} &= \frac{\kappa_f \gamma_c \gamma_n}{\gamma_c \gamma_n (1 - \kappa_f) + \gamma_p \gamma_s} \,, \\
\tilde{n}_{1st} &= \tilde{J} \frac{\gamma_p \gamma_s}{\gamma_c \gamma_n} \tilde{s}_{1st} \,, \\
\tilde{s}_{2st} &= -1 \,, \\
\tilde{n}_{2st} &= \tilde{J} \left(1 + \kappa_c + \kappa_c \tilde{s}_{1st} \right) \,, \qquad (6.13)
\end{aligned}
$$

for the solution named FP2, while FP3 is obtained by just exchanging this subindices 1 and 2. Finally, the steady-state conditions allow for one more fixed point defining the "on" state for both lasers (FP4):

$$
\begin{aligned}
\tilde{s}_{1st} &= \tilde{s}_{2st} = \frac{(\kappa_c + \kappa_f)\gamma_c \gamma_n}{(1 - \kappa_c - \kappa_f)\gamma_c \gamma_n - \gamma_p \gamma_s} \,, \\
\tilde{n}_{1st} &= \tilde{n}_{2st} = \tilde{J} \frac{\gamma_p \gamma_s}{\gamma_c \gamma_n} \tilde{s}_{1st} \,. \qquad (6.14)
\end{aligned}
$$

6.2   Bidirectional coupling without feedback

Here, we consider the situation in which the feedback loops are not included ($\kappa_f = 0$) and only the mutual coupling excites both lasers simultaneously. Next, we proceed by investigating the stability, route to chaos, and entrainment of instabilities developed under this configuration.

6.2.1   Stability analysis of fixed points

We start by analyzing the linear stability of the fixed points found in the modeling section. The characteristic equation particularized to our problem reads

$$det\left(-\lambda\mathbf{I}+ \frac{\partial\mathbf{f}}{\partial\mathbf{x}}\Big|_{\mathbf{x_{st}}} + \frac{\partial\mathbf{f}}{\partial\mathbf{x}_{T_1}}\Big|_{\mathbf{x_{st}}} \exp(-\lambda T_1)+ \frac{\partial\mathbf{f}}{\partial\mathbf{x}_{T_2}}\Big|_{\mathbf{x_{st}}} \exp(-\lambda T_2) \right)=0 \ , \qquad (6.15)$$

where $\mathbf{x} \equiv (\tilde{s}_1, \tilde{n}_1, \tilde{s}_2, \tilde{n}_2)^{\dagger}$ and $\mathbf{f}$ is the flow defined by the right-hand sides of Eqs. (6.6)-(6.9). The notation $\mathbf{x}_T$ stands for the delayed variable $\mathbf{x}(t - T)$. In the following, we focus on the study of the eigenvalues λ of Eq. (6.15) for the different fixed points.

Fixed point FP1

First, we treat the stability of the steady-state in which no laser is emitting light, i.e., FP1. Once linearizing Eq. (6.15) on the expression of FP1, Eq. (6.12), the resultant characteristic equation turns to have only a real solution, $\lambda = (\tilde{\gamma}_c\tilde{\gamma}_n + \tilde{\gamma}_p\tilde{\gamma}_s)/(\tilde{\gamma}_s)$. This eigenvalue becomes zero, and consequently the fixed point becomes unstable, at $\tilde{J} = 0$, i.e., at the solitary threshold.

This result supports the interpretation that threshold reduction in SLs can only occur through coherent interactions where a superposition of the intracavity laser and some injected fields is possible. In our case, since the optoelectronic interaction is by nature phase insensitive no threshold reduction is expected. Similarly to the solitary case, as the bias current is increased the loss of stability of the "off" state is mediated by a collision in the phase space with the "on" state (FP4) in a transcritical bifurcation.

Fixed points FP2 and FP3

The symmetry between these two fixed points allows for a simultaneous study of both of them. In this case the computation of the characteristic equation leads to the following four eigenvalues

$$\lambda_1 \quad = \quad -\gamma_s \ , \qquad\qquad\qquad\qquad\qquad\qquad (6.16)$$

$$\lambda_2 \quad = \quad \frac{\gamma_c\,\gamma_n+\xi_c\,\gamma_c\,\gamma_n+\gamma_p\,\gamma_s}{\gamma_s} \ , \qquad\qquad\qquad (6.17)$$

$$\lambda_{3,4} \quad = \quad \frac{-\gamma_n-\gamma_p-\gamma_s\pm\sqrt{\left(\gamma_n+\gamma_p+\gamma_s\right)^2-4\left(\gamma_c\,\gamma_n+\gamma_p\,\gamma_s\right)}}{2} \ . \qquad (6.18)$$

Evaluating the real part of these roots it is observed that only the second eigenvalue can have a zero real. This occurs when the coupling strength decreases down to the critical value defined by

$$\kappa_c^* = -1 - \frac{\gamma_p \gamma_s}{\gamma_c \gamma_n} \ . \qquad (6.19)$$

To inspect how these two asymmetric fixed points become stable as the coupling decreases we need to invoke here the study of a fixed point whose detailed stability is investigated in the next section; the symmetric steady-state FP4. The key observation consists of realizing that FP4 can lose its stability at exactly the same critical coupling strength κ_c^* for which FP2 and FP3 become stable. This transition is mediated by a real zero eigenvalue of FP4 becoming positive for further decrease of the coupling. Then, at the critical coupling given by Eq. (6.19) we have a situation in which the three fixed points FP2, FP3, and FP4 experience a simultaneous change or flip of their stability. Atypical in this situation is that exchanges of stability between steady-states usually involve collisions of fixed points in the phase space (as we have seen in the local bifurcations reviewed in Chapter 3) and nevertheless such collisions between FP2, FP3, and FP4 are strictly forbidden for the symmetric situation that we are considering here. This last point can be checked by noticing that expressions Eq. (6.13) and Eq. (6.14) cannot coincide regardless of the value of κ_c.

In Figure 6.2 we plot the paths and indicate the stability of FP2, FP3, and FP4 as a function of the coupling strength. Figure 6.2 is generated by assuming a short coupling time delay so that we guarantee that no Hopf bifurcation can affect FP4 as we will demonstrate in the next section. The way out to the former apparent contradiction relies on appreciating that only at the critical coupling the stationary conditions for system Eqs. (6.6)-(6.9) allow for an extra solution consisting of a continuum of fixed points (CFP in Figure 6.2). This continuum of steady-states, lying on the line $\tilde{s}_1 + \tilde{s}_2 = -1$, it is found to connect the other three fixed points involved in the stability flip and mediates in their exchange of stability.

In summary, the stability analysis tells us that when varying the coupling strength towards more and more negative values a sudden transition from the "on' state of both lasers (FP4) to the regime in which one of the laser switches off while the other remains lasing (FP2 or FP3), takes place. Physically, this transition corresponds to the point at which, if operating on FP4 the negative coupling starts generating an effective current (bias plus photocurrent) below the solitary threshold. Therefore, by any small perturbation the system departs from the "on' state in favor of one of the competing asymmetric fixed points. Once operating in FP2 or FP3 the dynamics is again stable because the light coming from one of the lasers is converted in enough negative photocurrent to switch-off its counterpart laser.

So far the perfectly symmetric configuration of the coupled lasers scheme has led us to a highly degenerate picture of the bifurcating mechanisms. To see how the breaking of this symmetric scenario modifies the former picture, in the following
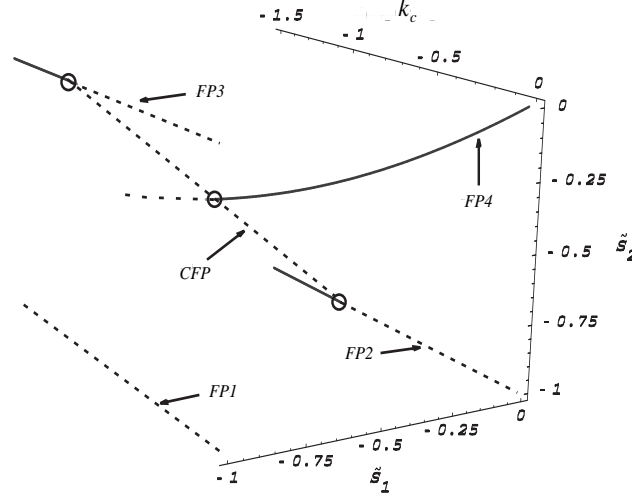
Figure 6.2. Paths of the fixed points in the $\tilde{s}_1 - \tilde{s}_2$ phase space projection as a function of the coupling strength κ_c. Solid and dashed lines indicate of the stable and unstable character of the fixed points, respectively. Different fixed points continuations are labeled as FP (1)-(4). The continuum of fixed points (CFP) only exists for the critical coupling strength at which the stability flip occurs.

we allow for different coupling strengths in the two ways of the interaction between lasers, i.e., $\kappa_{c1} \neq \kappa_{c2}$. To fix ideas we set $\kappa_{c1} = 0.5$, while κ_{c2} is varied up to cross the critical coupling. Figure. 6.3 shows the continuation of the different fixed points as a function of κ_{c2}. Under these asymmetric conditions it is observed that only the laser receiving the stronger negative coupling (in this case laser 2) switches-off. This occurs when the negative photocurrent received induces the crossing of the threshold current only for laser 2. Now, the stability flip uniquely occurs between FP2 and FP4 being mediated by a transcritical bifurcation.

Fixed point FP4

The fixed point FP4 represents the regime in which the two lasers operate in the "on' state emitting a constant optical intensity. While the former analyzed fixed points could only become unstable by the transition of one real zero eigenvalue, FP4 allows for more complex situations.

The bifurcation analysis for this fixed point starts as usual from its associated characteristic equation. For simplicity, we recover here the perfectly symmetric configuration for which both lasers emit an identical optical power, i.e., $\tilde{s}_{1st} = \tilde{s}_{2st} = \tilde{s}$ and $\tilde{n}_{1st} = \tilde{n}_{2st} = \tilde{n}$, as given by Eqs. (6.14). Thus, the characteristic
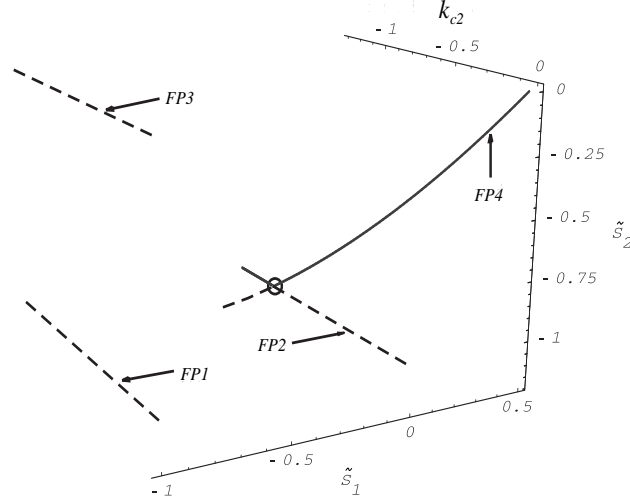
Figure 6.3. Paths of the fixed points in the $\tilde{s}_1 - \tilde{s}_2$ phase space projection as a function of the coupling strength κ_{c2}.sub κ_{c1} has been fixed to 0.5. Solid and dashed lines indicate of the stable and unstable character of the fixed points, respectively. Different fixed points continuations are labeled as F.P. (1)-(4).

equation for FP4 reads

$$\exp(-2\lambda T)\ [\kappa_c\,\gamma_c\,\gamma_n\,(1+\tilde{s})]^2=$$

$$\left[\gamma_p\,(\gamma_s+\lambda)\,(1+2\,\tilde{s})+\lambda\,(\gamma_n+\gamma_s+\lambda+\gamma_n\,\tilde{s})+\tfrac{\gamma_c\gamma_n}{\gamma_s\,J}\left(-\lambda\,\tilde{n}+\gamma_s\left(\tilde{J}-\tilde{n}+\tilde{J}\,\tilde{s}\right)\right)\right]^2,$$

$$(6.20)$$

where the delay times (T_1 and T_2) appear in the above equation only through their sum, $T \equiv (T_1 + T_2)/2$. A first important conclusion is that the individual value of each of the delay times is not important for the stability issue provided that the round-trip time of the system remains fixed.

Once the characteristic equation has been written down, we proceed to locate the Hopf bifurcations of FP4 in the control parameter space spanned by the current injection $\tilde{J}$, coupling strength κ_c, and delay time T. The bifurcation condition consists of inserting $\lambda = i\omega$ into the complex Eq. (6.20) and looking for real solutions for $\omega \neq 0$. After separating both sides of the equation into real and imaginary parts, the delay time T can be easily eliminated to obtain a single a biquadratic expression for ω

$$\omega^4 + b\,\omega^2 + c = 0 \;, \tag{6.21}$$

with coefficients b and c given by

$$
\begin{aligned}
b &= \left(\tfrac{\gamma_c\,\gamma_n\,\tilde{n}}{\gamma_s\,\tilde{J}}\right)^2 + \left({\gamma_s}^2 + {\gamma_n}^2\,(1+\tilde{s})^2 + (\gamma_p + 2\,\gamma_p\,\tilde{s})^2 + 2\,\gamma_n\,(1+\tilde{s})\,(\gamma_p + \gamma_s + 2\,\gamma_p\,\tilde{s})\right) \\
&\quad - \tfrac{2\,\gamma_c\,\gamma_n}{\gamma_s\,\tilde{J}}\left(\gamma_s\,\tilde{J}\,(1+\tilde{s}) + \tilde{n}\,(\gamma_n + \gamma_p + \gamma_n\,\tilde{s} + 2\,\gamma_p\,\tilde{s})\right)\;, \\
c &= \tfrac{\left(\gamma_p\,\gamma_s\,\tilde{J}\,(1+2\,\tilde{s}) + \gamma_c\,\gamma_n\,(\tilde{J} - \tilde{n} + \tilde{J}\,\tilde{s})\right)^2 - \left(\tilde{J}\,\kappa_c\,\gamma_c\,\gamma_n\,(1+\tilde{s})\right)^2}{\tilde{J}^2}\;,
\end{aligned}
$$

and whose solutions are

$$\boxed{\; \omega = \pm\frac{1}{\sqrt{2}}\sqrt{-b \pm \sqrt{b^2 - 4c}}\;. \qquad (6.22)}$$

It is important to recall here that the expressions of the coefficients b and c only depend on the internal and the control parameters $\tilde{J}$ and κ_c. Therefore, the values of the current injection and coupling strength fix the solutions for ω, i.e., the imaginary part of the eigenvalues that cross the imaginary axis. When associated to Hopf bifurcations this imaginary part corresponds to the angular frequency of the newborn limit cycles. It is clear then that the coupling time delay τ, even necessary for the appearence of periodic solutions does not play any role in determining the frequency of the limit cycles when they are born.

Once the proper values of ω have been obtained with Eq. (6.22) the critical time delay for which the transition of eigenvalues takes place can be determined as

$$\boxed{\; T^*(\omega) = \tfrac{1}{\omega}\arctan\left[-\left(\frac{\omega\,(\gamma_s\,\tilde{J}\,(\gamma_p + \gamma_s + 2\,\gamma_p\,\tilde{s}) + \gamma_n\,(-\gamma_c\,\tilde{n} + \gamma_s\,\tilde{J}\,(1+\tilde{s})))}{\gamma_s\,(\gamma_c\,\gamma_n\,(\tilde{J} - \tilde{n} + \tilde{J}\,\tilde{s}) + \tilde{J}\,(-\omega^2 + \gamma_p\,(\gamma_s + 2\,\gamma_s\,\tilde{s})))}\right)\right]\;. \qquad (6.23)}$$

Since the term $\exp(-2i\omega T)$ in Eq. (6.20) remains invariant under the transform $T \longmapsto T + m\pi/\omega$, $\forall m \in \mathbb{Z}$ (property known as clustering in Chapter 3), the former expression unfolds an infinite series of critical delay times given that at least one real T^* exists.

Thus, the necessary and sufficient condition for the existence of a Hopf instability in the system is given by the condition that at least one real solution for ω exists. From Eq. (6.22) it can be observed that this condition is that the quantity $-b \pm (b^2 - 4c)^{1/2}$ is a real and positive number. Since the sign of ω is irrelevant we can only distinguish two branches of solutions for ω depending on the sign we choose inside the square root of Eq. (6.22):

$$\omega_1 = \left(\left(-b + (b^2 - 4c)^{1/2} \right) /2 \right)^{1/2} \tag{6.24}$$

and

$$\omega_2 = \left(\left(-b - (b^2 - 4c)^{1/2} \right) /2 \right)^{1/2} . \tag{6.25}$$

To work out this condition a little bit more we define the discriminant $D \equiv b^2 - 4c$. The existence of a real solution for ω is guaranteed in the regions for which $D > 0 \cap (b < 0 \cup (b > 0 \cap c < 0))$. In the areas of the coupling strength versus injection current plane where such conditions are satisfied we can assure the existence of a real solution for ω and consequently, a critical delay time given by expression Eq. (6.23) beyond which at least a pair of complex eigenvalues have a positive real part.

In the next subsection we collect all the information about the fixed points bifurcation study in order to create stability charts in the most relevant parameter spaces.

6.2.2 Stability diagrams

Here we provide a complete overview of the stability of the different fixed points with respect to variations of the injection current, coupling strength, and time delay.

Current versus coupling strength

In Figure 6.4, we show the stability diagram of FP4 in the injection current versus coupling strength parameter space ($\tilde{J}$ vs. κ_c). From the formerly studied conditions of instability, three different regions can be identified in that plane.

Within the Delay-Independent Stable Region (DISR) the fixed point FP4 is stable regardless the values of the coupling times. There, the system tends to operate in its symmetric state given by FP4 no matter what the distance between the lasers is. At the Delay-Independent Unstable Region (DIUR) zone the fixed point FP4 is always unstable independently of the coupling times. The asymmetric FP2 and FP3 become stable as soon as the coupling strength decreases down to the critical value κ_c^* for which FP4 exactly enters into the DIUR zone. Finally, it is also observed the existence of two Delay-Dependent Stable Region (DDSR) where the stability of the symmetric fixed point FP4 is not only determined by the current and coupling strength but also depends on the exact value of the coupling time.

From Figure 6.4 one can observe some more remarkable features. First, it is important to notice that for a given coupling strength there is always a value of
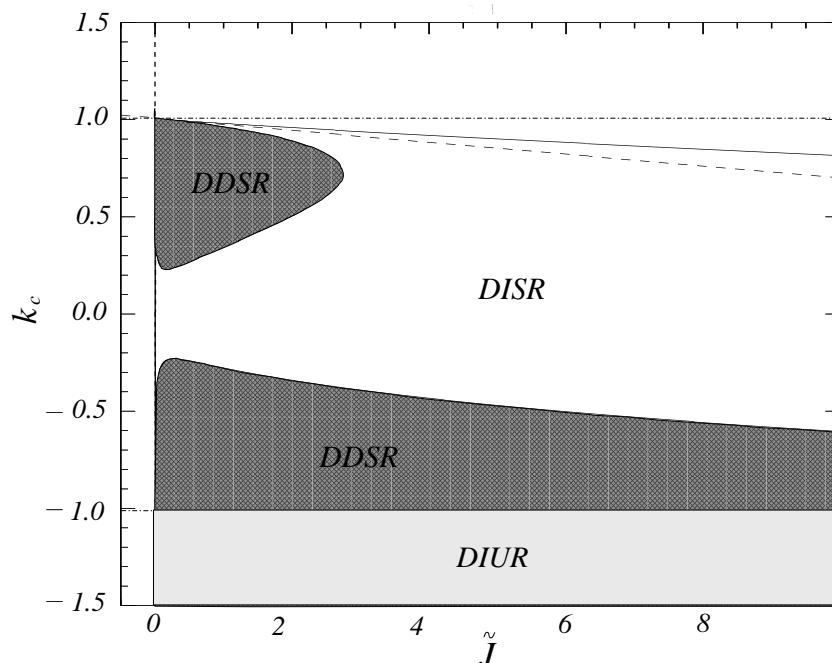
Figure 6.4. Stability diagram in the coupling strength versus injection current plane (κ_c vs. $\tilde{J}$) according to the signs of D, b and c. Solid, dashed and dotted lines represent the zero-level contours for D, b and c, respectively. DISR: Delay Independent Stable Region. DIUR: Delay Independent Unstable Region. DDSR: Delay Dependent Stable Region.

the bias current which is able to stabilize the symmetric steady-state operation of the system (to induce a transition into the DISR zone for FP4). Another interesting characteristic is that it is easier to destabilize the system through negative or inhibitory couplings than with positive or excitatory ones. Note that the border between the DDSR and DISR regions appears for smaller values when the coupling is negative than when it is positive. Both effects, the stabilization of the system for large currents and the larger instability threshold for positive couplings, can be related to the increment of the damping of the relaxation oscillations when the bias or the injected photocurrent increase. Finally, it is worth to mention that the sizes of the different stability regions in Figure. 6.4 strongly depend on the nonlinear carrier relaxation rate parameter γ_p. An increment of this parameter, which corresponds to the gain saturation of the lasers, yields to a reduction of the DDSR island located at positive coupling strengths. Hence, the nonlinear gain parameter, besides introducing an essential nonlinearity in the system, becomes a very important value since it tends to stabilize the dynamics and reduces the ranges of parameters where instabilities may develop.

Coupling strength versus time delay

In order to better understand the effect of the time delay on the stability properties, we fix now the value of the bias current to a moderate value $\tilde{J} = 1/3$. The goal here is to build from the bifurcating events affecting FP4 its stability chart in the coupling strength versus coupling time plane.

The procedure followed to construct such a stability diagram consists of:

1. fixing a value for the coupling strength κ_c,
2. find the corresponding values of $\omega_{1,2}$ given by Eqs. (6.24)-(6.25),
3. compute the critical delay times associated to $T^*(\omega_{1,2})$ for different values of m,
4. and repeat the former steps varying the coupling strength to obtain a family of Hopf curves in the κ_c versus T plane.

Figure 6.5 shows the critical delay time curves corresponding to both eigenfrequencies ω_1 and ω_2, for values of m ranging from 0 to 5.

For the stability issue besides the critical delay time curves, which tell us the exact parameter values for which a pair of eigenvalues lies on the imaginary axis, we still need to check when the eigenvalues cross from the left to the right half-plane of the complex plane or viceversa. This information is be obtained by computing the implicit derivative of Eq. (6.20) with respect to T

$$\frac{d\lambda}{dT} = \frac{-\lambda \exp(-2\lambda T)}{h(\lambda)\frac{\partial h}{\partial \lambda} + T \exp(-2\lambda T)} \; , \qquad (6.26)$$

where $h(\lambda)$ denotes the function

$$
\begin{aligned}
h(\lambda) &= [\kappa_c \gamma_c \gamma_n (\gamma_c \gamma_n + \gamma_p \gamma_s)]^{-1} \times [(1 - 2\kappa_c)\gamma_c^2 \gamma_n^2 + \\
&\quad 2\gamma_c \gamma_n \gamma_p \gamma_s + \gamma_p^2 \gamma_s^2 + \lambda^2(\gamma_c \gamma_n (1 - \kappa_c) + \gamma_p \gamma_s) + \\
&\quad \lambda(\gamma_p \gamma_s (\gamma_n + \gamma_p + \gamma_s) + \gamma_c \gamma_n (\gamma_n + \gamma_p + \gamma_s - \kappa_c \gamma_s))] \; . \; (6.27)
\end{aligned}
$$

We have numerically evaluated $d\Re(\lambda)/dT|_{\lambda=i\omega_{1,2}}$ from Eq. (6.26) as a function of m for several coupling constants. The results are shown in Figure 6.6. Since for all the values of κ_c and m investigated we obtain that $d\Re(\lambda)/dT|_{\lambda=i\omega_1} > 0$ and $d\Re(\lambda)/dT|_{\lambda=i\omega_2} < 0$, one must infer that the destabilization of eigenvalues occurs at the critical delay curves associated to the eigenfrequency ω_1, while stabilizationstake place at the lines associated with ω_2.
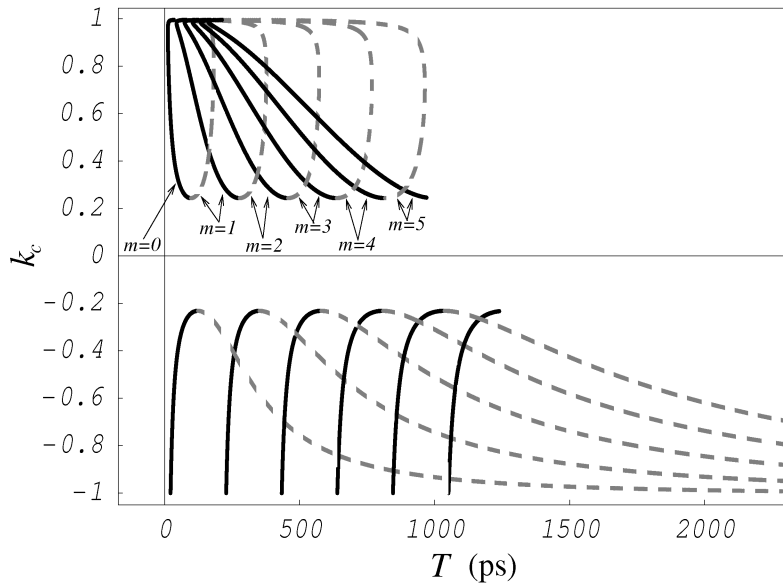
Figure 6.5. Hopf curves $T^*(\omega_{1,2})$ with $m = 0, 1, 2, 3, 4,$ and 5 in the coupling strength versus coupling time plane. Solid and dashed lines distinguish between the sequences associated to ω_1 and ω_2, respectively. The Hopf curve associated to $T^*(\omega_2)$ with $m = 0$ has not been considered here, since it appears at negative coupling delay times.
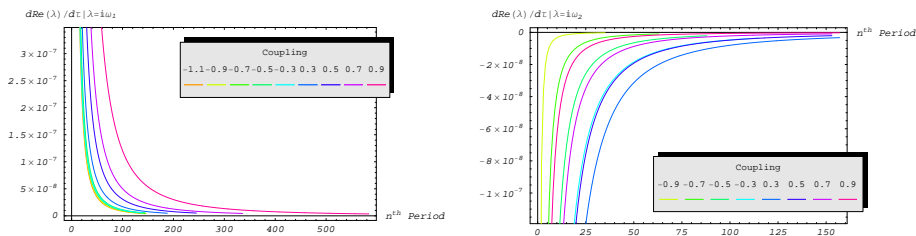
Figure 6.6: $d\Re(\lambda)/dT|_{\lambda=i\omega_{1,2}}$ as a function of the period order m for several coupling strengths.

From Figure. 6.6 it can be also deduced that the "velocity' at which the eigenvalues cross the imaginary axis, in one or other direction, decreases monotonically with the period order m. These results, together with the fact that $\omega_1 > \omega_2$ (which implies that the periodicity in T for the appearance of the destabilizing lines, $2\pi/\omega_1$, is smaller than the corresponding to the stabilizing curves $2\pi/\omega_2$), demonstrate that the rate at which the eigenvalues become unstable at ω_1, when increasing T, is larger than the rate they become stable at ω_2. Therefore, an arbitrarily large number of unstable eigenvalues can be achieved for sufficiently long delay times. It is at this point when we can guarantee the absence of stability islands inside the most external borders of the curves plotted in Fig. 6.5. The resulting stability diagram for FP4 is then shown in Fig. 6.7.
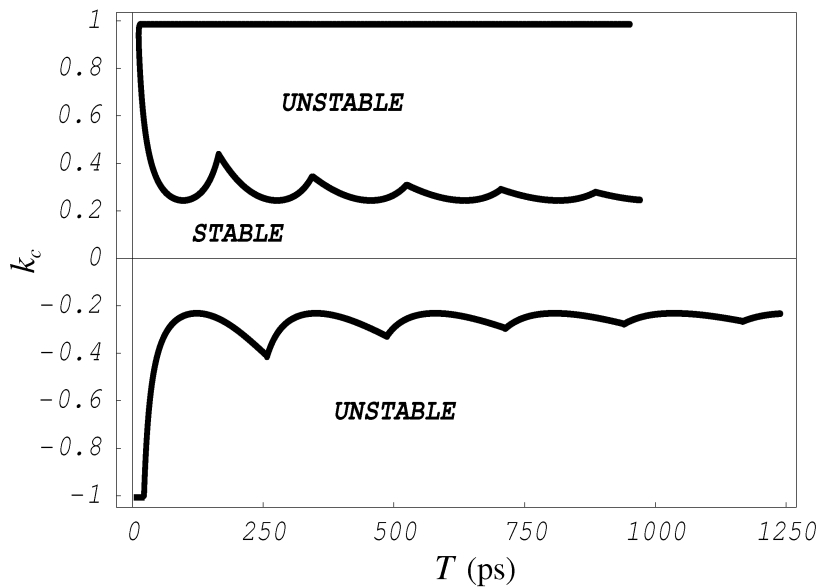
Figure 6.7. Stability diagram of the FP4 in the coupling strength vs. time delay plane obtained from the external margins of the critical lines in Figure 6.5 and the critical line $\kappa_c^* = -1 - \gamma_p \gamma_s / \gamma_c \gamma_n$.

Once the bifurcating study of the fixed points of the system has been completed and the main stability maps constructed, we further continue our investigations by looking at the properties of the periodic solutions and the route to chaos followed by the system.

6.2.3 Periodic solutions and the route to chaos

In the preceding part we have shown that the system can be destabilized through a Hopf bifurcations with imaginary part $\omega_{1,2}$, leading to the appearance of oscillations at the same frequencies. The characteristics and stability of these limit cycles are of fundamental importance to understand the transition of the system to more complex behaviors.

Here, we first study the evolution of the eigenfrequencies $\omega_{1,2}$ (i.e., the frequencies of the periodic solutions when they are born or die) as a function of the coupling strength. We also compare these values with those of the relaxation oscillation frequency (ROF) which defines a very important time scale of any semiconductor laser system. In the computation of the ROF values we use the effective injection current, i.e., bias plus photocurrent, in order to obtain a more accurate description of the relaxation oscillations occuring in the coupled system.

Figure 6.8 illustrates the values of the eigenfrequencies. For negative coupling, it is observed that the instability toward periodic solutions occurs at frequencies near the free-running relaxation oscillations $f_1 = 2\pi\omega_1 \sim ROF(\kappa_c = 0) = 2.4$ GHz. For positive couplings, however, f_1 grows close, but always above, the ROF of the coupled system. Concerning the frequency f_2, it is observed that when stabilization of the output of the lasers occurs, it is through an inverse Hopf bifurcation at a frequency close to 2.4 GHz for positive coupling values and at a much lower frequency for negative ones.

Once the period of the limit cycles solutions has been characterized we next analyze the structure and stability of these periodic solutions embedded in the phase space. In particular, we will focus on understanding their role in the route to chaos of the system as the coupling delay time or distance between the lasers increases.

Route to chaos

The bifurcation diagram obtained for the normalized photon density $\tilde{s}_1$ as a function of the coupling time between the lasers is shown in Figure 6.9. A similar diagram is registered for $\tilde{s}_2$. We will see in this section how the main features of this diagram, namely a) the sudden transitions from chaos (C) to periodic behavior (P), b) the increasing size of the quasiperiodic and chaotic regions (Q and C, respectively), and c) the clear repetitive structure of this diagram, are nothing else but the signature of the properties of the limit cycles on the dynamics of the system. In Figure 6.9 it is also noticeable that the route to chaos traced by our mutually interacting lasers resembles the one followed by a single laser subject to optoelectronic feedback [72].
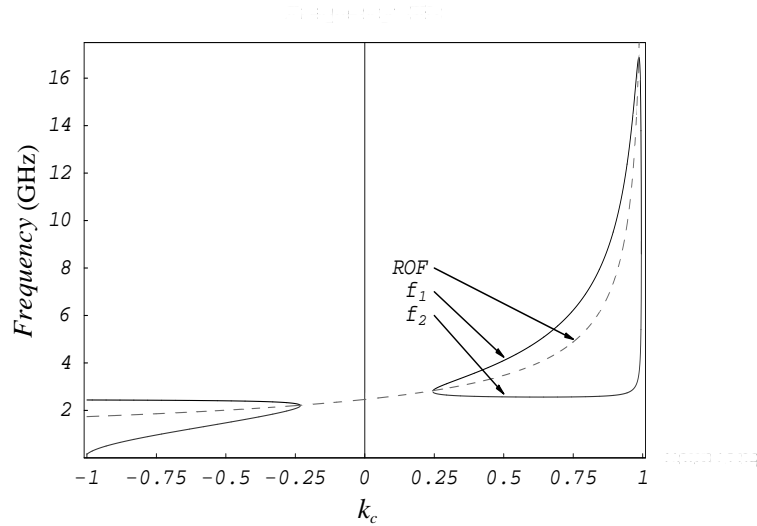
Figure 6.8. Eigenfrequencies $f_{1,2}$ (solid lines) and ROF (dashed line) as a function of the coupling strength κ_c.

To accomplish our goal we represent in Figure 6.10 the stability diagram for different limit cycles as a function of the coupling time. The interpretation of this plot and its relation to the bifurcation diagram goes as follows. First, we typically observe how decreasing the time delay a subcritical Hopf bifurcation (A) [83–85] gives rise to a limit cycle that undergoes a stabilizing fold bifurcation at another point (B). Then, this fold or saddle-node bifurcation for limit cycles is followed by a Naimark-Sacker (C) bifurcation. At this point the limit cycle in which the system is operating develops into a torus and a quasiperiodic dynamical state emerges. When further decreasing the time delay, a torus breakdown is generally observed leading to fully developed chaos. For even shorter delays, the sudden disappearance of the chaotic behavior observed in Figure 6.10 seems to be induced by a boundary crisis (D) that occurs when another unstable limit cycle collides with the chaotic attractor that was born around the torus. Finally, the amplitude of the periodic solution goes back to zero (E). Since the limit cycle is born (A) and annihilated (E) on FP4, the periodic orbit path connects different points on the continuation path of FP4. Similar periodic orbit bridges but between different steady-states have been reported in the literature of semiconductor lasers subject to coherent optical feedback [83, 84, 86].

This quasiperiodic route to chaos is rigorously checked through the computation of the Floquet multipliers at the appropriate points as it is illustrated in the right panels of Figure 6.10. At the point labeled as (B), we observe how a real Floquet multiplier is entering into the unit circle through the (1,0) coordinate, while
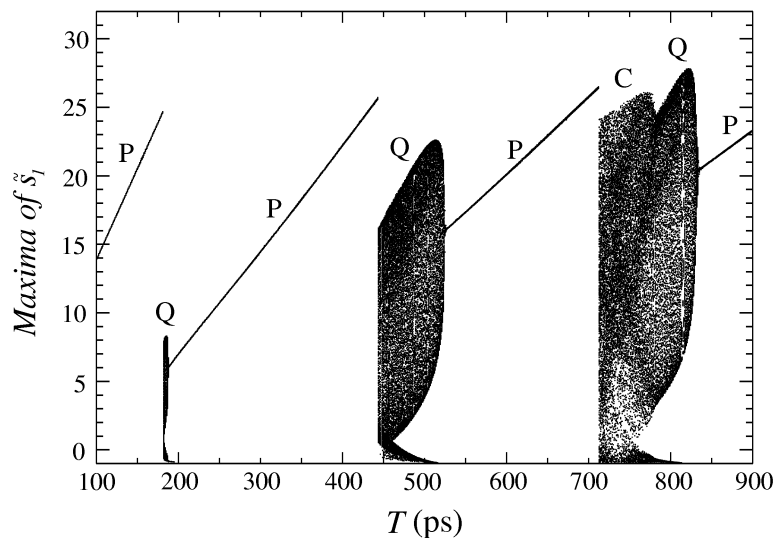
Figure 6.9. Bifurcation diagram for $\tilde{s}_1$ as a function of the coupling delay time. The coupling strength has been fixed to $\kappa_c = 0.5$. Only maxima of time series were recorded to plot the bifurcation diagram. The labels "P", "Q" and "C" on the top of the diagram identify the dynamical states as periodic, quasiperiodic and chaotic, respectively.

for the point (C) two complex conjugate Floquet multipliers are leaving the unit circle at $\pm \exp(i0.7\pi)$ giving rise to a toroidal attractor. The winding number or ratio between the periods of the two quasiperiodic motions taking place on the torus can be estimated and coincide with the numerical simulations to be around $2\pi/0.7\pi \sim 3$.

The above explanation was illustrated with the limit cycles covering the delay times in the range $\sim 440 - 720$ ps. Taken into account that any other limit cycle in Figure 6.10 has similar properties to the one just described, now we can easily understand that: a) all the sudden transitions from complex to regular behavior are probably induced by crisis events, b) the size of the islands of quasiperiodic or chaotic behavior amounts to the distance between the points (C) and (D) which increases for longer delay times, and c) the qualitatively repetitive structure found in Figure 6.9 comes from the fact that new periodic solutions with similar properties arise as the delay is increased.

We illustrate in Figure 6.11 the route to chaos obtained from the numerical
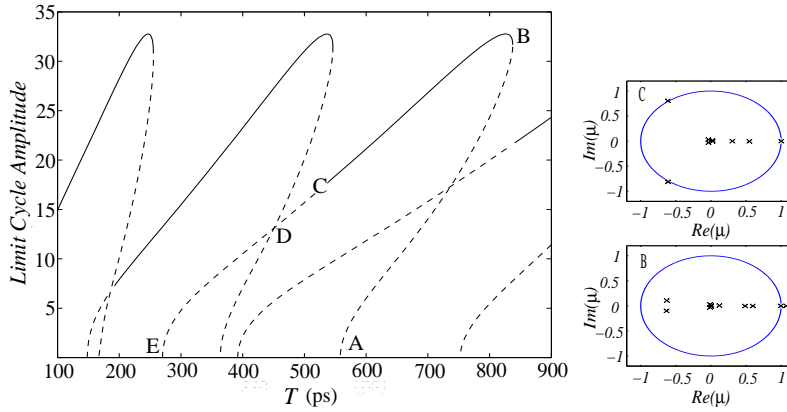
Figure 6.10. Left panel: Stability diagram for limit cycles as a function of the coupling delay time. The coupling strength has been fixed to $\kappa_c = 0.5$. Continuous and dashed lines indicate stability and instability, respectively. Right panel: Floquet multipliers at the points labeled as "B" and "C" in the left panel.

simulations when the coupling delay time is decreased. Temporal traces, power spectra, and return maps clearly indicate a quasiperiodic route to chaos that perfectly agrees with the theoretical analysis and is also experimentally confirmed in the following sections. In the first row, a perfectly periodic state is observed for a delay time of $T = 840$ ps, giving rise to a single peak in the power spectrum near the ROF and a single spot in the return map plot. Decreasing the delay down to $T = 800$ ps, the quasiperiodic state is revealed by the power spectrum. There, a slow frequency corresponding to the envelop frequency, a fast frequency coinciding with the pulsating frequency and several harmonics and beatings between fast and slow frequencies are clearly observed. The annular-shaped return map also confirms the quasiperiodic behavior. Finally, for a delay of $T = 720$ ps, a chaotically pulsating sequence is obtained. In this case, a broader spectrum and return map are expected as it can be checked in the figure.

6.2.4 Mutual entrainment of laser instabilities

Once the different dynamical states have been characterized and the transition from regular to complex behavior is well understood, it is interesting to know whether the lasers are able to mutual entrain their dynamics or not. To study this, here we compute the maximum of the cross-correlation function (ρ_{max}) between the two laser outputs as a function of the coupling strength, for a short (1 ns) and a long (15 ns) coupling time, T. Only values of $\kappa_c \gtrsim 0.25$ are considered since the system operates in a stable regime for smaller values.
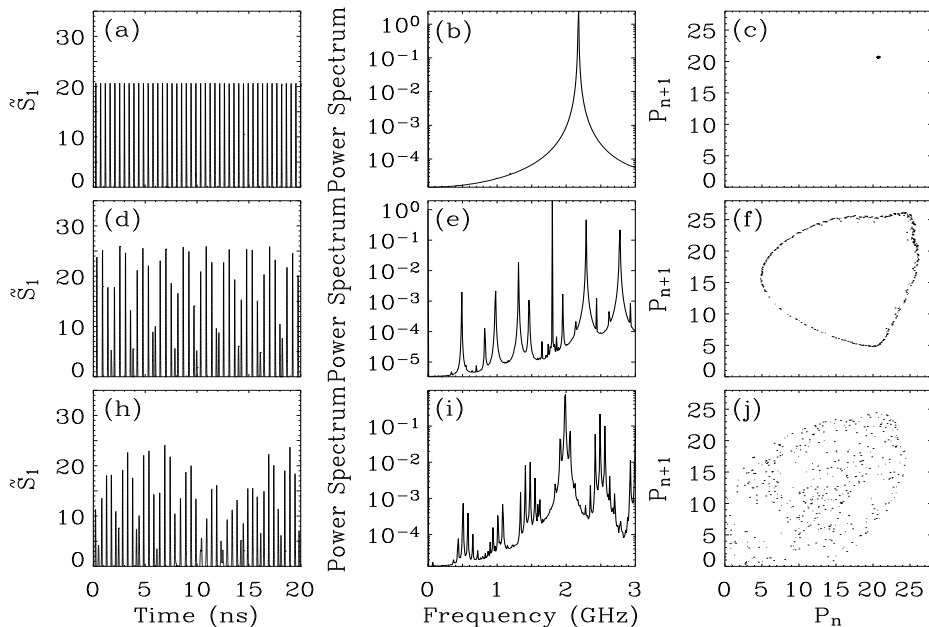
Figure 6.11. Numerically computed quasiperiodic route to chaos. Left column, time series; Central column, power spectra; Right column, return maps. From top to bottom the delay time T is 840 ps, 800 ps and 720 ps, respectively. The coupling strength is $\kappa_c = 0.5$.

In Figure 6.13(a) it can be seen that for short T a large correlation coefficient is obtained for a large range of the coupling coefficients. Nevertheless, it must be noticed that for most of the coupling rates both lasers operate in a periodic regime exhibiting synchronous (zero-lagged) pulsations. When the time delay is perturbed around ~ 1, perfectly entrained antiphase oscillations are also observed for most of the couplings. Only for values of κ_c around ~ 0.5 do the lasers operate in a quasiperiodic or chaotic regime and in these cases the maximum of the cross-correlation coefficient drops down to ~ 0.7.

When performing the same analysis but this time increasing the coupling time up to 15 ns, we observe that for almost any coupling coefficient both lasers enter into a quasiperiodic regime or even into a chaotic pulsating state for intermediate couplings. In this case, the maximum of the cross-correlation coefficient remains close to 1 except for intermediate coupling values for which it decays to ~ 0.8. Now, the time lag at which this maximum is found always corresponds to $\sim \pm T$. Contrary to the previous case, now when slightly changing the delay time (but still within the long delay time limit), the lag at which the maximum of the corre-
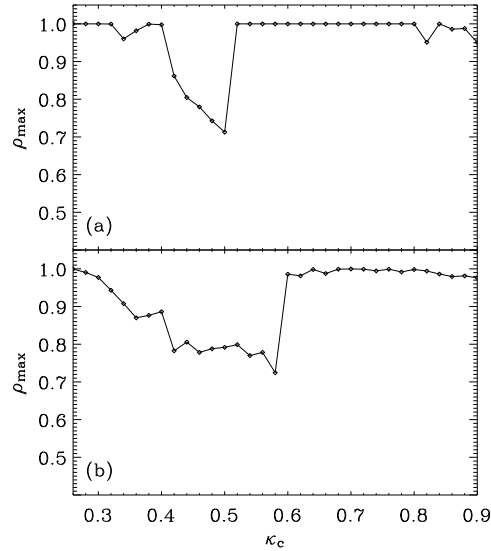
Figure 6.12. Maximum of the cross-correlation function (ρ_{max}) as a function of the coupling strength for (a) $T = 1$ ns and (b) $T = 15$ ns.

lation appears continues being located at $\sim \pm T$ and no zero-lagged solutions are found. When reversing the sign of the coupling coefficient, in order to take into account negative coupling values, we find that the cross-correlation function decays to much smaller values than for their positive coupling counterparts, revealing that mutual entrainment is more difficult to achieve in the case that inhibitory couplings are considered.

In order to further study the relative dynamics between the two lasers and its dependence on the coupling delay time, the maximum of the cross-correlation function and the time lag of this maximum are investigated as a function of T. The results are presented in Figure 6.13 for a fixed value of the coupling strength $\kappa_c = 0.5$. Figure 6.13(a) shows the maximum correlation between the two laser outputs. It can be clearly seen that the correlation maximum decreases from a value near 1 for short T, to a value around 0.8 for large delay times. We conclude that a high correlation between the two laser outputs is only obtained when they exhibit periodic behavior at short values of T, while it decreases when they enter into chaotic regimes. In panel (b) we plot the absolute value of the lag at which the maximum of the correlation appears. We have to stress that in all cases the cross-correlation is a symmetric function of the lag, which indicates that in average does not exist a defined leader or laggard role of any laser. For short T some windows

of in-phase and anti-phase dynamics, corresponding to the operation of both lasers
in corresponding in-phase and anti-phase limit cycles, are observed. There also
exist some windows appearing for intermediate distances in which the lag between
series is larger than the coupling delay time T. These regimes mainly correspond to
situations where both lasers operate in quasiperiodic orbits. After these windows
the lag between the two outputs tends to the coupling delay time $\pm T$ for large
values of T, where the lasers behave chaotically.
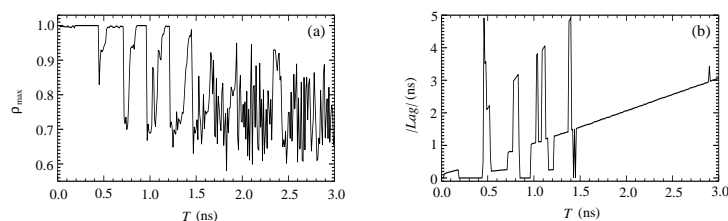
Figure 6.13. a) Maximum of the cross-correlation (ρ_{max}) as a function of the coupling delay
time T. b) Absolute value of the lag at which the maximum of the cross correlation function
occurs. In both cases the coupling strength has been fixed to $\kappa_c = 0.5$.

6.2.5   Experimental results

As it was mentioned in the introductory part, laboratory experiments were per-
formed in collaboration with the Electrical Engineering Department of the Univer-
sity of California, Los Angeles in order to confirm the robustness of some of the
theoretical expectations and push the theoretical model to account for more realis-
tic situations. Here, we concentrate on experimentally demonstrate the quasiperi-
odic route to chaos and to show the mutual entrainment properties of the lasers.

In the experiments, the lasers were InGaAsP/InP single-mode DFB lasers both
operating at 1.299 μm wavelength and temperature stabilized at 21°C. The two
lasers, which were chosen from the same wafer, are closely matched in their char-
acteristics to be highly identical and fit within the symmetric modeling assump-
tions. The photodetectors were InGaAs photodetectors with a 6-GHz bandwidth,
and the amplifiers were Avantek SSF86 amplifiers with $0.4 - 3$ GHz bandpass
characteristics. The laser intensities measured by the photodetectors were recorded
with a Tektronix TDS 694C digitizing sampling oscilloscope with a 3-GHz band-
width and a sampling rate up to 1×10^{10} Samples/s. Power spectra were measured
with an HP E4407B RF spectrum analyzer that has a spectral range from 9 kHz
to 26.5 GHz. The mutual coupling strength and the coupling delay time could be
adjusted by changing the attenuation on the coupled optical power and the optical
path length in the coupling channel, respectively.

Figure 6.14 shows a sequence of three dynamical states which are regular pulsing (RP), two-frequency quasiperiodic pulsing (Q2), and chaotic pulsing (C), respectively, obtained by varying the coupling delay times around $T_1 = T_2 \sim 15$ ns. Due to experimental limitations shorter coupling time were very difficult to explore and all experimental measurements were performed in the long coupling time limit. Although the coupling strength is experimentally difficult to measure, we estimate it to correspond to a value of κ_c between 0.5 and 7. For each dynamical state, the time series, power spectrum, and return map from the system output at the photodetectors are plotted as in the first, second, and third columns, respectively.
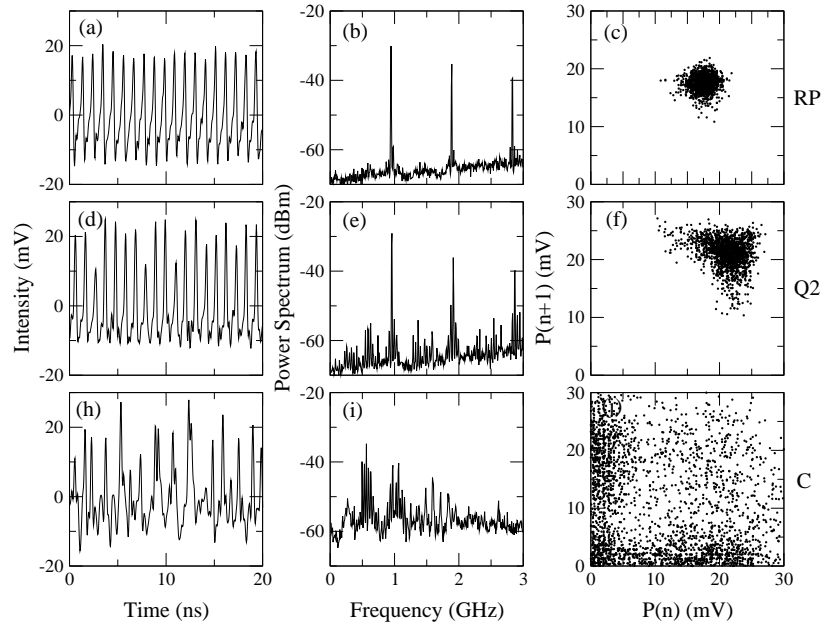
Figure 6.14. Experimental quasiperiodic pulsing route to chaos when decreasing the coupling delay time (from top to bottom T is decreased around $T = 15$ ns) for mutually coupled lasers with the configuration shown in Figure 6.1. RP: Regular pulsing state; Q2: Two-frequency quasiperiodic pulsing state; C: Chaotic pulsing state. First column, time series; Second column, power spectra; Third column, return maps.

In panels (a)-(c) the system is found in a regular pulsing state. The time series in Figure 6.14(a) shows a train of regular pulses with a constant pulsing intensity and interval. The power spectrum in Figure 6.14(b) has only one fundamental pulsing frequency, f_1, which is about 1 GHz, close to the experimentally determined ROF. The Poincaré map section in Figure 6.14(c) is obtained by recording a peak sequence $P(n)$ at the local intensity maxima of a pulse train and further plotting

$P(n)$ versus $P(n + 1)$, as it was done for the numerical results. In the regular pulsing state, the output has a constant peak intensity, and the return map shows only one spot. The fluctuations in the time series and, consequently, the scattering in the return map are mainly caused by the noise in the system and the sampling errors from the oscilloscope.

When the coupling delay time is decreased, we can observe how the system enters into a two-frequency quasiperiodic pulsing state with the pulsing intensity modulated at a frequency f_2 as shown in panels (d)-(f) of Figure 6.14. There, the time series clearly shows this modulation of the peak intensity. In the power spectrum, besides the pulsing frequency f_1, an incommensurate f_2 indicating the modulation of peak intensity shows up. The appearance of two incommensurate frequencies, f_1 and f_2, is the indication of quasiperiodicity in our coupled laser system. In the return map, the data points are still scattered due to noise and sampling errors. However, we can see that the distribution in Figure 6.14(f) is more scattered than that in Figure 6.14(c) because of the modulation on the pulse intensity.

In panels (h)-(j), when the delay is further decreased, the system enters into a chaotic pulsing state. From the time series, we find that both the pulse intensity and the pulsing interval vary chaotically. At the same time, the power spectrum of the chaotic pulsing state is broadened with a much increased background, indicating the onset of chaos. The return map shows a highly scattered distribution in a large area.

Therefore, the system is shown to enter a chaotic pulsing state through a quasiperiodic route as it was predicted by the analysis of the limit cycles embedded in the phase space.

Regarding the entrainment of instabilities emerging from the coupling of both lasers, we have also experimentally observed that for the long delay time limit the maximum of the cross-correlation function between the two intensity signals appears at $\sim \pm T$, as it happens in the numerical analysis. Figure 6.15 shows experimental temporal traces and the cross-correlation function between these two series. Although the correlation value is significantly lower (mainly due to noise originated in the sampling process) than the one predicted numerically (~ 0.8 for this operation regime), the two largest maxima still appear at the lags $\sim \pm T$.

Hence, these experimental results verify qualitatively the results obtained from the numerical simulations concerning the demonstration of the quasiperiodic route to chaos followed by the system when the distance between the lasers or delay time is varied, and the achronal synchronization between their chaotic dynamics.
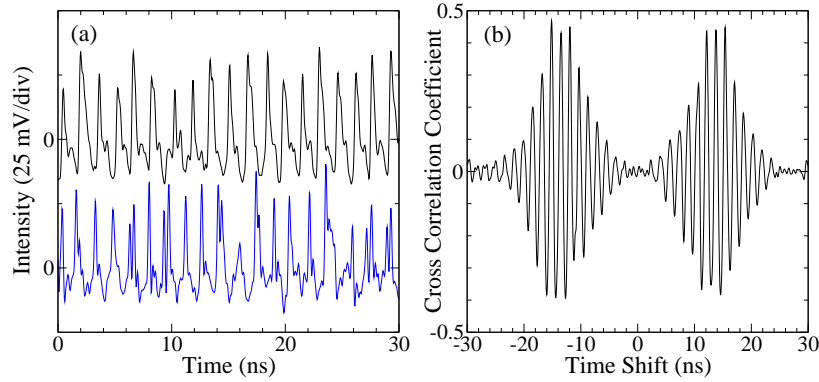
Figure 6.15. Experimental temporal series and their cross-correlation function in the long delay time limit. The coupling delay time is $T = 15$ ns.

6.2.6   Conclusions

In this first part of the chapter we have extensively studied by analytical, numerical, and experimental means the stability diagrams and synchronization of a system composed by two single mode semiconductor lasers with bidirectional optoelectronic delayed coupling.

Our analysis has provided a clear understanding of the basic mechanisms leading to the different dynamical instabilities and the role played by the different parameters, namely the injection current, coupling strength, and delay time.

The route to chaos when varying the coupling delay time has been theoretically identified and experimentally confirmed as a quasiperiodic scenario with crisis events.

The effect of the coupling delay time on the mutual entrainment properties between the lasers has also been investigated and confirmed by experimental results which qualitatively agree with the analytical and numerical analysis.

As a final conclusion it is worth remarking that the validity of the fixed points stability analysis performed in this chapter for the optoelectronic coupling can be directly translated to the case when the interaction between lasers is of incoherent optical nature [87]. This result comes from the observation that the characteristic equation for a general model of incoherent interactions, once linearized on the corresponding fixed points, leads to the same expression as that obtained in the optoelectronic case with negative coupling Eq. (6.20). Only a proper scaling of the coupling strengths $\xi_{c,incoherent} \longmapsto -\xi_{c,optoelectronic}$ needs to be performed in order to establish a complete analogy. The similarities between both types of interactions extend even to the nonlinear regime since numerical simulations show

the same route to chaos and entrainment phenomena are also shared by these two schemes.

6.3   Bidirectional coupling with feedback

Once the dynamics of our mutually-coupled configuration have been character-ized, we can now approach the different effects and questions risen by the addition of feedback loops to each one of the lasers. Thus in the second part of this chapter we investigate the instabilities arising from the delayed interaction between two self-oscillating lasers. Due to the inclusion of the feedback loops we can tune the dynamics of the uncoupled lasers between steady, oscillatory, pulsating, and chaotic behavior so that we can investigate the effect of the delay on different synchronization properties of the system. Other dynamical phenomena like the quenching of oscillations are also reviewed.

First, we start by investigating the stability problem of the fixed points in the presence of feedback loops. Unless explicitly mentioned, a symmetric configura-tion is chosen for the feedback lines ($\kappa_{f1} = \kappa_{f2} \equiv \kappa_f$ and $\tau_{f1} = \tau_{f2} \equiv \tau$).

6.3.1   Stability diagrams

The four fixed points that we considered in the previous sections can modify their location and stability properties due to the feedback loops. The main objective of this section is to build up the stability charts of these fixed points in the coupling versus feedback strengths plane and in the coupling versus feedback delay times.

Fixed point FP1

We start by analyzing the case of one of the symmetric steady-states. The behavior of FP1 ("off' state) is unaffected by the photocurrent that is feed back to the laser because they are not emitting any light. Thus its stability limit is still given by the solitary threshold $\tilde{J}$ regardless of the coupling and feedback interactions.

Fixed point FP4

For the study of the stability of the other symmetric fixed point, FP4, it is conve-nient to separate the cases where real or complex eigenvalues cross the imaginary axis.

Real eigenvalues.   The analysis of the characteristic equation for FP4 yields the condition to obtain a real zero eigenvalue ($\lambda = 0$) as

$$\boxed{\kappa_c - \kappa_f = -1 - \frac{\gamma_p \gamma_s}{\gamma_c \gamma_n}.} \qquad (6.28)$$

This is the generalization to the critical coupling strength given by Eq. (6.19) once feedback loops are included. Therefore, inside the region defined by the inequality $\kappa_c - \kappa_f < -1 - \gamma_p \gamma_s / \gamma_c \gamma_n$ in the coupling versus feedback strengths plane one can assure that there is at least one eigenvalue of FP4 with a positive real part and consequently the fixed point is unstable. We notice that this condition is independent of the time delays, i.e., regardless of the values of T and τ the simultaneous and symmetric CW operation of both lasers is unstable.

While discussing the transition of real eigenvalues to the right-hand side of the complex plane, we can take advantage and analyze some codimension-two bifurcating points. Takens-Bogdanov points (TB), for instance, are associated to a double zero eigenvalue crossing the imaginary axis. Thus, in order to find these points one must the set of parameters that simultaneously satisfy the nullity of the characteristic equation ($\Delta(\lambda = 0) = 0$) and its derivative ($\partial\Delta/\partial\lambda|_{\lambda=0} = 0$). The first condition is already given by Eq. (6.28) while the second one demands

$$\gamma_p \gamma_s (\gamma_n + \gamma_p + \gamma_s) + \kappa_f \gamma_c^2 \gamma_n^2 \tau + \gamma_c \gamma_n \left[\gamma_n + \gamma_p + (1 - \kappa_c - \kappa_f)\gamma_s + \kappa_f \gamma_p \gamma_s \tau \right]$$

$$= T \kappa_c \gamma_c \gamma_n (\gamma_c \gamma_n + \gamma_p \gamma_s) \ .$$

$$(6.29)$$

Consequently, the location of the parameters corresponding to a TB point can proceed for example, by fixing the feedback strength κ_f to a given level and obtain a compatible value for κ_c from Eq. (6.19). Then, Eq. (6.29) provides a linear relationship between the delay times τ and T for which a TB point must appear. Besides these mathematical conditions the positiveness of both delay times is an unavoidable physical requirement. The usual interpretation of these codimension-two points as accumulation points of a Hopf curve whose eigenfrequencies tend to zero has been numerically checked by continuing a family of Hopf bifurcations.

Complex eigenvalues.   A bit more complicated than the previous case is the detection of bifurcations involving complex eigenvalues. Let us begin by writing down the characteristic equation for FP4. Due to the symmetry of both the configuration and the solution that we are considering the characteristic equation factorizes as

$$\left(u e^{-\lambda\tau} + p\lambda^2 + q\lambda + y - v e^{-\lambda T} \right) \left(u e^{-\lambda\tau} + p\lambda^2 + q\lambda + y + v e^{-\lambda T} \right) = 0 \ ,$$

$$(6.30)$$

where u, v, p, q, and y are coefficients that only depend on the internal and control parameters κ_c, κ_f, and $\tilde{J}$.

The search for Hopf bifurcations starts from the finding of zeros of any of the two factors of Eq. (6.30) after having imposed the condition of pure imaginary eigenvalues, $\lambda = i\omega$. Then, the eigenfrequencies ω must satisfy at least one of the equations

$$ue^{-i\omega\tau} - p\omega^2 + iq\omega + y \mp ve^{i\omega T} = 0 \ . \tag{6.31}$$

The separation into real and imaginary parts of the former equations

$$u\cos\omega\tau - p\omega^2 + y = \pm v\cos\omega T = 0 \tag{6.32}$$

$$-u\sin\omega\tau + q\omega = \mp v\sin\omega T = 0, \tag{6.33}$$

allows an easy elimination of the coupling delay time T by squaring and adding Eqs. (6.32)-(6.33). After this manipulation the resulting equation for ω reads

$$\boxed{\omega^4 + b\,\omega^2 + c + (d\,\omega^2 + e)\cos(\omega\tau) + f\,\omega\sin(\omega\tau) = 0 \ , \qquad (6.34)}$$

where the coefficients are involved functions of the parameters

$$b\Lambda^2 = 2\left(-1+\kappa_c+\kappa_f\right)\gamma_c{}^3\gamma_n{}^3 + \gamma_p{}^2\gamma_s{}^2\left((\gamma_n+\gamma_p)^2 + 2\gamma_n\gamma_s + \gamma_s{}^2\right)$$
$$\quad + 2\gamma_c\gamma_n\gamma_p\gamma_s\left((\gamma_n+\gamma_p)^2 - \left(\left(-2+\kappa_c+\kappa_f\right)\gamma_n+\gamma_p\right)\gamma_s - \left(-1+\kappa_c+\kappa_f\right)\gamma_s{}^2\right)$$
$$\quad + \gamma_c{}^2\gamma_n{}^2\left((\gamma_n+\gamma_p)^2 - 2\left(\left(-1+\kappa_c+\kappa_f\right)\gamma_n - \left(-2+\kappa_c+\kappa_f\right)\gamma_p\right)\gamma_s + \left(-1+\kappa_c+\kappa_f\right)^2\gamma_s{}^2\right),$$

$$c\Lambda^2 = -\left((\gamma_c\gamma_n+\gamma_p\gamma_s)^2\left(\left(-1+\kappa_c{}^2-\kappa_f{}^2\right)\gamma_c{}^2\gamma_n{}^2 - 2\gamma_c\gamma_n\gamma_p\gamma_s - \gamma_p{}^2\gamma_s{}^2\right)\right),$$

$$d\Lambda = -2\kappa_f\gamma_c\gamma_n\left(\gamma_c\gamma_n+\gamma_p\gamma_s\right),$$

$$e\Lambda^2 = -2\kappa_f\gamma_c\gamma_n\left(\gamma_c\gamma_n+\gamma_p\gamma_s\right)^3,$$

$$f\Lambda^2 = -2\kappa_f\gamma_c\gamma_n\left(\gamma_c\gamma_n+\gamma_p\gamma_s\right)\left(-(\gamma_c\gamma_n\left(\gamma_n+\gamma_p\right)) + \left(-1+\kappa_c+\kappa_f\right)\gamma_c\gamma_n\gamma_s - \gamma_p\gamma_s\left(\gamma_n+\gamma_p+\gamma_s\right)\right),$$

$$\Lambda \equiv \left(-1+\kappa_c+\kappa_f\right)\gamma_c\gamma_n - \gamma_p\gamma_s \ .$$

Coupling versus feedback strengths.   As in the first part of this chapter where no feedback loops were considered, the location of the regions in the parameter space where a real solution for ω exists or not is of central importance. In constructing the stability diagrams these regions signal where Hopf bifurcations are possible. Thus, the Delay-Independent Stable Region (DISR) is composed by the

set of points in the κ_c versus κ_f plane where, independently of the values of the delay times τ and T, no real solution for ω exists. Within that zone of parameters, there is no combination of feedback and coupling delay times able to destabilize the constant and identical output of both lasers. On the contrary, there are also regions in the κ_c versus κ_f plane where the existence of a real solution for ω depends on the specific values of the feedback and coupling delay times. Such zones form the delay-dependent stable region (DDSR), and there one can always find a proper combination of delay times that induces oscillations in the lasers through a Hopf bifurcation. Finally, we can define the delay independent unstable region (DIUR), where no matter the delay times we chose the operation on FP4 is unstable. In this case, the condition given in Eq. (6.28) defines an area where an eigenvalue with positive real part exists independently of τ and T, and as a consequence FP4 is unstable regardless the distance between lasers and the feedback loop lengths.

The search of these different stability regions directly face us to deal with the existence of real solutions for the transcendent equation Eq. (6.34). At this point of the analysis, one of the possible approaches to construct such a stability diagram consists of fixing the coupling κ_c and feedback κ_f strengths, and numerically look if any real solution for ω appears when scanning the feedback delay time τ. It is important to remind that the coupling delay time T has been eliminated from Eqs. (6.32)-(6.33). Hence, depending on the output of this search for real solutions one could classify the points (κ_c, κ_f) as belonging to one stability region or another (DISR, DDSR, or DIUR).

This procedure, however, requires a nested sweeping of three parameters plus the numerical resolution of a transcendent equation for each of the parameter points scanned. Instead, we develop here a much less computational demanding approach that will enable us to find analytical conditions on the coefficients of Eq. (6.34) for the stability of the system. Since the coefficients of Eq. (6.34) only depend on κ_c and κ_f one can finally translate the stability conditions on the coefficients to the coupling versus feedback strength parameters plane and obtain the desired stability map.

Let us start by considering the left-hand side of Eq. (6.34) as a function of the two variables ω and τ, $Q(\omega, \tau)$. The main question is how can we obtain analytical conditions for the existence of real roots of Q? The idea behind the method considered here is that when looking for zeros of $Q(\omega, \tau)$ one could scan the ω versus τ plane in a suitable manner to make the problem easier. From the infinitely-many choices for scanning such a plane we find that a great advantage can be taken if it is scanned through the family of hyperbolas $\omega\tau \equiv h = constant$. By doing so, on each of these curves Eq. (6.34) reduces to a fourth-order polynomial $Q_h(w) = \omega^4 + r\omega^2 + s\omega + t$, where the coefficients r, s and t are functions κ_f, κ_c, and h. Now, the conditions on the coefficients to have no real solutions can

be obtained from the algebraic structure of polynomials on a real variable.

Thus, in the same way that the sign of the quantity $b^2 - 4ac$ distinguishes the cases when a quadratic function $P(x) = x^2 + bx + c$ has any real root or not, a series of discriminants can be defined for higher order polynomials giving us conditions on the coefficients for the existence and multiplicity of real roots. To our purposes, all we need to know is that the discriminants that will help us to classify the roots of Q_h can be computed as determinants of some minors of the Sylvester matrix between Q and its derivative Q' [88]. The expressions of the discriminants of a fourth-order polynomial are

$$
\begin{aligned}
\Delta_1 &= 1, \\
\Delta_2 &= -r, \\
\Delta_3 &= -2r^3 - 9s^2 + 8rt, \\
\Delta_4 &= -4r^3s^2 - 27s^4 + 16r^4t + 144rs^2t \\
&\quad -128r^2t^2 + 256t^3.
\end{aligned}
$$

The relation between the number of real zeros (counting their multiplicity) and the discriminants of a quartic polynomial is collected in Table 6.1.

Number of real roots	Multiplicity	Discriminant conditions
0	0	$\Delta_4 > 0 \cap (\Delta_3 \leq 0 \cup \Delta_2 \leq 0)$
0	0	$(\Delta_4 = \Delta_3 = 0) \cap \Delta_2 < 0$
2	1,1	$\Delta_4 < 0$
2	2	$\Delta_3 < 0 \cap \Delta_4 = 0$
4	1,1,1,1	$\Delta_2 > 0 \cap \Delta_3 > 0 \cap \Delta_4 > 0$
4	1,1,2	$\Delta_2 > 0 \cap \Delta_3 > 0 \cap \Delta_4 = 0$
4	2,2	$\Delta_2 > 0 \cap (\Delta_3 = \Delta_4 = 0) \cap s = 0$
4	1,3	$\Delta_2 > 0 \cap (\Delta_3 = \Delta_4 = 0) \cap s \neq 0$
4	4	$\Delta_2 = \Delta_3 = \Delta_4 = 0$

Table 6.1: Classification of the real zeros of a quartic polynomial.

Now, only varying one parameter (h) with the former criteria we analytically obtain a series of regions in the κ_c versus κ_f plane where we guarantee that no real roots can be found. These points determine the DISR zone since no matter what the values of the delay times amount to, Eq. (6.34) cannot have an eigenvalue on the imaginary axis. Numerical simulations also confirm the location of the DISR zone on the parameter space here predicted.

Only now we are in conditions to obtain the full stability diagram of FP4. With the former procedure placing the DISR zone and Eq. (6.28) limiting the DIUR region, the stability chart for $\tilde{J} = 1/3$ is presented in Figure 6.16. It is important to notice that for the value of bias chosen, κ_c and κ_f play a highly symmetrical role at destabilizing FP4. It must be observed that by increasing the magnitude of the coupling or feedback strength the system is able to enter into the DDSR independently of the sign of these interactions, excitatory or inhibitory. However, this is not the case regarding the DIUR zone where it is very important the sign of the strengths considered. For instance, only with either a very negative coupling or a very large positive feedback, or a combination of both the system falls into the DIUR regime. So, we see how an inhibitory coupling and an excitatory feedback complement each other in order to destabilize the symmetric FP4.

A naive interpretation of the destabilizing role of the inhibitory coupling in our system is that a negative coupling interaction tends to establish a kind of competition between both lasers. Thus, the lasers simultaneously try to decrease the power of their counterpart what eventually favors the operation in one of the asymmetric states of the system.
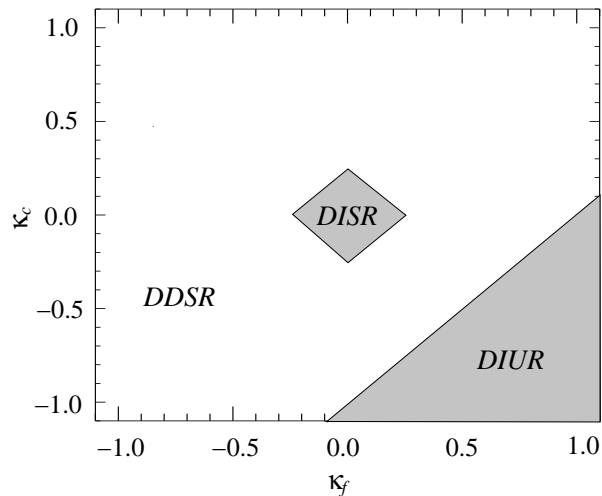
Figure 6.16. Stability diagram in the κ_c versus κ_f plane for FP4, showing the delay-independent stable region (DISR), the delay-dependent stable region (DDSR), and the delay-independent unstable region (DIUR). The boundary between the DDSR and DIUR is defined by the transcritical line, Eq. (6.28). $\tilde{J} = 1/3$.

Coupling versus feedback delay times. So far we have identified the effect of the different strength values in the stability of the system. Next, we fix the cou-

pling and feedback strength values and focus on the role of the several delay times in the system.

To this respect, once a solution ω has been obtained from Eq. (6.34) the critical coupling delay times T are recovered from Eqs. (6.32)-(6.33) as

$$T_c(\omega) = \frac{1}{\omega} \left(\arctan \frac{p(\kappa_c, \kappa_f, \tau, \omega)}{q(\kappa_c, \kappa_f, \tau, \omega)} + m\pi \right) , \qquad (6.35)$$

where $m \in \mathbb{Z}$, and p and q are defined by the following expressions

$$p \equiv \left[\gamma_p \gamma_s (\gamma_n + \gamma_p + \gamma_s) + \gamma_c \gamma_n (\gamma_n + \gamma_p - (-1 + \kappa_c + \kappa_f) \gamma_s) \right] \omega$$
$$+ \kappa_f \gamma_c \gamma_n (\gamma_c \gamma_n + \gamma_p \gamma_s) \sin(\omega \tau) ,$$
$$q \equiv -\gamma_c^2 \gamma_n^2 + \gamma_p \gamma_s (\omega^2 - \gamma_p \gamma_s) - \gamma_c \gamma_n \left[2\gamma_p \gamma_s + (-1 - \kappa_c + \kappa_f) \omega^2 \right]$$
$$+ \kappa_f \gamma_c \gamma_n (\gamma_c \gamma_n + \gamma_p \gamma_s) \cos(\omega \tau) .$$

For such combination of delays we can guarantee that at least one pair of conjugate eigenvalues lie on the imaginary axis. The Hopf curves in the coupling versus feedback delay times are shown in Figure 6.17 for the case $\kappa_c = \kappa_f = 0.25$ and $\tilde{J} = 1/3$.

The most salient feature of this figure is the similar role played by the feedback and coupling delay times in destabilizing the system. Consequently, the pattern of dynamical behavior observed when increasing the distance between the lasers and keeping constant the feedback lengths is qualitatively identical to the one obtained by maintaining fixed the coupling time parameter and enlarging the feedback loop times. However, an important time scale difference between the two delay times is noticed. For instance at appropriate parameter values the minimum coupling time needed to excite oscillations is ~ 10 ps, while the equivalent for the feedback delay time exceeds the 60 ps.

In the same figure, at the intersection of these Hopf curves we identify the double Hopf codimension-two points where two pairs of purely imaginary conjugate eigenvalues exist. To complete our findings on codimension-two bifurcating points it is worth to comment that the simultaneous requirement of Eq. (6.28) and Eq. (6.35) provides a set of parameters where a single zero and a pair of purely imaginary eigenvalues coexist.

Fixed points FP2 and FP3

The study of the stability of the asymmetric steady states FP2 and FP3 through their characteristic equation turns out to be challenging for any analytical treat-
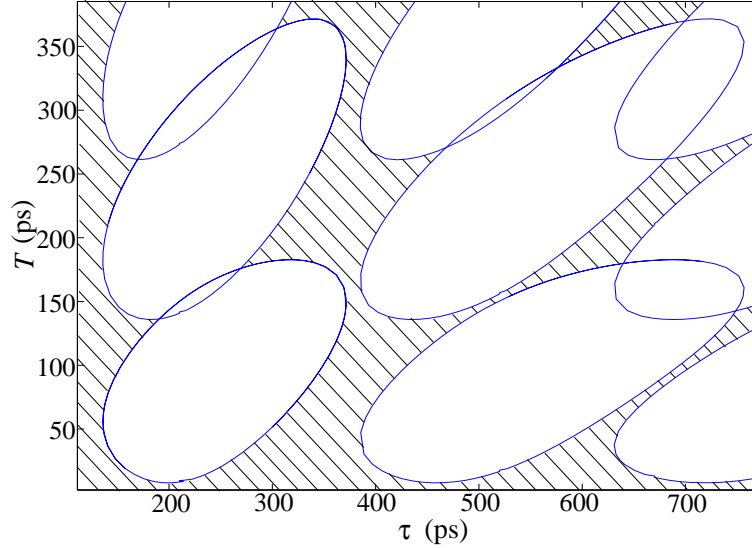
Figure 6.17. Hopf curves and stability diagram in the T versus τ plane for FP4. The oblique lines indicate the regions where the fixed point is stable. At the crossing of the Hopf curves, a double Hopf codimension-two bifurcation takes place. Both the feedback and coupling strength are fixed at 0.25. $\tilde{J} = 1/3$.

ment. Nevertheless, we have undertaken extensive numerical simulation of Eqs.(6.6)-(6.9) to analyze their stability map. The stability charts for FP2 and FP3 are equivalent and presented in Figure 6.18. The boundary between DIUR and DDSR is defined by the condition Eq. (6.28). There also exists a small delay-independent stable region (DISR) for FP2 and FP3 bounded by the critical line given by Eq. (6.28) on one side, and by the minimum feedback coefficient that is able to excite oscillations in the solitary laser case ($\kappa_f \sim 0.24$ for $\tilde{J} = 1/3$), on the other side.

With the former analysis we have gained the necessary insight into the stability and bifurcations of the system to approach new problems in our configuration. In the subsequents sections we address the prediction of the "death by delay" effect in our system as well as some general phenomena in the theory of coupled oscillators, such as frequency locking and chaotic synchronization.

6.3.2   Death by delay

When uncoupled, a proper combination of the feedback strength and feedback delay time can set the lasers to operate as periodic oscillators, i.e., with their optical intensities varying periodically. Then, once they are coupled, it is interesting to know which are the effects of increasing the distance between the oscillators or
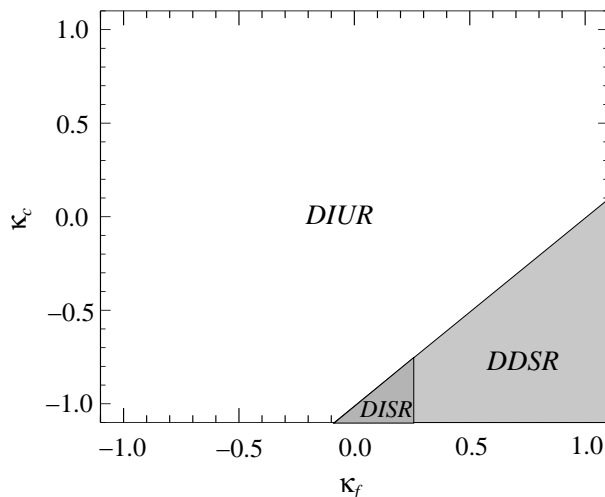
Figure 6.18. Stability diagram in the κ_c versus κ_f plane for FP2 and FP3, showing the delay-independent stable region (DISR), the delay-dependent stable region (DDSR) and the delay-independent unstable region (DIUR). $\tilde{J} = 1/3$.

lasers. In particular, we investigate the phenomenon of oscillation death by which the coupling between two oscillators might be able to quench their oscillations through a collapse to the zero-amplitude state [2, 13, 89, 90]. As we have seen in Chapter 3, when delay is absent in the coupling term a large dispersion or detuning in the natural frequencies of the oscillators besides a diffusive coupling are required to observe this phenomenon [1, 2, 50]. Only recently, Ramana et al. [13] showed that these restrictions can be relaxed if the coupling is delayed, i.e., if the communication between both oscillators cannot be considered instantaneous compared to their internal time scales.

This important effect, commonly known in the literature as "death by delay" can be predicted in our laser system with the help of our former bifurcation analysis. We tackle the problem of finding these quenching regions by computing the Hopf curves for FP4 in the κ_c versus T plane, and checking the direction of crossing of the eigenvalues at these borders.

Following this procedure, we are able to find closed regions in the parameter space κ_c versus T where the fixed point FP4 is again stable and induces the death of the oscillations in the system. These regions which are surrounded by supercritical Hopf lines (if subcritical, bistability could easily prevent trajectories to converge to FP4) are called "death islands" and are shown in Figure 6.19 for different feedback delays. κ_f is fixed to 0.3 and $\tilde{J} = 0.1$. Under these conditions when uncoupled

both lasers oscillate with a fundamental period ~ 600 ps.
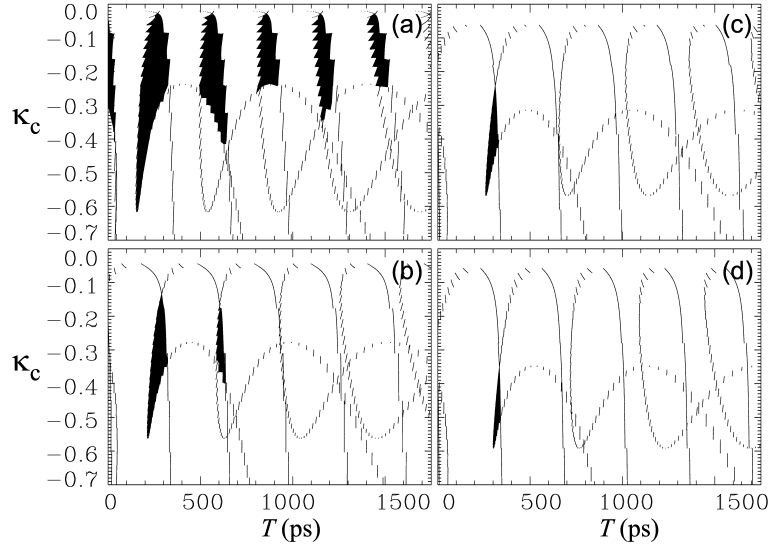
Figure 6.19. Hopf curves and "death islands" (shadowed regions) in the κ_c versus T plane for FP4 for several values of the feedback delay time 975 ps (a), 1050 ps (b), 1125 ps (c), 1200 ps (d). The feedback strength is $\kappa_f = 0.3$ and the bias current is set to 10% above threshold, i.e., $\tilde{J} = 0.1$.

We find that the "death by delay" phenomenon appears in a wide parameter range in our system. For feedback delay times below $\tau = 925$ ps, not shown in the figure, no "death islands" appear since the lasers are stable even when decoupled. "Death islands" start to emerge when the solitary lasers undergo self-sustained oscillations at $\tau \sim 950$ ps. Several "death islands" computed for $\tau = 975$ ps can be observed in Figure 6.19(a), which are regularly, although not completely, spaced. The existence of multiple islands when varying T it is also experimentally demonstrated in the corresponding section of this chapter. It is interesting to observe that the size of these islands decreases when the coupling delay time T increases until they completely disappear for $T \gtrsim 1500$ ps. Moreover, the number of islands and their size continuously decrease when increasing τ until they completely disappear for $\tau = 1225$ ps. In the regions surrounding the "death islands" each laser usually operates in a limit cycle. When varying T new limit cycles are created and they are born in alternation between in-phase and anti-phase, this is, after a limit cycle where both lasers oscillate in-phase is born, the next limit cycle that is created is an anti-phase one, and so on. Consequently, when jumping into a "death island", the mutual drift to the stationary-state occurs through either a series of in-phase or anti-phase oscillations of exponentially decreasing amplitude, depending on the limit cycle in which the lasers were operating before the jump.

This is illustarated in Figures 6.20 and 6.21. In the first case we have analyzed

the behavior of the laser outputs when moving into the first "death island" of Figure 6.19(a). When running a simulation of Eqs. (6.6)-(6.9), after transients have been skipped, at $t = 5$ ns we vary the coupling delay from $T = 50$ ps to $T = 0$ ps. This change in T causes a mutual drift to the zero-amplitude state through a series of in-phase pulses with a decreasing exponential envelope (see Figure 6.20).
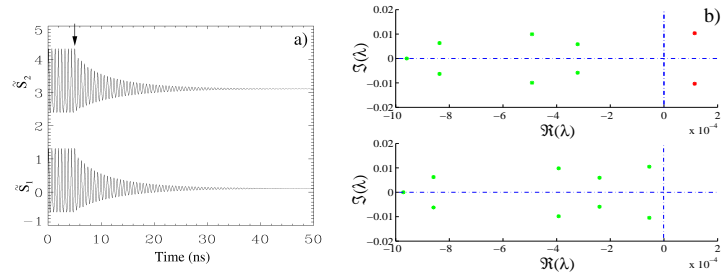
Figure 6.20. (a) Quenching of the oscillations when the coupling delay in changed ($T = 50$ ps $\mapsto T = 0$ ps). The temporal series of laser 2 has been vertically displaced for clearness reasons. (b) Top: eigenvalues at $T = 50$ ps; bottom: eigenvalues at $T = 0$ ps. The bias, feedback coefficient, and feedback delay time correspond to those of the Figure 6.19(a). The coupling is fixed at $\kappa_c = -0.2$.

Figure 6.21 shows the oscillation death when the distance between lasers is changed from $T = 350$ ps to $T = 250$ ps, i.e., the coupling parameters move within the second island in Figure 6.19(a). Notice that now the transition to CW occurs through anti-phase oscillations of decreasing amplitude.
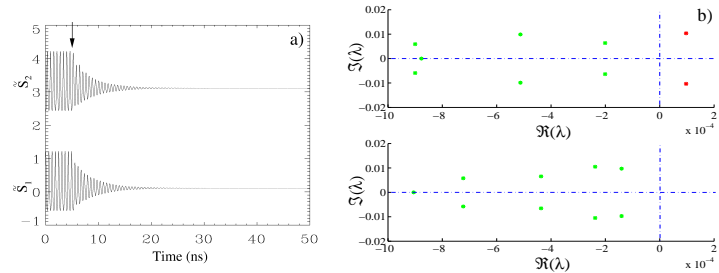
Figure 6.21. (a) Quenching of the oscillations when the coupling delay in changed ($T = 350$ ps $\mapsto T = 250$ ps). The temporal series of laser 2 has been vertically displaced for clearness reasons. (b) Top: eigenvalues at $T = 350$ ps; bottom: eigenvalues at $T = 250$ ps. The bias, feedback coefficient, and feedback delay time correspond to those of Figure 6.19(a). The coupling is fixed at $\kappa_c = -0.2$.

A very interesting feature of Figure 6.19(a) is the fact that one of the "death islands" reaches the $T = 0$ axis. This is also illustrated in the oscillatory death induced in Figure 6.20 where the coupled delay time is moved toward zero and still

a quenching of the oscillations is observed. These feature (oscillations quench-
ing for $T = 0$) is also independently confirmed by the direct computation of the
eigenvalues of the characteristic equation with the MATLAB package for analysis
of delay differential equations DDE-Biftool [60]. Therefore, there is an apparent
contradiction with the above-mentioned arguments that no identical oscillators can
drive each other to a zero-amplitude state in the absence of delay in the coupling,
as it was illustrated in the Figure 2.2 of Chapter 2.

And however in our scheme we detect the quenching of two identical oscilla-
tors even for a zero-delay in the coupling. We have checked in our laser setup and
in some universal models of oscillators (Ginzburg-Landau) that this controversy
arises from the special origin of the pulsating behavior in our laser system. Based
on these observations we conjecture that if a system is lead to oscillations under the
presence of a delayed feedback term no delay in the coupling between oscillators
is needed in order to observe the death effect for identically-coupled oscillators.
Most of preceding studies of "death by delay" [13,50,61,91] have only considered
a time delay in the interaction between subsystems but not in the feedback loops, if
any was included. Thus, our results indicate that in order to induce the quenching
of oscillations neither an asymmetry nor a delayed coupling are required. Just a
delay, independently of its origin, is necessary to relax the quenching conditions
for identical coupled oscillators.

The role of a finite bandwidth of the photodetector-amplifier response on the
lines of Figure 6.19 have also been taken into account for a better comparison with
the experiments presented below. The effects of a high cutoff frequency of the
filters is not important when this cutoff occurs at frequencies higher than the relax-
ation oscillations frequency of the lasers (as mostly happens in the experiments).
On the contrary, a low cutoff frequency removes the continuous part of the spec-
trum of the lasers, what is found to entail an increase of the size of the death islands
and to even create new ones.

6.3.3 Synchronization

The synchronization of both lasers is studied here for three different situations. For
identical lasers, we first consider the case of coupled limit cycle oscillators, and
secondly we address the synchronization of chaotic oscillators. Finally, we ana-
lyze the role of slightly asymmetric operation of the lasers. The different types of
synchronization are characterized by two figures of merit, namely, the correlation
degree between amplitudes and the relative phase of the oscillations.

Identical systems

Several phenomena related to synchronization concepts appear in our multiple de-layed system. Starting from a configuration in which both lasers are self-sustained oscillators due to their own feedback loop, we study the amplitude and phase syn-chronization between the laser intensities as a function of the coupling strength and coupling delay time.

The correlation between the amplitudes of the signals is characterized through the maximum of the cross-correlation function, while the phase synchronization is studied by means of the analytical signal concept constructed with the aid of the Hilbert transform [23]. The Hilbert phase allows us to generalize the concept of phase for arbitrary signals, although it has only a clear physical meaning when the spectrum of the signal is narrow-band. See Chapter 2 for a short definition of the Hilbert phase.
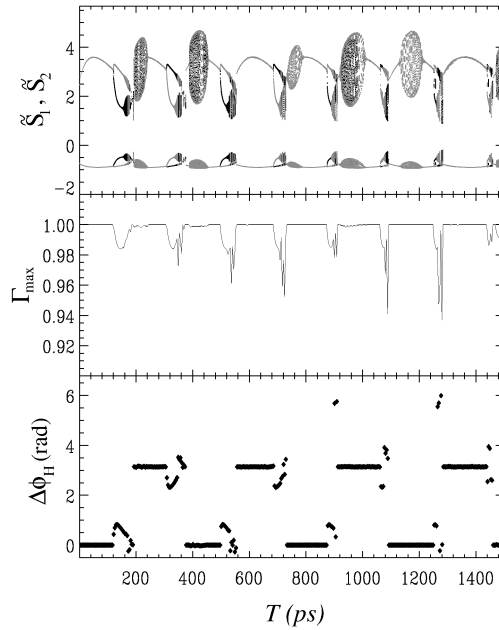
Figure 6.22. Bifurcation diagram for $\tilde{s}_1$ (black) and $\tilde{s}_2$ (grey) as a function of T. Maximum of the cross-correlation function Γ. Mean Hilbert phase difference $\Delta\phi_H$. The feedback pa-rameters are $\kappa_f = 0.3$ and $\tau = 1$ ns, while the coupling strength is fixed at $\kappa_c = -0.1$. The bias is set to $\tilde{J} = 1/3$.

In Figure 6.22, we find from top to bottom the bifurcation diagram of the laser intensities when T is varied, the maximum of the cross-correlation function, and

the mean Hilbert phase difference between the laser signals. Interestingly, we can observe how increasing the coupling delay time a sequence of symmetry-breaking or pitchfork bifurcations for limit cycles occurs. The breaking of the $\mathbb{Z}_2$-symmetry under the exchange of laser 1 and 2 in the Eqs. (6.6)-(6.7) is for instance, clearly observed at $T \sim 500$ ps. Before that point the two lasers operate in an in-phase symmetric limit cycle and both lasers display oscillations with the same amplitude. After the bifurcation, the system operates in one of the two newly created asymmetric limit cycles where each laser pulses with a different amplitude but at the same frequency. A plot of the symmetric and the two asymmetric limit cycles created at the pitchfork bifurcation that occurs at $T \sim 500$ ps is shown in Fig. 6.23.
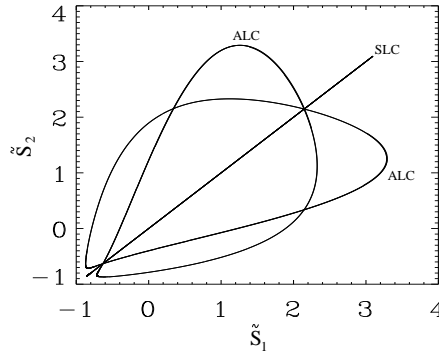
Figure 6.23. Portrait of the limit cycles involved in the spontaneous symmetry-breaking bifurcation. SLC and ALC stand for symmetric limit cycle and asymmetric limit cycle, respectively. The SLC is plotted when is still stable at $T = 496$ ps, while the ALC are showed just after the bifurcation takes place at $T = 498$ ps.

Thus, depending on the initial conditions the perfectly symmetric system spontaneously tends to operate in one of the asymmetric limit cycles. The amplitude of the oscillations in each laser becomes different, as shown in Fig. 6.24. There lies the localized synchronization concept by which two mutually coupled systems can exhibit synchronized oscillations with different amplitudes [40, 92]. We also note that by increasing further the coupling delay, larger ratios between the amplitudes of both lasers can be achieved, as is illustrated in Fig. 6.25.

The localized synchronization is also characterized by a non-zero relative phase between the two oscillators. By increasing the delay coupling time each of these asymmetric limit cycles bifurcate to a torus and quasi-periodic dynamics with different amplitude are observed for each laser. Further increasing the bifurcating parameter a transition to a more complex behavior occurs, where both lasers show irregular oscillations with similar amplitudes and an anti-phase dynamics is observed. For larger delays, we can appreciate how the system tends to operate in
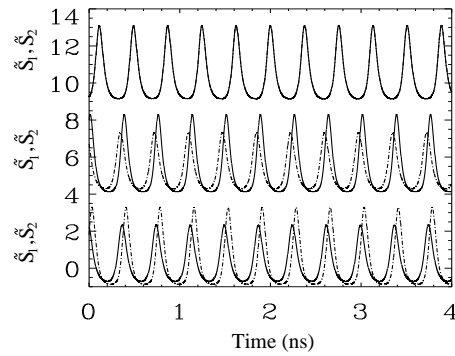
Figure 6.24. Temporal series of the lasers when operating in the SLC and ALC. The time traces has been vertically displaced for clearness reasons. Top: the lasers oscillating with in-phase dynamics on the SLC; middle: the lasers are operating in one of the ALC and pulsating with different amplitudes; and bottom: changing the initial conditions the lasers operate in the other ALC. Solid line: laser 1; dashed line: laser 2.
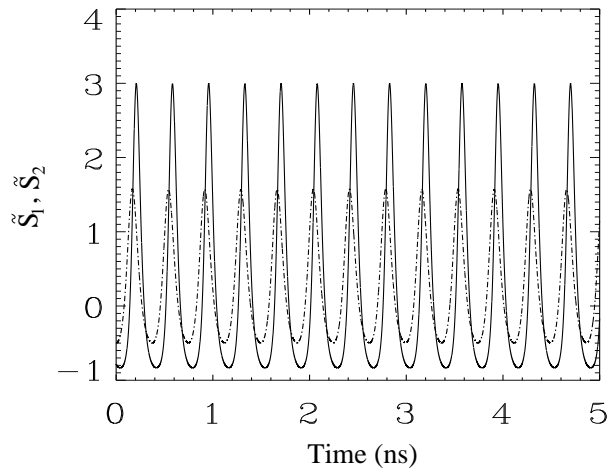
Figure 6.25. Increasing the coupling delay time to $T = 530$ ps, the ratio between amplitudes becomes as large as 2. Solid line: laser 1; dashed line: laser 2.

an anti-phase limit cycle, which eventually undergoes the same type of bifurcations than those commented for the previous in-phase limit cycle. This kind of structure going from an in-phase limit cycle to an anti-phase limit cycle and vice versa is repeated as T increases and consequently several islands of localized synchronization, quasi-periodic dynamics, and in-phase and anti-phase pulsating behavior are found.

The correlation degree, defined as the maximum of the cross-correlation function, is relatively high $(0.96 - 1)$ for the entire bifurcation diagram. The correlation degree is almost perfect during the in-phase and anti-phase limit cycles whereas a small drop in correlation can be observed when the system operates in the localized synchronization regime.
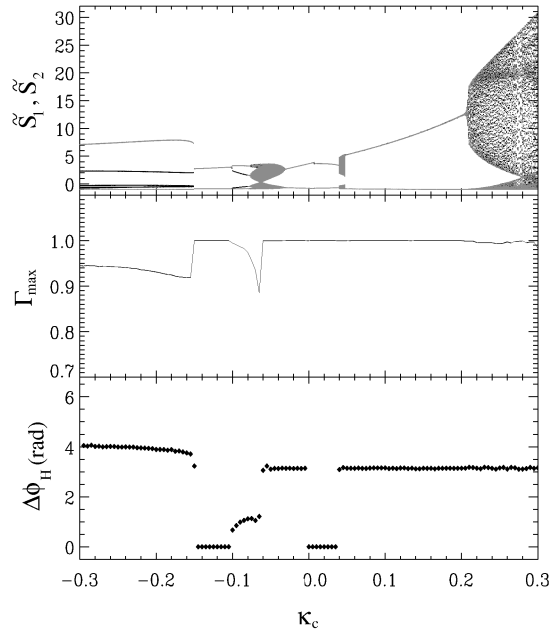
Figure 6.26. From top to bottom: bifurcation diagram for $\tilde{s}_1$ and $\tilde{s}_2$, maximum of the cross-correlation function Γ, and mean Hilbert phase difference. The feedback parameters are $\kappa_f = 0.3$ and $\tau = 1$ ns, while the coupling delay time is fixed at $T = 500$ ps. The coupling strength is scanned from $\kappa_c = -0.3$ up to $\kappa_c = 0.3$.

Different type of structures and dynamical regimes show up when the bifurcation parameter considered is the strength of the interaction. Figure 6.26 shows the bifurcation diagram, maximum of the cross-correlation function, and Hilbert phase difference between the two laser signals as a function of the coupling rate κ_c. Starting from an uncoupled configuration at the point $\kappa_c = 0$, the phase dif-

ference depends on the initial conditions and has been set at zero for convenience. Upon increasing the coupling strength we observe how the two oscillators remain in an in-phase limit cycle. Further increment the coupling rate leads to a sudden transition to quasi-periodic behavior in both lasers whose phase difference slightly oscillates around π. After this island of quasi-periodic behavior, which appears from $\kappa_c = 0.04$ to $\kappa_c = 0.047$, a regime with anti-phase periodic oscillations is reached. The amplitude of this limit cycle grows with the coupling strength until it reaches the value $\kappa_c = 0.2$. Beyond that value complex dynamics develops.

When inhibitory coupling strengths are considered in the left part of the diagram new dynamical regimes and synchronization properties are found. For slightly negative couplings, $\kappa_c \in (-0.03, 0)$, we obtain an anti-phase dynamics between the two laser outputs. When further decreasing the coupling rate from zero the system enters into a chaotic behavior area which ends with a symmetry-restoring bifurcation around $\kappa_c \sim -0.1$. Before this point is reached the two lasers have passed through a regime of localized synchronization with a phase difference approaching zero as the coupling tends to the symmetry-restoring bifurcation point. In-phase oscillatory behavior is then observed until the coupling value is decreased down to $\kappa_c = -0.15$. Beyond this point and at least until the minimum coupling strength we investigated ($\kappa_c = -0.3$) the two lasers oscillate with very different amplitudes. More important is the fact that the laser with smaller amplitude enters into a period-two state while the one with larger amplitude remains in a period-one state. This constitutes a second type of asymmetric dynamical regime we have identified for this perfectly symmetric system. We notice that associated to this sudden jump to a period-two asymmetric limit cycle there is a discontinuous change in the amplitude and frequency of the oscillations in both lasers.

Chaotic synchronization

An important point we have just considered is the study of the relative dynamics between the two lasers when they operate as self-sustained oscillators, i.e., periodically oscillating when uncoupled. Regarding the dynamics developed with this starting regime, we have numerically observed that both in-phase and anti-phase dynamics appear for both positive and negative coupling coefficients at certain values of the coupling delay time T.

However, by increasing the feedback strength and delay time we can force the lasers to operate in a chaotic regime even when they are uncoupled and study if they manage to synchronize their intrinsically chaotic fluctuations once the interaction is switched-on. In contrast to what occurs in the optically coupled face-to-face semiconductor lasers [10], we find that the isochronal (zero-lag) solution between the two lasers can be stable in a wide range of operation. This is shown in Figure 6.27 where the temporal traces, synchronization plot, and cross-correlation

function between the laser intensities are shown. For the simulations the coupling and feedback delay times are set to 3.5 ns and 3.85 ns, respectively. We can see in this case that the maximum of the cross-correlation function occurs at zero time shift between the intensity signals, in agreement with the experimental findings [89]. We also noticed that similar coupling and feedback delay times are needed in order to stabilize the zero-lag synchronization which it is lost when the two delays become very different.
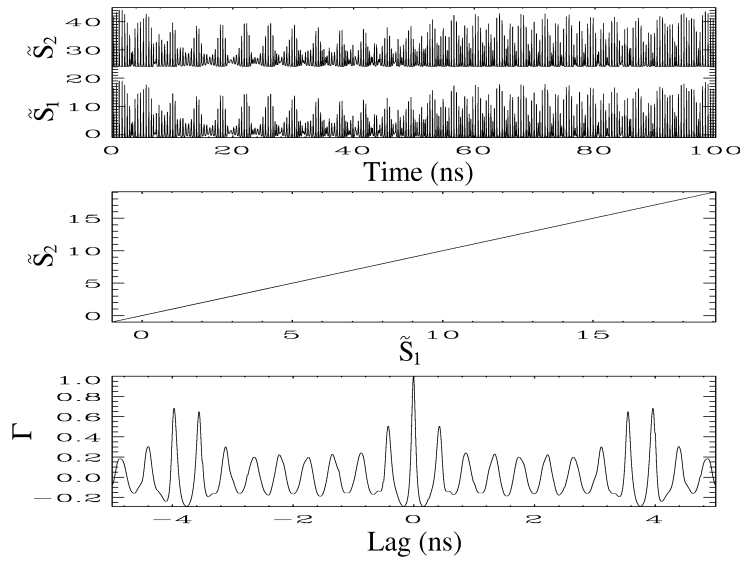
Figure 6.27. Top: chaotic temporal series of the lasers intensities after coupling; middle: synchronization plot; bottom: cross-correlation function Γ between the two chaotic outputs. When uncoupled, both lasers operate in the chaotic regime due to their feedbacks loops with $\kappa_f = 0.4$ and $\tau = 3.5$ ns. The coupling strength is $\kappa_c = 0.05$ while the coupling delay is $T = 3.85$ ns.

Slightly mismatched systems: Arnold Tongues

Another central aspect in coupled dynamical systems is its locking behavior. In particular the frequency locking properties of two coupled oscillators is a subject of wide interest for both theoretical and practical applications (see Chapter 2). In fact, the phenomenon of adjusting the internal rhythms of a system by an external or mutual perturbation is one of the most investigated effects in the synchronization concept [1].

Here, we are interested in studying the effect of the coupling delay time on these locking properties. In particular, we focus on the dependence of the Arnold tongues size (or frequency locking regions in the coupling strength versus detuning plane) on the coupling delay time between lasers. This is, how the ability to

lock between two oscillators depend on their distance. To this end, we retake the configuration of two isolated lasers that are self-pulsating due to their feedback loops. We consider the operation of both lasers in a pulsating regime where one of the feedback loops is slightly changed with respect to the other. This change, that we identify as a detuning, induces different natural pulsation frequencies. In our case, the Arnold tongues define a region in the coupling strength versus detuning space where the intensity oscillations of both lasers lock to the same frequency. In this section, we numerically evaluate the dependence of the Arnold tongues on the coupling delay time between the lasers. The computed main (1:1) Arnold tongues are shown in Figure 6.28.
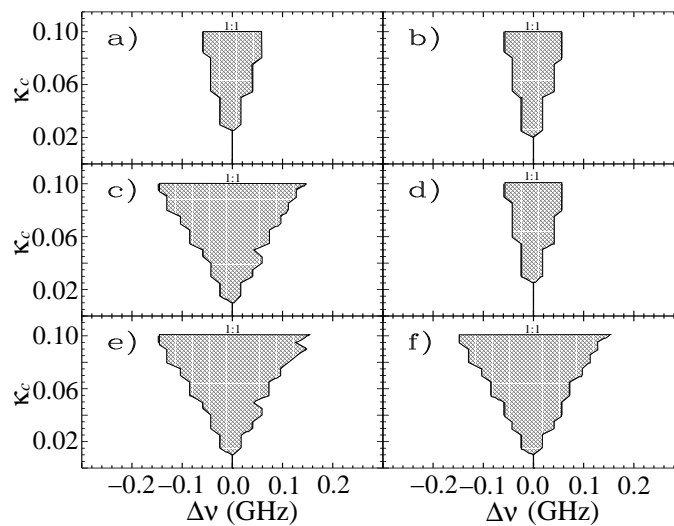
Figure 6.28. Arnold tongues for different coupling delay times. a), b), c), d), e), and f) panels correspond to $T = 0$, 1/4, 1/2, 3/4, 1, and 2 times the natural period of the oscillations when the lasers are uncoupled, which is about 348 ps. The feedback strength is $\kappa_f = 0.3$. The bias is $\tilde{J} = 1/3$.

We find that a change in the coupling delay time induces a change in the width of this tongue. The dependence of this width when the coupling delay time is changed is shown in Fig. 6.29 for a coupling coefficient $\kappa_c = 0.08$. It can be seen that the width of the Arnold tongue displays repetitive variations whose period is close to one half of the period of the intensity oscillations, which is about ~ 348 ps. The salient feature is the capability of the coupling delay time to enhance the width of the instantaneous Arnold tongue by a factor larger than two.

To complete the study of the Arnold tongue we have analyzed the physical mechanisms underlying this repetitive variation of the locking width. In our case, the variation of the Arnold tongue width can be understood as follows. In the ab-

sence of coupling, the electrical feedback loops generate gain modulation in the lasers. If we couple two of these lasers unidirectionally in a master-slave configuration, the slave laser locks to the externally imposed clock, and the coupling delay time only imposes a relative phase to the oscillations. We note, however, that may exist a certain time shift between the emission of the optical pulse and the externally-injected electrical-signal since the process is mediated by the dynamics of the carrier reservoirs in the active region of the lasers; the electrical injection from the coupling slightly modifies the gain modulation created by the feedback loops. This process allows for small adjustments of the repetition rate through small temporal shifts of the pulses. Now, the role of the coupling delay time becomes significant in the case of bidirectional coupling since it can enforce the locking of the oscillations as we explain now in more detail. A necessary condition for periodic locking is that the time required by a pulse to travel along the complete path and returning to a given reference point must be an integer number of the period of the locked oscillations. This time comprises the total coupling time $2T$ and the (small) nonlinear time shifts introduced by the lasers ΔT_1 and ΔT_2. Hence, the locking condition can be written as $2T + \Delta T_1 + \Delta T_2 = nT_{osc}$, with n an integer and T_{osc} the period of the oscillations. This condition has a repetitive structure when T is changed by $\sim T_{osc}/2$, which is reproduced in the oscillations of the locking width (Figure 6.29(b)). We have seen that the allowed values of $\Delta T_1 + \Delta T_2$ as a function of the detuning is limited in a certain interval given by the actual coupling strength. This limited tunability of $\Delta T_1 + \Delta T_2$ leads to the conclusion that there exist some values of T for which the locking condition can be more easily satisfied (leading to large Arnold tongues). It is worth noting that this effect can be exploited in any possible application where a robust locking state between lasers is required.
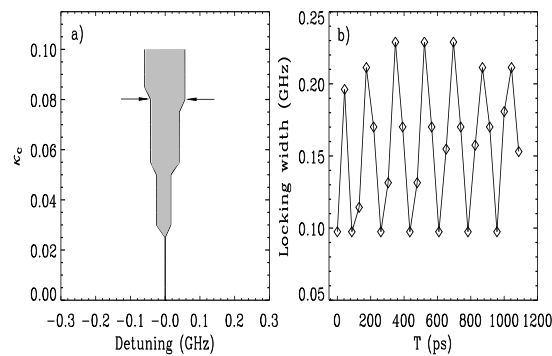
Figure 6.29. (a) The main Arnold tongue for $T = 0$. (b) Dependence of the locking width with the coupling delay time for $\kappa_c = 0.08$. The feedback strength is $\kappa_f = 0.3$, and the bias current is 33% above threshold. The natural period of the oscillations when the lasers are uncoupled is about 348 ps.

6.3.4 Experimental results

The laboratory equipment used to obtain the results that we present here is that described in the experimental section 6.2.5.

Starting with an experimental scheme similar to that sketched in Figure 6.1, we are able to experimentally reproduce the "death by delay" effect. Thus, for the first time in semiconductor laser setups we observe the quenching of laser intensity oscillations upon varying the coupling delay time. When uncoupled, both lasers exhibit an oscillatory behavior due to their feedback loops. However, as soon as the coupling strength and delay are adjusted to make the system fall into a "death island", an amplitude shrinkage in the oscillations is obtained. Figure 6.30 shows the dynamical states of the two lasers before, inside, and after passing over a "death island", as T is varied from 14.95 ns to 15.45 ns. Due to experimental limitations, no shorter delays were able to be explored, although it is expected that the quenching of the oscillations can be found for shorter values of T. Multiple "death island" are found as predicted by the theoretical analysis although they continue to appear for larger delay times than expected from the analysis of the idealized model of Eqs (6.1)-(6.4).
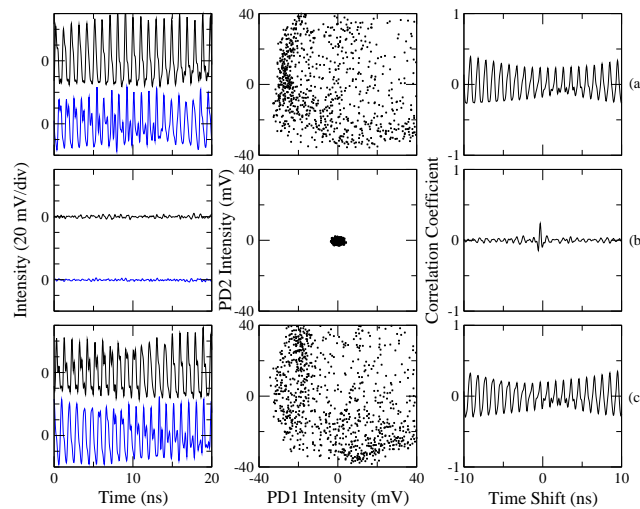
Figure 6.30. From top to bottom, sequence of dynamical states showing the evolution of the laser characteristics before, inside and after passing through a death island, respectively. The coupling delay time T is varied from 14.95 ns to 15.45 ns.

Within the same experimental setup, and just by choosing appropriate strengths and delays in such a manner that both lasers are driven to a chaotic state, we can also study the issue of the chaos synchronization between lasers [89]. Figure 6.31 shows the synchronization plot and the cross-correlation function between the two

laser outputs for coupling delay times of $T_1 = T_2 = 15.4$ ns. It is clear from the figure that both lasers exhibit highly correlated chaotic oscillations. The maximum of the cross-correlation function is located at the zero-lag point and is as high as 0.9. If we allow for different coupling delay times in each one of the coupling lines between lasers (i.e., $T_1 \neq T_2$), then we also observe how the largest peak of the correlation function shifts away from the center by a magnitude of $|(T_2 - T_1)/2|$ and with a direction dependent on which coupling delay time is shorter.
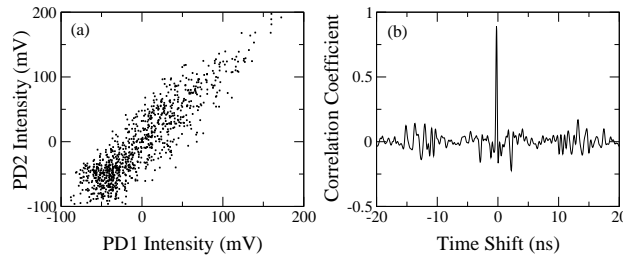
Figure 6.31. Chaos synchronization induced by mutual coupling. Left panel shows a typical synchronization plot between the two laser outputs. Right panel contains the cross-correlation function Γ between the two laser intensities. $\tau \sim 15$ ns.

These experimental results agree qualitatively with the results obtained from numerical simulations, and provide the verification that the most interesting features that were predicted in this system are robust enough to be observed in a real system.

6.3.5 Conclusions

In summary, we have theoretically investigated the nonlinear dynamics and synchronization properties of two bidirectionally coupled semiconductor lasers subject to optoelectronic feedback loops.

We have presented analytical and numerical studies for this system. The stability analysis provides a first understanding of the mechanisms leading to instability, and the exact role played by the different parameters (coupling and feedback strengths and delay times) in such a process. In particular, we have found a new scenario for the quenching of the oscillations that occurs in the absence of delay time in the coupling line and even for identical oscillators. We attribute this interesting behavior to the inclusion of delayed feedback loops.

We have also concentrated on the synchronization properties of both lasers when they operate as limit cycle oscillators. We have investigated the synchronization scenario that occurs upon increasing the mutual coupling strength and coupling delay time. When varying the coupling delay time, we have identified a sequence for the formation of in-phase, and anti-phase limit cycles separated by

symmetry-breaking bifurcations which lead to localized synchronization between the lasers. Regarding sthe slightly mismatched operation of the lasers it is shown that a delay time in the coupling between them may improve their capability to lock their oscillations.

At the laboratory level, analytical and numerical predictions are in qualitative agreement with the experimental findings of "death by delay" and synchronization scenarios.

Chapter 7

Mutually-coupled VCSELs: a study of synchronization in vectorial oscillators

THE[1] understanding and control of the lightwave polarization in lasers is of fundamental importance in any polarization-sensitive application. The heterostructure of a conventional edge-emitting semiconductor laser (the ones considered in the former chapter) induces a large anisotropy between the TE and TM lasing modes. This fact forces this type of lasers to generally emit in a single and well defined polarization state unless band structure engineering techniques such as induced-strain are applied. On the other hand, vertical-cavity surface-emitting lasers (VCSELs) preferentially emit linearly polarized (LP) light along two orthogonal preferred directions ($\hat{x}$ and $\hat{y}$) due to a combined effect of their weak material and cavity anisotropies [15]. This polarization degree of freedom provides these type of laser structures a vectorial nature where new synchronization phenomena can emerge.

Different instabilities affecting the polarization vector of VCSELs are found in several setups. Polarization switching (PS) between the $\hat{x}$ and $\hat{y}$ eigenaxes is often observed for VCSELs when either varying the temperature or the injection current [93], when feeding back part of the emitted light [94], or when injecting external light into the laser structure [95]. Moreover, recent experimental studies [96] have demonstrated that in the long distance regime the mutual coupling of two similar VCSELs can also induce instabilities with a high degree of synchronization in both total intensity and polarization variables. However, a general study of

---

[1]This chapter is based on the papers:

R. Vicente, J. Mulet, C.R. Mirasso, and M. Sciamanna , Optics Letters **31**, 996 (2006);

R. Vicente, J. Mulet, C.R. Mirasso, and M. Sciamanna , Proceedings of SPIE, Semiconductor Lasers and Laser Dynamics II **6481**, 648113 (2006).

the properties of synchronization between two bidirectionally-coupled VCSELs is still lacking in the laser dynamics literature.

In this chapter we investigate the mutual coupling of two similar VCSELs in order to determine the role of light polarization dynamics in their mutual entrainment or synchronization. The system consists of two VCSELs facing each other and bidirectionally injecting part of their emitted light into the counterpart laser active cavity. In a more general context, we can say that the dynamics of two vectorial oscillators interacting with a time delay is studied. The modeling equations of a face-to-face configuration of two VCSELs are presented in Section 7.1, where the values of the main parameters are specified and justified. We describe in section 7.2 a new coupling-induced polarization switching scenario, where multiple PS occur when continuously varying either the coupling strength or the propagation phase between the two lasers. With the help of a bifurcation analysis we conclude that PS events are correlated to the creation of new linearly polarized compound-cavity modes with higher gain. In addition, a bistable region around each PS which hysteresis width can be controlled by varying the coupling parameters is characterized within the same section. It is important to remark that controllable bistable PS in mutually-coupled VCSELs can add new functionalities to those applications employing a bistable region for fast switching applications [97]. Close to each polarization switching point, we find that the VCSELs may exhibit a richer nonlinear dynamics including time-periodic, quasiperiodic, or even chaotic behaviors. In Section 7.3 we analyze the nonlinear dynamics accompanying the PS as a function of the laser parameters, and in particular the spin-flip relaxation rate. The effect of a rotational misalignment between the VCSELs is investigated in Section 7.4 where elliptic polarization states of light are found to be stable under this configuration, as well as we describe sudden jumps of the polarization vector for some critical angles. Section 7.5 collects the synchronization properties of perfectly symmetric VCSELs which enhance the fully vectorial nature of these devices. To conclude Section 7.6 summarizes the main findings discussed in this chapter.

7.1   Model and parameters

Each solitary VCSEL is described according to the well established spin-flip model which takes into account two spin sub-levels in the conduction and valence band of the semiconductor material. [15]. Within this framework a low or moderate mutual optical injection between two VCSELs in a face-to-face configuration is considered by including delayed optical injection terms [98]. Then, the equations governing the dynamics of the electric field and the population inversion in each spin sublevel of the interacting lasers read

$$
\begin{aligned}
\dot{E}_{1\pm} &= -i\Delta E_{1\pm} + \kappa(1+i\alpha)\left[N_1 \pm n_1 - 1\right]E_{1\pm} - (\gamma_a + i\gamma_p)E_{1\mp} \\
&\quad + \xi e^{(-i\Omega\tau\mp\theta)}E_{2\pm}(t-\tau) + F_{1\pm}(t)\,, & (7.1) \\
\dot{N}_1 &= -\gamma_e\left[N_1 - \mu + (N_1+n_1)|E_{1+}|^2 + (N_1-n_1)|E_{1-}|^2\right]\,, & (7.2) \\
\dot{n}_1 &= -\gamma_s n_1 - \gamma_e\left[(N_1+n_1)|E_{1+}|^2 - (N_1-n_1)|E_{1-}|^2\right]\,, & (7.3) \\[2ex]
\dot{E}_{2\pm} &= i\Delta E_{2\pm} + \kappa(1+i\alpha)\left[N_2 \pm n_2 - 1\right]E_{2\pm} - (\gamma_a + i\gamma_p)E_{2\mp} \\
&\quad + \xi e^{(-i\Omega\tau\pm\theta)}E_{1\pm}(t-\tau) + F_{2\pm}(t)\,, & (7.4) \\
\dot{N}_2 &= -\gamma_e\left[N_2 - \mu + (N_2+n_2)|E_{2+}|^2 + (N_2-n_2)|E_{2-}|^2\right]\,, & (7.5) \\
\dot{n}_2 &= -\gamma_s n_2 - \gamma_e\left[(N_2+n_2)|E_{2+}|^2 - (N_2-n_2)|E_{2-}|^2\right]\,, & (7.6)
\end{aligned}
$$

where the subindices $1,2$ label the VCSELs. $E_\pm$ are the circularly-polarized components of the electric field ($E_\pm = (E_x \pm iE_y)/\sqrt{2}$). N represents the total inversion population while n is the difference of population inversions between the up and down spin reservoirs associated to the emission of opposite circularly-polarized photons. The last term in the field equations Eq. (7.1) and Eq. (7.4) are Langevin noise sources that account for spontaneous emission processes. Their expressions are $F_\pm(t) = \sqrt{\beta\gamma_e(N\pm n)}\chi_\pm(t)$, where $\chi_\pm(t)$ are independent complex random numbers with zero mean and δ-correlation.

Unless it is explicitly mentioned we consider the same internal parameters for both VCSELs. The only mismatches that we consider at some points of the analysis are a detuning between the free-running frequencies of both lasers $\Delta = \omega_2 - \omega_1$, and a misalignment between their two $\hat{x}$ and $\hat{y}$ eigenaxes, which is taking into account by a rotation angle θ. The meaning and values of the parameters in Eqs. (7.1)-(7.6) are collected in Table 7.1. The range of spin-flip rates (γ_s) that we have explored range from 50 ns^{-1} to 1000 ns^{-1}, in agreement with the usual values reported in experiments on PS in VCSELs [99]. The distance between both VCSELs is set to $L = 6$ cm ($\tau = 0.2$ ns). Consequently, the situation we are considering here corresponds to a short or moderate coupling time regime. Nevertheless, the effect of the delay on the interaction between the VCSELs is fundamental to understand the dynamics of the system.

It is worth noting that since we consider $\gamma_a < 0$ and $\gamma_p > 0$, the $\hat{x}$-LP mode exhibits a lower frequency and a larger gain than the $\hat{y}$-LP mode. Thus, $\hat{x}$ is the selected polarization mode for currents close to its threshold value. Figure 7.1 shows the light-current characteristics of a solitary VCSEL with the typical parameters of Table 7.1 and a low spin-flip rate ($\gamma_s = 50$ ns^{-1}) when the bias current is scanned in discrete steps. There, a current-induced switching of the polarization of the VC-

Symbol	Parameter	Value
α	linewidth enhancement factor	3
κ	field decay rate	300 ns^{-1}
γ_e	total carrier number decay rate	1 ns^{-1}
γ_s	spin-flip rate	50-1000 ns^{-1}
γ_a	amplitude anisotropy	-0.1 ns^{-1}
γ_p	phase anisotropy	3 ns^{-1}
μ	normalized pump	1.5
ξ	coupling strength	0-30 ns^{-1}
$\Omega\tau$	propagation phase	0-2π
τ	injection delay time	0.2 ns
Δ	frequency detuning	-20-20 GHz
β	spontaneous emission factor	0-1$\times 10^{-5}$

Table 7.1: Range of values used in this chapter for the parameters appearing in Eqs. (7.1)-(7.6).

SEL ($\hat{x} \longmapsto \hat{y}$) is found at $\mu \sim 1.35$ mediated by the simultaneous excitation of both modes. An increase of the spin-flip rate postpones this PS to higher bias currents. For instance, for $\gamma_s = 1000$ ns^{-1} no PS can be observed up to the maximum current explored, i.e., up to $\mu = 2$.

In the next section we demonstrate that even for such a large value of the spin-flip rate non-trivial polarization dynamics can occur when two VCSELs are coupled. In fact, we demonstrate that multiple PS can actually be induced by varying our main bifurcating parameters, namely the coupling strength ξ and propagation phase $\Omega\tau$.

7.2 Polarization switching and hysteresis

7.2.1 Coupling-induced PS

We first consider the case of two mutually-coupled VCSELs with identical laser parameters, zero frequency-detuning, and with their polarization eigenaxes perfectly aligned.

We begin by investigating the effect of varying the coupling and phase propagation values on the polarization dynamics of each VCSEL. Figure 7.2 shows maps of the LP mode intensities of both VCSELs upon the variation of the coupling strength (ξ) and propagation phase ($\Omega\tau \bmod 2\pi$). Intensities are plotted after removing transients and averaging over 50 ns. The alternation between high
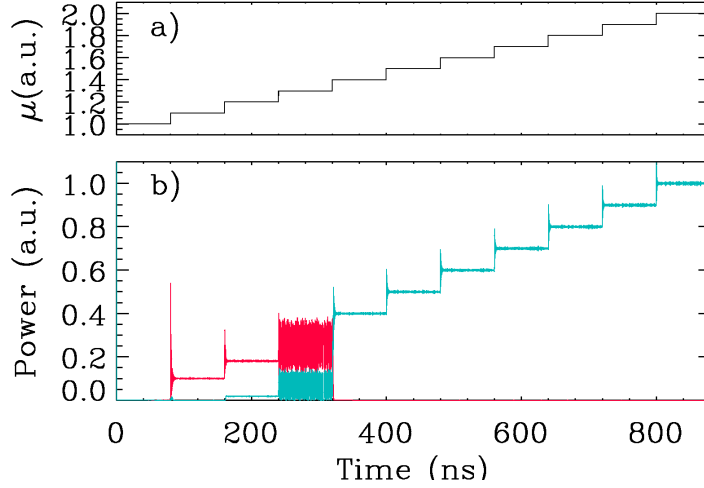
Figure 7.1. Light-current curve for a solitary VCSEL with a low spin-flip rate, $\gamma_s = 50$ ns^{-1}. Red (blue) color indicates the optical intensity of the $\hat{x}$ ($\hat{y}$) polarization mode. A current-induced PS can be observed at $\mu \sim 1.3$. The spontaneous emission factor is set to $\beta = 1 \times 10^{-5}$.

(red) and low (blue) power regions demonstrates successive PS between orthogonal LP states, i.e., sudden jumps to different polarization regimes induced by the increment of the coupling constant or the propagation phase between the lasers. Moreover, it is also clear from the figure that these PS events appear with a defined periodicity in the coupling parameters. The maps of VCSEL 2 are identical to those of VCSEL 1 indicating that PS jointly occur at the same coupling conditions for both VCSELs.

We have cheked that the coupling-induced PS scenario described in Figure 7.2 is not sensitive to small modifications of the laser parameters or the breaking of the symmetry of the configuration. Numerical simulations show that this coupling-induced PS scenario is robust against small mismatch of the two laser parameters including: linear anisotropies, different injection currents, spin-flip relaxation rates, detuning, and misalignment of the polarization axes. In particular, we still observe the multiple bistable PS when the two modes operate on the lower side of the gain curve ($\gamma_a > 0$), i.e., with the lower frequency mode having a smaller gain.

Bifurcation analysis

In order to gain insight into the origin of the observed coupling-induced PS, we must have a look at the bifurcations of LP solutions of Eqs. (7.1)-(7.6) when the coupling strength and propagation phase are changed. Two kinds of monochro-
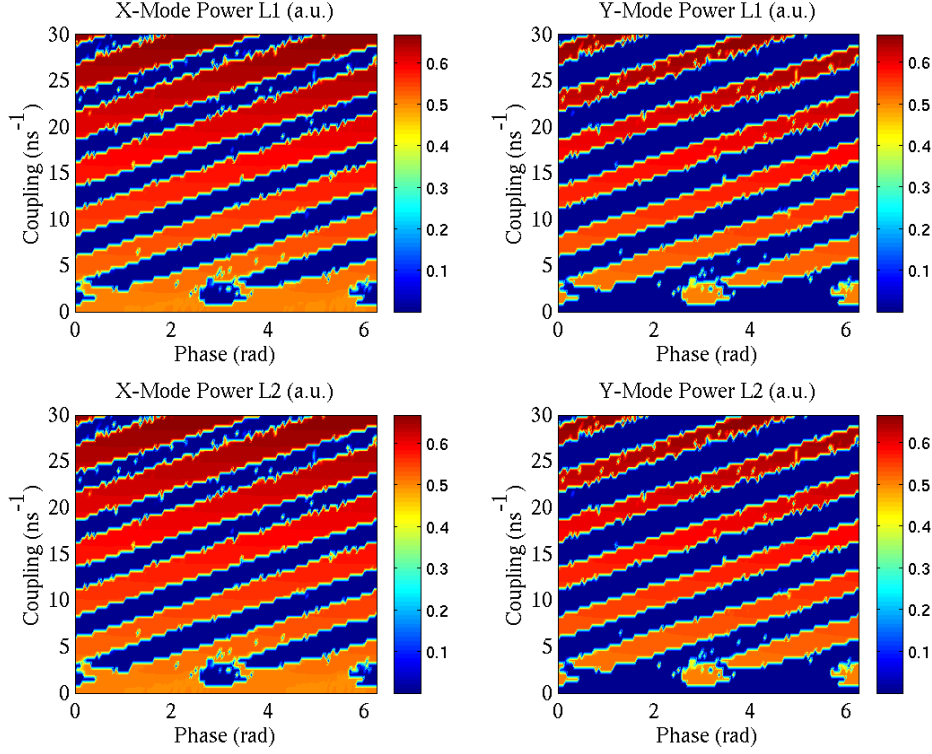
Figure 7.2. Time-averaged intensities in the $\hat{x}$- and $\hat{y}$-LP modes of VCSEL 1 and 2 as a function of ξ and $\Omega\tau$. Parameters are specified in Table 7.1.

matic LP solutions appear. Symmetric (asymmetric) fixed points corresponds to identical (different) output power and inversion of both lasers. In our case, numerical simulations have indicated that only symmetric LP solutions play a role in the dynamics of the VCSELs. Therefore, we focus on the symmetric fixed points.

These type of fixed points are obtained by imposing the intensity steady-state conditions; $E_{1+} = E_0 e^{i\omega t}$, $E_{1-} = E_0 e^{i(\omega t + \varphi)}$, $E_{2+} = E_0 e^{i(\omega t + \phi)}$, $E_{2-} = E_0 e^{i(\omega t + \phi + \varphi)}$, $N_{1,2} = N_0$, and $n_{1,2} = 0$. Here φ describes the polarization direction of the LP mode and ϕ takes into account the relative phase between the electric fields of both lasers. Such conditions are only satisfied for a relative phase $\phi = 0$ ($\phi = \pi$) leading to in-phase (anti-phase) electric fields in both lasers. After a little algebra, the frequency shift and inversion of the symmetric monochromatic solutions read

$$
\begin{aligned}
\omega &= \pm(\alpha\gamma_a - \gamma_p) - \xi\sqrt{1+\alpha^2}\sin\left(\phi - \Omega\tau - \omega\tau - \arctan\alpha\right), &\text{(7.7)} \\
N &= \frac{1}{\kappa}\left[\kappa \pm \gamma_a - \xi\cos\left(\phi - \Omega\tau - \omega\tau\right)\right], &\text{(7.8)}
\end{aligned}
$$

where $\pm$ stands for $\hat{x}$ and $\hat{y}$ polarized states.

As shown in Figure 7.3, the corresponding LP steady-states along the $\hat{x}$ and $\hat{y}$ polarization directions are located on two different ellipses in the frequency (ω) versus inversion (N) plane. The steady-states are plotted for increasing values of the coupling strength near a PS event ($13 \leq \xi \leq 13.8 \text{ ns}^{-1}$). For $\xi = 13 \text{ ns}^{-1}$ in panel (a), we observe that the system operates in the lowest inversion fixed point, which in this case corresponds to an in-phase $\hat{y}$-LP solution. An increase of the coupling strength in panel (b) creates a new pair of $\hat{x}$-LP modes through a saddle-node bifurcation. One of them is then a stable node and hence accessible as a stable attractor for the system. However, at this stage the system continues operating in the most stable maximum gain mode (MGM) of the $\hat{y}$-polarized states ellipse. For larger coupling strengths in panel (c), the $\hat{y}$-LP MGM destabilizes to a limit cycle through a Hopf bifurcation at the relaxation oscillation frequency ($\sim$ 2.7 GHz). Further increasing ξ, the oscillatory dynamics is interrupted and the laser finally switches to the $\hat{x}$-LP in-phase fixed point, which has become the new MGM in panel (d).
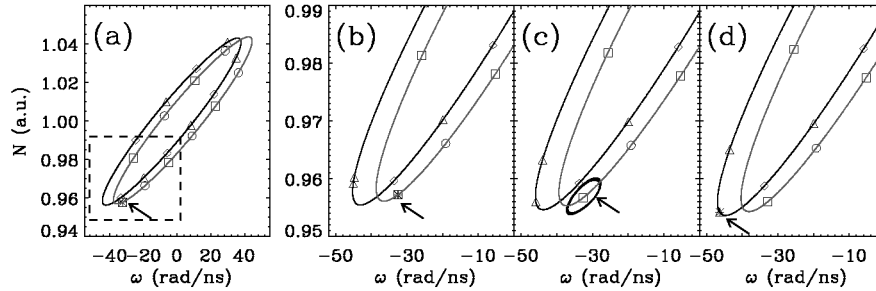
Figure 7.3. Panels (a)-(d) show the location of the symmetric fixed points in the N vs. ω phase space for $\xi = 13 \text{ ns}^{-1}$, $\xi = 13.25 \text{ ns}^{-1}$, $\xi = 13.6$, and $\xi = 13.8 \text{ ns}^{-1}$, respectively. Diamonds and triangles stand for the in-phase and anti-phase $\hat{x}$-polarized solutions. Squares and circles stand for the in-phase and anti-phase $\hat{y}$-polarized solutions. Arrows identify the attractor at which the system operates at every stage.

If the coupling rate is continously increased the formerly described process repeats and new PS are periodically induced following the same mechanisms. From the simulations, we find that the periodicity of PS when ξ is varied approximately amounts to the periodicity in the creation of a new saddle-node pair. For a fixed polarization and relative phase, the number of solutions of Eqs. (7.7)-(7.8) is proportional to $1 + \xi\tau \left(1 + \alpha^2\right)^{1/2} / \pi$. Consequently, taking into account that the creation of new steady-states alternates between in-phase and anti-phase modes, the periodicity in the PS events in a definite direction when ξ is changed can be

approximated by

$$\Delta\xi_{PS} = \frac{\pi}{\tau\,(1+\alpha^2)^{1/2}}\,. \qquad (7.9)$$

This value corresponds to the increase in ξ necessary to create a new pair of modes with a given polarization. For our set of parameters this quantity corresponds to 4.96 ns^{-1}, which agrees very well with the numerical results shown in Figure 7.2 where different PS, with the same transition ($\hat{x} \mapsto \hat{y}$, for example), are regularly spaced with an interval of ~ 5 ns^{-1}.

The PS events induced by changing the propagation phase (i.e., by moving horizontally in Figure 7.2) can also be understood in terms of the bifurcation of the LP solutions. When the phase is continously decreased from 2π to 0 it is observed a pulling of the steady-states around the ellipses from the low to high inversion regions. At the same time, a new pair of modes is created at the lowest vertex of each of the ellipses while they are annihilated by an inverse saddle-node bifurcation at the highest vertex. A similar bifurcating mechanism has been reported in mutually coupled edge-emitting lasers [100]. The novelty of this bifurcation scenario for VCSELs is that since the process of creation of new pairs of modes at the lowest corner of the ellipse occurs in alternation for the $\hat{x}$ and $\hat{y}$ polarization modes, this results into PS events when varying the propagation phase. The transformation $\Omega\tau \mapsto \Omega\tau + \pi$ interchanges the in-phase and anti-phase modes and defines the periodicity of the PS induced by phase changes.

Hysteresis

Now, if we reduce the coupling rate ξ from large values down to zero, we find that the PS events are slightly shifted from the locations at which we found them when the coupling was increased. This non-exact correspondence of the PS locations when increasing or decreasing the coupling strength is a clear indication of the existence of a hysteresis loop caused by coexistence of several stable orthogonal modes. The origin of this bistability is due to the fact that the saddle-node bifurcation, which creates the stable $\hat{x}$-LP mode, is located at a smaller ξ than the PS point where another attractor losses its stability.

Thus, in our mutually-coupled VCSELs system the selection of stable compound-cavity modes is accompanied by new features such as polarization switching with hysteresis. Figure 7.4 shows the multiple PS events when varying ξ or $\Omega\tau$, clarifying the bistability that occurs when increasing, and then decreasing, a control parameter. When sweeping the coupling strength both the switch-off and switch-on events of the $\hat{x}$-LP mode are accompanied by hysteresis, whose widths are labelled

as H_1 and H_2 respectively in Figure 7.4(a). The orthogonal polarization compo-
nent (not shown) displays a complementary behavior. Interestingly, as shown in
Figure 7.4(c), H_1 and H_2 grow while increasing ξ, hence showing that the hys-
teresis width can be tuned with the coupling parameter. A scan of the propagation
phase also leads to multiple PS in Figure 7.4(b) but, in contrast to the previous
case, i) only the switch-on events of the $\hat{x}$-LP mode are accompanied by bistabil-
ity, and ii) the hysteresis width keeps constant when changing $\Omega\tau$ as a consequence
of the symmetry of Eqs. (7.1)-(7.6) with respect to a change of $\Omega\tau$ in π.
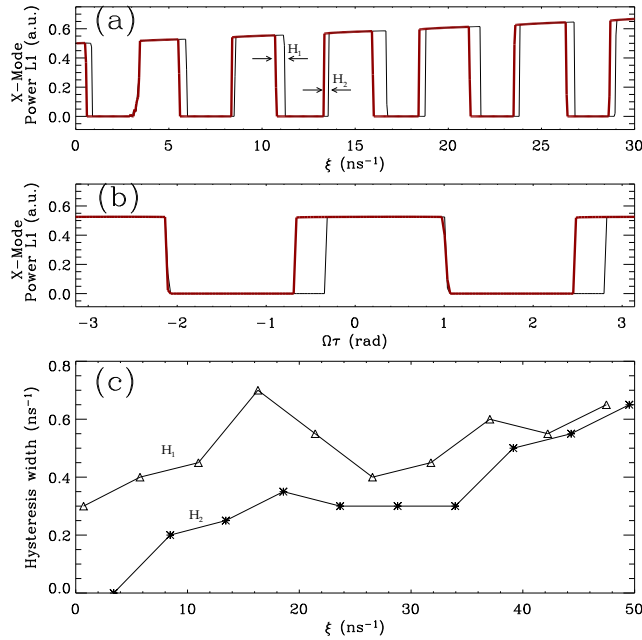
Figure 7.4. Panels (a) and (b) show the evolution of the $\hat{x}$-LP mode intensity as we increase
(thin line) and then decrease (thick line) ξ (a) and $\Omega\tau$ (b). In (c) are shown the two hysteresis
widths H_1 and H_2, labelled in panel (a), as a function of ξ.

Numerical simulations show that this bistable coupling-induced PS scenario
is qualitatively preserved for different spin-flip rate values ranging from $\gamma_s = 50$
ns^{-1} to 10^4 ns^{-1}. However, the range of coupling strengths around the PS where
a total intensity instability appears increases for small γ_s, i.e., the system becomes
more unstable around a PS event for smaller values of the spin-flip rate. Moreover,
the amount of spontaneous emission noise slightly modifies the PS positions. Since
two stable orthogonal LP attractors coexist around each PS, noise fluctuations may
favor the jump to an orthogonal LP-mode anticipating the PS point.

7.2.2   Detuning-induced polarization dynamics

Even in carefully controlled experimental setups, the presence of small mismatches between the lasers and a slight deviation from perfectly symmetric coupling conditions are almost unavoidable. In this section we focus on the effect of one of these sources of mismatches. In particular we study the influence of a detuning between the optical frequencies of the two VCSELs on the PS dynamics.

It is important to note that when uncoupled a small variation of few GHz in the free-running optical frequency of the lasers is not able to induce a PS. However, we show here that once coupled the continuous variation of the optical frequency difference between the two VCSELs can be responsible for a series of transitions from a polarization state of the light to the orthogonal one.
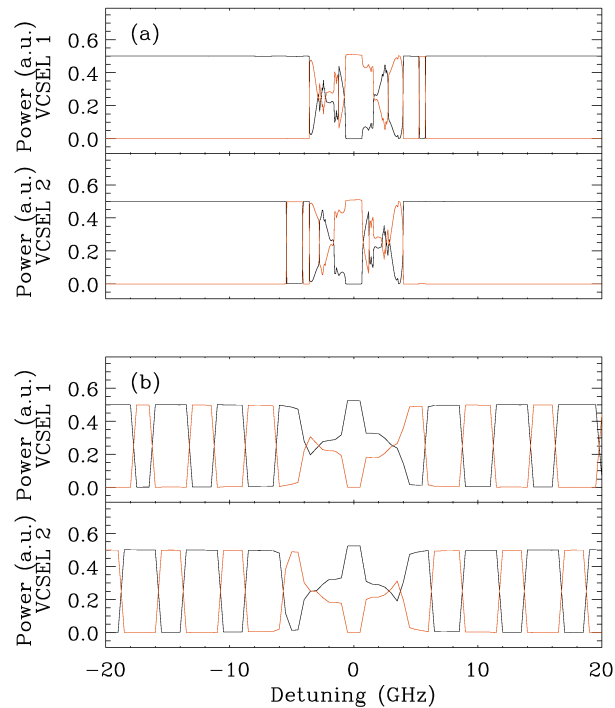
Figure 7.5. Averaged polarization resolved optical power of VCSEL 1 and VCSEL 2 as a function of the detuning for $\xi = 2$ ns^{-1} in panel (a), and for $\xi = 5$ ns^{-1} in panel (b). The propagation phase has been fixed at zero.

Figure 7.5 shows the optical power for the $\hat{x}$ and $\hat{y}$-polarization directions for each VCSEL averaged over 1000 ns as a function of the frequency detuning. Panel (a) corresponds to a coupling strength set to 2 ns^{-1}, while panel (b) assumes a

coupling rate of 5 ns^{-1}. In the first case, we observe how the power associated to the $\hat{y}$-mode, which is the dominant one in the absence of detuning, undergoes significant drops as the detuning is increased to finally experience a complete disappearance in both lasers for $\Delta/2\pi \gtrsim 6$ GHz. For larger detunings, in panel (a) the intensity of the now dominant $\hat{x}$-mode oscillates with a frequency close to $\Delta/2\pi$.

The results contained in panel (b), obtained for a larger coupling strength $\xi = 5$ ns^{-1} show again multiple switchings from one polarization mode to the orthogonal one. However, even more interesting is the fact that these polarization transitions can occur in opposite directions for each VCSEL. This leads to the result that two mutually-coupled identical VCSELs with slightly different optical frequencies can operate simultaneously at stable orthogonal polarization modes. For instance, in panel (b) we observe that at zero-detuning both lasers emit $\hat{x}$-polarized photons while for $\Delta/2\pi = 5$ GHz, VCSEL 1 operates at the $\hat{y}$-polarization mode and VCSEL 2 at the $\hat{x}$ one. At $\Delta/2\pi = 8$ GHz the roles of the dominant and suppressed polarizations have been exchanged in both lasers and VCSEL 1 is now lasing horizontally polarized photons, while VCSEL 2 is lasing in the $\hat{y}$-mode.

Interestingly, these detuning-induced PS are also accompanied by hysteresis effects. Thus, in Figure 7.6 we represent the hysteresis widths of the different PS as a function of the detuning. An increment of the hysteresis width can be observed for larger detunings.
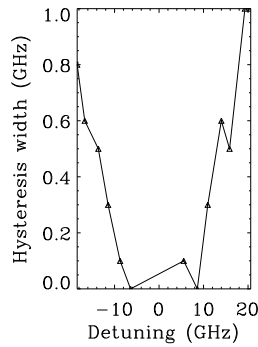
Figure 7.6. Hysteresis width of the PS events as a function of the detuning. Larger hysteresis widths are clearly appreciated when increasing the detuning mismatch.

7.3 Dynamics accompanying polarization switchings

Figure 7.4(a) showed the evolution of the time-averaged $\hat{x}$-LP mode intensity as the coupling strength is increased and then decreased. Any dynamics in the light intensity that occurs on a time-scale faster than the averaging time is therefore removed from the time-series analysis. Nevertheless, even though any detection scheme effectively introduces a filtering process, the fast dynamics accompany-

ing a PS can be of great help in understanding the details of mechanism of the switching and the undergoing synchronization between the VCSELs.

Thus, Figure 7.7 complements the analysis of Figure 7.4(a) by showing the corresponding bifurcation diagram of the polarization intensities as a function of the coupling strength. Here, the extrema of the $\hat{x}$-LP ($\hat{y}$-LP) mode intensity time-traces are plotted in black (red) for VCSEL 1 (left panels) and VCSEL 2 (right panels). In the upper panels (lower panels) of Figure 7.7 the coupling strength ξ is adiabatically increased (decreased).
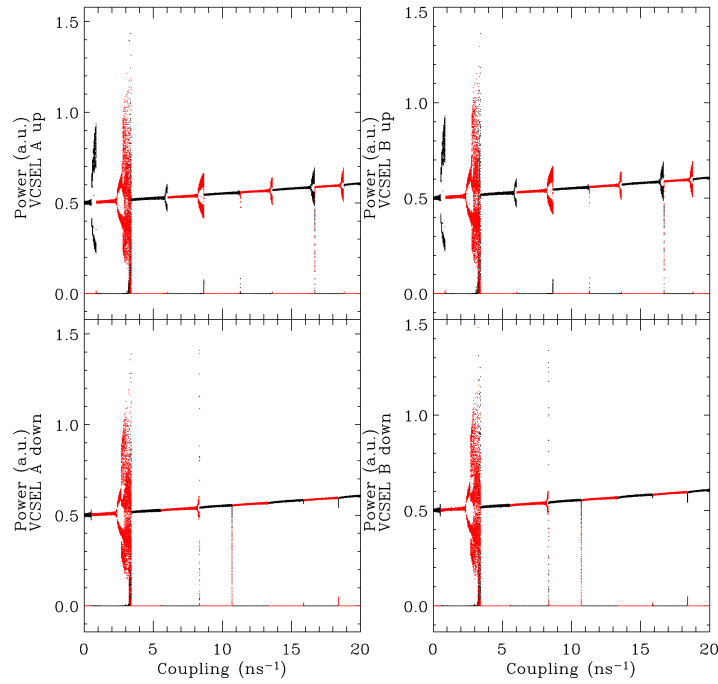
Figure 7.7. Bifurcation diagram of the polarization-resolved optical power as a function of the coupling strength. The coupling rate is adiabatically varied upwards (upper panel) and downwards (lower panel) for both VCSELs. The spin-flip rate is $\gamma_s = 1000 \text{ ns}^{-1}$.

As the coupling strength is increased each VCSEL displays a sequence of polarization switchings to steady-state solutions that are the compound-cavity modes analyzed in the previous section. However, the VCSEL can also exhibit a pulsating dynamics when the coupling strength is slightly smaller than that corresponding to a polarization switching point. The pulsating dynamics induced by the coupling may correspond to a regular time-periodic, quasiperiodic or even chaotic dynamics as seen in various points of Figure 7.7. An example of limit cycle attractor associated to a periodic dynamics near a PS point was shown, for example in Figure 7.3(b) in a projection of the infinite dimensional phase plane.

7.3.1   Spin-flip rate influence

The value of the spin-flip relaxation rate γ_s considered so far is $\gamma_s = 1000 \text{ ns}^{-1}$ being comparable to measured values from experiments on several VCSEL devices. Other experiments have, on the other hand, concluded on smaller values of the spin-flip relaxation rate, of the order of $\gamma_s = 100 \text{ ns}^{-1}$ or even less [101, 102]. It is known from the literature that the value of γ_s may have a strong influence on the VCSEL light polarization dynamics, in particular for the dynamics that accompany the polarization switchings [103–106]. In order to study the effect of the spin-flip rate on the dynamics accompanying PS in Figure 7.8 we plot the same bifurcation diagrams than in Figure 7.7 but for a smaller γ_s value ($\gamma_s = 100 \text{ ns}^{-1}$).
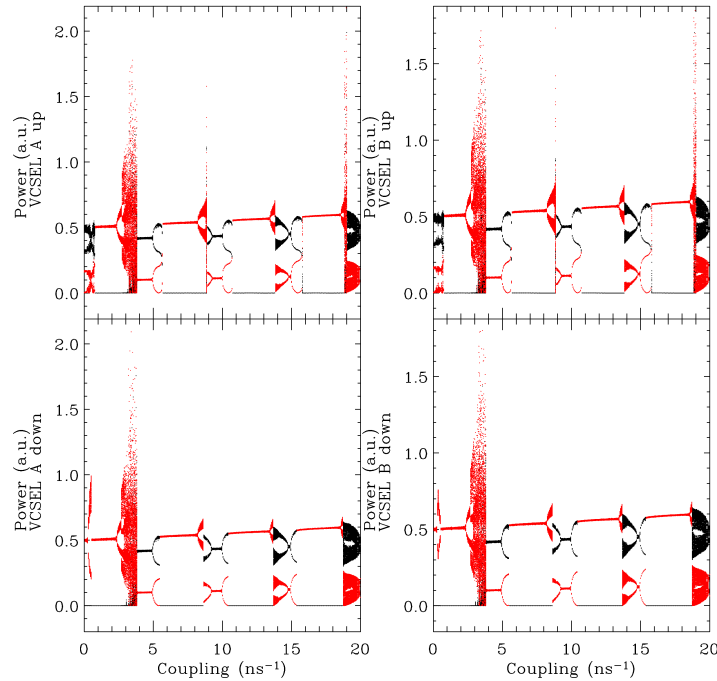
Figure 7.8. Bifurcation diagram of the polarized-resolved optical power as a function of the coupling strength. The coupling rate is adiabatically varied upwards (upper panel) and downwards (lower panel) for both VCSELs. The spin-flip rate is $\gamma_s = 100 \text{ ns}^{-1}$.

Interestingly, each VCSEL still exhibits a sequence of polarization switchings to steady-state single LP mode solutions. However, between the polarization switching points the VCSELs may exhibit a richer dynamical behavior, including a two-mode steady-state solution that destabilizes to time-periodic, quasiperiodic or chaotic behaviors. Typical time-traces of the two LP modes of one of each VCSEL are shown in Figure 7.9 for specific values of the coupling strength ξ. The

corresponding optical spectra are shown in Figure 7.10.
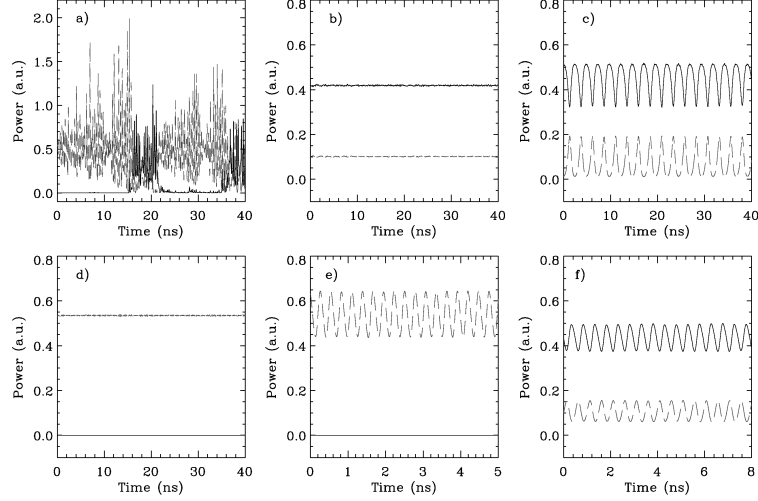
Figure 7.9. Temporal traces for the optical power of VCSEL 1 for different coupling strengths. a) $\kappa = 3.5$, b) $\kappa = 4.5$, c) $\kappa = 5.2$, d) $\kappa = 7.0$, e) $\kappa = 8.5$, and f) $\kappa = 9.0$ ns^{-1}. The rest of parameters are as in Figure 7.8.

In particular, in Figure 7.9(a) for $\xi = 3.5$ ns^{-1}, the two VCSELs exhibit a chaotic dynamics. Regarding the polarization dynamics within each VCSEL we observe how the $\hat{y}$-LP mode is dominant and exhibits fast pulsations with large intensity modulation. When the $\hat{y}$-LP power drops, the $\hat{x}$-LP mode is suddenly excited and becomes the dominant mode. The LP modes, therefore, exhibit a mode hopping on a time-scale much larger than that corresponding to the fast intensity pulsations in each modes.

For a larger coupling strength as in panel (b) where $\xi = 4.5$ ns^{-1}, the VCSELs dynamics bifurcate to a steady-state solution, with both LP modes emitting simultaneously. As shown in the optical spectra the two LP-modes are locked to the same frequency. Moreover, the two LP-modes of the second VCSEL (not shown in Figure 7.10) share the same optical frequencies unveiling that the two VCSELs are locked. Four modes (LP-modes of the two VCSELs) are therefore locked to exactly the same frequency.

The two-mode steady-state solution in Figure 7.9(b) bifurcates to a limit cycle dynamics in Figure 7.9(c) for $xi = 5.2$ ns^{-1}. The limit cycle frequency is 420 MHz, which is very close to half the birefringence (γ_p/π) that separates the frequencies of both solitary $\hat{x}$ and $\hat{y}$ LP modes.

For a stronger coupling strength ($\xi = 7.2$ ns^{-1}) this two-mode limit cycle dynamics undergoes a transition to a single polarization mode steady-state solution,
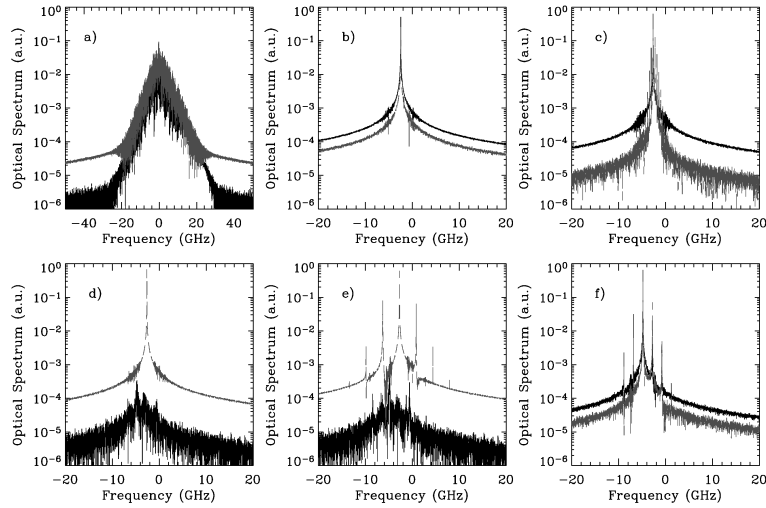
Figure 7.10. Optical spectra of VCSEL 1 for different coupling strengths. a) $\kappa = 3.5$, b) $\kappa = 4.5$, c) $\kappa = 5.2$, d) $\kappa = 7.0$, e) $\kappa = 8.5$, and f) $\kappa = 9.0$ ns^{-1}. The rest of parameters are as in Figure 7.8.

Figure 7.9(d). When analyzing the bifurcation diagram of Figure 7.8, we observe that this transition seems to occur at a defined coupling strength. The bifurcation to a single polarization mode is found at the coupling where the minimum of the intensity oscillations of the $\hat{x}$-mode becomes equal to the maximum of the oscillations of the $\hat{y}$-mode. This observation hints the fact that a collision of limit cycles may have an influence on the polarization switching.

As we further increase the coupling strength the single polarization mode steady-state Figure 7.9(d) bifurcates to a single-mode time-periodic dynamics with frequency close to 3.6 GHz, Figure 7.9(e), and then to a two-mode time-periodic dynamics with a slower frequency close to 2.2 GHz observed in Figure 7.9(f) for $\xi = 9$ ns^{-1}.

Therefore, the two-mode limit cycle dynamics exhibited in panels (c) and (f) of Figure 7.9 even appearing for slightly different coupling strentgh values ($\xi = 5.2$ ns^{-1} and $\xi = 9.0$ ns^{-1}, respectively) oscillate at very different frequencies, 420 MHz and 2.2 GHz, respectively, what possibly indicates a different origin of the oscillations. Another interesting observation comes from the correlation analysis between both VCSELs intensities. In Figure 7.9(c) the two polarization modes in VCSEL 1 are completely in-phase with those of VCSEL 2, while in Figure 7.9(f) they are in a perfect anti-phase regime. In both cases, however, it should be noticed that the correlation between the polarization modes within the same VCSEL shows

that both modes are phase locked in an anti-phase regime. Consequently, we show that different correlation properties between the two VCSELs (from complete in-phase to complete anti-phase) can be obtained depending on the exact value of the coupling strength linking the dynamics of both laser oscillators.

The visualization of these simulations in the Poincaré sphere provide us a complete picture of the polarization dynamics when increasing the coupling strength Figure 7.11. For small coupling strengths corresponding to panel a), we can observe both lasers exhibit a chaotic polarization dynamics where the polarization visiting all possible sections in the Poincaré sphere. Moreover, the polarizations of the two lasers run uncorrelated over the surface of such sphere indicating that no synchronization is occuring between the VCSELs. In former figures we showed that steady-states with non-zero $\hat{x}$ and $\hat{y}$-polarization components were found for intermediate coupling strengths. In panel b) we show that such states are associated to stable elliptic polarization modes instead of just to LP modes. It is also observed that the slow oscillations in panels c) and f) of Figure 7.9 correspond to limit cycle orbits on the Poincaré sphere, while fast oscillations in panel e) are induced by fast changes in the total optical power with a fixed linear polarization.
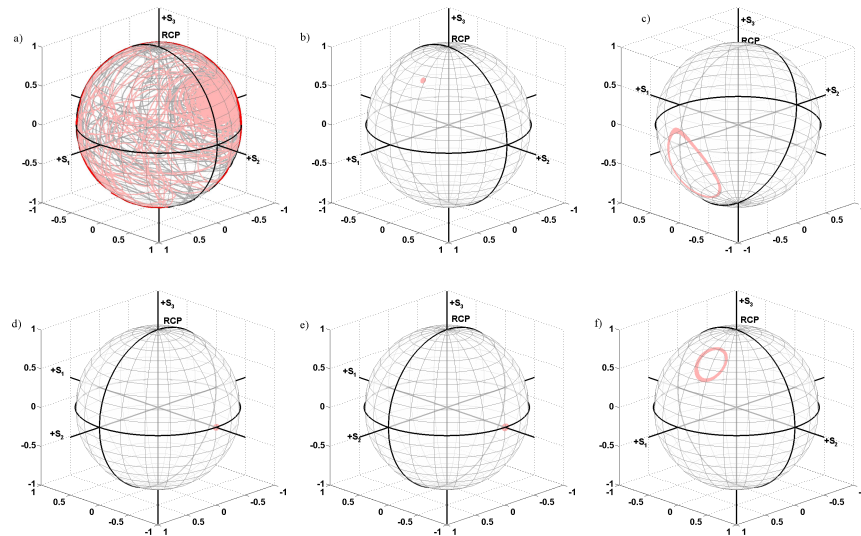
Figure 7.11. Stokes parameters in the Poincaré sphere for different coupling strengths. a) $\kappa = 3.5$, b) $\kappa = 4.5$, c) $\kappa = 5.2$, d) $\kappa = 7.0$, e) $\kappa = 8.5$, and f) $\kappa = 9.0$ ns^{-1}. The rest of parameters are as in Figure 7.8. Black and red distinguish VCSEL 1 and VCSEL 2, respectively.

7.4   Misalignment effects

So far all the results concerning the coupling-induced PS and the accompanying dynamics, including the synchronization properties have been obtained assuming a perfect alignement between the eigenaxes ($\hat{x}$ and $\hat{y}$) of both VCSELs. In this section we investigate the possible consequences of breaking up such a condition by rotating one of the VCSELs with respect to the other. This manipulation is easily accessible from an experimental point of view and calls for a fully vectorial study of the polarization degree of freedom.

Numerical integration of Eqs. (7.1)-(7.6) when scanning the coupling and rotation angle between the VCSELs leads to the output of Figure 7.12. For a fixed coupling, we notice that the effect of the rotation of a VCSEL is to continuosly decrease the power associated to one of the LP-modes while it increases the intensity corresponding to the orthogonal one. For example at $\xi = 5$ ns^{-1}, the $\hat{x}$-mode starts decreasing its power simultaneously in VCSELs 1 and 2, while the $\hat{y}$-mode gradually increments its power in both lasers. This tendency is maintained until the rotation angle becomes a bit larger than one quarter of revolution $\theta = \pi/2$ for which the power of the $\hat{y}$-mode reaches its maximum and the $\hat{x}$-mode its minimum value. From that point, the recovery of the initial values finishes at $\theta = \pi$, i.e., half a revolution of one of the VCSELs, demonstrating that the system is invariant to an upside-down turning of one of the VCSELs.

Figure 7.12, although indicating that there is a transfer of power between the $\hat{x}$ and $\hat{y}$ linearly polarized projections, it does not capture how this transition occurs. In the following we analyze the evolution of the components of the polarization vector of both VCSELs as a function of the rotation angle θ.

The four Stokes parameters are represented in Figure 7.13 for the polarization of both VCSELs when we rotate one of the VCSELs. In Figure 7.13(a) the evolution of S_0, which represents the total intensity of light, indicates that upon rotation of one of the VCSELs the total power emitted remains constant and identical in both VCSELs except for a tiny window where the intensity becomes chaotic. Panel b) of Figure 7.13 demonstrates that the projection of the vector of polarization on the S_1 axis is the same for the two lasers. This projection decreases from its maximum attained at $\theta = 0$ and π down to zero for values of θ slightly larger than $\pi/2$ and $3\pi/2$. Regarding the S_2 and S_3 components, in panels c) and d) it is observed that the two VCSELs always exhibit an opposite sign for the S_2 and S_3 projections of their respective polarization vectors.

Two key features are remarkable in Figure 7.13. One comes from the observation that S_3 is in general different from zero for most of the values of θ. This fact yields to stable elliptic polarization states of light in our coupled configuration which moreover can be induced by a pure mechanical operation, i.e., by rotating one of the lasers. One must remind that such states are not usually found to be sta-
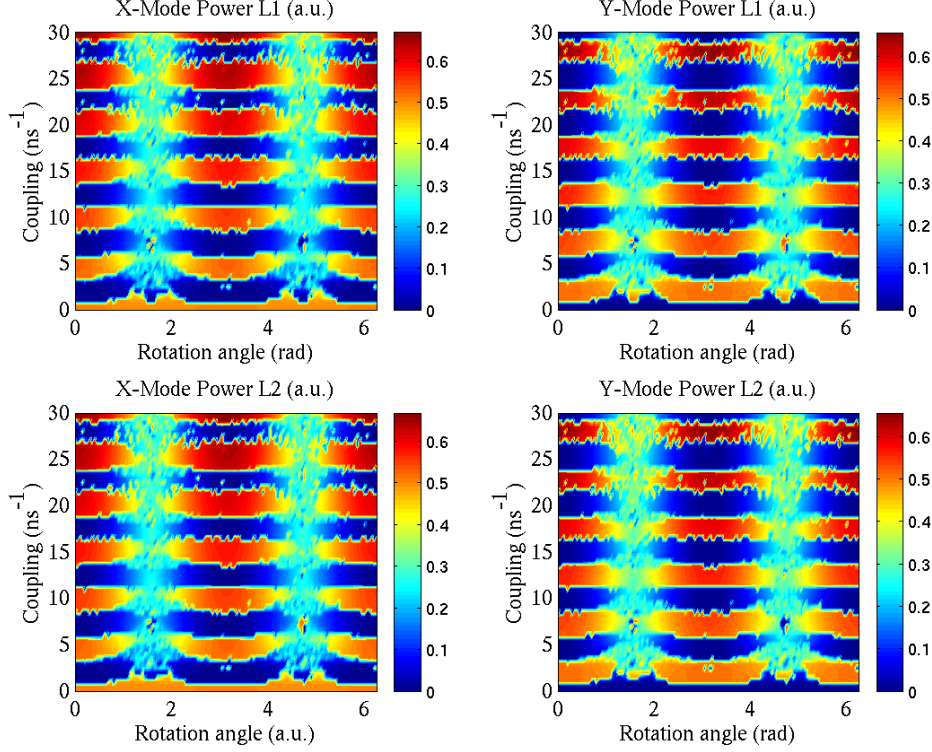
Figure 7.12. Time-averaged intensities in the $\hat{x}$- and $\hat{y}$-LP modes of VCSEL 1 and 2 as a function of ξ and θ. Parameters are specified in Table 7.1.

ble in solitary VCSELs. A second attracting characteristic is related to the sudden jumps in the S_2 and S_3 components of the polarization vectors found for values of the rotation angle near $\theta \sim \pi/2$ and $\sim 3\pi/2$. Thus, when crossing one of these critical angles the polarization state of the VCSELs suffers the sharp transition $(S_0, S_1, S_2, S_3) \longmapsto (S_0, S_1, -S_2, -S_3)$. These jumps correspond to an inversion of the polarization vector on the S_1 axis, occuring when one of the VCSELs is rotated by approximately half a revolution respect to the other laser. Near the critical angles of $\theta = \pi/2$ and $3\pi/2$ we found that $S_1 \sim 0$ and S_3 is small compared to S_2. Consequently, the abrupt inversion of the sign of S_2 for those angles can be thought as a sharp transition from a -45 to a $+45$ quasi-linearly-polarized emission of light in VCSEL 1, and the opposite transition for VCSEL 2.

We have also shown in Figure 7.14 that by reversing the rotation angle (i.e., turning the same VCSEL in the opposite sense) the sharp polarization switchings occur at similar but slightly different angles. Thus, if by increasing the rotation angle the first PS occurs at $\theta \sim 103°$ when rotating the laser in the other sense the PS appear at $\theta \sim 75°$. This difference provides a clear hysteresis spanning more
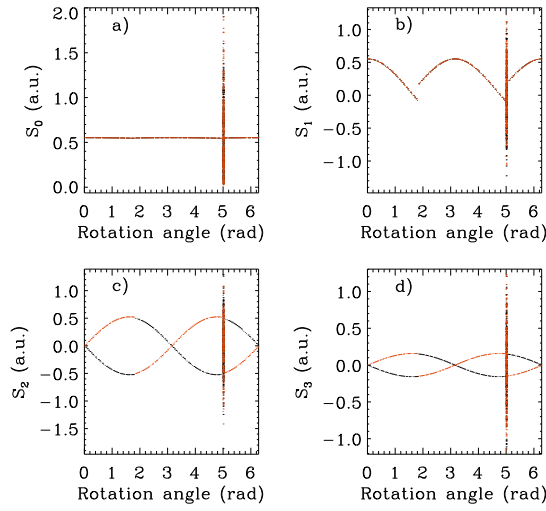
Figure 7.13. Stokes parameters evolution of the light emitted by the two VCSELs as a function of the rotation angle. Black and red traces represent the Stokes components of the VCSEL 1 and 2 polarization vectors, respectively. The coupling strength is fixed to $\xi = 10 \, \text{ns}^{-1}$.
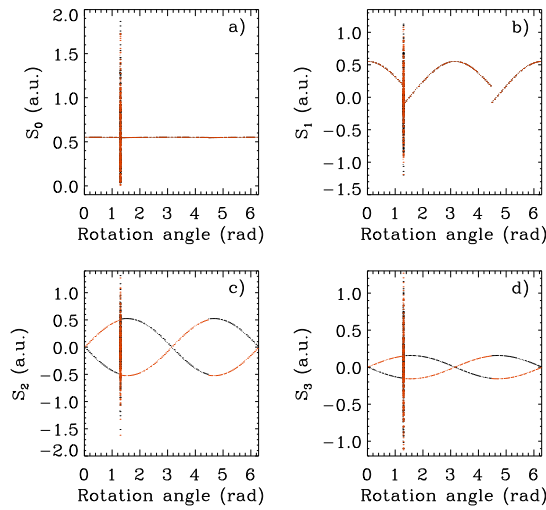
Figure 7.14. Stokes parameters evolution of the light emitted by the two VCSELs when decreasing the rotation angle. Black and red traces represent the Stokes components of the VCSEL 1 and 2 polarization vectors, respectively. The coupling strength is fixed to $\xi = 10 \, \text{ns}^{-1}$.

than 30 angular degrees around the values of $\theta = 90°$ and $\theta = 270°$.

Figure 7.15 contains the evolution of the Stokes parameters on the Poincaré sphere for increasing and decreasing the angle of rotation. In such a representation, the PS and hysteresis effects are evident.
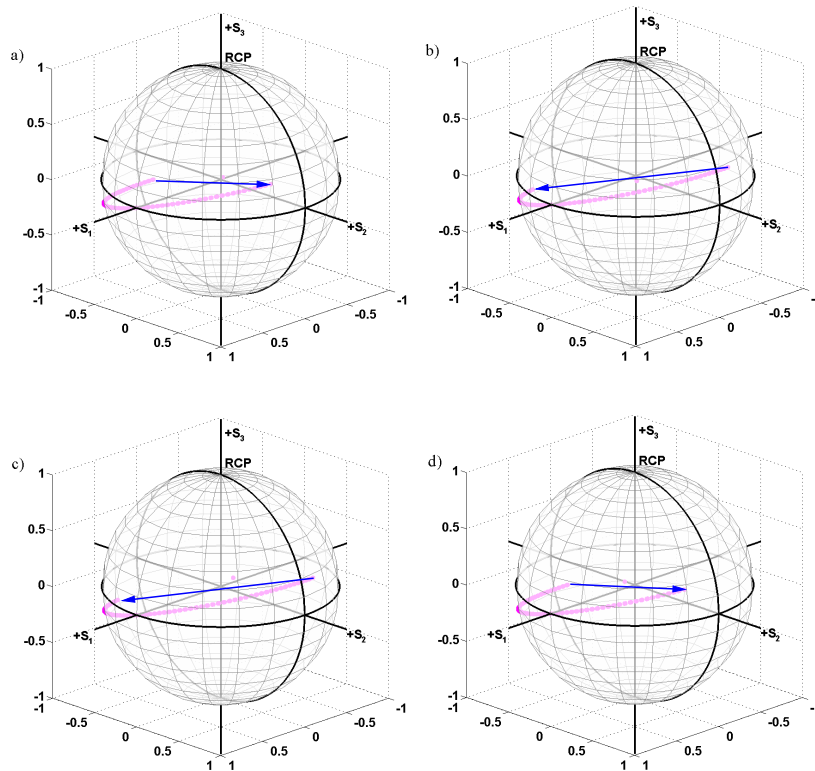
Figure 7.15. Stokes parameters evolution on the Poincaré sphere of the light emitted by the two VCSELs when increasing and decreasing the rotation angle; a) VCSEL 1 increasing θ, b) VCSEL 2 increasing θ, c) VCSEL 1 decreasing θ, and d) VCSEL 2 decreasing θ. Black and red distinguish VCSEL 1 and VCSEL 2, respectively. The arrows indicate the sharp transitions when varying the rotation angle.

Thus, in conclusion we have first described how the mechanical rotation of one of the devices around the critical angles can be optically encoded by the macroscopic polarization state of light of the VCSELs, and second how the bistability found around such PS also permits to detect and record the sense of the induced rotation.

7.5   Synchronization

In Section 7.3, we have reported that two mutually-coupled VCSELs can oscillate in regimes of periodic in-phase or anti-phase dynamics. There, the transition from one to another solution was induced by varying the interaction strength ξ. However, in those cases the cavity anisotropies induce that the two eigenaxes $\hat{x}$ and $\hat{y}$ are favored directions of the polarization state, thus imposing serious constraints to the vectorial nature of the synchronization scenario.

Here, in order to investigate the synchronization properties between the complete polarization vectors of two VCSELs we assume that the anisotropies of both laser cavities are negligible. By doing so we achieve to relax the preference of the VCSELs to emitt light polarized along some definite directions. In such conditions the fundamental question to be answered is how the polarization vector of each VCSEL is going to evolve?

First we analyze the situation corresponding to a solitary VCSEL. In the pure deterministic case it is observed that all the linearly polarized states are equivalent and neutrally stable. Consequently, there is no preference for a particular state and depending on the initial condition the polarization vector settles on a given direction. In the presence of spontaneous emission noise, the polarization vector of each solitary VCSEL is found to diffuse around the equator of the Poincaré sphere, i.e., to perform a random walk visiting all the possible linearly polarized states.

Panel a) in Figure 7.16 shows the polarization vectors of two VCSELs when they are uncoupled and free from anisotropies. Clearly, both vectors diffuse without any correlation between each other. For low coupling rates such in panel b), a kind of synchronization must occur between both polarization vectors because now they scan at the same time the same Poincaré sphere region. For intermediate couplings (panel c)) one finds a region of chaotic states where the polarization vectors visit all the sphere surface, while for larger interaction strengths $\xi \geq 7$ ns^{-1} both vectorial oscillators diffuse again around the equator. We have also noticed that the larger the coupling strength the smaller the area of the Poincaré sphere that is visited in the same time.

Now, we can study whether such random walks can synchronize. Figure 7.17 (left panel) shows the maxima of the cross-correlation functions between the Stokes parameters of both lasers as a function of the coupling strength. Remarkably, both polarization vectors continue to diffuse mainly around the equator of the Poincaré sphere driven by independent spontaneous noise sources and nevertheless, a large correlation value is found between the dynamics of the three components of both polarization vectors. The effect of the time delay in the interaction between the VCSELs is reflected in the timing of the synchronization of the polarization dynamics. Figure 7.17 (right panel) plots the lag at which the
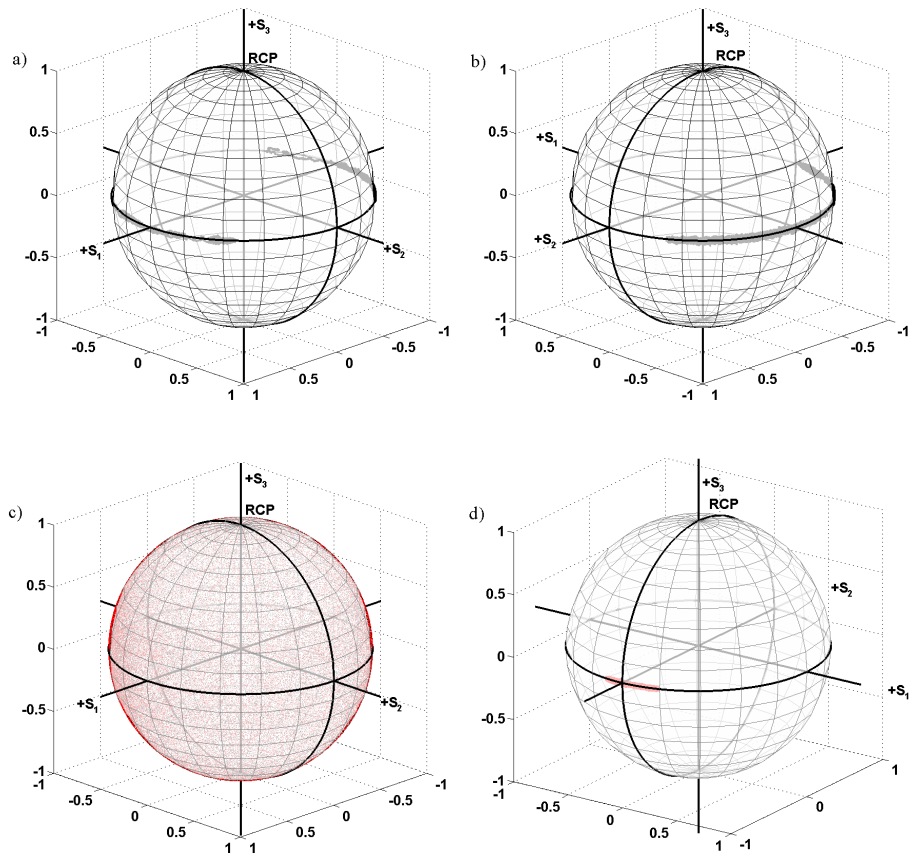
Figure 7.16. Stokes parameters evolution on the Poincaré sphere of the light emitted by the two VCSELs for different values of the coupling strength; a) $\xi = 0$ ns^{-1}, b) $\xi = 2$ ns^{-1}, c) $\xi = 4$ ns^{-1}, and d) $\xi = 20$ ns^{-1}. Black and red distinguish VCSEL 1 and VCSEL 2, respectively.

maximum of the cross-correlation function between the two polarization vectors is attained. For most of the coupling values the cross-correlation function is almost symmetric around zero with two similar maxima at $\pm\tau$. This fact is reflected in Figure 7.17 where for large coupling rates the lag randomly fluctuates between 200 ps and -200 ps, i.e., the coupling time.
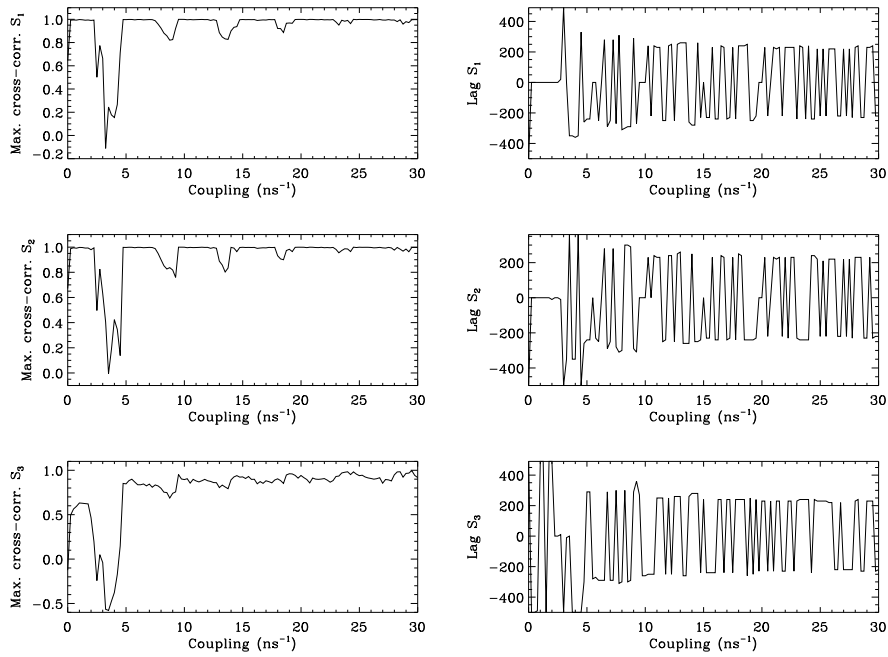
Figure 7.17. Left: maxima of the cross-correlation functions between the polarization components of both VCSELs as a function of the coupling strength. Right: lag at which the maxima of the cross-correlations are found as a function of the coupling strength.

7.6   Conclusions

In this chapter we have shown that mutual coupling may induce multiple bistable polarization switchings in otherwise polarization stable VCSELs.

A sequence of PS events has been found when varying the coupling strength or the propagation phase between the VCSELs. The definite periodicity of these PS events has been related to the creation of new compound-cavity modes with higher gain and orthogonal polarization. Each PS is accompanied by a large hysteresis whose width can be tuned by the coupling parameters. Such controllable bistable PS system is interesting for fast optical switching applications. We have also checked that this coupling-induced PS scenario is robust against modifications of the corresponding laser and coupling parameters.

Moreover, the effect of a detuning between the lasers free-running optical frequencies has been found to induce another type of PS.

Stable elliptic polarization states are achieved by the rotation of one of the VCSEL respect to the other. This situation is also responsible for the appearance of sharp jumps in some components of the polarization vector of each VCSEL.

Finally, we have observed the temporal synchronization of the polarization vectors of isotropic VCSELs. Thus, a true vectorial synchronization in mutually-coupled VCSELs has been numerically demonstrated.

Chapter 8

Synchronization of three mutually-coupled semiconductor lasers

EXPERIMENTS[1] and numerical simulations have demonstrated that the coupling-induced dynamics of two semiconductor lasers interacting through the mutual injection of their coherent optical fields exhibit a symmetry breaking [10, 12]. Instead of showing an identical behavior, spontaneously, the two twin lasers develop an achronal generalized synchronization between them. This type of sync is mainly characterized by peaks at $\pm\tau$, with τ being the coupling time, in the cross-correlation function between the lasers intensities.

From a different perspective, investigations of three instantaneously-coupled semiconductor or solid-state lasers interacting through their overlapping optical fields were performed by Winful et al. [16], and Roy and collaborators [17]. These authors observed that when arranged in a linear array, a identical synchronization between the first and third lasers showed up, while the temporal traces of any of the extreme lasers and the central one appeared rather uncorrelated.

These interesting results motivate a deeper study on how the number of lasers and the network of couplings modify the synchronization properties of SLs interacting with a finite time delay. New questions need to be addressed. For instance, can the isochronous solution between the first and third lasers be maintained even when the lasers need a time to communicate? How will the sync look like if we add a fourth laser to the array? What is the role of the symmetry on selecting possible sync patterns? With a view to answer these questions, we study here the

---

[1]This chapter is based on the paper: "Zero-lag long-range synchronization via dynamical relaying" by I. Fischer, R. Vicente, J. Buldu, M. Peil, C.R. Mirasso, M.C. Torrent, and J. Garcia-Ojalvo, to appear in Physical Review Letters (2006)

synchronization properties of semiconductor lasers arranged in open-end (linear chain) and ring configurations. Arrays up to six SLs have been explicitly analyzed. Symmetry arguments support the opinion that the patterns of solutions found for arrays of those size are maintained for larger number of units.

After introducing the modeling equations and parameters, we present our main results in Section 8.2. There we focus on the open-end configuration of three mutually-coupled SLs. In particular, we show that zero-lag synchronization between the extreme lasers in an open-end configuration can be achieved by relaying the dynamics via the central laser, which surprisingly lags behind the synchronized outer elements. The characterization of the coupling-induced instabilities and their robustness are also analyzed there. Subsequent sections are devoted to the effect of increasing the number of laser elements in both the open-end and ring configurations. The role of the symmetry and delay in restricting the possible synchronization spatial profiles is also explained there. A connection between the chaotic synchronization solutions and the time-periodic patterns of oscillation is proposed. Finally, zero-lag synchronization between distant coupled lasers is used to propose a new chaotic communication scheme in Section 8.4. Conclusions are summarized in Section 8.5 where the experimental confirmation by the groups of Darmstadt and Terrassa of the zero-lag sync in a laser setup is also briefly commented.

8.1   Model

The system under investigation consists of single-mode SLs coupled via the delayed mutual injection of their lasing modes in a given network of connections. For numerical purposes the modeling is performed at the level of rate equations according to Ref. [98], which take into account the different delayed coupling terms between the SLs.

Figure 8.1. Open-end scheme of three mutually-coupled semiconductor lasers interacting with a time delay.

The adaptation of such a modeling to the case of three mutually-coupled SLs interacting in an open-end configuration (as sketched in Figure 8.1) reads

$$
\begin{aligned}
\dot{E}_1 &= i\Delta\omega_1 E_1 + \frac{1}{2}\left(1+i\alpha\right)G(N_1, \|E_1\|)E_1 \\
&+ \kappa_{21}\exp(i\phi_{21})E_2(t-\tau_{21}) \tag{8.1} \\
\dot{N}_1 &= \frac{I_1}{e} - \gamma_e N_1 - G(N_1, \|E_1\|)\|E_1\|^2 \tag{8.2} \\
\\
\dot{E}_2 &= i\Delta\omega_2 E_2 + \frac{1}{2}\left(1+i\alpha\right)G(N_2, \|E_2\|)E_2 \\
&+ \kappa_{12}\exp(i\phi_{12})E_1(t-\tau_{12}) + \kappa_{32}\exp(i\phi_{32})E_3(t-\tau_{32}) \tag{8.3} \\
\dot{N}_2 &= \frac{I_2}{e} - \gamma_e N_2 - G(N_2, \|E_2\|)\|E_2\|^2 \tag{8.4} \\
\\
\dot{E}_3 &= i\Delta\omega_3 E_3 + \frac{1}{2}\left(1+i\alpha\right)G(N_3, \|E_3\|)E_3 \\
&+ \kappa_{23}\exp(i\phi_{23})E_2(t-\tau_{23}) \tag{8.5} \\
\dot{N}_3 &= \frac{I_3}{e} - \gamma_e N_3 - G(N_3, \|E_3\|)\|E_3\|^2 \; , \tag{8.6}
\end{aligned}
$$

where $E_m(t)$ is the complex amplitude of the optical field generated by laser m and N_m represents the corresponding carrier number. $\|\cdots\|$ denotes the amplitude of the complex field. The nonlinear gain function $G(N_m, \|E_m\|^2)$ is given by:

$$
G(N_m, \|E_m\|) \equiv \frac{g(N_m - N_o)}{1 + s\|E_m\|^2} - \gamma \; .
$$

The coupling parameters that define the interaction between any two lasers are given by the coupling weight $[\kappa_{mn}]$, the coupling time $[\tau_{mn}]$, and the coupling phase $[\phi_{nm}] = \Omega[\tau_{mn}] \mod 2\pi$ matrices. Thus, in the case of a general network the equations defining the interaction between lasers are written as

$$
\begin{aligned}
\dot{E}_m &= i\Delta\omega_m E_m + \frac{1}{2}\left(1+i\alpha\right)G(N_m, \|E_m\|)E_m \\
&+ \sum_{n\neq m}\kappa_{nm}\exp(i\phi_{nm})E_n(t-\tau_{nm}) \tag{8.7} \\
\dot{N}_m &= \frac{I_m}{e} - \gamma_e N_m - G(N_m, \|E_m\|)\|E_m\|^2 \tag{8.8}
\end{aligned}
$$

8.2 Dynamics of three semiconductor lasers in an open-end configuration

In the subsequent sections we focus first on the open-end configuration of three mutually-coupled SLs. The internal laser parameters are assumed identical for the three lasers; the linewidth enhancement factor $\alpha = 3$, the differential gain $g = 1.2 \times 10^{-5}$ ns^{-1}, the transparency value for the carrier number $N_0 = 1.25 \times 10^8$, the saturation coefficient $s = 5 \times 10^{-7}$, the photon decay rate $\gamma = 496$ ns^{-1}, and the carrier decay rate $\gamma_e = 0.651$ ns^{-1}. With these internal parameters the threshold current of the three lasers is $I_{th} = 17.35$ mA. In the former equations, the reference frequency for the slowly-varying amplitude of the electric fields is chosen to be $\Omega = (\omega_1 + \omega_2 + \omega_3)/3$, where ω_i is the central frequency of each solitary laser. Detunings ($\Delta\omega_i$) are taken with respect to Ω. Unless other coupling conditions are explicitly mentioned in the text the coupling strengths, delay times, and propagation phases are assumed to be identical in the two coupling branches of Figure 8.1; $\kappa_{1,2} = \kappa_{2,1} = \kappa_{3,2} = \kappa_{2,3} = 20$ ns^{-1}, $\tau_{1,2} = \tau_{2,1} = \tau_{3,2} = \tau_{2,3} = 3.65$ ns, and $\phi_{1,2} = \phi_{2,1} = \phi_{3,2} = \phi_{2,3} = 0$ rad.

8.2.1 Coupling-induced instabilities

In order to explore the instabilities emerging from the mutual coupling of three semiconductor lasers interacting with a time delay, we first set the lasers to operate in a highly symmetric configuration namely, within a perfect free-running frequency tuning ($\Delta\omega_1 = \Delta\omega_2 = \Delta\omega_3 = 0$) and a moderate and identical current pump $I = I_1 = I_2 = I_3 = 27.5$ mA. With this level of pumping the solitary relaxation oscillation frequency of the three lasers amount to 4.33 GHz.

Once coupled under standard conditions the three semiconductor lasers are observed to enter into a fully chaotic regime known as Coherence Collapse (CC). Remarkably, after some transient the traces of the outer lasers, i.e., SL1 and SL3, start to become more and more alike up to the point that they end up being perfectly synchronized at zero-lag. The numerical results are shown in Figure 8.2. In order to check the robustness of this synchronization phenomena we have simulated Eqs. (8.1)-(8.6) starting from various and non-identical initial conditions for the lasers. All the simulations returned the same results; the zero-lag synchronization of the lasers occupying the extreme positions in the array. At this point it is worth to remember that the symmetry under the exchange between lasers 1 and 3 only assures the existence of the synchronized solution but not its stability. Of course, in this zero-lag synchronization no superluminal effect is taking place, but this is another example of self-organizing dynamics where the units composing the system negotiate a complex and unexpected behavior.

Moreover, the computation of the cross-correlation functions between the lasers reveals a high degree of similarity between any of the outer laser traces
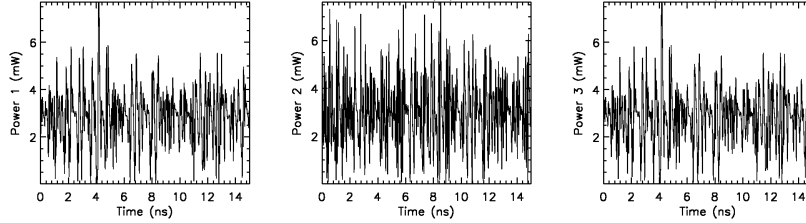
Figure 8.2. Temporal traces of the open-end configuration with three lasers. $\kappa = 20$ ns^{-1} and $\tau = 3.65$ ns.

and the central one. In Figure 8.3 it is observed that once properly shifted a high degree of correlation (~ 0.8) appears between the traces of any of the extreme lasers and the laser 2. In this case, however, the lag for which the maximum of the cross-correlation function appears corresponds to the coupling time. The asymmetric cross-correlation function between SL1 (or SL3), and SL2 signals that the outer lasers are advancing the dynamics of the central one by a time delay τ. Surprisingly, the mediator element is lagging behind the synchronized outer units for which it is acting as a communicating bridge. This type of dynamics excludes the interpretation of the central element as a simple leader directly forcing the extreme lasers.
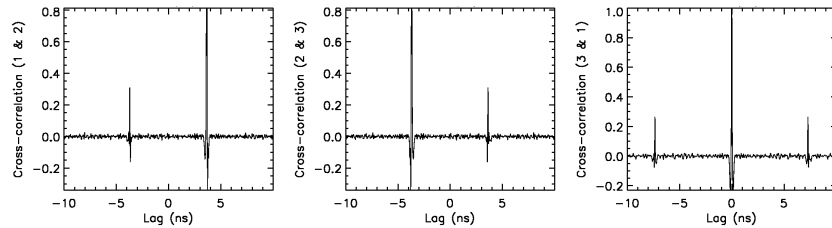
Figure 8.3. Cross-correlation functions for the open-end configuration with three lasers. $\kappa = 20$ ns^{-1} and $\tau = 3.65$ ns.

Interaction strength effect

How this synchronization scenario depends on the strength of the interaction between lasers is investigated next. To this end, we adiabatically increase the coupling strength between the three SLs and record a time series for each value of the coupling rate. The common coupling strength $\kappa = \kappa_{12} = \kappa_{21} = \kappa_{23} = \kappa_{32}$ is varied from 0 ns^{-1} to 30 ns^{-1}. The common coupling delay time is maintained constant at $\tau = 3.65$ ns. For each time series, we compute the cross-correlation function between pairs of lasers and the lag for which the maximum of this func-

tion appears. The correspoinding results are shown in Figure 8.4. For most of the coupling strength values the three lasers are operated in the chaotic CC regime. Nevertheless, some windows of periodic behavior are also observed for small coupling rates. Interestingly, regardless the dynamics exhibited by the lasers, the perfect synchronization at zero-lag between the extreme units extends to all the coupling values explored. No coupling threshold for the transition from unsynchronized to synchronous motion can be observed for this pair of lasers which achieve the sync state for arbitrarily small couplings. The central laser, on the other hand, varies its correlation coefficient with the outer units from a value of 1 obtained for small couplings and periodic dynamics to a value around ~ 0.8 attained for large strengths where chaotic dynamics develops. From coupling rates $\kappa \gtrsim 6 \text{ ns}^{-1}$ the lag between SL2 and SL1 (or SL3) stabilizes around τ. The fluctuations in the lag value for small coupling strengths can be associated to the high symmetry of the cross-correlation functions that appear for regular dynamics stages.
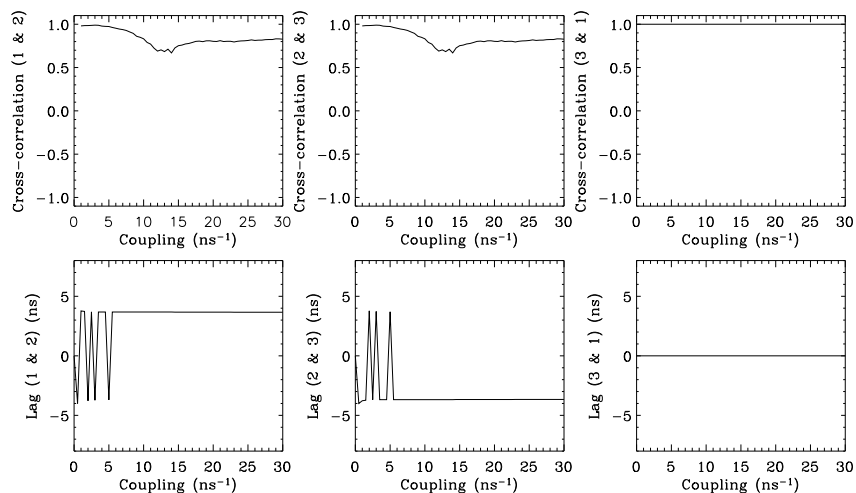
Figure 8.4. Cross-correlation and lag between pairs of SLs as a function of their common coupling strength κ.

The transition from the two-laser problem

To better understand the link from the two-coupled lasers problem to our case with three interacting lasers, we performed the following numerical experiment. Now, instead of symmetrically increasing the coupling strength between the three lasers, we start from a configuration where only SL1 and SL2 are interacting with

a constant coupling strength ($\kappa_{12} = \kappa_{21} = 20$ ns^{-1}). Laser 3 is put into play by continously increasing the coupling rates $\kappa_{23} = \kappa_{32}$ from 0 ns^{-1} to 30 ns^{-1}. In Figure 8.5 we can appreciate the cross-correlation and lag analysis.
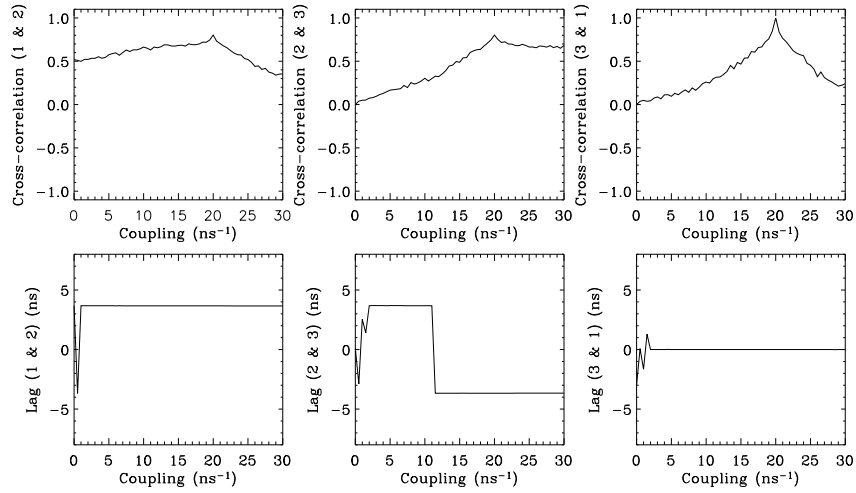
Figure 8.5. Cross-correlation and lag between the pairs of SLs as a function of the coupling strength between SL2 and Sl3 ($\kappa_{23} = \kappa_{32}$).

We observe that the cross-correlation function between the outer lasers grows as the coupling strength is varied up to the value where $\kappa_{23} = \kappa_{32} = 20$ ns^{-1}, for which the degree of sync is maximum. The lag between SL1 and SL3 is again zero for most of the coupling rates investigated. The synchronization quality between any of the extreme lasers and the central one continously grows to exhibit a peak at $\kappa_{23} = \kappa_{32} = 20$ ns^{-1}. After that point, the correlation between SL1 and SL2 starts to decrease, while the sync between lasers2 and 3 is maintained almost constant at a value around ~ 0.7. It is interesting to note that for example at $\kappa_{23} = \kappa_{32} = 30$ ns^{-1}, the interaction between lasers 2 an 3 is stronger than when the coupling is set at $\kappa_{23} = \kappa_{32} = 20$ ns^{-1}, and nevertheless, the sync between these two lasers is better in this last case due to symmetry reasons. Regarding the lag analysis, we observe that for moderate to large coupling values ($\gtrsim 10$ ns^{-1}) both extreme lasers advance the dynamics of the central one by a time τ.

So far we have only considered symmetric mutual interactions between any pair of lasers. This is, for any pair of lasers (n, m) the coupling strength was such that $\kappa_{nm} = \kappa_{mn}$. Keeping this situation, it is clear that the central laser is always receiving more optical injection than the outer ones because it is the only one linked to two lasers simultaneously. To check whether the synchronization solu-

tions we have observed until now are maintained when reversing this situation, i.e., SL2 receiving less optical injection than SL1 and SL3, we perform the following numerical simulations. We fix the coupling strengths from SL2 to the outer lasers at $\kappa_{21} = \kappa_{23} = 20$ ns^{-1}, and scan the input coupling of SL2 from $\kappa_{12} = \kappa_{32} = 0$ ns^{-1} up to 30 ns^{-1}. The correlation analysis is presented in Figure 8.6.
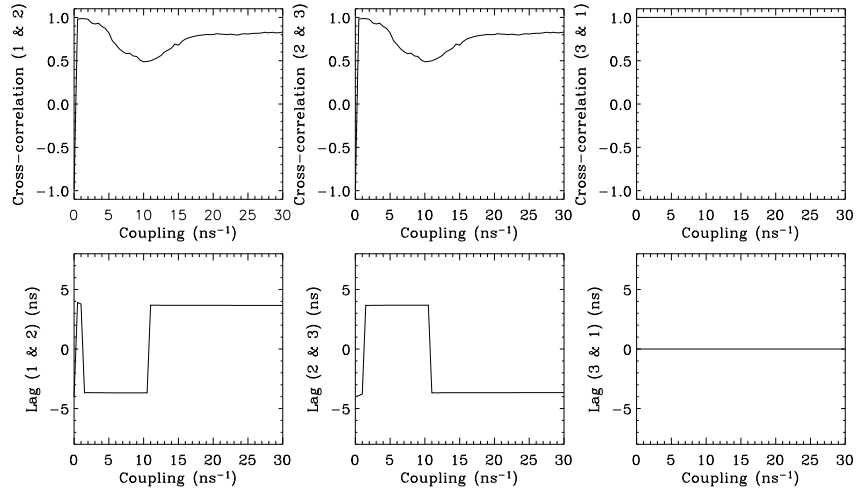
Figure 8.6. Cross-correlation and lag between the pairs of SLs as a function of the central laser input strength ($\kappa_{12} = \kappa_{32}$).

Under these conditions the synchronization between the extreme lasers at zero-lag is still a compatible state of the system Eqs. (8.1)-(8.6), and it appears to be stable in all the range of coupling strengths investigated. Regarding the leader-laggard role between any of the extreme lasers and the central one, there is a clear change of tendency occurring at $\kappa_{12} = \kappa_{32} \sim 10$ ns^{-1}. We first analyze the case for coupling strengths below such a critical rate. There, the cross-correlation function between any of the extreme lasers and SL2 typically shows two peaks at $\pm\tau$. However, in such functions the peak associated to the situation in which the central laser advances the extreme ones is only a little bit higher than the other peak which is related to the opposite situation. Since the difference between the two peaks is very small, it is difficult then to speak about a leader-laggard dynamics. On the contrary, for coupling strengths above ~ 10 ns^{-1}, the difference between peaks is now much larger than in the previous case, and hence indicates a clearly defined leader-laggard dynamics. For this large coupling regime, the dynamics of the extreme lasers is always found to advance the central one by an injection delay time τ.

8.2.2   Robustness of the synchronization solution

Natural detuning

The ability exhibited by a set oscillators to synchronize is strongly dependent on how far their natural frequencies are. This characteristic naturally leads to the concept of Arnold tongue, which has been already studied in Chapter 6 for optoelectronically-interacting lasers. Moreover, the role of a moderate detuning between the free-running optical frequencies of two coherently-coupled edge-emitting lasers has been found to establish a leader-laggard role, with the high-frequency laser advancing the dynamics of its counterpart [10, 12]. Since a small detuning is almost unavoidable in real experiments, we have strong motivations to investigate here what the effects of a small detuning between the different lasers in our open-end scheme are.

We first recover the standard coupling conditions by setting all the coupling constants at $\kappa = \kappa_{12} = \kappa_{21} = \kappa_{23} = \kappa_{32} = 20$ ns^{-1}, and the delay times at $\tau = \tau_{12} = \tau_{21} = \tau_{23} = \tau_{32} = 3.65$ ns.

We start with the case where the outer lasers share a common solitary frequency ($\Delta\omega_1 = \Delta\omega_3 = 0$) and we only allow for a detuning with respect to the central laser ($\Delta\omega_2 \neq 0$). The central laser frequency detuning is scanned from -22.5 GHz up to 22.5 GHz in Figure 8.7. The graphics show that the zero-lag synchronization between SL1 and SL3 is perfectly maintained in all the range of values considered for the detuning. In most cases, both extreme lasers advance the dynamics of the central one and only for very high positive detunings this lag changes its sign. However, looking in more detail at this hypothetical reversal of the leader-laggard role we must notice that it occurs for a value of the detuning where the synchronization between the central and extreme lasers is almost lost (at $\Delta\omega_2 = 18$ GHz the maximum of correlation is ~ 0.2). In fact, around $\pm\tau$ the cross-correlation function also presents two negative peaks reaching the value of ~ -0.5, and hence, indicating that actually an anticorrelated dynamics between the central and the outer lasers is taking place. The observation of this antisynchronization regime can be related to the properties of a laser injected by a field largely detuned from its cavity resonance. The key point is that this type of injection produces an incoherent interaction where the injecting field suppresses the gain function of the laser by consuming carriers that cannot be devoted to its own lasing action. Thus, a fluctuation in the amplitude of the injecting field is associated with a variation of the laser power with an opposite sign.

If a detuning occurs between the extreme units ($\Delta\omega_1 - \Delta\omega_3 \neq 0$), we have numerically checked that the qualitative features of the solution obtained for the perfectly symmetric case are preserved to some extend. The robustness of the isochronal sync between SL1 and SL3 is observed to amount to a few Gigahertz
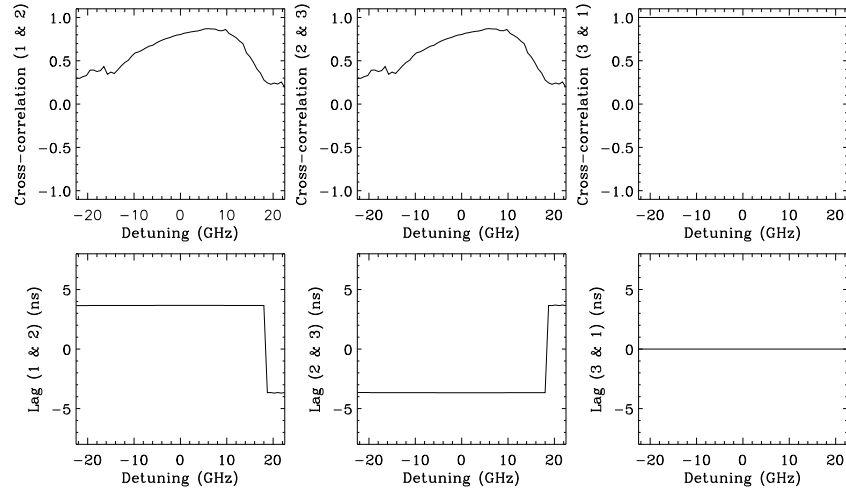
Figure 8.7. Cross-correlation and lag between the pairs of SLs as a function of the central laser frequency deviation, $\Delta\omega_2$.

(see Figure 8.8). The relative dynamics, i.e., the leader-laggard role, between the three lasers outside the zero-detuning point becomes difficult to interpret since the correlation coefficient drops very fast down to zero.
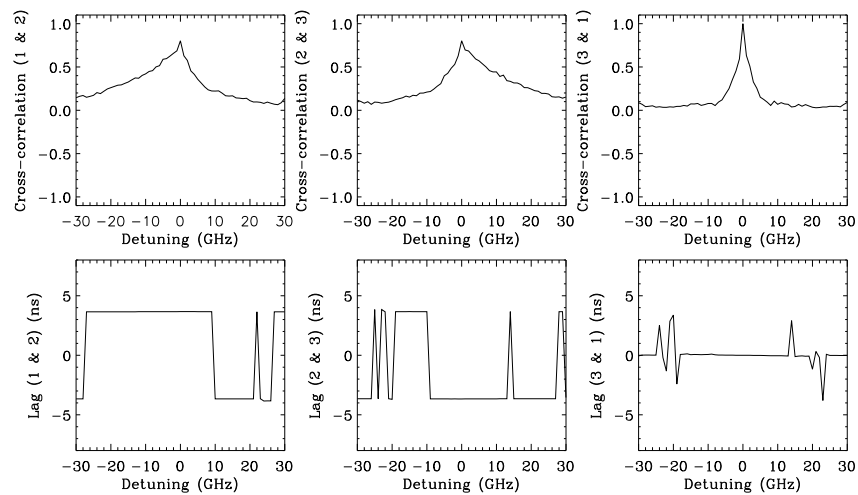
Figure 8.8. Cross-correlation and lag between the pairs of SLs as a function of the detuning between the extreme lasers ($\Delta\omega_1 - \Delta\omega_3$).

Pumping mismatch

Even if the electrical current injected into the active layer of a semiconductor laser can be very well controlled at the experimental level, it is still very interesting to check the stability of the synchronization solution upon current mismatches between the coupled lasers. Moreover, different dynamical regimes and synchronization characteristics only appear at certain injection current rates. For this reasons in this section we evaluate the effect of considering different pumping levels for each laser and we check the robustness of the synchronization solution. As in the previous study of the detuning effect, the coupling strengths are fixed at $\kappa_{12} = \kappa_{21} = \kappa_{23} = \kappa_{32} = 20$ ns^{-1}, and the delay times at $\tau_{12} = \tau_{21} = \tau_{23} = \tau_{32} = 3.65$ ns.

We first proceed by varying the bias current of the central laser I_2 from 17.5 mA to 37.5 mA, while keeping the extreme laser pumps constant at $I_1 = I_3 = 27.5$ mA. As we observe from Figure 8.9 the only effect of increasing I_2 is to monotonically decrease the synchronization level between the extreme lasers and the central one. However, the degradation of the sync quality is not severe and the correlation coefficient only decreases from almost 1 down to ~ 0.7 when varying the pump current of the central laser by more than 20 mA. It is worth noting that the maximum of the correlation between SL2 and SL1 or SL3, is not attained in the symmetric configuration where all three lasers are operating at 27.5 mA but at pump levels of the central laser close to the threshold. These results together Figure 8.4 are indicative of the very low optical power that is needed to bring the outer elements SL1 and SL3 into synchrony.

Regarding the timing of the synchronized solutions it is observed that the lags at which the maxima of the cross-correlation functions appear do not shift with the pump level.

One can also consider pump mismatches between the lasers occupying the extreme positions, i.e., SL1 and SL3. We observe how the effects on the synchronization are much more severe now. The results are summarized in Figure 8.10 where the bias current of SL3 is scanned from 17.5 mA to 37.5 mA. The levels of SL1 and SL2 are fixed to 27.5 mA. In this case the sync between the outer lasers is only maintained for a range a few miliamperes wide. For small pump deviations, series of bursts of desynchronization perturb the generalized synchronization solution between SL1 and SL3.

Pulse propagation

In the former subsections we have demonstrated that the synchronization between the extreme lasers is only moderately robust against a mismatch between them. On the other hand, the effect of mismatches between the central laser and the extreme
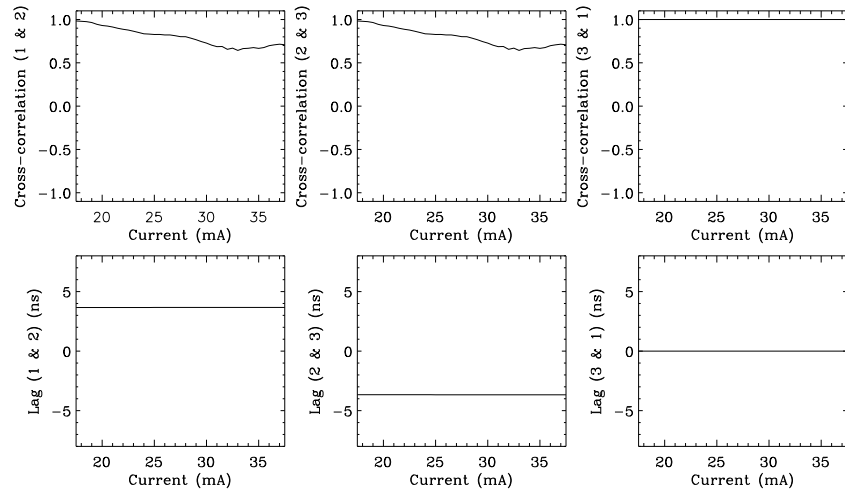
Figure 8.9. Cross-correlation and lag between the pairs of SLs as a function of the current level of the central laser.
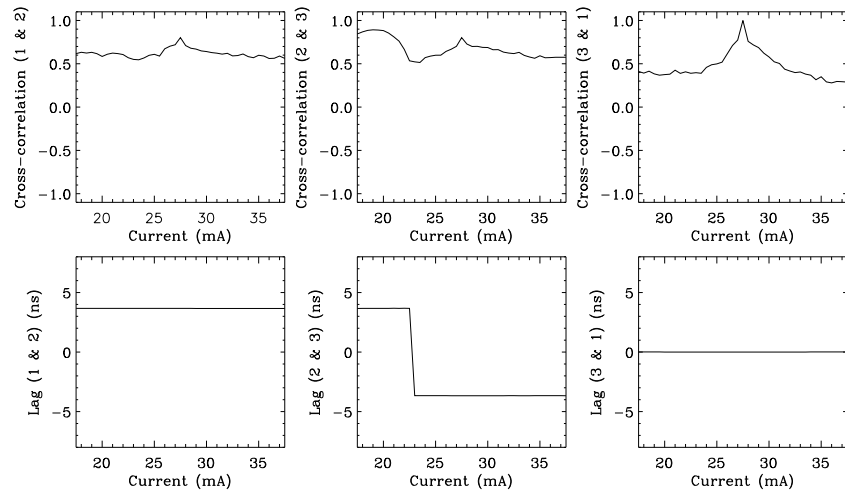
Figure 8.10. Cross-correlation and lag between the pairs of SLs as a function of the current level of laser 3.

units turned out to be hardly significant and the synchronization between SL1 and SL3 was found to be extremely robust upon changes in the parameters of central laser.

These results have been obtained under the conditions of stationary mismatches, i.e., once the differences in the natural frequencies or pumping levels were set they were kept constant along the temporal evolution of the lasers. Here, we investigate the effects of a dynamical perturbation on the synchronization pattern that we have previously reported. In particular, we generate a pulse of current in one of the lasers and study how this perturbation propagates in the system and affects the synchronization solutions.

Within the standard and symmetrical coupling conditions, we start by generating in the central laser a current pulse of Gaussian profile with amplitude 10 mA and full width at half maximum (FWHM) of 1.2 ns. The time series of the three lasers, the pulse profile, and the synchronization error and sync plot for SL1 and SL3 are all collected in Figure 8.11. The synchronization solution between the extreme lasers is perfectly maintained, even at the moment in which the perturbation reaches the lasers SL1 and SL3, one coupling time after the pulse was generated. We see then that the perturbation remains completely unnoticed from the synchronization point of view.
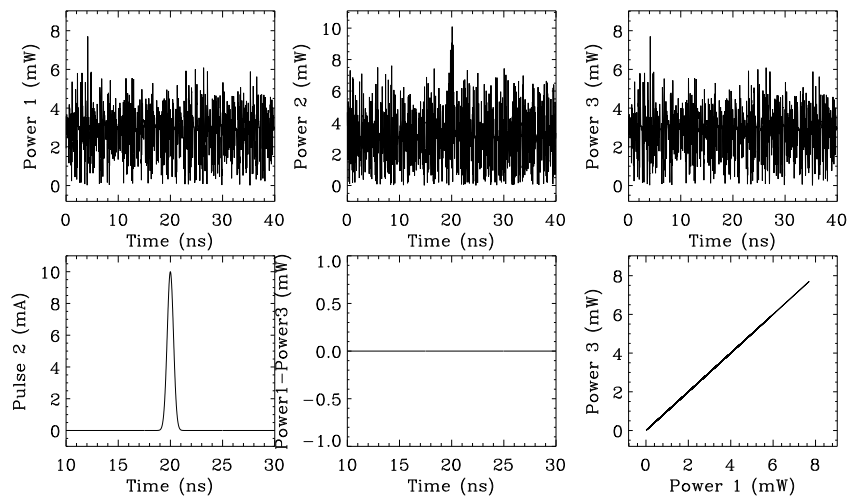
Figure 8.11. Top: temporal traces of the optical power of the three lasers. Bottom: pulse waveform, sync error and sync plot between lasers 1 and 3.

If the same pulse is now generated in one of the lasers occupying the extreme positions, Figure 8.12 clearly shows that the sync error between lasers 1 and 3

becomes different from zero only during the pulse generation. This means that immediately after the perturbation on SL1 ends, even still traveling through the system, it has no more effects on the synchronization solution. This result strongly suggests that once the perturbation reaches the central laser, it is symmetrically distributed toward SL1 and SL3. Otherwise, replicas of the original disturbance in the synchronization error would be expected for time 2τ and multiples of it, after the pulse generation.
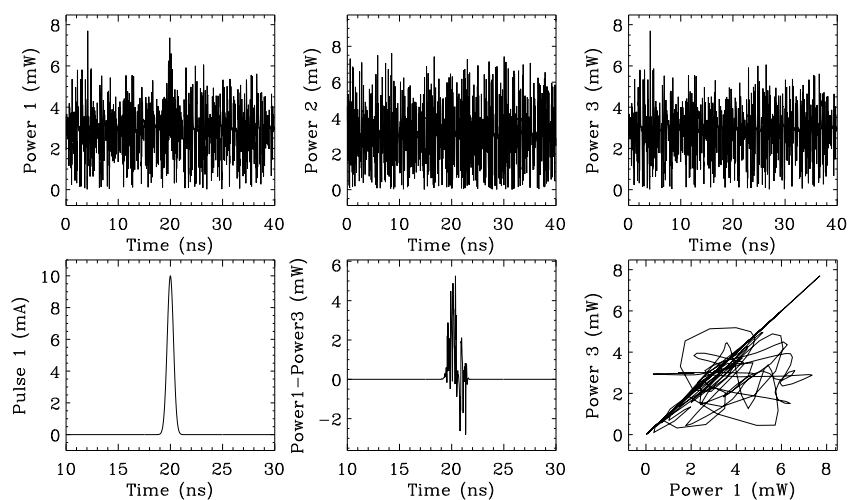
Figure 8.12. Top: temporal traces of the optical power of the three lasers. Bottom: pulse waveform, sync error and sync plot between lasers 1 and 3.

In cases where the amplitude of the pulses was increased up to 50 mA (note that this value is almost double than the bias current level) or the width of the pulse enlarged up to 12 ns (a value much larger than the coupling delay time), the same phenomena were found. Hence, the sync between lasers is proven to be quite stable under dynamical perturbations pushing away the solution from the synchronization manifold.

8.2.3   Synchronization for asymmetric coupling times

So far, we have taken both branches of the network module in Figure 8.1 to be identical and to give rise to the same coupling times. But, will synchronization exist and be stable if different lengths for the paths between lasers are considered?

To test this interesting scenario we set the coupling delay times in both branches to be very different. We choose $\tau_a = \tau_{12} = \tau_{21} = 12$ ns and

$\tau_b = \tau_{23} = \tau_{32} = 3$ ns. For moderate coupling strengths, now the synchronization between SL1 and SL3 appears when comparing $P_1(t)$ with $P_3(t + \Delta\tau)$, where $\Delta\tau = \tau_b - \tau_a$. This is, the outer laser of the shortest branch (in this case SL3) is able to advance the behavior of the other one (SL1), which is more than 15 ns apart, by the difference of coupling times.

As we have done before the stability of this solution can be checked by subjecting the central laser to a given perturbation. A Gaussian pulse of current is again chosen to test the robustness of the solution. Figure 8.13 shows the temporal traces of the three lasers, the pulse generated in SL2, and the synchronization error and sync plot between SL1 and SL3 once the corresponding shift ($\Delta\tau = \tau_b - \tau_a$) has been compensated for. The temporal traces already demonstrate the timing of the synchronization solutions, where SL3 clearly advances the behavior of SL1. The synchronization plots show that within our numerical precision the lagged synchronization here attained is a perfect solution, not even affected by a perturbation in the element mediating the synchronization.
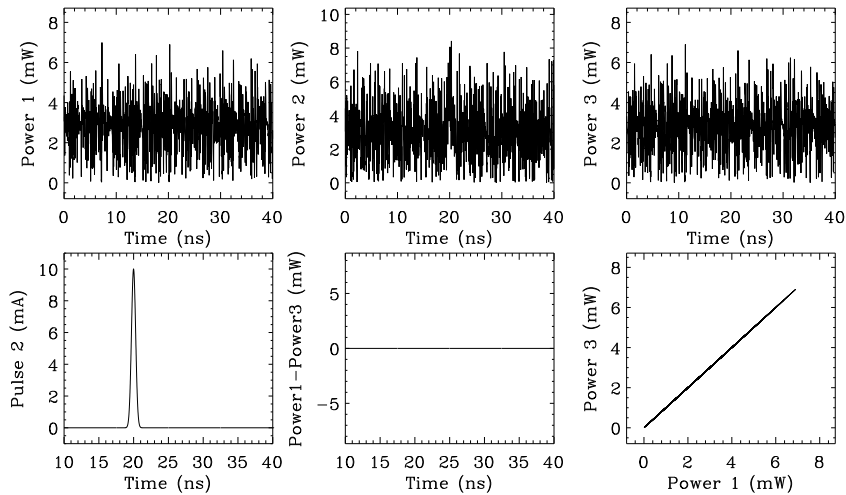
Figure 8.13. Top: temporal traces of the optical power of the three lasers. Bottom: pulse waveform, sync error and sync plot between lasers 1 and 3. $\tau_a = \tau_{12} = \tau_{21} = 12$ ns and $\tau_b = \tau_{23} = \tau_{32} = 3$ ns. The coupling strength is fixed to $\kappa = 20$ ns^{-1}.

Other sets of values for the coupling times have been tested (such as $\tau_a = \tau_{12} = \tau_{21} = 5$ ns and $\tau_b = \tau_{23} = \tau_{32} = 0.2$ ns) and in all cases a synchronization solution with lag $\tau_b - \tau_a$ have been obtained between SL1 and SL3. Note that in the later case, without the presence of a third laser the pairs of mutually-coupled lasers $(1, 2)$ and $(2, 3)$ would exhibit very different dynamics due to the disparity in the coupling times. Nevertheless, when all three are coupled lasers 1 and 3 are

able to perfectly synchronize.

In general, the cross-correlation function between pairs of lasers shows several peaks related to the delay times and their differences. Figure 8.14 contains the cross-correlation function for the three pairs of lasers $(1, 2)$, $(2, 3)$, and $(3, 1)$ when $\tau_a = 1.5$ ns and $\tau_b = 3.6$ ns. Different delay values have been simulated and in all cases the main peaks of the cross-correlation functions appeared at the lags: $(\tau_a, -\tau_a, 2\tau_b - \tau_a)$ for the pair of lasers $(1, 2)$, $(\tau_b, -\tau_b, \tau_b - 2\tau_a)$ for the lasers $(2, 3)$, and $(\tau_b - \tau_a)$ for the pair composed of the extreme lasers 3 and 1.
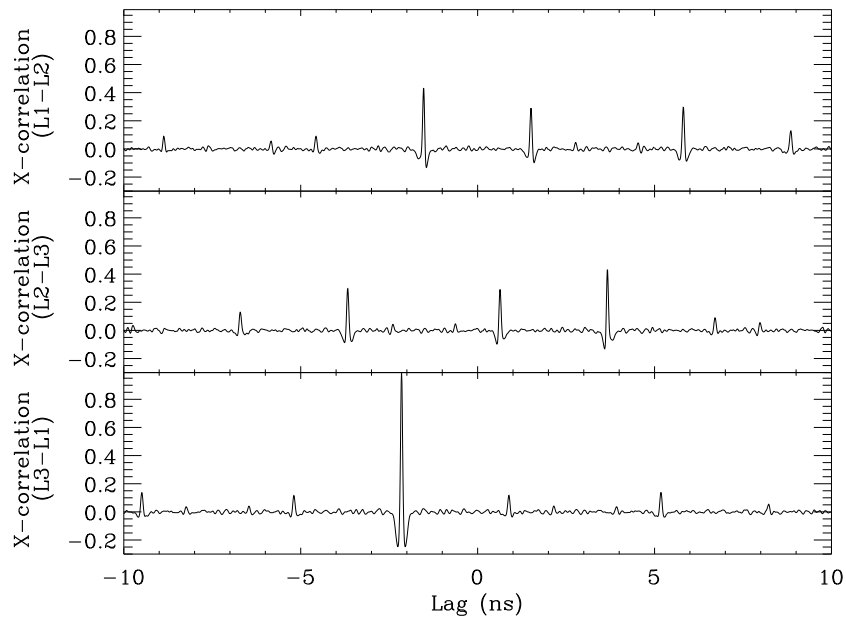
Figure 8.14. Cross-correlation functions between pairs of lasers with different coupling times. $\tau_a = 1.5$ ns and $\tau_b = 3.6$ ns. The coupling strength is fixed to $\kappa = 20$ ns^{-1}.

8.2.4   Synchronization of semiconductor lasers with feedback

In the previous sections we have approached the study of the entrainment properties of three mutually-coupled semiconductor lasers in a linear array. We must notice that before coupling them the stand-alone lasers emit CW optical power. To see whether synchronization occurs when each laser develops its own dynamics, we consider in this section the situation where at least the outer lasers in the array produce their own instabilities before being coupled.

To this end, we add an optical feedback loop to SL1 and SL3 and fix the feed-

back strength and delay times to values for which these lasers enter into a chaotic dynamics when uncoupled, known as Low Frequency Fluctuations (LFF). We reach this regime by setting the bias current very close to the threshold $I = 17.5$ mA, the feedback strength to 10 ns^{-1}, and the feedback delay time to 3.4 ns. Before switching on the coupling, both extreme lasers oscillate chaotically in the LFF regime, but their traces are completely uncorrelated. After activating the mutual interactions ($\kappa_{12} = \kappa_{21} = \kappa_{23} = \kappa_{32} = 20$ ns^{-1} and $\tau_{12} = \tau_{21} = \tau_{23} = \tau_{32} = 3.65$ ns), the LFF dynamics of both lasers exhibit a very good synchronization at zero-lag. Figure 8.15 shows the temporal traces and the cross-correlation functions between the three lasers after being coupled. The lags of the synchronization solutions, and consequently the leader-laggard roles between the lasers, are in general similar to those obtained without feedback. However, we should notice an important difference with the former case. In the presence of feedback there exists a finite coupling strength below which the dynamics of the extreme laser cannot synchronize. The value of this threshold is found to be very sensitive to the strength of the feedback, the feedback round-trip time, and the bias current.
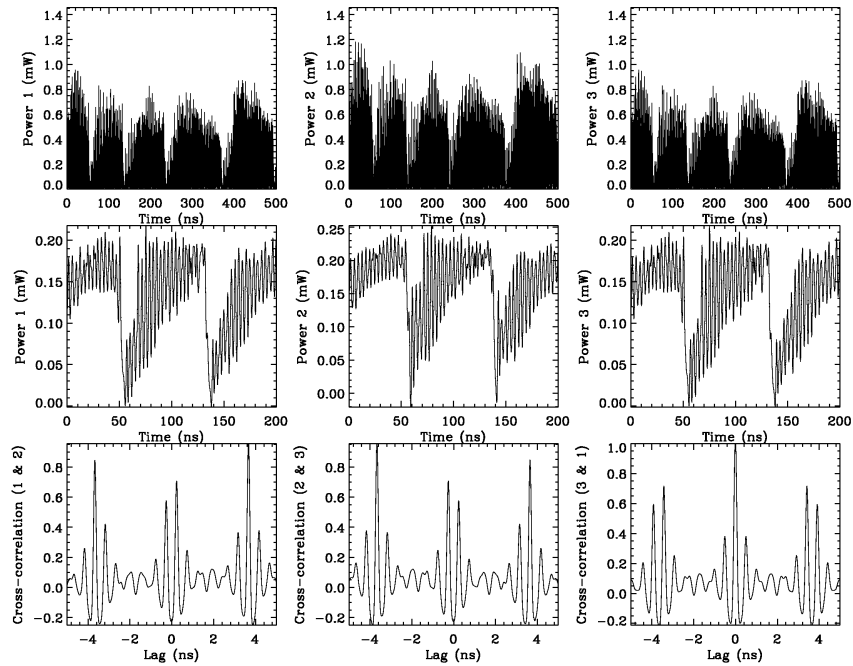
Figure 8.15. Top: temporal traces. Middle: zoomed-in filtered temporal traces. Bottom: cross-correlation function of the three lasers scheme. Lasers 1 and 3 subject to moderate feedback, $\kappa_f = 10$ ns^{-1} and $\tau_f = 3.4$ ns. The bias of all three lasers is set to $I = 17.5$ mA.

8.3 The role of network on the synchronization properties

The profound qualitative changes observed when comparing the synchronization properties between two and three mutually-coupled lasers, strongly suggest us to proceed our investigation by including a larger number of lasers in the array. The main goal here is to answer the question of how the synchronization characteristics depend on the number of lasers and the network of connections in a system with delayed interactions? Two different topologies are considered for such a study, namely the open-end array and the ring configuration.

8.3.1 Open-end arrays

In the following, we present our results concerning the synchronization patterns across the elements of an open-end array composed of four, five, and six semiconductor lasers. In all cases, the coupling strength between neighbor lasers is fixed to $\kappa_{nm} = \kappa_{mn} = 20$ ns^{-1} except for the six lasers setup where the strength is increased up to 40 ns^{-1}. In this case, we observed that a higher coupling is required in order to excite instabilities in the system and study synchronization phenomena. The coupling times between adjacent lasers are adjusted to $\tau_{nm} = \tau_{mn} = 3.65$ ns for all the configurations and the current bias is set to $I = 17.5$ mA. Under such conditions once coupled the lasers develop a chaotic LFF dynamics. Figures [8.16-8.18] contain the temporal traces and cross-correlation analysis for all pairs of lasers in the case of 4, 5, or 6 semiconductor lasers, respectively. For conceptual convenience we discuss the results for different number of units altogether.

The correlation functions clearly indicate that zero-lag synchronization appears between second-neighbor lasers in the array, i.e., between pairs of lasers occupying positions m-th and $m + 2$-th. Moreover, the cross-correlation analysis also reveals that adjacent neighbors exhibit a high degree of similarity once the temporal series of one laser is shifted forward or backwards a coupling time τ.

Thus, in the open-end scheme we find that the lasers isochronously synchronize within two clusters; one group is defined by the lasers placed in the odd positions of the linear array (SL$_1$, SL$_3$, SL$_5$, $\cdots$) while the other assemble is composed by the lasers located at even positions (SL$_2$, SL$_4$, SL$_6$, $\cdots$). Any pair of lasers belonging to different clusters exhibits achronal generalized synchronization and its cross-correlation function displays two peaks at $\pm\tau$, as in the original two-laser problem. It is also noticeable by the asymmetry of some cross-correlation functions that the lasers occupying the outer positions of the array advance the dynamics of their inner neighbors. Numerical simulations with different initial conditions support the generality of these results for arrays of different lengths.
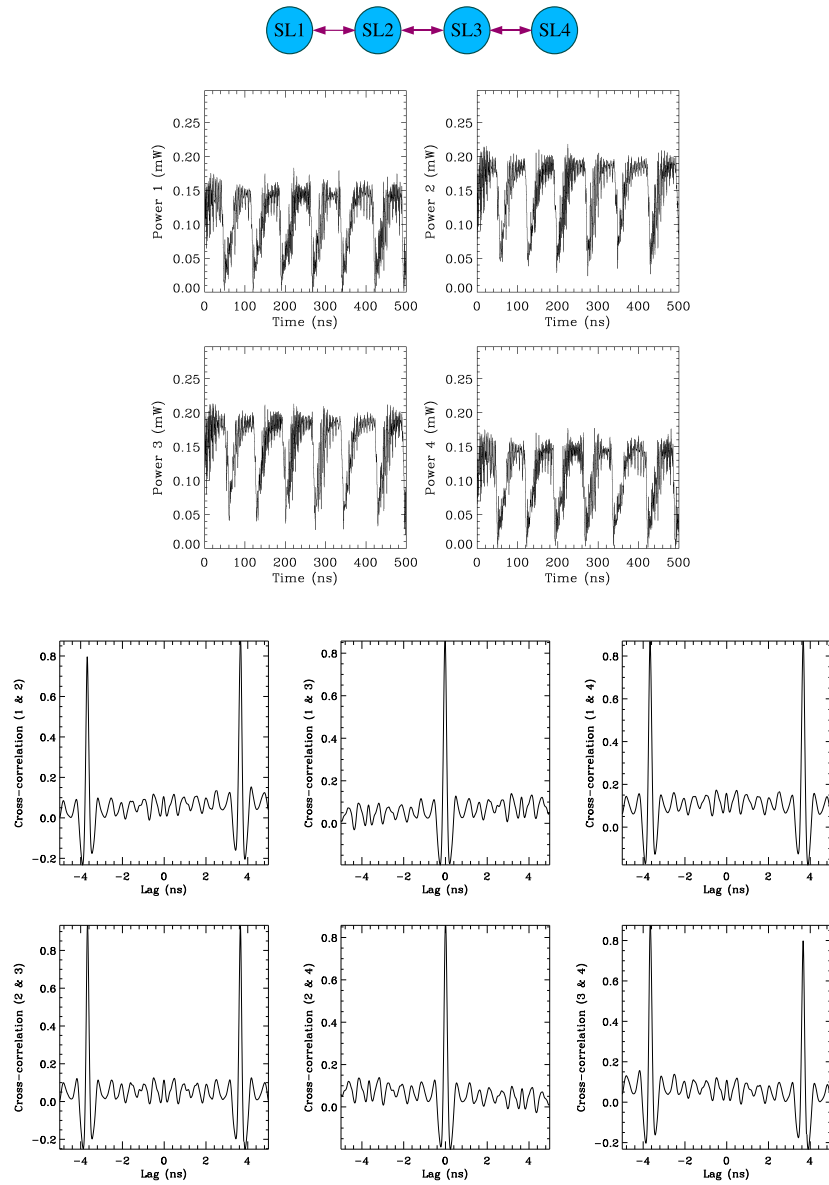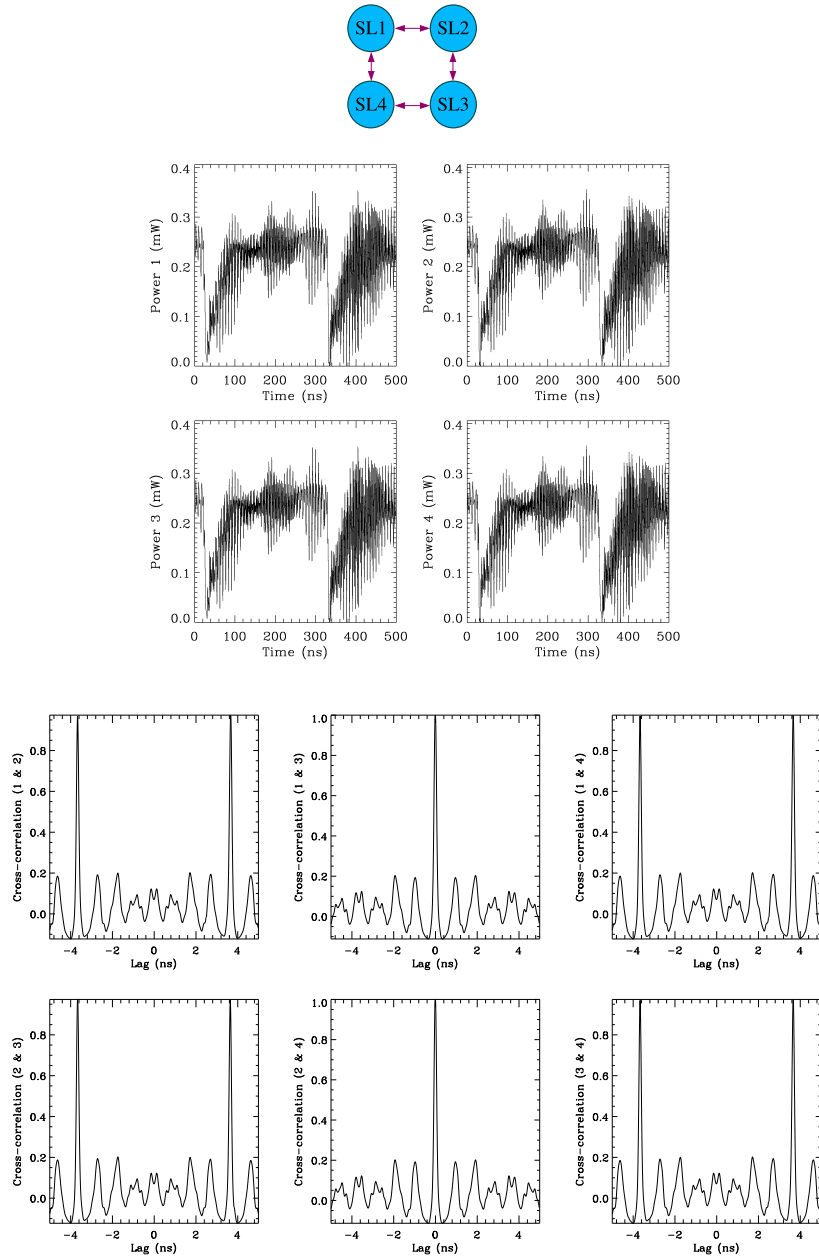
Figure 8.16. Synchronization in a 4-lasers open-end array. Top: Lasers configuration; Middle: temporal traces; Bottom: Cross-correlation functions.
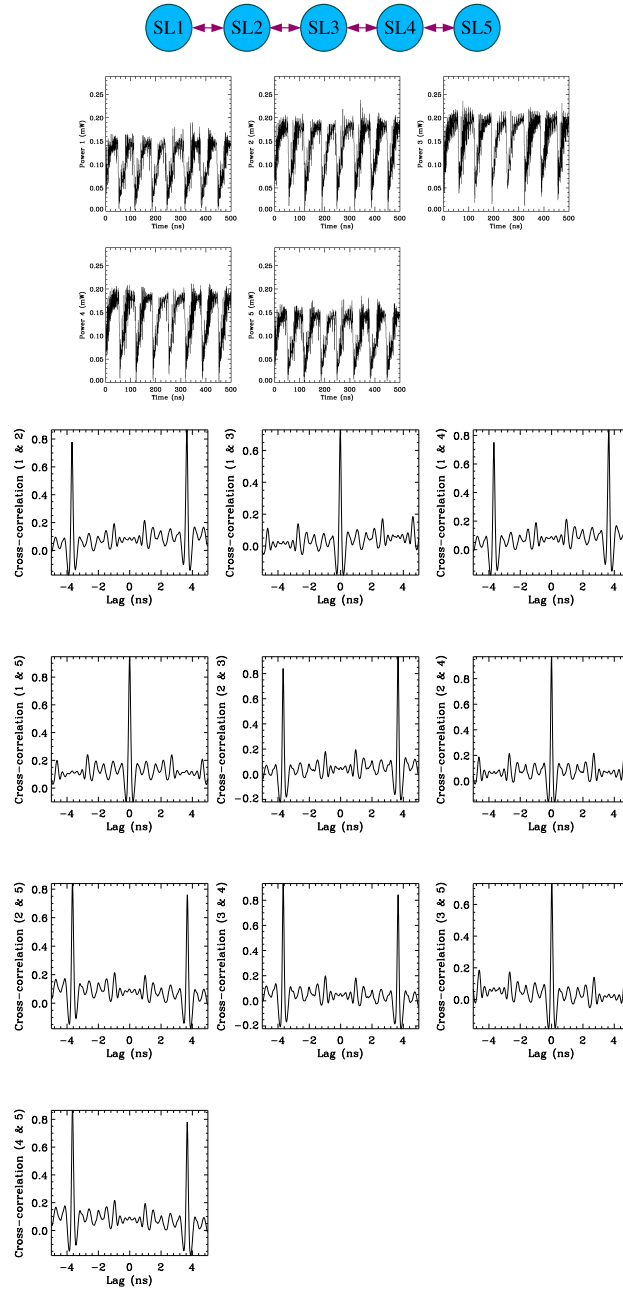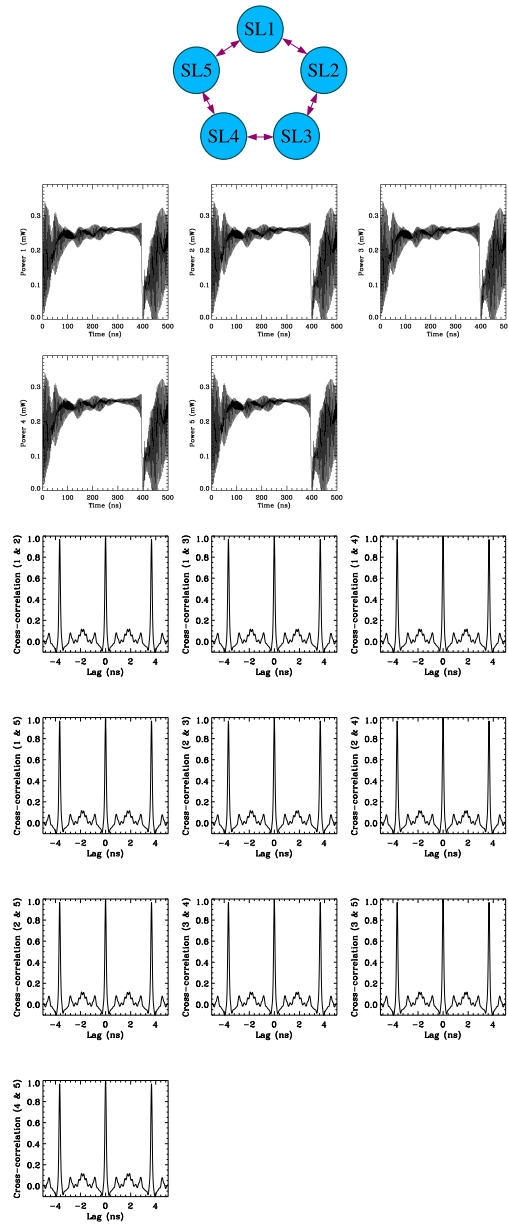
Figure 8.17. Synchronization in a 5-lasers open-end array. Top: Lasers configuration; Middle: temporal traces; Bottom: Cross-correlation functions.
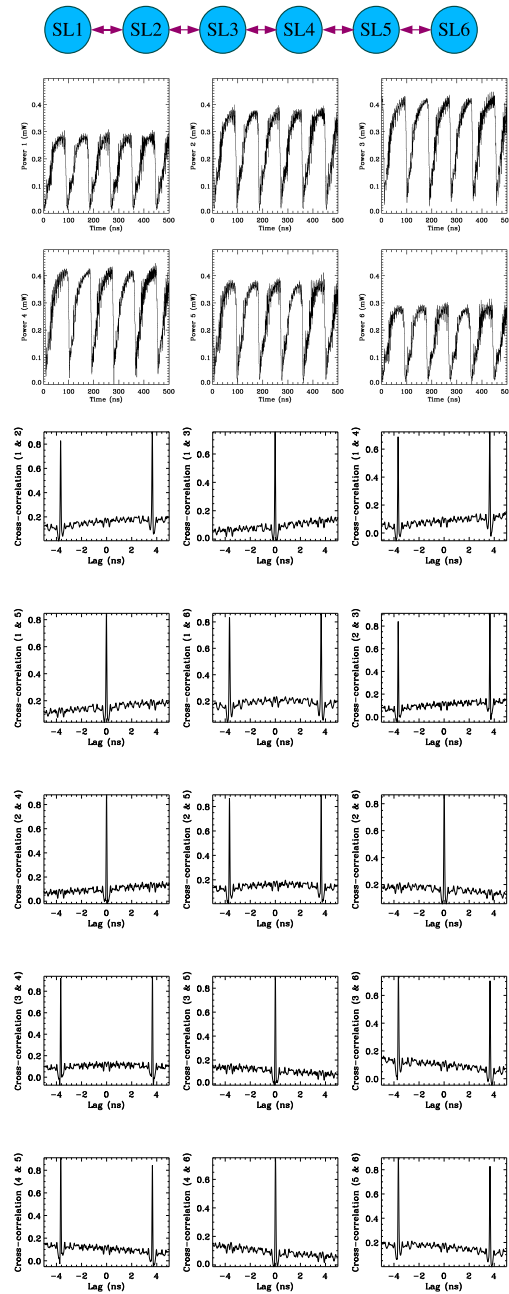
Figure 8.18. Synchronization in a 6-lasers open-end array. Top: Lasers configuration; Middle: temporal traces; Bottom: Cross-correlation functions.

8.3.2 Ring networks

Another important network motif is the ring structure. When the lasers are arranged in such a circular array configuration (for instance in the case of three lasers by adding a new link between SL1 and SL3) the synchronization solutions radically change. Hereafter, we establish the mutual coupling strengths between neighbor lasers to be 20 ns^{-1}, while coupling times are all equally set to 3.65 ns. Rings formed by 3, 4, 5 and 6 semiconductor lasers developing LFF dynamics are explicitly investigated under this section.

Figure 8.19 shows that the interaction between three mutually-coupled units in a ring can consistently lead to an isochronous synchronization state of all three elements. It is remarkable that even in the presence of delays in the communication between the synchronizing units, the mutual interaction is able to self-organize the dynamics into an isochronous state.

Figures [8.19-8.22] suggest that when the ring is composed by an odd number of lasers, zero-lag synchronization appears between all the elements of the network. However, for rings with an even number of lasers the situation is similar to the open-end scheme, i.e., lasers isochronously synchronize within two clusters formed by the lasers occupying alternating positions in the structure. In this case, it is also noticed that any pair of lasers belonging to different clusters exhibit achronal synchronization.

In summary, these results strongly suggest that a kind of anti-correlation or repulsive interaction (over a delay time temporal scale) between nearest neighbor lasers can explain all the synchronization patterns found across the network elements for both the open-end and ring configurations.

For the open-end arrays, this type of repulsive interaction would naturally lead to zero-lag synchronization between alternating lasers in the array and consequently, for arrays with an odd number of units to the the zero-lag sync between the extreme lasers.

On the other hand, for the ring network the lasers isochronously synchronize within one or two different clusters depending on whether the number of units is odd or even, respectively. Here, it seems that the repulsive interaction leads to an achronal synchronization between nearest neighbor lasers unless a frustration phenomenon occurs (for an odd number of elements the achronal solution cannot be consistently fulfilled) and then an isochronous solution is maintained across the ring.

8.3.3 The symmetry connection

In many examples the qualitative dynamics of systems with very different origins are found to be identical. The ubiquity of these model-independent behaviors can
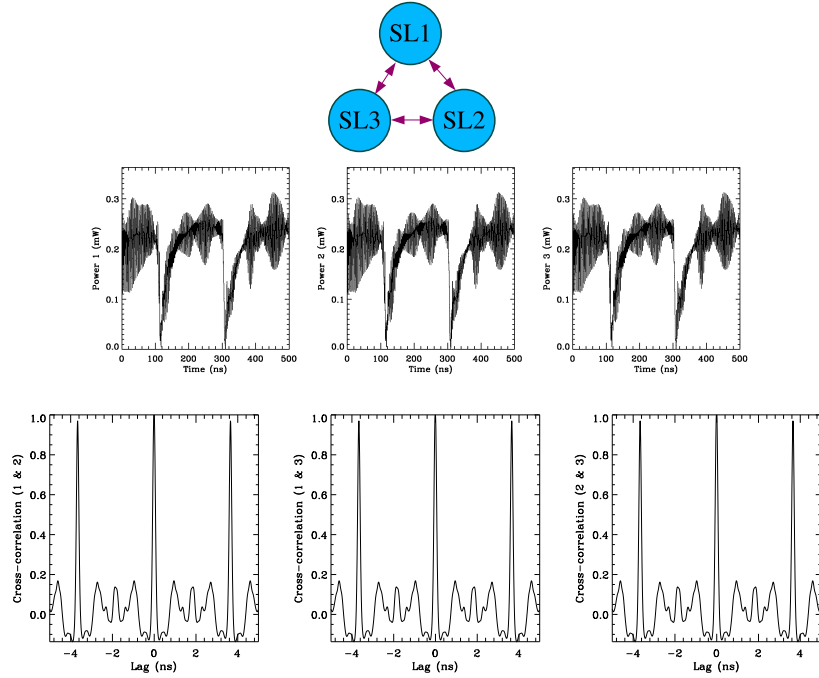
Figure 8.19. Synchronization in a 3-lasers ring network. Top: Lasers configuration; Middle: temporal traces; Bottom: Cross-correlation functions.

be often understood within a single framework provided by the symmetries of the system. This is also the case for our networks of lasers. Numerical simulations of Ikeda oscillators or even realistic neuronal models have also reproduced the synchronization solutions that we have just reported above, and thus they have enhanced the importance of the network properties over the details of the oscillator model. This section is developed to understand the patterns of synchronization solutions that we have presented before in terms of the symmetries of the system. The main novelty of this case compared to standard analysis in the equivariant theory of systems (the study of bifurcations of dynamical systems possesing some symmetry), is the addition of a new ingredient into the dynamics: the delay time.

Next, we analyze the interplay between symmetries and delay in conforming the catalogue of typical forms of behavior of our system and in particular the synchronization solutions. Based on numerical simulations and other arguments we conjecture here a connection between the synchronization solutions (possibly chaotic) found across a delay-coupled network and the patterns of oscillation of time-periodic solutions.

To illustrate these concepts we explicitly analyze here a unidirectional and a bidirectional ring of three semiconductor lasers. It is important to recall that the

Figure 8.20. Synchronization in a 4-lasers ring network. Top: Lasers configuration; Middle: temporal traces; Bottom: Cross-correlation functions.

Figure 8.21. Synchronization in a 5-lasers ring network. Top: Lasers configuration; Middle: temporal traces; Bottom: Cross-correlation functions.
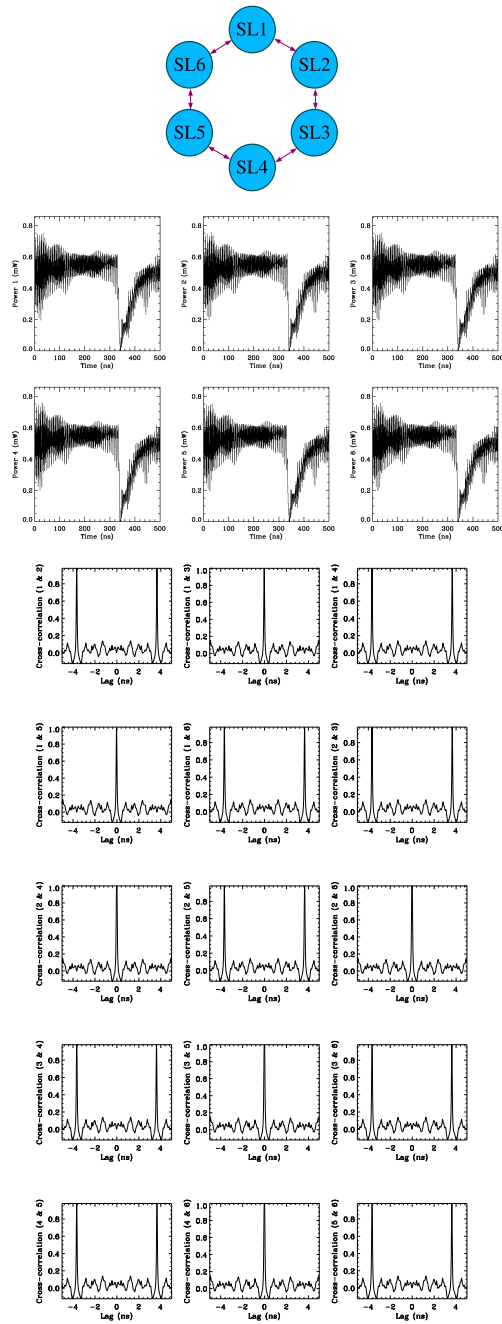
Figure 8.22. Synchronization in a 6-lasers ring network. Top: Lasers configuration; Middle: temporal traces; Bottom: Cross-correlation functions.

symmetry of a unidirectional ring with N elements is the cyclic group of order N $\mathbb{Z}_N$, i.e., the structure is preserved under rotations only, while a bidirectional architecture is invariant under the dihedral group $\mathbb{D}_N$, which has an order equal to $2N$ and describes the preservation of a regular N-gon under rotations and reflections in the plane.

Figure 8.23 and Figure 8.19 show the typical dynamics and correlation analysis under standard coupling conditions for the unidirectional and the bidirectional ring of lasers, respectively. As previously stated, the bidirectional network exhibits a complete isochronous synchronization between all three lasers, i.e., $P_1(t) = P_2(t) = P_3(t)$, $\forall t$. Moreover, the time series and correlation diagrams of such configuration indicate a very strong periodicity of the optical power of each laser with a period $\sim \tau$.

The unidirectional arrangement of identical lasers, however, offers another sync solution. From the cross-correlation graphs it can be inferred that in the unidirectional case each laser SL-(j) is advancing the dynamics of its neighbor SL-$(j+1)$ (where j is taken modulo 3). Thus, SL1 seems to advance the dynamics of SL2 by a coupling time, and SL2 advances SL3 by the same quantity, as well as SL3 is also advancing its neighbor SL1 by τ, and so on. Of course, such a circular process cannot continue indefinitely unless such dynamics is strictly periodic. What we observe is that even if the dynamics of the lasers is clearly chaotic there is a marked periodicity amounting to 3τ, i.e., the complete round-trip time along the ring, in the temporal traces of all three lasers so that $P_1(t) \approx P_2(t+\tau) \approx P_3(t+2\tau) \approx P_1(t+3\tau), \cdots$.

In general, the state variable $x(t)$ of a delay-differential equation representing the coupling of several units shows a strong correlation with its delayed value $x(t - m\tau)$, for some integer m. If the coupling strength is large enough such a high auto-correlation can make the solution to inherit some properties of periodicity even if the solution is still chaotic. Our main result here is that we find that the chaotic synchronization motifs observed in our laser network and with other type of oscillators can be always associated to a particular pattern of time-periodic solutions in the array.

In the same sense that the isotropy lattice of a symmetry group is a hierarchical tree of subgroups that order the possible symmetry-breakings of steady-states, there exists a similar arrangement that predicts the types of periodic solutions that can appear in a given network of coupled systems. In order to proceed with our analysis we must introduce here some concepts on the spatio-temporal symmetries of periodic solutions.

The symmetries of a time-periodic solution ($x(t+T) = x(t)$, $\forall t$) of a system of equations invariant under a symmetry group (Γ) can be divided into spatial symmetries ($K = \{\gamma \in \Gamma \mid \gamma x(t) = x(t), \ \forall t\}$) and spatio-temporal symmetries
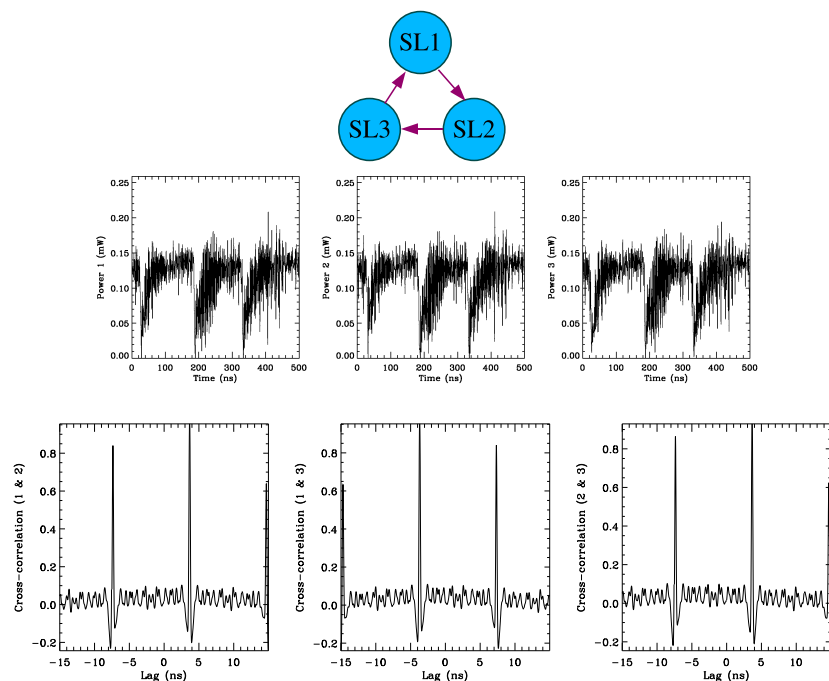
Figure 8.23. Synchronization in an unidirectional 3-lasers ring network. Top: Lasers config-
uration; Middle: temporal traces; Bottom: Cross-correlation functions.

($H = \{\gamma \in \Gamma \mid \gamma\{x(t)\} = \{x(t)\}\}$). This is, the spatial symmetries are those
operations that leave invariant the state of the system for all times, while the spatio-
temporal symmetries only preserve the trajectories. Results from representation
group theory assure us that the only possible periodic solutions appearing in a
coupled system are basically those for which the quotient group H/K is cyclic
[67].

Thus, we can now guarantee that the only possible periodic solutions of our
unidirectional ring composed by three lasers (with symmetry group $\mathbb{Z}_3$) are given
by the patterns $(P_1(t), P_2(t), P_3(t))$ collected in Table 8.1, where T is the period
of the oscillations.

H	K	Pattern of oscillation
$\mathbb{Z}_3$	$\mathbb{Z}_3$	$(P(t), P(t), P(t))$
$\mathbb{Z}_3$	$\mathbb{I}$	$(P(t), P(t + T/3), P(t + 2T/3))$
$\mathbb{I}$	$\mathbb{I}$	$(P(t), Q(t), R(t))$

Table 8.1: Patterns of oscillations in three laser unidirectional rings.

For our standard coupling conditions, the observed chaotic synchronization solution (Figure 8.23) of three lasers corresponds to the second pattern of oscillation where T is assimilated to 3τ. Such a solution is also called a discrete rotating wave since all three units oscillate with the same waveform but with a phase shift and consequently such an oscillation it is observed to propagate along the ring.

The bidirectional coupling of three units in a ring configuration exhibits a symmetry group $\mathbb{D}_3$ with possible oscillation patterns given by:

H	K	Pattern of oscillation
$\mathbb{D}_3$	$\mathbb{D}_3$	$(P(t), P(t), P(t))$
$\mathbb{D}_1$	$\mathbb{D}_1$	$(P(t), P(t), Q(t))$
$\mathbb{Z}_3$	$\mathbb{I}$	$(P(t), P(t + T/3), P(t + 2T/3))$
$\mathbb{D}_1$	$\mathbb{I}$	$(P(t), P(t + T/2), S(t))$
$\mathbb{I}$	$\mathbb{I}$	$(P(t), Q(t), R(t))$

Table 8.2: Patterns of oscillations in three laser bididirectional rings.

where $S(t) = S(t + T/2)$, i.e., the third unit oscillates with at double frequency than the others. In our laser case, the numerical simulations for typical coupling parameters show that the selected synchronization solution corresponds to the most symmetric pattern where all three lasers oscillate in unison. Rings with a larger number of units can be analyzed in similar fashion and the synchronization solutions can always be associated to one of the oscillatory patterns forced by the symmetry.

Numerical simulations with Ikeda and Hodgkin-Huxley models assembled in different structures have been also undertaken. By changing parameters such as the coupling strength or delay time we have observed how different symmetry-breakings lead to different synchronization solutions. In the bidirectional linking of three Ikeda oscillators we have observed complete identical synchronization of all three units, the identical sync of two oscillators while the third unit is synchronized in a generalized manner with the other two, discrete rotating waves, and non-synchronized solutions. In all cases, such synchronization behaviors and their cross-correlation properties can always be mapped to one of the oscillatory patterns collected in Table 8.2, once the identification $T \sim 3\tau$ has been performed.

8.4   Bidirectional chaos-based communications with semiconductor lasers

In this section we take advantage of the synchronization properties of the open-end configuration of three semiconductor lasers to demonstrate the feasibility of a

chaotic communication scheme allowing for simultaneous bidirectional message transmission over the same communication channel.

The simultaneous exchange of information between two nodes of a communication network is a highly desirable property which is however not always compatible with other technical requirements. In particular, optical chaos-based communication, which has been largely benefitted from a better understanding of the laser dynamics and synchronization, has been limited to unidirectional transmission so far, due to the synchronization properties of the schemes used for these purposes.

While unidirectional transmitter-receiver configurations of chaotic lasers have been successfully demonstrated to send and recover messages in chaos-based real communication schemes [107], their use in bidirectional transmission applications would require the duplication of most of the system components. This solution is clearly inconvenient and advanced bidirectionally coupled schemes are requested.

Two mutually delayed-coupled lasers have also been thought as a possible scheme to overcome the directionality of the message transmission. However, this type of system inherently suffers from a symmetry-breaking that can result in a switching leader-laggard behavior between the lasers. This effect ultimately prevents the simultaneous transmission of information. By introducing a detuning between the free-running optical frequencies of the lasers a permanent control of the leader-laggard role is possible [10]. Lamentably, detuning also induces asymmetric chaos pass filtering properties. Therefore, even if a variation of the detuning allows for a possible mechanism to switch the direction of the information flow, information cannot be simultaneously transmitted from both sides of the communication link.

A scheme that could overcome all the former drawbacks is the configuration in Figure 8.1. As we have seen in precedents sections, a key property of this configuration is the identical synchronization with symmetric properties achieved by the extreme lasers of the array. We will see below how exactly this property is the one that allows for an efficient bidirectional transmission of information between the outer lasers.

At this point, one could ask for the role played by the central laser in a potential communication based on this scheme. In principle, it is just a mediator element assuring the maintenance of the isochronous synchronization between lasers 1 and 3. Moreover, in previous sections we have demonstrated that a central laser with very different characteristics still allows for a robust synchronization between the extreme ones. The natural question that arise in this context is then: do we really need the central element to be a laser at all?

In the following, we demonstrate that if the central laser is replaced by a linear element, whose function will be to linearly redistribute the dynamics between SL1 and SL3, the resulting scheme still maintains the observed synchronization

properties. Moreover, it is expected that such a setup would provide an excellent configuration for the bidirectional transmission of information between two distant points over a single communication channel since it will posses the capability to recover messages by local measurements.

The proposed setup for such a bidirectional communication is sketched in Figure 8.24. Two free-running semiconductor lasers (renamed as SL1 and SL2) are bidirectionally coupled through a semi-transparent mirror (M) placed in the pathway connecting both lasers. Due to the mirror the total light injected in each laser is partially received from its own reflection at the mirror and partially by the light originated at the active region of its counterpart laser. With the configuration shown in Figure 8.24, identical synchronization between the dynamics of both lasers can be obtained for arbitrary distances between the lasers. It is worth to mention that in the following we will show that the position of the mirror is not relevant for the synchronization quality but only shifts the lag between the laser dynamics. Zero-lag synchronization is, for instance, only obtained when the mirror is placed at the middle of the pathway. The reflection and transmission characteristics of the mirror are not important either, provided that the transmission coefficient is above a threshold value that guarantees synchronization to occur.
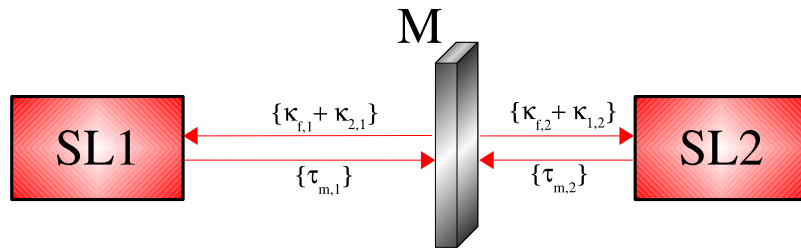
Figure 8.24. Scheme for the simultaneous recovery of bidirectional messages composed by two semiconductor lasers coupled through a semi-transparent mirror.

Numerical simulations of the system are performed using a modified version of the modeling Eqs. (8.1-8.6). The coupling and feedback strengths are those corresponding to a 50% transparent mirror; $\kappa_{1,2} = \kappa_{2,1} = \kappa_{f,1} = \kappa_{f,2} = 20 \text{ ns}^{-1}$. Regarding the coupling delay times we take $\tau_{m,1} = 1.4$ ns and $\tau_{m,2} = 2.4$ ns. The propagation phases in both branches are set to $\phi_{1,2} = \phi_{2,1} = \phi_{m,1} = \phi_{m,2} = 0$ rad.

In the absence of any external perturbation both lasers develop a chaotic behavior when coupled to each other through the semitransparent mirror, as shown in Figure 8.25. From the time traces plotted in panel a) it can be clearly seen that the lasers operate in the coherence collapse regime. To be as general as possible we have placed the mirror closer to one of the lasers (SL2) in order to induce an asymmetry in the two branches of Figure 8.24. Consequently, identical synchro-

nization at zero-lag is not observed. In the inset we plot the cross-correlation function between the output powers P_1 and P_2. It can be seen that the cross-correlation function exhibits its maximum peak at a time lag that amounts to the difference between the coupling times of both lasers with the mirror $\Delta t = \tau_{m,2} - \tau_{m,1} = 1$ ns, with a correlation coefficient of 1. This fact signals an identical synchronization between their dynamics. When the mirror is moved to the center the maximum of the cross correlation function moves towards zero.
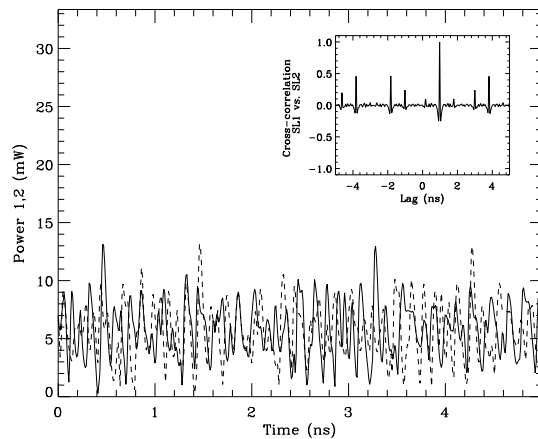
Figure 8.25. Temporal traces of the optical power of SL1 (solid) and SL2 (dashed) under the configuration of Figure 1. The inset shows the cross-correlation function between the two laser outputs.

Once identical synchronization has been proven between the lasers we next proceed to use such a scheme to simultaneously exchange information between SL1 and SL2 by using a single communication channel. We encode the information by simultaneously modulating the bias currents of both lasers with two independent pseudorandom digital messages of amplitude 2 mA at 1 Gbit/s. The two transmitted messages (m_1 and m_2) are shown in panels a) and b) of Figure 8.26. Since the amplitude of the messages is kept small the information is well hidden within the chaotic carriers. The procedure to decipher the messages starts by subtracting the optical power of of both lasers. The synchronization error between the lasers' powers ($P_1(t)$ and $P_2(t + \Delta t)$) allows to reproduce the difference between the messages that have been sent (panel d)) which reproduces the difference between the original messages (panel c)) after the appropriate lag has been compensated for ($m_1(t) - m_2(t + \Delta t)$). After digitalizing this difference only the sender of m_2 can completely recover the content of m_1 and viceversa. As it can be seen in panels e) and f) of Figure 8.26, by this procedure the recovered messages are identical to the encoded ones.

At this point it is worth to discuss the security aspects of our novel configuration scheme. Since both output powers (P_1 and P_2) are accessible from the
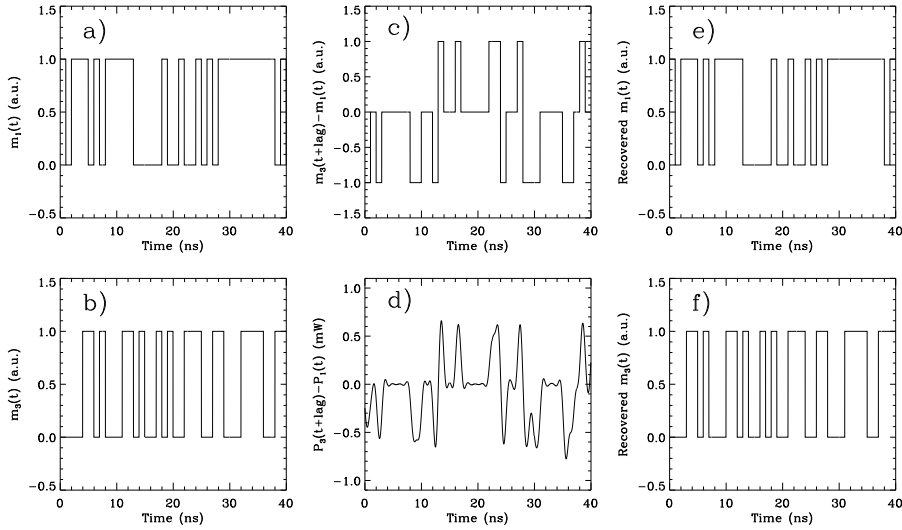
Figure 8.26. Illustration of the message decryption process. Panels a) and b) show the original messages encoded by SL1 and SL2, respectively. Graphics c) reproduces the substraction of messages $(m_1(t) - m_1(t + \Delta t))$ with a given time lag, which is analogically reconstructed by the synchronization error $(P_1(t) - P_2(t + \Delta t))$ in panel d). Finally, the recovery of the message sent by the partner laser (i.e., SL1) is performed by adding to the messages difference the message sent by the own laser (SL2).

same communication channel (a simple beam-splitter easily allows for separating the signals coming from SL1 and SL2) an eavesdropper could easily monitor the difference $P_1 - P_2$ and consequently, the difference in the messages being transmitted. Thus, a level of 1 in the message difference would clearly indicate that at the proper time the bit associated to SL1 was "1" while the bit sent by SL2 was a "0". Similar argument holds when the message difference is -1. Only when the message difference is zero (i.e., both lasers are codifying same bit), the eavesdropper has no clue about which are the bits that are being sent. Hence, this type of mutually-synchronized configurations could be used to simultaneously negotiate a key in a similar fashion than in some quantum cryptography key distribution protocols. Both sides of the link can agree to discard those bits that are different to each other while accepting that the key is formed by the first N bits that coincide with each other. In this way a key is encrypted with the same level of security than in the unidirectional chaos schemes. The main advantage resides in the fact that both sender and receiver now can negotiate a key through a public channel.

Small mismatches between the coupling coefficients or feedback rates have been simulated to confirm the robustness of the scheme. Moreover, the positioning of the mirror in the geometrical center between the two lasers has been also

perturbed without compromising the efficiency of the message recovery. Simultaneous message extraction in schemes presenting mismatches in the coupling times as high as 75 % have been successfully obtained.

8.5 Conclusions

Here, we have proposed a simple network motif in which distant elements interacting with a time delay are nevertheless able to reach a state of zero-lag or isochronous synchronization. In particular, we have focused on studying the synchronization properties of three optically-coupled semiconductor lasers arranged in a open chain configuration.

Numerical results as well as experiments conducted by Michael Peil and Ingo Fischer at the Technical University of Darmstadt, and Javier Buldú, Jordi García-Ojalvo and Mari Carme Torrent from the Universitat Politècnica de Catalunya, have demonstrated that the zero-lag synchronization between two distant lasers can be obtained by relaying their dynamics via a third laser, which surprisingly lags behind the outer synchronized elements. Experimentally, other synchronization solutions where the central element leads the dynamics of the outer lasers have been also observed when a moderate detuning is present between the lasers.

In this chapter we have also checked the robustness of the synchronized solutions against natural detuning, different pump levels, and dynamical perturbations. The numerical simulations and the fact that the zero-lag synchronization was observed in the laboratory indicate the persistence and endurance of the synchronizing mechanism under the presence of mismatches. A difference in the coupling times of the two branches of the chain was observed to still lead to synchronization between the outer lasers once the proper lag was compensated for.

When studying the effect of increasing the number of lasers in the open-end array configuration a zero-lag synchronization between pairs of alternating neighbors was found. In ring architectures, two types of solutions appear; for an odd number of elements all lasers were observed to synchronize at zero lag, while for an even cardinal only alternating neighbors were isochronously correlated. A phase-repulsive interaction between neighbor lasers seems to be able to explain all the synchronization patterns found across the different networks elements.

Finally, in the last section of this chapter we have proposed a simple scheme that allows for bidirectional and simultaneous transmission of information encoded within chaotic carriers. By coupling two semiconductor lasers bidirectionally through a semi-transparent mirror we obtain identical synchronization which has been proven to be very robust. The scheme can be used to exchange an encrypted key through a public channel.

Chapter 9

Concluding remarks

IN this dissertation we have investigated the instabilities due to the mutual interaction between two or more semiconductor lasers. The work was initially motivated by the willing to know the role of a delay, naturally arising as a consequence of the finite distance separating the lasers, on the synchronization properties of coupled systems. Three different schemes were studied: two mutually-coupled semiconductor lasers interacting optoelectronically, two VCSELs in a face-to-face configuration, and three semiconductor lasers arranged in a chain with bidirectional interactions between nearest neighbors.

The results presented in this thesis are mainly based on analytical calculations and numerical simulations of appropriate models (modified rate equations) for interacting semiconductor lasers. However, most of the properties described in the former chapters are expected to be model-independent and thus, to appear in other types of oscillators.

Here the most important conclusions obtained during the realization of this work are highlighted .

Two mutually-coupled semiconductor lasers:

- A delay in the interaction between two mutually-coupled semiconductor lasers is needed for the emergence of instabilities in the system. Instantaneously face-to-face coupled lasers cannot develop any dynamics.

- The route to chaos followed by optoelectronically coupled lasers as a function of the delay is identified in Chapter 6 to be a quasiperiodic route with crisis events.

- Coupling and feedback delay times are found to play very similar roles in

destabilizing bidirectionally coupled lasers.

- The death by delay effect is predicted and experimentally confirmed to occur in the setup introduced in Chapter 6. In particular, we have demonstrated that the addition of delayed feedback loops removes the necessity of a delay in the coupling line between two oscillators in order to observe this quenching effect.

- A delay in the coupling between two interacting semiconductor lasers has also been found to be responsible of a series symmetry-breaking events which can eventually lead to a localized synchronization between the lasers.

- The presence of a delay in the interaction between two oscillators has been observed to improve the capability to lock their oscillations.

Polarization dynamics in coupled VCSELs:

- A new scenario of polarization switchings has been identified in a VCSEL when the mutual coupling strength between two of such devices is enhanced. The periodicity in the appearance of such PS events has been related to the emergence of new compound-cavity modes with higher gain and orthogonal polarization. A hysteresis region is found to surround each PS, which leads to bistable PS interesting for fast optical switching applications.

- Stable elliptic polarization states of light are found by rotating one VCSEL with respect to other in a face-to-face configuration. Moreover, another type of bistable PS is found when the rotation angle is continuosly changed.

- The fully vectorial synchronization between the polarization states of two mutually coupled VCSELs has been numerically demonstrated.

Synchronization of three and more semiconductor lasers:

- Zero-lag synchronization between the distant outer elements of a chain of three semiconductor lasers has been obtained via the relay of their dynamics on a central element. The robustness and stability of such synchronization solution has been tested upon the most typical sources of mismatches and dynamical perturbations.

- The role of the topology of the network linking the lasers and the number of units are also analyzed. The ring structure with an odd number of elements is shown to isochronously synchronize all its members, while the open-end array with an odd number of units allows for the zero-lag sync of the most outer lasers.

- The different synchronization solutions in delay-coupled networks have been proposed to correspond to different spatio-temporal patterns of time-periodic solutions allowed by the symmetry. In particular, after the identification of an effective period with a combination of the coupling delay times in the network has been established, the timing or lags between the chaotic waveforms of the synchronized elements can be predicted from the oscillatory solutions.

- A new chaos-based scheme has been proposed in Chapter 8 which allows the bidirectional exchange of messages in a single communication channel and provides the codification with a given level of security.

A variety of lines for continuing this work are opened depending on the spirit and the vision with which this thesis is viewed.

For optics and laser oriented research it would be very interesting to refine some of the predictions here established with more accurate models and laboratory experiments. In particular, a deeper study of the different PS reported in Chapter 7 constitutes an attractive option with a view to possible applications. The bistable nature of the PS events presented here calls for a better characterization of the energy needed to induce such optical switchings as well as the response times. The origin of the polarization switching induced by the mechanical rotation of one of the VCSELs and the stable elliptic polarization states of light possibly deserve a more careful study than the provided in Chapter 7. Current research is also directed to another synchronization issue in coupled VCSELs. When isolated, each VCSEL can be operated in a bistable polarization regime, where noisy fluctuations induce jumps between two polarization states according to a Kramers law. The idea is to follow the relation between jumps in two VCSELs once they are mutually-coupled. In a more general framework, we would like to study the synchronization of two mutually-coupled bistable systems focusing on the role of the delay in the interaction.

The communication scheme proposed in Chapter 8, which allows for the bidirectional exchange and encryption of information using a single channel, is also a good starting point for growing a more rigorous study of its performance and feasibility as an engineering application. Nevertheless, chaotic based communication

should face at some point the requirement of not only privacy but other standard information security demands such as data integrity, entity authentication, or access control. Of course, the idea of encrypting information in the physical layer can be complemented by software techniques that can perform these and others tasks. In any case a good estimator of the security of message transmission using chaos-based techniques is another more than attractive goal.

Within the framework of the nonlinear dynamics the effect of a delay on the dynamics and synchronization of coupled systems continues being an exciting ingredient to explore. More specifically, the role of the delay as a symmetry-breaking or symmetry-restoring parameter in the dynamics of coupled oscillators needs to be systematically addressed. Our preliminary results in some models of coupled oscillators have suggested the identification of the different chaotic synchronization solutions with the possible patterns of oscillations permitted by the symmetry of the network.

On the other hand, the generation of multirhythms solutions (fourth pattern in Table 8.2) could be of interest for some engineering applications (including optical sciences) where systems oscillating at multiples of a fundamental frequency are needed.

From a more interdisciplinary point of view, the experience and insight gained during the investigation of the simple network motifs of Chapter 8 can be helpful in analyzing the role of the delay in complex networks which appear in many different fields and contexts. Experiments regarding zero-lag synchronization between distant cortical areas of the brain have received a lot of attention since a long time [108]. Such neuronal synchronization is believed to bind different neuronal responses when a subject is performing some cognitive tasks and motivate further studies of the synchronizing mechanisms in realistic neural networks. Current research is going on in order to better understand how simple mechanisms could allow for a stimulus-dependent zero-lag synchronization between pools of neurons which connectivity belongs to the realm of the complex networks.

In conclusion, I consider that the spirit of this thesis has been to contribute a little bit to the problem of coupled oscillators from an interdisciplinary point of view. The fact that the oscillator models used here are semiconductor lasers has enhanced the possibility that the theoretical and numerical predictions could find a real test in the optical tables of different laboratories. Moreover, the interesting and complex dynamics of the real light-matter interaction continuosly challenge and motivate further theoretical studies that toy models can hardly offer.

One of the advantages of this type of research from which I hope I have been benefitted is, as I said before, its interdisciplinary nature. Tools and techniques from different branches (bifurcation theory and nonlinear dynamics, optics, group

theory, etc...) have been used along this thesis. Moreover, analysis of theoretical, numerical, and experimental nature have all been mixed and complemented each other in order achieve our goals.

Regarding the future of the subjects studied here, I consider that the topics of synchronization and delay effects still cover a lot of surprises to basic nonlinear dynamics research and engineering applications, but especially to the modeling and analysis of the life sciences. The more and more popular field of biophysics is offering an incredible large set of challenging situations (where could one find more incredible examples of self-organization of complex systems than in real life?) that are calling for an answer. From biological clocks to central pattern generators, I consider that there is a lot of room for more detailed and physiological meaningful synchronization studies that can help us to better comprehend issues like the organization and tendency to order of the living matter or the generation and maintenance of our biological rhythms, a fundamental issue with important medical and pharmacological applications.

Bibliography

[1] A. Pikovsky, M. Rosenblum, and J. Kurths. *Synchronization: A Universal Concept Nonlinear Science*. Cambridge University Press, 2002.

[2] D. G. Aronson, G. B. Ermentrout, and N. Koppel. Amplitude response of coupled oscillators. *Physica D*, 41:403, 1990.

[3] Z. Neda, E. Ravasz, Y. Brechet, T. Vicsek, and A.L. Barabasi. Self-organizing processes: The sound of many hands clapping. *Nature*, 403:849, 2000.

[4] L. Glass. Synchronization and rhythmic processes in physiology. *Nature*, 410:277, 2001.

[5] S. Strogatz. *Sync*. Hyperion, 2003.

[6] J. Pantaleone. Synchronization of metronomes. *American Journal of Physics*, 70:992, 2002.

[7] L. M. Pecora and T. L. Carroll. Synchronization in chaotic systems. *Phys. Rev. Lett.*, 64:821, 1990.

[8] K. M. Cuomo and A. V. Oppenheim. Circuit implementation of synchronized chaos with applications to communications. *Phys. Rev. Lett.*, 71:65, 1993.

[9] P. Colet and R. Roy. Digital communications with synchronized chaotic lasers. *Optics Lett.*, 19:2056, 1994.

[10] T. Heil, I. Fischer, W. Elsasser, J. Mulet, and C. Mirasso. Chaos synchronization and spontaneous symmetry-breaking in symmetrically delay-coupled semiconductor lasers. *Phys. Rev. Lett.*, 86:795, 2001.

[11] J. Javaloyes, P. Mandel, and D. Pieroux. Dynamical properties of lasers coupled face to face. *Phys. Rev. E*, 67:036201, 2003.

[12] J. Mulet, C.R. Mirasso, T. Heil, and I. Fischer. Synchronization scenario of two distant mutually coupled semiconductor lasers. *J. Opt. B: Quantum Semiclass. Opt.*, 6:97, 2004.

[13] D. V. Ramana Reddy, A. Sen, and G. L. Johnston. Time delay induced death in coupled limit cycle oscillators. *Phys. Rev. Lett.*, 80:5109, 1998.

[14] S. Strogatz. Death by delay. *Nature*, 394:316, 1998.

[15] M. San Miguel and J. V. Feng, Q. Moloney. Light polarization dynamics in surface emitting semiconductor lasers. *Phys. Rev. A*, 52:1728, 1995.

[16] H.G. Winful and L. Rahman. Synchronized chaos and spatiotemporal chaos in arrays of coupled lasers. *Phys. Rev. Lett.*, 65:1575, 1990.

[17] J.R. Terry, K.S. Jr. Thornburg, D.J. DeShazer, G.D. VanWiggeren, S. Zhu, P. Ashwin, and R. Roy. Synchronization of chaos in an array of three lasers. *Phys. Rev. E*, 59:4036, 1999.

[18] F. Rogister, K.S. Thornburg, L. Fabiny, M. Moller, and R. Roy. Power-law spatial correlations in arrays of locally coupled lasers. *Phys. Rev. Lett.*, 92:093905, 2004.

[19] H. Kantz and T. Schreiber. *Nonlinear Time Series Analysis*. Cambridge University Press, 2000.

[20] V. I. Arnold. Small denominators. i. *Izv. Akad. Nauk. Ser. Mat.*, 25:21, 1961.

[21] R. Adler. A study of locking phenomena in oscillators. *Proc. IEEE*, 61:1380, 1973.

[22] D. Gabor. Theory of communication. *J. IEE*, 93:429, 1946.

[23] A. Poularikas. *The Transforms and Applications Handbook*. CRC Press and IEEE Press, 1996.

[24] J.P. Lachaux, E. Rodriguez, J. Martinerie, and F.J. Varela. Measuring phase synchronization in brain signals. *Hum. Brain Mapp.*, 8:194, 1999.

[25] S. Boccaletti, L. M. Pecora, and A. Pelaez. Unifying framework for synchronization of coupled dynamical systems. *Phys. Rev. E*, 63:0662191, 2001.

[26] L. M. Pecora, T. L. Carroll, Johnson G.A., Mar D.J., and J.F. Heagy. Fundamentals of synchronization in chaotic systems, concepts and applications. *Chaos*, 7:520, 1997.

[27] L. M. Pecora and T. L. Carroll. Master stability functions for synchronized coupled systems. *Phys. Rev. Lett.*, 80:2109, 1998.

[28] K. Fink, G. Johnson, T. Carrol, D. Mar, and L. Pecora. Three coupled oscillators as a universal probe of synchronization stability in coupled oscillator arrays. *Phys. Rev. E*, 61:5080, 2000.

[29] N. Rulkov, M. Sushchik, L.S. Tsimring, and H. Abarbanel. Generalized synchronization of chaos in directionally coupled chaotic systems. *Phys. Rev. E.*, 51:980, 1995.

[30] K. Pyragas. Weak and strong synchronization of chaos. *Phys. Rev. E*, 54:4508, 1996.

[31] L. Kocarev and U. Parlitz. Generalized synchronization, predictability, and equivalence of unidirectionally coupled dynamical systems. *Phys. Rev. Lett.*, 76:1816, 1996.

[32] H. D. I. Abarbanel, N. F. Rulkov, and M. M. Sushchik. Generalized synchronization of chaos: The auxiliary system approach. *Phys. Rev. E*, 53:4528, 1996.

[33] Z. Zheng, X. Wang, and M.C. Cross. Transitions from partial to complete generalized synchronizations in bidirectionally coupled chaotic oscillators. *Phys. Rev. E*, 65:056211, 2002.

[34] M. Choi, K.V. Volodchenko, S. Rim, W.H. Kye, and C.M. Kim. Transition from phase synchronization to complete synchronization in mutually coupled nonidentical nd:yag lasers. *Opt. Lett.*, 28:1013, 2003.

[35] M. Zhang, G.M. Wei, and C.H. Lei. Transition from intermittency to periodicity in lag synchronization in coupled rossler oscillators. *Phys. Rev. E*, 65:036202, 2002.

[36] H. U. Voss. Anticipating chaotic synchronization. *Phys. Rev. E*, 61:5115, 2000.

[37] S. Tang and J. M. Liu. Experimental verification of anticipated and retarded synchronization in chaotic semiconductor lasers. *Phys. Rev. Lett.*, 90:194101, 2003.

[38] C. Masoller. Anticipation in the synchronization of chaotic semiconductor lasers with optical feedback. *Phys. Rev. Lett.*, 86:2782, 2001.

[39] M. Cisjak, O. Calvo, C. Masoller, C.R. Mirasso, and R. Toral. Anticipating the response of excitable systems driven by random forcing. *Phys. Rev. Lett.*, 90:204102, 2003.

[40] A. Hohl, A. Gavrielides, T. Erneux, and V. Kovanis. Localized synchronization in two coupled nonidentical semiconductor lasers. *Phys. Rev. Lett.*, 78:4745, 1997.

[41] A. Hohl, A. Gavrielides, T. Erneux, and V. Kovanis. Quasiperiodic synchronization for two delay-coupled semiconductor lasers. *Phys. Rev. A*, 59:3941, 1999.

[42] R. Toral, C.R. Mirasso, E. Hernandez-Garcia, and O. Piro. Analytical and numerical studies of noise-induced synchronization of chaotic systems. *Chaos*, 11:665, 2001.

[43] M. San Miguel and R. Toral. *Stochastic Effects in Physical Systems*. Kluwer Academic Publishers, 2000.

[44] M. Rosemblum, A. Pikovsky, and J. Kurths. From phase to lag synchronization in coupled chaotic oscillators. *Phys. Rev. Lett*, 78:4193, 1997.

[45] T. Schreiber. Measuring information transfer. *Phys. Rev. Lett.*, 85:461, 2000.

[46] Y. Kuramoto. *Chemical Oscillations, Waves and Turbulence*. Springer, 1984.

[47] K. Bar-Eli. On the stability of coupled chemical oscillators. *Physica D*, 14:242, 1985.

[48] J. Rayleigh. *The Theory of Sound*. Dover, 1945.

[49] J. Belair, L. Glass, U. Heiden, and J. Milton. Dynamical disease: Identification, temporal aspects and treatment strategies of human illness. *Chaos*, 5:1, 1995.

[50] D. V. Ramana Reddy, A. Sen, and G. L. Johnston. Time delay effects on coupled limit cycle oscillators at hopf bifurcation. *Physica D*, 129:15, 1999.

[51] R. D. Driver. *Ordinary and Delay Differential Equations*. Springer-Verlag, 1977.

[52] T.L. Saaty. *Modern Nonlinear Equations*. Dover, 1981.

[53] V. Volterra. Sur la theorie mathematique des phenomenes hereditares. *J. Math. Pures Appl.*, 7:149, 1928.

[54] P.J. Wangersky and W.J. Cunningham. Time lag in prey-predator population dynamics. *Ecology*, 38:136, 1957.

[55] N.. MacDonald. *Biological Delay Sytems: linear stability theory*. Cambridge University Press, 1989.

[56] M.C. Mackey and L. Glass. Oscillations and chaos in physiological control systems. *Science*, 197:287, 1977.

[57] A. Bellen and M. Zennaro. *Numerical Methods for Delay Differential Equations*. Oxford University Press, 2003.

[58] N. Olgac and R. Sipahi. The cluster treatment of characteristic roots and the neutral type time-delayed systems. *Journal of Dynamic Systems, Measurements, and*

Control, 127:88, 2005.

[59] K. Pyragas. Synchronization of coupled time-delay systems: Analytical estimations. *Phys. Rev. E*, 58:3067, 1998.

[60] K. Engelborghs, T. Luzyanina, and G. Samaey. Dde-biftool v. 2.00 user manual: a matlab package for bifurcation analysis of delay differential equations. *Technical Report TW-330, Department of Computer Science, K. U. Leuven, Leuven, Belgium*, 2001.

[61] R. Herrero, M. Figueras, J. Rius, F. Pi, and G. Orriols. Experimental observation of the amplitude death effect in two coupled nonlinear oscillators. *Phys. Rev. Lett.*, 84:5312, 2000.

[62] J.M.T. Thompson and H.B. Stewart. *Nonlinear Dynamics and Chaos*. Wiley, 2000.

[63] J.D. Crawford. Introduction to bifurcation theory. *Rev. Mod. Phys.*, 63:991, 1991.

[64] R.C. Hilborn. *Chaos and Nonlinear Dynamics*. Oxford University Press, 2000.

[65] S. Wiggins. *Introduction to Applied Nonlinear Dynamical Systems and Chaos*. Springer-Verlag, 1990.

[66] J. Guckenheimer, P. Holmes, and F. John. *Nonlinear Oscillations, Dynamical Systems, and Bifurcations of Vector Fields*. Springer Verlag, 1997.

[67] M. Golubitsky and I. Stewart. *The Symmetry Perspective*. Birkhauser, 2003.

[68] G. Giacomelli, M. Calzavara, and F.T. Arecchi. Instabilities in a semiconductor laser with delayed optoelectronic feedback. *Optics Comm.*, 74:97, 1989.

[69] C.H. Lee and S.Y. Shin. Self-pulsing, spectral bistability, and chaos in a semiconductor lasers diode with optoelectronic feedback. *Appl. Phys. Lett.*, 62:922, 1992.

[70] N. A. Loiko and A. M. Samson. Possible regimes of generation of a semiconductor laser with a delayed optoelectric feedback. *Optics Comm.*, 93:66, 1992.

[71] E. V. Grigorieva, H. Haken, and S. A. Kaschenko. Theory of quasiperiodicity in model of lasers with delayed optoelectronic feedback. *Optics Comm.*, 165:279, 1999.

[72] S. Tang and J. M. Liu. Chaotic pulsing and quasi-periodic route to chaos in a semiconductor laser with delayed opto-electronic feedback. *IEEE J. of Quantum Electron.*, 37:329, 2001.

[73] F. Y. Lin and J. M. Liu. Nonlinear dynamics of a semiconductor laser with delayed negative optoelectronic feedback. *IEEE J. of Quantum Electron.*, 39:562, 2003.

[74] H. D. I. Abarbanel, M. B. Kennel, L. Illing, S. Tang, H. F. Chen, and J. M. Liu. Synchronization and communication using semiconductor lasers with optoelectronic feedback. *IEEE J. of Quantum Electron.*, 37:1301, 2001.

[75] S. Tang and J. M. Liu. Synchronization of high-frequency chaotic optical pulses. *Optics Lett.*, 26:596, 2001.

[76] J. P. Goedgebuer, P. Levy, L. Larger, C.C. Chen, and W. Rhodes. Optical communication with synchronized hyperchaos generated electrooptically. *IEEE J. of Quantum Electron.*, 38:1178, 2002.

[77] M.W. Lee, L. Larger, V. Udaltsov, E. Genin, and J.P. Goedgebuer. Demonstration of a chaos generator with two time delays. *Optics Letters*, 29:325, 2004.

[78] C. R. Mirasso, P. Colet, and P. Garcia-Fernandez. Synchronization of chaotic semi-condcutor lasers: Application to encoded communications. *IEEE Phot. Tech. Lett.*, 8:299, 1996.

[79] J. M. Liu, H. Chen, and S. Tang. Synchronized chaotic optical communications at high bit rates. *IEEE J. of Quantum Electron.*, 38:1184, 2002.

[80] S. Donati and C. Mirasso. Eds. feature section on optical chaos and applications to crytography. *Eds. Feature section on optical chaos and applications to crytography, IEEE. J. of Quantum Electron.*, 38:1138, 2002.

[81] G.P. Agrawal and N.K. Dutta. *Long-Wavelength Semiconductor Lasers*. Van Nostrand Reinhold, 1986.

[82] A. Yariv. *Optical Electronics*. Saunders College Publishing, 1991.

[83] D. Pieroux, T. Erneux, B. Haegeman, K. Engelborghs, and D. Roose. Bridge of periodic solutions and tori in semiconductor lases subject to delay. *Phys. Rev. Lett*, 87:193901, 2001.

[84] M. Sciamanna, F. Rogister, O. Deparis, P. Megret, and M. Blondet. Bifurcation to polarization self-modulation in vertical-cavity surface-emitting lasers. *Optics Lett.*, 27:261, 2002.

[85] B. Haegeman, K. Engelborghs, D. Roose, D. Pieroux, and T. Erneux. Stability and rupture of bifurcation bridges in semiconductor lasers subject to optical feedback. *Phys. Rev. E*, 66:046216, 2002.

[86] M. Sciamanna, T. Erneux, F. Rogister, O. Deparis, P. Megret, and M. Blondet. Bifurcation bridges between external-cavity modes lead to polarization self-modulation in vertical-cavity surface-emitting lasers. *Phys. Rev. A*, 65:041801, 2002.

[87] F. Rogister, A. Locquet, D. Pieroux, M. Sciamanna, O. Deparis, P. Megret, and M. Blondel. Secure communication scheme using chaotic laser diodes subject to incoherent optical feedback and incoherent optical injection. *Optics Letters*, 26:1486, 2001.

[88] Haijun Su, C. L. Collins, and J. M. McCarthy. Classification of rrss linkages. *Mechanism and Machine Theory*, 37:1413, 2002.

[89] S. Tang, R. Vicente, M. Chiang, C. R. Mirasso, and J. M. Liu. Nonlinear dynamics of semiconductor lasers with mutual optoelectronic coupling. *IEEE J. of Selected Topics in Quantum Electron.*, 10:936, 2004.

[90] J. B. Ermentrout and N. Kopell. Oscillator death in systems of coupled neural oscillators. *SIAM J. Appl. Math.*, 50:125, 1990.

[91] B. F. Kuntsevich and A. N. Pisarchik. Synchronization effects in a dual-wavelength class-b laser with modulated losses. *Phys. Rev. E*, 64:046221, 2001.

[92] R. Kuske and T. Erneux. Localized synchronization of two coupled solid states lasers. *Optics Communications*, 139:125, 1997.

[93] K. D. Choquette, R. P. Schneider, K. L. Lear, and R. E. Liebenguth. Gain-dependent polarization properties of vertical-cavity lasers. *IEEE J. Selected Topics in Quantum Electronics*, 1:661, 1995.

[94] M. Sciamanna, K. Panajotov, H. Thienpont, I. Veretennicoff, O., P. Megret, and

M. Blondet. Optical feedback induces polarization mode hopping in vertical-cavity surface-emitting lasers. *Optics Lett.*, 28:1543, 2003.

[95] Z. G. Pan, S. Jiang, M. Dagenais, R. A. Morgan, K. Kojima, M.T. Asom, R. E. Leibenguth, G.D. Guth, and M.W. Focht. Optical injection induced polarization bistability in vertical-avity surface-emitting lasers. *Appl. Phys. Lett.*, 63:2999, 1993.

[96] N. Fujiwara, Y. Takiguchi, and J. Ohtsubo. Observation of the synchronization of chaos in mutually injected vertical-cavity surface emitting semiconductor lasers. *Optics Lett.*, 28:1677, 2003.

[97] K. Panajotov, F. Berghmans, M. Peeters, G. Verschaffelt, J. Danckaert, I. Veretennicoff, and H. Thienpont. Data transparent reconfigurable optical interconnections using polarization switching in vcsel's induced by optical injection. *IEEE Photon. Technol. Lett.*, 11:985, 1999.

[98] J. Mulet, C. Masoller, and C. R. Mirasso. Modeling bidirectionally coupled single-mode semiconductor lasers. *Phys. Rev. A*, 65:063815, 2002.

[99] R.F.M. Hendriks, M.P. van Exter, J.P. Woerdman, K.H. Gulden, and M. Moser. Memory effect for polarization of pump light in optically pumped vertical-cavity semiconductor lasers. *IEEE J. of Quantum Electron.*, 34:1455, 1998.

[100] H. Erzgraber, D. Lenstra, B. Krauskopf, E. Wille, M. Peil, I. Fischer, and W. Elsasser. Mutually delay-coupled semiconductor lasers: mode bifurcation scenarios. *Optics Communications*, 255:285, 2005.

[101] M. P. van Exter, A. Al-Remawi, and J. P. Woerdman. Polarization fluctuations demonstrate nonlinear anisotropy of a vertical-cavity semiconductor laser. *Phys. Rev. Lett.*, 80:4875, 1998.

[102] M. Sondermann, M. Weinkath, T. Ackemann, J. Mulet, and S. Balle. Two-frequency emission and polarization dynamics at lasing threshold in vertical-cavity surface-emitting lasers. *Phys. Rev. A*, 68:033822, 2003.

[103] J. Martin-Regalado, J. L. A. Chilla, J. J. Rocca, and P. Brusenbach. Polarization switching in vertical cavity surface emitting lasers observed at constant active region temperature. *Appl. Phys. Lett.*, 70:3350, 1997.

[104] P. Besnard, F. Robert, M. L. Chares, and G. M. Stephan. Theoretical modeling of vertical-cavity surface-emitting lasers with polarized optical feedback. *Phys. Rev. A*, 56:3191, 1997.

[105] M. Sciamanna and K. Panajotov. Two-mode injection locking in vertical-cavity surface-emitting lasers. *Optics Lett.*, 30:2903, 2006.

[106] M. Sciamanna and K. Panajotov. Route to polarization switching induced by optical injection in vertical-cavity surface-emitting lasers. *Phys. Rev. A*, 73:023811, 2006.

[107] A. Argyris, D. Syvridis, L. Larger, V. Annovazzi-Lodi, P. Colet, I. Fischer, J. Garca-Ojalvo, C.R. Mirasso, L. Pesquera, and Shore K.A. Chaos-based communications at high bit rates using commercial fibre-optic links. *Nature*, 437:343, 2005.

[108] W. Singer. Striving for coherence. *Nature*, 397:391, 1999.

List of Figures

179

CURRICULUM VITAE

Raúl Vicente Zafra

Personal Data

First name	: Raúl
Surnames	: Vicente Zafra
Date of birth	: 11/23/1979
Place of birth	: Palma de Mallorca, (Spain)
Nationality	: Spanish
Civil Status	: Single
DNI	: 43111438-P
Address	: 100 San Rafael, Palma de Mallorca, Baleares
Post Code	: 07008
Home Phone	: +34 971 246598
Office Phone	: +34 971 172505
e-mail	: raulv@imedea.uib.es
URL	: http://www.imedea.uib.es/∼raulv

Academic Degrees

Degree: M.Sc. in Physics
Center: University of the Balearic Islands
Years: 1997/98-2000/01

Degree: Ph.D. in Physics
Dissertation: Nonlinear Dynamics and Synchronization
of Bidirectionally Coupled Semiconductor Lasers
Center: University of the Balearic Islands
Years: 2006 (July)

Current Affiliation

1. Scolarship holder of a Formación del Personal Investigador (FPI) Fellowship of the Ministerio de Educación y Cultura of Spain since 07/01/2002 at the University of the Balearic Islands.

Awarded Fellowships

1. Fellowship of Ayuda al Estudio del Ministerio de Educación y Cultura in the years 1997/98, 1998/99, 1999/00, and 2000/01.

2. Collaboration Fellowship of the Ministerio de Educación y Cultura with the Physics Department of the University of the Balearic Islands during the academic year 2000/01 with the project "Relativistic Star Models".

3. Collaboration Fellowship under the European Community project OCCULT from 10/01/2001 to 06/30/2002 under the supervision of Dr. Claudio Mirasso.

Other Merits

1. Premio Extraordinario de Licenciatura de Física (First Class Honors), in the year 2000/01.

2. Second position in the local phase (Balearic Islands) of the "VIII Olimpiada Española de Física", February 1997, Palma de Mallorca, Spain.

3. Bronze Medal in the national phase of the "VIII Olimpiada Española de Física", 04/16/1997 to 04/19/1997, Logroño, Spain.

4. Collaborator Student with the Relativity Group of the Physics Department of the University of the Balearic Islands, 2000/01.

5. Student member of the IEEE.

6. Referee for the IEEE International Journal of Quantum Electronics and Physica D.

Specialization Courses

`Ph.D. courses in the University of the Balearic Islands`

- *Mètodes de simulació numérica en física*. R. Toral. UIB, 2002 [3 credits]
- *Sistemes dinàmics*. O. Piro and E. Hernández. UIB, 2003 [3 credits]
- *Dinàmica d'estructures espaciotemporals*. E. Hernández, O. Piro, and M. San Miguel. UIB 2002 [5 credits]
- *Components de sistemes de comunicacions óptiques per fibra*. C.R. Mirasso. UIB 2002 [3 credits]

- *Làsers de semiconductor*. S. Balle. UIB 2002 [3 credits]

- *Punts quantics i nanoestructures bidimensionals*. A. Puente and L. Serra. UIB 2002 [3 credits]

- *Tècniques de supercomputació*. J. Masso. UIB 2003 [3 credits]

- *Models de cooperació basats en agents*. M. San Miguel. UIB 2002 [3 credits]

<u>Other specialization courses</u>

- *Comunicaciones Caóticas*, 07/02/2001 to 07/06/2001 , Santander. Organized by the Departamento de Física Moderna of the Universidad de Cantabria and the Instituto de Física de Cantabria (IFCA).

- *Tecnologías Fotónicas Emergentes: Cristales Fotónicos*, 07/15/2003 to 07/19/2003, Valencia. Organized by the Universidad de Valencia and the Comité de Optoelectrónica y Óptica Integrada de la Sociedad Española de Física.

- *Delay Equations and Applications*, 09/08/2003 to 09/12/2003, Workshop organized by the University of Bristol, UK.

Stays at research centers

- 03/01/2003 to 05/31/2003 at the Electrical Engineering Department, University of California at Los Angeles (UCLA), Los Angeles, CA (USA), under the supervision of Professor Jia-ming Liu.

- 01/28/2004 to 06/31/2004 at the Electrical Engineering Department, University of California at Los Angeles (UCLA), Los Angeles, CA (USA), under the supervision of Professor Jia-ming Liu.

- 11/28/2005 to 12/02/2005 at the Departament de Fisica i Enginyeria Nuclear, Universitat Politecnica de Catalunya, Terrassa, Barcelona, (Spain), under the supervision of Professor Jordi Garcia Ojalvo.

Seminars

- *Open- versus Closed- Loop Performance of Synchronized Chaotic External-Cavity Semiconductor Lasers*, 09/17/2002, Interdisciplinary Physics Department (IMEDEA), Palma de Mallorca, Spain.

- *Bidirectionally Coupled Semiconductor Lasers*, 04/01/2003, Department of Electrical Engineering, UCLA, Los Angeles, USA.

- *Two-Mode Lasers with Added Degrees of Freedom*, 05/13/2003, Department of Electrical Engineering, UCLA, Los Angeles, USA.

- *Simple Interpretation of the Dynamics of Two Mutually Coupled Lasers with Detuning*, 02/09/2004, Department of Electrical Engineering, UCLA, Los Angeles, USA.

- *Dynamics of Mutually Coupled VCSELs*, 06/14/2004, Department of Electrical Engineering, UCLA, Los Angeles, USA.

- *Nonlinear Dynamics of Mutually Coupled Semiconductor Lasers*, 10/20/2004, Interdisciplinary Physics Department (IMEDEA), Palma de Mallorca, Spain.

- *Delay Effects in Coupled Oscillators*, 04/24/2006, Max-Planck Institute for Brain Research, Frankfurt, Germany.

Congress presentations

- *Open- versus Closed- Loop Performance of Synchronized Chaotic External-Cavity Semiconductor Lasers*, 09/06/2002, OCCULT Meeting, Athens (Greece). Oral.

- *Dynamical Properties of Two Mutually Coupled Semiconductor Lasers*, 01/30/2003, SPIE 2003, San Jose (USA). Oral.

- *Analysis and Characterization of the Hyperchaos Generated by Semiconductor Lasers Subject to a Delayed Feedback Loop*, 01/30/2003, SPIE 2003, San Jose (USA). Oral.

- *Complexity and Parameter Mismatch in All-Optical Chaos Encryption Schemes*, 02/14/2003, OCCULT Meeting, Pavia (Italy). Oral.

- *Performance Comparison of Different Encoding Schemes in Chaotic Optical Communication Systems*, 06/27/2003, CLEO-Europe/EQEC, Munich (Germany). Oral.

- *Dynamical Properties of Semiconductor Lasers with Optoelectronic Bidirectional Coupling*, 06/25/2003, CLEO-Europe/EQEC, Munich (Germany). Poster.

- *Analysis and Characterization of the Hyperchaos Generated by Semiconductor Lasers Subject to a Delayed Feedback Loop*, 06/25/2003, CLEO-Europe-EQEC, Munich (Germany). Poster.

- *Dynamics of Two Semiconductor Lasers with Bidirectional Optoelectronic Coupling*, 09/16/2003, Workshop on Dynamics of Semiconductor Lasers, Berlin (Germany). Oral (Invited).

- *Effect of Parameter Mismatch on the Performance of an All-Optical Chaos Communication Scheme*, 09/19/2003, OCCULT Meeting, Beçanson (France). Oral.

- *Analysis and Characterization of the Hyperchaos Generated by Semiconductor Lasers Subject to a Delayed Feedback Loop*, 09/23/2003 to 09/27/2003, Dynamic Days, Palma de Mallorca (Spain), Poster.

- *Simple Interpretation of the Dynamics of Two Mutually Coupled Lasers with Detuning*, 01/28/2004, SPIE 2004, San Jose (USA). Oral.

- *Dynamics of Mutually Coupled VCSELs*, 01/28/2004, SPIE 2004, San Jose (USA). Oral.

- *Dynamics of Mutually Coupled Semiconductor Lasers*, 09/27/2004, XX Trobades científiques de la Mediterranea, Mahon (Spain). Poster.

- *Dynamics of Mutually Coupled Semiconductor Lasers: a potential picture*, 03/30/2005, International Workshop on Physics and Applications of Semiconductor Lasers (PHASE), Metz (France). Oral.

- *Polarization Switching in Mututally Coupled VCSELs*, 03/30/2005, International Workshop on Physics and Applications of Semiconductor Lasers (PHASE), Metz (France). Poster.

- *Polarization Switching in Mututally Coupled VCSELs*, 06/13/2005, CLEO-Europe-EQEC, Munich (Germany). Poster.

- *Dynamics of Three Mutually Coupled Semiconductor Lasers*, 06/13/2005, CLEO-Europe-EQEC, Munich (Germany). Poster.

- *Polarization Switching in Mututally Coupled VCSELs*, 06/28/2005, FISES, Madrid (Spain). Poster.

Publications

Articles

- R. Vicente, T. Pérez, and C.R. Mirasso, "*Open- versus Closed- Loop Performance of Synchronized Chaotic External Cavity Semiconductor Lasers*", IEEE Journal of Quantum Electronics **38**, pp. 1197-1204 (2002).

- J.M. Buldú, R. Vicente, T. Pérez, C.R. Mirasso, M.C. Torrent, and J. García-Ojalvo, "*Periodic Entrainment of Power Dropouts in Mutually Coupled Semiconductor Lasers*", Applied Physics Letters, **81**, pp. 5105-5107, (2002).

- J.M. Buldú, M.C. Torrent, J. García-Ojalvo, R. Vicente, T. Pérez, and C.R. Mirasso, "*Low Frequency Fluctuations Entrainment is Enhanced by Coupling*", Fluctuation and Noise Letters, **3**, pp.127-134, (2003).

- C.R. Mirasso, R. Vicente, P. Colet, J. Mulet, and T. Pérez, "*Synchronization Properties of Chaotic Semiconductor Lasers and Applications to Encryption*", Comptes Rendus de l'Académie de Sciences, Physique, **5**, pp. 613-622, (2004).

- R. Vicente, S. Tang, J. Mulet, C.R. Mirasso, and J.M. Liu, "*Dynamics of Semiconductor Lasers with Bidirectional Optoelectronic Coupling: Stability, Route to Chaos and Entrainment*", Physical Review E, **70**, pp. 46216(1-11), (2004).

- S. Tang, R. Vicente, M. Chiang, C.R. Mirasso, and J.M. Liu, "*Nonlinear Dynamics of Semiconductor Lasers with Mutual Optoelectronic Coupling*", IEEE Journal of Selected Topics in Quantum Electronics, **10**, pp. 936-943, (2004).

- R. Vicente, J. Dauden, P. Colet, and R. Toral, "*Analysis and Characterization of the Hyperchaos Generated by a Semiconductor Laser Subject to a Delayed Feedback Loop*", IEEE Journal of Quantum Electronics, **41**, pp. 541-548, (2005).

- R. Vicente, S. Tang, J. Mulet, C.R. Mirasso, and J.M. Liu, "*Synchronization Properties of Two Self-Oscillating Semiconductor Lasers Subject to Delayed Optoelectronic Mutual Coupling*", Physical Review E, **73**, pp. 047201(1-4), (2006).

- R. Vicente, J. Mulet, C.R. Mirasso, and M. Sciamanna, "*Bistable Polarization Switching in Mutually Coupled Vertical-Cavity Surface-Emitting Lasers*", Optics Letters, **31**, pp. 996-998, (2006).

- I. Fischer, R. Vicente, J.M. Buldú, M. Peil, C. R. Mirasso, M. C. Torrent, and J. García-Ojalvo, "*Zero-lag Long-range Synchronization Via Dynamical Relaying*", Physical Review Letters, , accepted, (2006).

- R. Vicente, Ingo Fischer, and Claudio Mirasso, "*Simultaneous Bidirectional Message Transmission in a Chaos Based Communication Scheme*", , submitted, (2006).

Proceedings

- T. Pérez, R. Vicente, and C.R. Mirasso, "*Dynamical Entrainment of Unidirectionally Coupled Single-Mode Diode Lasers*", Proceedings of SPIE, Physics and Simulations of Optoelectronic Devices X, **4646**, pp. 479-486, (2002).

- R. Vicente, J. Mulet, S. Tang, C.R. Mirasso, and J.M. Liu, "*Dynamical Properties of Two Semiconductor Lasers with Bidirectional Optoelectronic Coupling*", Proceedings of SPIE, Physics and Simulations of Optoelectronic Devices XI, **4986**, pp. 440-451, (2003).

- R. Vicente, J. Dauden, P. Colet, and R. Toral, "*Analysis and Characterization of the Hyperchaos Generated by a Semiconductor Laser Subject to a Delay Feedback Loop*", Proceedings of SPIE, Physics and Simulations of Optoelectronic Devices XI, **4986**, pp. 452-462, (2003).

- R. Vicente, J. Mulet, M. Sciamanna, and C.R. Mirasso, "*Simple Interpretation of the Dynamics of Mutually Coupled Semiconductor Lasers with Detuning*", Proceedings of SPIE, Physics and Simulations of Optoelectronic Devices XII, **5349**, pp. 307-318, (2004).

- S. Tang, M. Chiang, J.M. Liu, R. Vicente, and C.R. Mirasso, "*Experimentally Observed Dynamical Characteristics of Mutually Coupled Semiconductor Lasers With or Without Optoelectronic Feedback*", Proceedings of SPIE, Physics and Simulations of Optoelectronic Devices XII, **5349**, pp. 319-330, (2004).

- R. Vicente, and C.R. Mirasso, "*Dynamics of Mutually Coupled VCSEL's*", Proceedings of SPIE, Physics and Simulations of Optoelectronic Devices XII, **5349**, pp. 331-338, (2004).

- R. Vicente, J. Mulet, M. Sciamanna, and C.R. Mirasso, "*Polarization Switching Dynamics and Bistability in Mutually Coupled Vertical-Cavity Surface-Emitting Lasers*", Proceedings of SPIE, Semiconductor Lasers and Laser Dynamics II, **6184**, 618413, (2006).

Computer experience and languages

- Programming: Fortran, IDL, Basic, Mathematica, Matlab, Maple.

- Operative systems: UNIX, Windows, DOS.

- Languages: Spanish (native), Catalan (native), English (good).